Structural and ion exchange study of nanostructured materials

Alessandro Contini

Keele University

Doctor of Philosophy

August 2024

A volte non si può contare su una formula...

A volte non si riesce a controllare ogni variabile...

A volte... Molte volte... Le cose vengono male...

A volte faremo bruciare la lasagna...

Quindi mangeremo gli avanzi stasera...

Bambini apparecchiate... Vostra madre ha bisogno di tregua...

Elizabeth Zott, Lezioni di chimica

Supervised by: Dr Richard J. Darton

Dr Charles E. Creissen

Research institute: Faculty of Natural Sciences, School of Chemical and Physical Sciences, Birchall Centre.

The project was funded by Keele University.

Abstract

In this thesis, the structural and acidic properties of two zeolites LTL and MAZ are compared and reported. Commercial LTL and MAZ were ion exchanged with metal alkali cations, to obtain the corresponding ion exchanged forms, and characterised by IR spectroscopy, X-Ray diffraction, N_2 adsorption-desorption and SEM-EDX. Attention was given to the interactions of cations with zeolites and to the cation migration mechanism to enter to the structure of the material. The acidic properties of produced materials were evaluated by pyridine adsorption to discriminate Brønsted and Lewis acid sites. X-Ray diffraction analysis and Rietveld method were employed to understand cation migration mechanism involved during the ion exchange process. This was complemented by several investigation techniques, such as N_2 physisorption evaluating the surface area and pore size distribution. Modeling through the application of the Rietveld method was employed to investigate the migration of cations preferential route by producing simulated patterns as a predictive model. Results showed that cations of reduced size were able to reach inner cages at increasing ion exchange steps through the 12MR (main channel) of the zeolite LTL. For zeolite MAZ only the main channels were accessible. Respectively, up to 3 Cs^+ for LTL and 2 Cs^+ for MAZ, per unit cell were found. FTIR results, through Py adsorption, showed preferential poisoning of Brønsted acid sites located in the main cage of LTL after ion exchange with large cations and low BAS concentrations were found in comparison with the samples ion exchanged with smaller cations. The same trend was found for MAZ samples but with lower concentrations of BAS.

In this project zeolites such as LTL, NaX and NaY were also combined with graphite in a uniform mixture which was employed to produce electrodes. The sensing properties of these materials were investigated through potentiometry, cyclic voltammetry and impedance spectroscopy. Sensors were employed to observe the selectivity of the composite materials towards cations in solution by potentiometry. Results for NaX and NaA showed very low response, around 14 mV/decade and far from the target Nernstian response (59.2 mV/decade). In comparison, K-LTL gave a closer response around 44 mV/decade. Cyclic voltammetry was performed on potassium ferricyanide. Results suggested the presence of an irreversible system, which is not in agreement with the redox couple employed and the literature data. These aspects are justified by the insulating nature of the zeolites employed which affected the redox processes occurring at the electrodes. Electrochemical Impedance spectroscopy was also employed to observe the diffusivity aspects related to the cation migration of species from the solution onto the electrode in contact. Results showed high resistance between the substrate and the composite deposited on it, as consequence of a slow electron transfer between these two components.

Acknowledgements

I would like to thank all the people who contributed to my education during the years spent on this PhD project, people that helped me in finding motivation and providing moral support during these challenging years affected by the pandemic.

I am very grateful to my family, my mother Maria, my father Salvatore, my sister Claudia, who supported my choice to leave Sardinia and Italy to begin this unexpected journey in the United Kingdom. I would like to thank Nora, my girlfriend, for her love, support and for her patience (a lot) during the difficult years I encountered after I arrived in this country. She has always been by my side, offering her help to overcome the difficulties that life held here.

Words cannot express my gratitude to Dr Vladimir L. Zholobenko and Dr Aleksandar Radu who gave me the opportunity to start my PhD at Keele. I could not have undertaken this journey without them, who generously provided knowledge, expertise, as well as patience. I would like to extend my sincere thanks to Dr Richard J. Darton and Dr Charles E. Creissen, who supervised me during the last year of my PhD project, providing advice and suggestions. Additionally, this endeavour would not have been possible without the generous support from Keele University, which funded this project.

I would like to thank Dr Richard Jones and Dr Charleene Greenwood for the help provided during my research and for their invaluable expertise in diffraction. I am also grateful to Professor Kamal Vidanapathirana and Professor Kumudu Perera for sharing their knowledge in electrochemistry with me and for the interesting conversations we shared during their stay in the UK.

Many thanks to the people met in LJ: Sarah, Ernesto, Cátia, Salma, Emma, Matt, Isabel, Martin and to the visiting students Sergio, Iván, Miguel, Vullnet, Erjona, Arjeta, Regina, Nataliya and Ostap for their friendship and the great time spent in their company making my studies at Keele an unforgettable experience.

Special thanks to Maestro Mario Sechi for sharing his knowledge with me and for letting me still be part of SK after many years, in spite of the distance, and thanks to all the students of the school for the amazing training sessions with all of them.

I'd like to acknowledge my Italian friends Mabel, Roberto, Alessandro, Ilaria, Nicola, Raffaela, Manuela, Massimiliano, Andrea, Daniele, Gabriele, Walter, Emanuele, Luca and Luigi for showing that, in spite of the distance and living in different countries, friendship can last over time.

I would like to thank my international friends met in Newcastle: Apolo, Griselda, Nemy, Nikos, Edward and Christine for their friendship and for being a great addition to my life.

Thanks to all of you…

Personal statement

During this PhD project, I attended the following workshops and training courses to improve my skills:

- "*Academic English for Postgraduate Science Students*" – module organised by Keele University.
- "*Introduction to teaching and demonstrating*" – module organised by Keele University.
- "*Instrument operation and radiation safety training*"- module organised by Keele University.
- "*Postgraduate Research English*" – module organised by Keele University.
- "*ICDD Clinic on Fundamentals of X-ray Powder Diffraction*" – module organised by International Centre for Diffraction Data.
- "*ICDD In Session - Quantitative Analysis with JADE*" – module organised by International Centre for Diffraction Data.

During this PhD project my research was presented at the following conferences, workshops and symposia.

- "*FEZA 2021*" - Virtual Conference.
- "*Faculty of Natural Sciences Postgraduate Research Symposium*" – 3-minute thesis oral presentation, 2022, Keele, UK.
- "*Keele Chemical Sciences Symposium*" – Poster presentation, 2022, Keele, UK
- "*BZA Annual Meeting*" – Poster presentation, 2022, Durham, UK.

- "*KPA Postgraduate Recognition Awards 2022 - Bob Beattie Postgraduate Recognition Awards*" – 3-minute thesis oral presentation, 2022, Keele, UK.
- "*20th International Zeolite Conference*" – Oral presentation, 2022, Valencia, Spain.

I have received the following awards during my PhD project:

- "*Best 3-minutes thesis – Winner at the faculty of natural sciences"* – 2022 Postgraduate symposium, Keele, UK
- "*Runner-up of the Keele University Three minute thesis 2022*", Keele, UK.

During my PhD project the following papers were prepared:

- F. Sopaj, F. Loshaj, A. Contini, E. Mehmeti, A. Veseli, Preparation of an efficient and selective voltammetric sensor based on screen printed carbon ink electrode modified with TiO_2 nanoparticles for Azithromycin quantification, Results in Chemistry, 6 (2023) 101123.
- W. M. Saod, I. W. Oliver, D. F. Thompson, S. Holborn, A. Contini, V. Zholobenko, Magnesium oxide loaded mesoporous silica: Synthesis, characterisation and use in removing lead and cadmium from water supplies, Environmental Nanotechnology, Monitoring & Management, 20 (2023) 100817.
- W. M. Saod, I. W. Oliver, D. F. Thompson, A. Contini, V. Zholobenko, Zinc oxide – mesoporous silica nanocomposite: preparation, characterisation and application in water treatment for lead, cadmium and chromium removal, International Journal of Environmental Analytical Chemistry, (2023) 1-13.

Papers submitted and under review:

- A. Contini, M. Jendrlin, V. Zholobenko, Structural and acidic properties of the LTL zeolite ion-exchanged with alkali metal cations.
- A. Contini, M. Jendrlin, A. Al-Ani, V. Zholobenko, Structural and acidic properties of ion-exchanged mazzite.

Table of contents

Abbreviations

$[Fe(CN)_6]^{3-}$	Ferricyanide
$[Fe(CN)_6]^{4-}$	Ferrocyanide
12MR	12 membered ring
4MR	4 membered ring
5MR	5 membered ring
6MR	6 membered ring
8MR	8 membered ring
BAS	Brønsted acid sites
BASF	Badische Anilin und Sodafabrik (German company)
BEA	Zeolite Beta
Benzoviologen	1,4-Bis(1,2,6-triphenyl-4-pyridyl)benzene
BET	Brunauer–Emmett–Teller
BJH	Barrett–Joyner–Halenda
CAN	Cancrinite
CHA	Chabazite
CME	Chemical modified electrodes
CV	Cyclic Voltammetry
DFT	Density functional theory
DTA	Differential thermal analysis
EDX	Energy-dispersive X-ray spectroscopy
EIS	Electrochemical impedance spectroscopy
FAU	Faujasite
FTIR	Fourier-transform infrared spectroscopy
GIS	Zeolite gismondine-type
GME	Gmelinite
HEU	Heulandite
ICP-OES	Inductively coupled plasma optical emission spectroscopy
ISE	Ion selective electrodes

ISP	Ion selective pencil
IZA	International Zeolite Association
LAS	Lewis acid sites
LEV	Levynite
LTA	Zeolite Linde Type A
LTL	Linde type L
MAUD	Materials Analysis Using Diffraction
MAZ	Mazzite
MCM-41	Mobil Composition of Matter No. 41
MFI	Mobil Five
MOF	Metal-organic framework
MOR	Mordenite
NaX	Sodium X zeolite
NaY	Sodium Y zeolite
NH_3-TPD	Ammonia temperature controlled desorption
NLDFT	Non-local density functional theory
PET	Polyethylene terephthalate
Py	Pyridine
QMS	Quadrupole mass spectrometers
RGA	Residual gas analyser
SBA-15	Santa Barbara Amorphous-15
SDA	Structure-directing agent
SEM	Scanning electron microscopy
SOD	Sodalite
TEM	Transmission electron microscope
TEOS	Tetraethylorthosilicate
TGA	Termogravimetry
TMA^+	Tetramethylammonium cation
TMOS	Tetramethylorthosilicate
VESTA	Visualization for electronic and structural analysis

XRD	X-ray diffraction
XRF	X-ray fluorescence
ZME	Zeolite modified electrodes
ZSM-5	Zeolite Socony Mobil five

Chapter 1

Introduction

1.1 History

In the field of material science, the structure of a material defines its properties and applications. A class of materials, of which the structure represents an important aspect, is the group of porous materials. Their properties, such as high surface area and pores dimension, make these materials suitable for many applications. Also, they may cover important roles in many fields such as purification of water, heterogeneous catalysis, separation and storage of gases and sensors science. Among porous materials, there is a kind, which shows remarkable properties. Their name is zeolites.

The history of zeolites began in 1756. This group of materials was given its name when the Swedish mineralogist and founder of modern mineralogy A. F. Cronstedt described two specimens of unknown materials; they exhibited moisture on its surface and intumescence upon heating in a blowpipe flame, and he recognized them as members of a new class of minerals [1], [2]. Cronstedt's evidence represents the first documented experience in the science of zeolites and he reported the properties of these materials in a paper titled "Observation and description of an unknown mineral species, called zeolites". He described them as a new type of hydrated minerals, which shows unique fronting features. Through the observation of the behaviour showed by these "boiling stones" he coined the term "zeolite" from the greek zéō (boil) and lithos (stone). In his paper, Cronsted described three zeolite types named in Latin: "*particulis impalpabilibus*", "*spatosus*" and "*crystallisatu*" [3].

His discovery set the beginning of the research of natural zeolites under chemical, physical and mineralogical aspects. However, at the time of the discovery, the short availability [4] of material and the limited capabilities to study the structural aspects inhibited the research on these class of materials. However, research efforts, although sparse in part for the previous listed reasons, did not stop during the next 200 years and many researchers provided their contribution to zeolite science by setting the foundation for today's applications of natural and synthetic zeolites.

Among them, Sainte-Claire Deville gave his contribution when in 1862 conducted a study about the composition of natural aluminosilicates. In his paper entitled "Reproduction of the Lévyne" [5], he reported the first hydrothermal synthesis of a zeolite called "levynite" (LEV) an alkaline aluminosilicate with similarities to natural zeolites.

In 1896, Friedel [6] developed the idea that dehydrated zeolites consist of a structure with open spongy frameworks. This description came from the observation of various liquids occluded by these materials. In 1910, Grandjean observed adsorption of molecules like ammonia, hydrogen and air on chabazite [7].

However it was only few years later that the interest in the field of zeolites was regained when, in 1925, Weigel and Steinhoff reported the first molecular sieve effect noticing the selectivity of chabazite [8] in adsorbing liquids such as water, methanol, ethanol and formic acid and observing at the same time the exclusion of diethyl-ether, acetone and benzene.

Based on these studies, McBain, in 1932 [9], defined porous solid materials that act as sieves on a molecular scale by calling this class of materials "molecular sieves". These studies prepared the ground for many other processes described in the literature such as ion exchange, adsorption and molecular sieving associated with zeolites. In 1944 Barrer reported the separation of linear alkanes such as propane, *n*-butane, *n*-pentane, from their branched isomers using chabazite [10]. The molecular sieving property attracted the interest of researches in the field, however the number of natural zeolites represented a limit along with the contamination of these materials by other minerals such as metal and quartz. The need to produce zeolites by synthesis pushed in 1948 R. M. Barrer with R. Milton to prepare synthetic zeolites as an alternative to natural zeolites, and this attempt revolutionised the field [11]. Although, it was not the first case, since Sainte-Claire Deville performed a synthesis before them, the success of R. M. Barrer and R. Milton was revolutionary because they reported the first case of synthetic zeolite with no naturally occurring counterpart through the synthesis of mordenite zeolite starting from sodium aluminosilicate gels and performed under high temperature and pressure conditions.

The importance of their contribution can be explained by considering that today among ~260 known zeolites only 67 are natural while almost 200 are synthetic [12]. The preparation of zeolites through a synthetic route was attempted during the following years from only inorganic systems. These attempts increased the number of zeolites with the addition of zeolite P, zeolite Q by R. M. Barrer [13] and zeolites A, B and C prepared by R. Milton [14]. There is no doubt that the development of characterisation techniques, such as X-Ray powder diffraction [15], contributed to the progress of the field since without them it would have been impossible to identify and confirm structural aspects related to these materials.

In 1965 Barrer gave another contribution to the synthesis of zeolites. He introduced the structure directing agents (SDA). Aiming to control pore size and volume during the synthesis. In addition, the use of SDA allowed the synthesis of high silica zeolites such as BEA and MFI, with Si/Al ratios from 5 up to 100.

The official definition of zeolites arrived in 1997 and it was presented by IZA. They stated:

"*A zeolite mineral is a crystalline substance with a structure characterized by a framework of linked tetrahedra, each consisting of four O atoms surrounding a cation. This framework contains open cavities in the form of channels and cages. These are usually occupied by* H_2O *molecules and extra-framework cations that are commonly exchangeable. The channels are large enough to allow the passage of guest species. In the hydrated phases, dehydration occurs at temperatures mostly below about 400°C and is largely reversible. The framework may be interrupted by (OH,F) groups; these occupy a tetrahedron apex that is not shared with adjacent tetrahedra*. [16]". It can be seen from this definition that zeolites are not a class of materials restricted only to silicon and aluminium but they include AlPOs (aluminophosphates), SAPOs (silico-aluminophosphates), MeAPOs (metal-containing AlPO) and MeAPSOs (metal-containing SAPO).

Because of their properties such as uniform microporosity, ion exchange capacity and framework acidity along with thermal stability, these unique materials attracted the attention of many researchers with the aim to find solutions for different needs. Over time, this research area has grown since many other applications for these materials have been discovered.

1.2 Classification of porous materials

According to IUPAC nomenclature [17] and to more recent papers [18], porous systems can be divided into groups on the basis of the average diameter of pore structure and the chemical nature of the pore wall. IUPAC subdivides porous materials in three groups:

- **Microporous materials**: pore diameters smaller than 2 nm (Zeolites, $AlPO_4$).
- **Mesoporous materials**: pore diameters between 2 and 50 nm (MCM-41, MCM-48).
- **Macroporous materials**: pore diameters greater than 50 nm (Porous gel).

Pores can differ from each other depending on the types of accessibility and shape. Pores can be closed, open, blind and through with different levels of accessibility. Pores can show a cylindrical shape, open or blind, ink-bottle shaped, funnel shaped and roughness (Figure 1.1).

Voids in a material show different geometries. They can be isolated cavities, parallel channels or even three dimensional structures with interconnected pores.

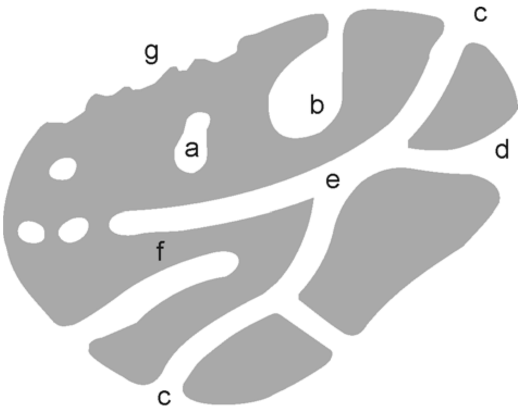

Figure 1.1: Cross section scheme of a porous material. Accessibility: (a) Closed pores, (b, c, d, e, f) open pores, (b, f) blind pores (dead end), (e) through pores. Shape: (f) cylindrical blind, (b) ink bottle shaped, (d) funnel shaped, (g) roughness. Adapted from reference [19].

In addition, there are systems with permanent and non-permanent porosity. The first case describes those materials that maintain the ordered and porous structure after the removal of the solvent or templating agent; the non-permanent porosity is typical of a material that when crystallised, under suitable conditions after the removal of the solvent, undergoes a collapse of the structure. Porous materials can also be classified into crystalline, and amorphous. A crystalline system is highly ordered including pore shapes and distribution. However, being crystalline not a necessary condition for high porosity, needed, there are examples of amorphous systems that show high levels of porosity. As well as mesoporous silica such as SBA-15, MCM-41 is an example of amorphous porous material. Compared to zeolites MCM-41 shows larger pore sizes and unless it is Al-doped, it does not show significant acidic properties [20][21]. Another interesting class is represented by hybrids, such as MOF and organosilica, which combine of organic and inorganic components showing properties that differ from the individual ones.

In conclusion, porous materials can be also classified depending on the chemical nature of the system:

- **Inorganic systems**: porous silica, zeolites.
- **Hybrid systems**: organosilica, MOF
- **Organic systems**: porous organic polymers.

1.3 Structure of zeolites

Zeolites are a class of porous materials defined as crystalline aluminosilicate and structured with a 3D framework. Their structure is based on a rigid anionic framework which consists of TO_4 tetrahedra where a T atom may be Si or Al. Si and Al are surrounded by 4 oxygen atoms (SiO_4, AlO_4) and are interconnected by sharing corners. SiO_4 and AlO_4 are considered primary building units (Figure 1.2) of the zeolite structure.

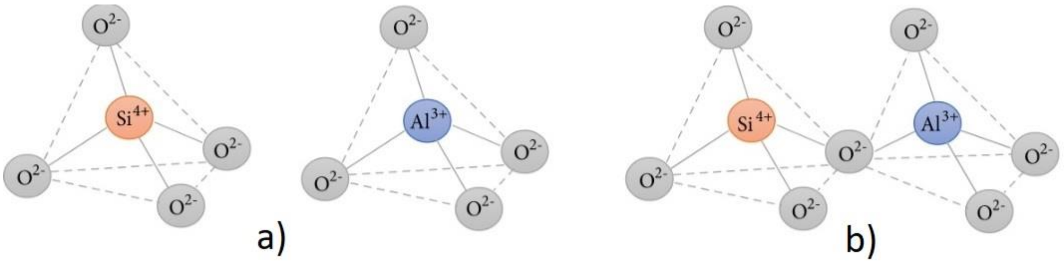

Figure 1.2: a) TO_4 tetrahedra, b) Corner-sharing TO_4 tetrahedra. Picture adapted from reference [22].

Since TOT bonds angles are very flexible and they can vary between 130 and 180 degrees, several structures can be obtained. These patterns called secondary building units (Figure 1.3) consists of up to 16 T atoms with 18 different ways of combinating the TO_4 tetrahedra [23].

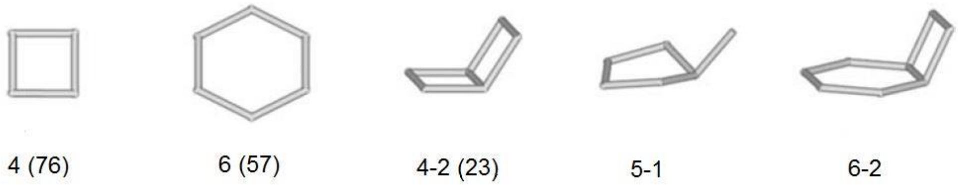

Figure 1.3: Selection of most common SBUs. Picture adapted from ref [24].

The combination of such units generates cages (figure 1.4) and a well-defined pores system, which intersects cavities and contains exchangeable metal cations. The structure of a zeolite is open due to the presence of such pore openings and of the dimensionality of the channel system. Pore openings depend on the size of the ring, which are described by using the term **n-membered ring** where **n** represents the number of T-atoms in the ring itself, which usually corresponds also to the number of oxygen atoms.

According to the value assigned to “n” in “n-membered ring”, pores can be classified as small, medium or large pore openings when **n** is respectively 8, 10, 12 but it is important to consider that pores can be also distorted. The different types of SBU and their combination can also give a specific zeolite structure.

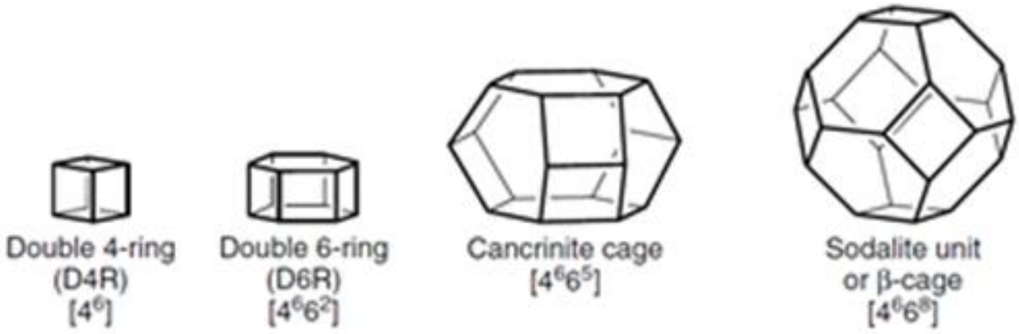

Figure 1.4: Zeolite subunits and cages. Pictures adapted from ref [25].

In addition, depending on their combination, SBU can produce a wide range of chains and 2D networks which are also interconnected. Also, channels, of different size and shape, can be obtained. Chains are used to describe frameworks (Figure 1.5) [25]. Double zig-zag chain, double sawtooth and Narsarsukite chain are some examples and it is common to find them even in single chain form. Some of them can be found in specific zeolites such as Narsarsukite chain, which is found more in $AlPO_4$ structures than in silicates.

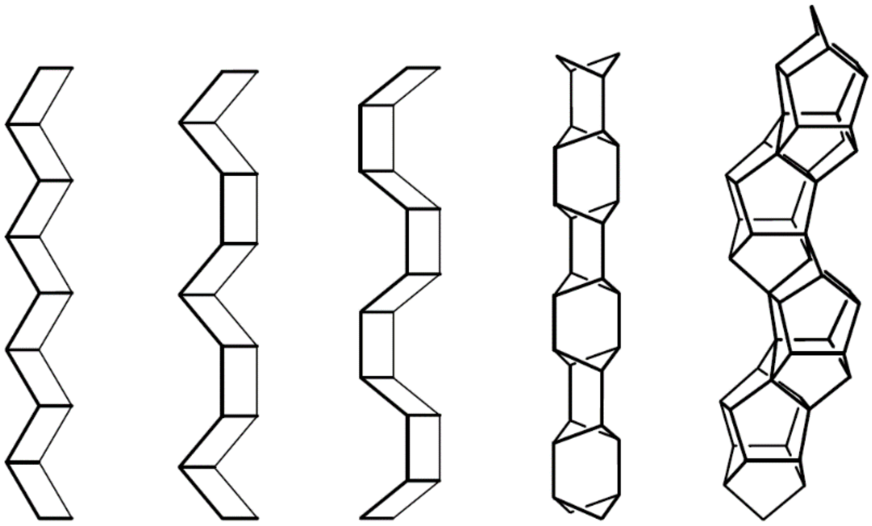

Figure1.5: Types of chains in zeolites. Pictures adapted from ref [25].

Channel walls of zeolites are also used to describe zeolites frameworks (Figure 1.6) [25]. They consist of 6MR such as in the case of 6-ring wraps. Also a 2-dimensional, 3–connected sheets or nets are used to describe frameworks structures such as 4.8^2 net where in this case its structure is a combination of 4-membered ring and two 8-membered ring.

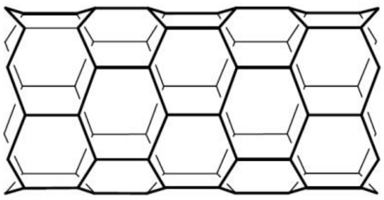

Channel wall in **AFI**

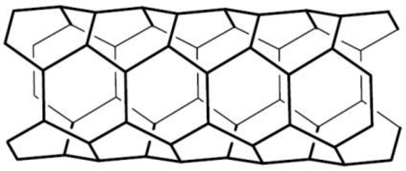

Channel wall in **CAN**

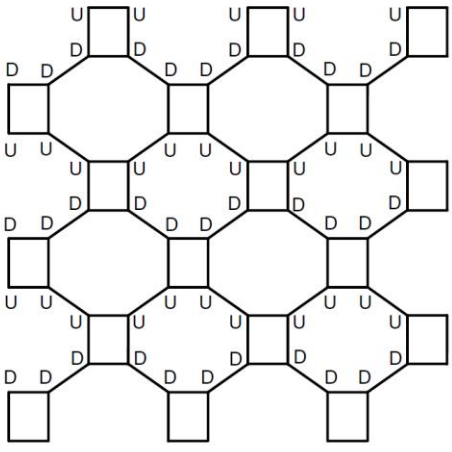

4.8^2 sheet or net

Figure 1.6: Walls and nets of zeolites. Pictures adapted from ref [25].

The rules to describe these nets and sheets structures are similar to those used for cages. The net in Figure 1.6, for instance, shows that each node is associated with one 4-membered ring and two 8-membered rings and according to these rules this is why it is designated as 4.8^2. In addition, net and sheet structures show an orientation where points go up or down from the plane of the sheet. This information can be given by using “U” and “D” letters (UP and DOWN from the sheet). The example in Figure 1.6, where the net is depicted, describes the GIS framework type where half of the connections of each 8-membered ring points up and the other half points down. In some cases, to describe the stacking sequence of layers of closest packed atoms in metals or oxides, cages and rings of a zeolite framework the ABC system is used. This terminology is typical of families of zeolites framework such as SOD and CHA (Figure 1.7) [25].

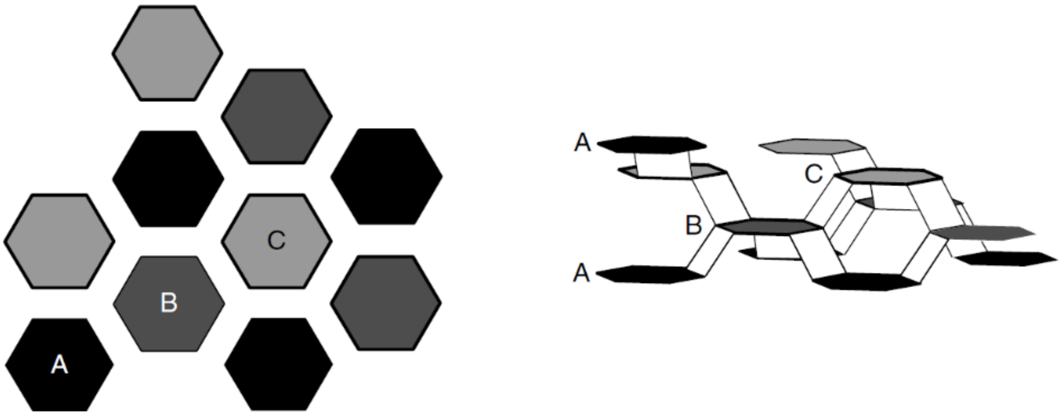

Figure 1.7: ABC Stacking of 6-rings. Pictures adapted from ref. [25].

All these single sets of coordination systems, when considered together, make a unique structure and this makes it simple to recognise if a framework is novel or not.

Depending on how these units are linked, it is possible to obtain different structures. As an example it is reported the formation of LTA zeolite below (figure 1.8)

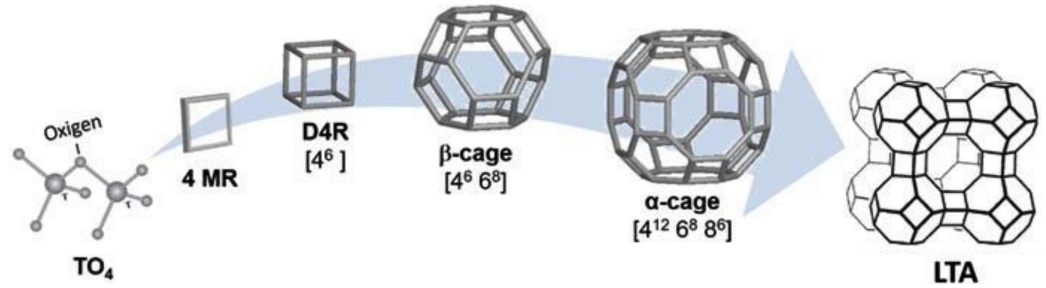

Figure 1.8: PBUs (TO_4) forming the SBUs and formation of the LTA structure (zeolite A). Picture adapted from reference [26].

So far 235 zeolite structure are known and each type is labelled with a 3 letters symbol code according to "Structure commission of international zeolite association" [12][27].

The general formula of a zeolite is $M_{x/n}\cdot[Al_x\cdot Si_y\cdot O_2(_{x}+_{y})]\cdot mH_2O$ where M represents a cation of valence "n" (Li^+, K^+, Mg^{2+}). A cation neutralizes the resulting (negative) formal charge on the aluminosilicate frameworks when a process of isomorphous substitution occurs. In this process, a Si atom is replaced by an Al atom which affects the electro-neutrality because of a lower formal charge resulting in an electrical imbalance. Other trivalent ions can replace Si in the zeolite structure like Fe^{3+}, Ga^{3+} as well as In^{3+} and B^{3+}, however, Al^{3+} is the most common.

According to the "Löwenstein's rule" [28] zeolite framework cannot incorporate more aluminium than silicon, which excludes the presence of Al-O-Al bonds. Aluminium atoms in the structure can be only surrounded by oxygen bridges with four silicon atoms, which results in a Si/Al ratio that is at least one or greater than one.

Cations held in cavities preserving the electro-neutrality of the zeolite can also be exchanged.

Channel structures in zeolites consist of 1D, 2D and 3D channel systems (Figure 1.9). Some zeolites show a mixing of different channel systems.

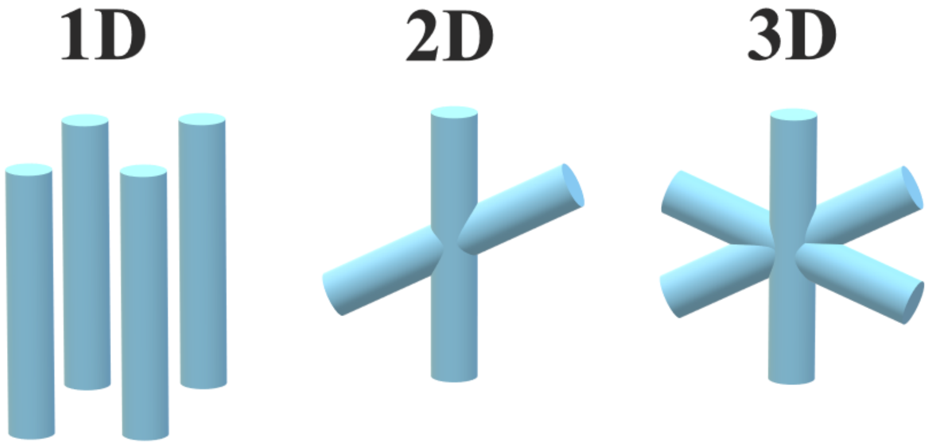

Figure 1.9: Channel systems in zeolites structure.

A notation has been adapted to describe channels in the various framework taking into account the channel direction relative to the type material structure, the number of T-atoms that form the rings and the crystallographic free diameters of the channel in Å unit. The number of asterisks, in addition, indicate if the system is 1-, 2-, or 3-dimensional. Interconnected channels are indicated by a double arrow (↔), and if there is no direct access between different channel systems, a vertical bar is used (|) [12]. Below are reported some examples:

- CAN is an example of 1D system parallel to [001] with 12-membered ring circular apertures. According to the rules listed above, its notation is: [001] 12 5.9 x 5.9* [12].

- MOR-type zeolite possesses a one-dimensional (1D) channel system of a combination of elliptical parallel 12-membered ring (12-MR) micropores (0.67 x 0.70 nm) along the c [001] direction. Its notation is: ([001] 12 6.5 x 7.0* ↔ {[010] 8 3.4 x 4.8 ↔ [001] 8 2.6 x 5.7}*) [12].

- BEA (<100> 12 6.6 x 6.7** ↔ [001] 12 5.6 x 5.6*) and MFI ({[100] 10 5.1 x 5.5 ↔ [010] 10 5.3 x 5.6}***) are two examples of 3D channel system. [12].

- FAU: <111> 12 7.4 x 7.4*** [12].

In addition, notations of systems that will be studied in this project are reported:

- MAZ structure is composed of 1D and 3D 12-and 8-MB ring channels, respectively: [001] 12 7.4 x 7.4* | [001] 8 3.1 x 3.1* [12].

- LTL frameworks is comprised of 1-D pores with 12- and 8-membered ring apertures: [001] 12 7.1 x 7.1* [12].

Zeolites have many interesting properties and are used for many different purposes. Many of their applications are the consequence of their structures and of their porous systems. This allowed to use these materials in a wide range of applications such as molecular sieves in purification of water and laundry detergents, as catalysts in petrochemicals industries and in agriculture and also in medicine. Zeolites are also used for gas separation applications due to their adsorption properties.

1.4 Synthesis of zeolites

Zeolites can be natural or synthetic. In the past, research in this field was focused on studying natural zeolites. Synthetic zeolites and their synthesis methods arrived only later representing the expansion of zeolite science.

The discovery of synthetic zeolites was described in the pioneering work of Barrer where, he attempted the synthesis of mordenite zeolite using reactive silica and alumina as reagents under hydrothermal conditions at high alkaline pH. Through a process of copolymerisation of the silicate and aluminate ions, he obtained a gel which was heated in an autoclave for several days and that generated a condensated zeolite. Synthetic zeolites show a wide range of useful properties like higher purity, thermal stability as well as a more uniform particle size [29], [30]. They can be engineered with a wide variety of chemical properties, different pore sizes and an improved thermal stability.

Synthesis of zeolites starts from standard chemical reagents, which are a silica source and an alumina source. The conventional synthesis procedure consists of mixing a silica and an aluminate solution with alkali hydroxides with also organic bases. From this reaction, it is obtained an aluminosilicate gel. The hydrothermal crystallisation of this gel is performed in a closed hydrothermal system under conditions of increasing temperature, autogenous pressure and time, which varies from few hours to days.

Alongside reagents and the factors presented above, a list of additional parameters must be taken into account during the synthesis.

- **Batch composition:** the reaction mixture of the reactants significantly affects the final crystallized products. The influence of batch composition on the resulting phases was demonstrated by Breck's work [31]. Na_2O-

Al_2O_3-SiO_2-H_2O system with 90-98% of water was prepared at 100 °C using sodium silicate as the source of silica. The obtained products were zeolites A, X, Y, B and HS. A different result was obtained by decreasing the water content to 60 – 85%. In this case, only zeolite HS (SOD) was obtained. A different result was reported by using colloid silica instead of sodium silicate as the silica source. In this case, the obtained phases were zeolites A, X and Y along with zeolites R (CHA) and S (GME).

A system such as K_2O-Al_2O_3-SiO_2-H_2O at 100 °C with a water content of 95–98% allowed to obtain zeolite W and H as resulting phases.

- **Si and Al sources:** the nature of reactants plays a key role in the crystallisation of the final products. Sodium waterglass, colloidal silica, fumed silica, tetramethylorthosilicate (TMOS) and tetraethylorthosilicate (TEOS) are example of reactants used as silica source. The choice of the source differing in reactivity and solubility may influence nucleation and crystallisation. Among the parameters that could affect the crystallisation step, surface area of material plays a key role. It is reported that for the synthesis of zeolite LTL, depending on the silica source chosen and on its surface area it may affected crystallization rate, the crystal size and the particle size distribution of the final product [32]. Silica sources with high surface area are much more easily dissolved in a basic medium and allow a faster nucleation step as well as the formation of smaller crystals. Lower surface areas show the opposite behaviour in terms of nucleation and crystal size. Al sources as well have influence on the crystallization step. In zeolite synthesis, some of the examples of the most commonly used are sodium aluminate, pseudo-boehmite, aluminium hydroxide, aluminum nitrate and aluminum sulfate. For instance, the effect of the Al source used in the synthesis was investigated for the preparation of high silica mordenite [33]. It was found pure MOR-type zeolite when $AlCl_3$ and $Al(NO_3)_3$ were used as Al source. With $Al_2(SO_4)_3$ zeolite beta BEA was obtained.

- **Si/Al ratio:** This parameter affects physical properties, structure and composition of the crystallized products. In general, it has been found that reaction mixtures with low Si/Al ratio in alkaline environment were used to prepare zeolites with Si/Al ≤ 5 such as Zeolite A (LTA), X (FAU) and hydroxysodalite (SOD). Zeolites with Si/Al>5 were prepared from reaction mixture with high Si/Al ratio in alkaline environment. However, there is not quantitative correlation between the ratio of the initial reaction mixture and the result. Also, the Si/Al ratio of the final products cannot be easily adjusted by changing the Si/Al ratio of the initial reaction mixture. However, it was reported in the work of Corma et al. the synthesis of pure silica zeolite LTA [34]. Typically, LTA zeolite show a Si/Al ratio of 1 but in this work it was synthesized with a framework Si/Al ratio of 3. Also in this paper a series of materials named ITQ-29 were prepared with Si/Al ratio up to infinity (pure silica) using a supramolecular organic structure-directing agent.
- **Alkalinity:** Many zeolites are prepared from the crystallisation of Na_2O-Al_2O_3-SiO_2-H_2O systems. In this case, the alkalinity is defined as OH^-/Si ratio or H_2O/Na_2O. For these systems, high alkalinity increases the solubility of Si and Al sources. In addition, it decreases the polimerisation degree of silicate anions and increases the polymeration of polysilicate and aluminate anions. The increase in alkalinity shortens the induction and nucleation periods and accelerates the crystallisation of the product. It is

reported in reference [32] that zeolite LTA with molar composition $5Na_2O:Al_2O_3:2SiO_2$: (100–200)H_2O at 70 °C, showed an decreasing effect on the particle size due to the increase of alkalinity.

- **Structure directing agents:** during the synthesis of a zeolite, the presence of organic molecules may have a structure directing role. These molecules usually are quaternary ammonium cations such as tetramethylammonium (TMA^+) and aluminophosphate molecular sieves using organic ammines as templates. These molecules, during the gelation or nucleation process, organise oxide tetrahedral into a particular geometric topology around themselves generating a particular structure.

- **Temperature of the process:** Temperature plays a key role in the synthesis of zeolites and especially during the crystallisation process and the crystal size. Nucleation and crystal growth are strongly affected by the temperature. Particularly, temperature increases the crystal growth over the nucleation rate [35], [36] which is inversely proportional to the former. Higher growth rates and larger crystals have been obtained at higher temperatures. Temperature not only affects crystal size but also affects morphology.

- **Time.** Alongside the temperature of the process, time also affects the synthesis. Crystallinity increases with time. Zeolites are metastable phases and during the synthesis they appear first and then, more stable phases replace them and each other. With a longer crystallisation time, for instance, zeolite A (LTA) and zeolite X (FAU) dissolve and form respectively zeolite sodalite (SOD) and zeolite P (GIS) in alkaline aluminosilicate gel.

The synthesis of zeolites can be carried out by using a continuous or semi-continuous mode making these procedures compatible for industrial applications.

Zeolites are mainly prepared by using hydrothermal, solvothermal or ionothermal methods.

1.4.1 Hydrothermal method

Hydrothermal synthesis has became the basic route for zeolite production since the pioneering work of Barrer and Milton for these material [11], [14]. This synthesis method refers to reactions, which occur under conditions of high temperature, in a range between 90 – 180°C, and high pressure. These reactions occur in a closed system and in aqueous solution, where water or a base solution can act as mineralizer. The hydrothermal synthesis method is also applied for the production of chemical sensors, electronically conducting solids and also for magnetic materials.

Among the advantages that this approach offers, in terms of high reactivity of reactants, we can list the easy control of solutions, formation of metastable phases, reduced air pollution and low energy consumption. The hydrothermal synthesis of zeolite materials is performed in sealed vessels. Attention must be payed to the high autogenous pressures and the elevated temperatures generated in these closed systems due to the pressures of reactants. All chemicals involved in the synthesis reacts in a stainless steel autoclave (Figure 1.10).

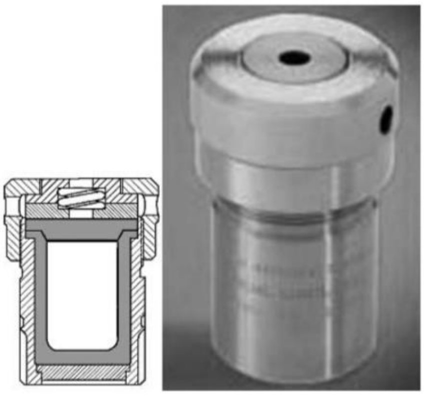

Figure 1.10: Example of stainless-steel autoclave. Picture adapted from http://www.parrinst.com.

The models shown above are suitable for reaction in strong acidic or alkaline media and are lined with a thick wall of Teflon for use at elevated temperature and pressures up to 250°C and 124 bar. There are also larger capacity autoclaves that can work even at higher pressures with volumes up to 100 ml. Compared to other methods, the hydrothermal synthesis occurs at lower temperature and it is cheaper [37].

1.4.2 Solvothermal method

In this method, no water is added to the reaction mixture because the reagents themselves generate it. The solvothermal is a synthetic method that uses organic or mixed organic-water solvents instead of water, it has been developed and applied for the synthesis of zeolites. The first patent of this method was reported in 1982 by BASF for the synthesis of ZSM-5 (MFI) where ether, as well as ether-water mixtures, have been used as solvents. For non aqueous solvent mediated synthesis is commonly observed a slow reaction rate due to the lower solvating ability compared to water. Viscosity of non-aqueous solvents also plays a key role during the synthesis as it affects the crystallisation. Higher viscosity reduces mass transfer by convection and generates large crystals. Through this method many high silica zeolites have been prepared and after crystallisation with resulting large crystal size. Later on, in the 90s various alcohols also have been used as solvent for this synthesis method [38], [39]. In this case the solvent not only represents a medium but also dissolves or partially dissolves the reactant with the result to form solvent-reactant complexes that affect the chemical reaction rate. The solvent can vary from non-polar and hydrophobic to polar and hydrophilic [30]. The polarity is an important parameter to describe the solvating property of the solvent and it represents the sum of the interactions between solvent and solute (coulombic, induction and dispersion forces) and this influences the structure of the final materials produced.

1.4.3 Ionothermal method

Morris and co-workes, reported this method for the first time in 2004. It was employed for the synthesis of aluminophosphate zeolite and it involved the use of ionic liquids and eutectic mixtures as solvent. It was distinguished from hydrothermal and solvothermal procedures for the different kind of solvents utilised [40]. In this synthesis, 1-methyl-3-ethylimidazolium bromide was used as the solvent and template to prepare four different open frameworks. The ionic liquid solubilized the starting materials almost completely at the reaction temperature. According to these studies the synthesis depends strongly on the ionic character of the solvent since molecular water disrupt the process preventing the formation of zeolite. The templating effect depends on the interaction between cations of the ionic liquid and cations of the framework species. Compared to the hydrothermal route, the ionothermal method has the advantage to remove the competition of template-framework interactions and solvent-framework interactions. In addition, since ionic solvents have low vapour pressure, the ionothermal synthesis eliminates the safety concerns of the hydrothermal method related to the high autogenous pressure. Ionothermal method has been also coupled with microwaves as some ionic solvents are good microwave absorbers while acting also as SDA. Microwave-enhanced ionothermal synthesis has also shown fast crystallisation rate, low synthetic pressure and high structure selectivity.

1.4.4 Other synthetic routes

Additional synthesis methods are the F^- synthetic route, microwave-assisted hydrothermal synthetic route, microemulsion-based hydrothermal synthetic route, dry-gel conversion synthetic route and combinatorial synthetic route.

The hydrothermal synthesis is the most used method for zeolites synthesis. Starting materials used to synthetise zeolites consist of primary sources of SiO_2 and Al_2O_3 which can be found as commercial chemicals [41]. In alternative to commercial chemicals, different ways have been explored for production of starting materials and several raw materials [42] has been tested for this purpose. Clay minerals [43], [44] municipal solid waste, coal ashes [45], kaolin [46]–[48] industrial slag and incineration ashes represent a small part of this raw materials list. But, if, on one hand, all these solutions might be considered a cheaper alternative, on the other hand, there is another remarkable aspect to take into account which, considered the global situation, is even more important than money: the environmental problem. Such materials, which are the result of waste treatment, contribute to mitigate the environmental problem and are generally used in several fields such as water purification for the removal of heavy metals as well as ammonium.

1.5 Acidic properties

One of the most important features of zeolites is the presence of strong acid sites in their structures. Zeolites are solid acids and both Brønsted and Lewis acid sites can be found in zeolite structure (figure 1.11). Brønsted acid sites are bridging hydroxyl groups, such as SiOHAl groups, that transfer protons to strong and weak bases. Lewis acid sites are electron pair acceptor sites, which can be metal alkali cations in exchangeable positions (weak Lewis acid sites) and Lewis acid sites can be also coordinatively unsaturated higher valent cations, like trigonal aluminium cations in extraframework positions (strong Lewis acid sites).

Sites interact with basic molecules. The presence of trivalent aluminium creates inside a framework an electrical imbalance, which is compensated by the presence of extra-framework cations.

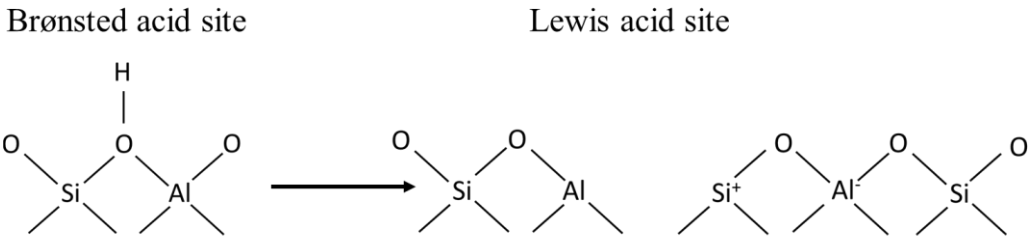

Figure 1.11: Example of Brønsted and Lewis acid sites. Picture adapted from reference [49].

Exchanging a zeolite with ammonium based solutions followed by thermal decomposition allows the formation of protons which, working as cations, compensate close Al centres. Depending on certain conditions, these protons in the H-form zeolite may work as Brønsted acid sites. Protonic zeolites are also obtained by using SDA agents and their subsequent decomposition. According to early reports [50], zeolite acidity is due to aluminium tetrahedral bonding. Another paper [51] suggests that Lewis centres are the result of tricoordinated silicons located on a small structure defect which acts as electron acceptor sites. Also, Lewis sites result from defect sites and metal cations. One of the major areas of interest in the field of zeolites is catalysis. Brønsted acid sites are important in catalytic processes that involve the aromatic conversion through dehydrogenation of alkanes to olefins. The importance of Lewis sites is mainly in catalysis with transition metals for reduction or oxidation reactions.

Through patents and papers, literature offers several examples and results, which highlight how zeolites and their acid properties play a key role in catalysis.

In order to differentiate Brønsted from Lewis sites, basic molecules such as pyridine can be employed. The frequency of the ring vibrations helps to understand if pyridine is adsorbed on Brønsted sites (as pyridium ion) or coordinatively adsorbed on Lewis sites.

The channel system in the structure of a zeolite is a crucial feature in catalysis as it acts as the “access route” to acid sites for molecules and species. However, reduced dimensions of the channels in some cases may limit the accessibility to the acid sites.

In general, this can be solved through specific chemical procedures, which involves structure modification.

1.6 Synthetic treatments and secondary porosity

The presence of features such as strong acidity makes zeolites good candidates for catalysis. Along with acidity, microporosity represents an important feature, which makes these materials capable to enhance reaction rates and makes them more selective towards some molecules and species. Microporosity represents a limitation and a secondary mesoporosity level might be a benefit. Some zeolites show remarkable acid properties, which make these materials an interesting resource for catalysis. However, for some of these materials, the access to the acid sites is limited due to pore sizes. In order to improve the accessibility of a zeolite, two approaches are adopted: a post-synthesis approach (top-down) and a nanostructured synthesis (bottom up) (Figure 1.12).

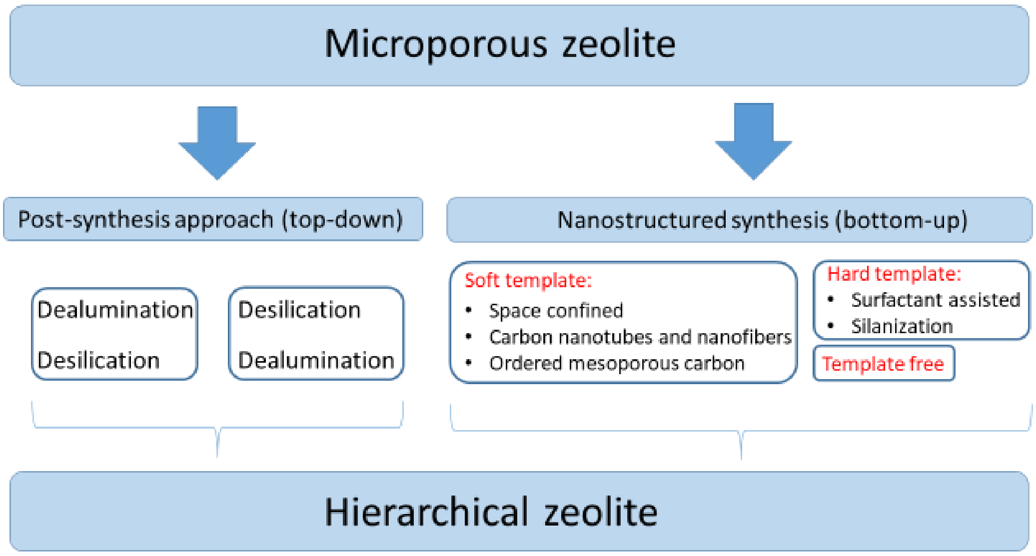

Figure 1.12: Scheme of strategies adopted to produce hierarchical zeolites.

Top-down approach consists of a post synthetic modification where the bimodal porosity is achieved with preferential extraction of the two main components of the zeolite structure: Si or Al [30]. Desilication [30], [52] and dealumination [30], [53] processes can be done through chemical etching and steaming for instance. These methods represent a destructive approach as they generate extraframework fragments that affect the pore size control. The removal of Si is an effective approach in order to obtain a uniform intracrystalline mesoporosity. In some cases, depending on the method chosen to remove Si, it can involve also the removal of Al. The number of Si and Al that can be extracted depends on Si/Al ratio and on the framework topology. Other factors to take into account are the concentration of the desilicating and dealuminating agents because they affect the mesoporous system and influence the acidic properties.

An example of top-down approach is described in reference [54]. In this work, Na and K-form of zeolite L samples (Si/Al=3) have been modified through several routes. This modification process involved both sequential desilication and dealumination approaches. Two series (S1 and S2) has been discussed. S1 and S2 has followed respectively a desilication → dealumination and a dealumination → desilication approach to obtain a mesoporous system.

In S1, after the desilication process through alkaline leaching (NaOH), a HNO_3 leaching was performed in order to remove extraframework Al species formed during desilication. Samples from the route 1 subjected to desilication (NaOH) have shown a decrease in Si/Al ratio values. However, the alkaline leaching has shown low efficiency. This result is due to the presence of a high number of Al atom in the structure which makes the zeolite less prone to desilication. The OH^- ions are repelled by AlO_4^- tetrahedral and this condition inhibits the desilication process. The ion exchange procedure also leads to a minor dealumination as Si/Al ratio increases. The HNO_3 treatment increased the Si/Al ratio due to the partial removal of Al extraframework from the material accumulated in channels and mesopores.

The second route (S2) has shown increased Si/Al ratios after the preliminary dealumination process (HNO_3). Following alkaline leaching (NaOH) enriched crystals in Al atoms and has shown a decrease in Si/Al ratio values. This result suggests that a preliminary removal of Al atoms improves the efficiency of desilication process. A factor to take into account is the severity of the acid conditions as it shows partial amorphization. Under milder conditions, the structure retains its crystallinity even after the desilication treatment preserving also the micropore volume of the modified zeolite.

A type-IV isotherm of micro-mesoporous materials and an enhancement of mesoporosity has been observed through N_2 adsorption-desorption analysis in both routes. However, the approach adopted for the second route made the sequential dealumination-desilication treatment the most effective for the mesopore generation under relative severe conditions of 0.2 M HNO_3.

The methods chosen in reference [54] work and the proper sequence of dealumination and desilication procedures allowed to obtain a high degree of mesoporosity. In addition, preserved crystallinity as well as an increased micropore volume, was observed according to XRD and N_2 adsorption-desorption results.

It should be pointed out that some alkaline treatments are applied to specific zeolites in terms of Si/Al ratio and n-membered rings. Because of the Si/Al ratio, it is also important to choose the proper strategy to modify the zeolite. Al-rich zeolites for instance need dealumination as first step due to the protecting role of the negatively charged AlO_4^- tetrahedra towards OH^- which makes a base treatment less effective. Dealumination as first approach would allow to increase Si/Al ratio and would make the subsequent desilication process more effective.

A nanostructured synthetic method employs hard and soft templates such as carbon nanotubes, polymers and structure directing agents with the aim to generate a secondary mesoporosity. Although this approach appears less destructive towards zeolite structures, it shows two disadvantages. The first is related to the costs of templates. The second is related to the difficulties in removing the organic species. In addition, a template-free method [55] can also be applied to generate mesoporosity and it consists of three approaches:

- Intracrystalline mesoporosity generated by nanocrystals aggregation.
- Intracrystalline mesoporosity formed by controlling the crystallisation of amorphous gels.
- Mesoporosity created between self-pillared zeolite nanosheets made by rotational intergrowth of zeolites.

The drawback of the method described above is related to the unstable structure obtained due to the tight agglomeration among nanocrystals.

Preparation of a mesoporous network in zeolites using a template-surfactant approach is described in reference [56]. In this paper several parent zeolites such as FAU, MOR and BEA have been treated utilising a one-step procedure to introduce mesoporosity and a surfactant-templating approach has been used. This procedure allowed to obtain an intracrystalline network of mesopores avoiding an excessive degradation of zeolite structure. The method applied consists of a base or an acid leaching to initiate the desilication or dealumination of the zeolite in presence of a long-chain alkyl quaternary amine cationic surfactant (CTAB). In MOR case for instance, this one-step approach, succeeded in generating mesopores on zeolite crystals. In addition, surfactant-templating method has shown to be less destructive compared to the more “severe” recrystallization process. Furthermore, cases such as FAU, through surfactant-templating procedure, avoided the formation of amorphous silica expected in recrystallization [57], and obtained an intact crystalline structure. Compared to the “two steps” recrystallization approach, the introduction of the surfactant (CTAB) during desilication is important. When the base interacts with zeolite during the base treatment, it hydrolyses Si-O bonds. This step creates negatively charged defects sites, which attract CTA^+ cations into the zeolite crystals. The micelles agglomeration inside the crystals generate a system of ordered mesopores as the reaction proceeds. Results suggest that this procedure is facile in large pore zeolites (FAU, BEA, LTL) but not in medium pore zeolites as the accessibility for the surfactant is restricted.

XRD results for these materials revealed that crystallinity is preserved as the severity of the acid or base treatment decreases. Under mild conditions, mesostructured zeolites maintained significant crystallinity, which decreases as the severity of the acid or base treatment increases. Low angle measurements also suggested that levels of ordered pore arrangement are present in mesostructured zeolites. The effectiveness of the surfactant action depends on the n-membered ring dimensions present in the zeolite framework. For instance, a 12-membered ring would allow the surfactant species to access to zeolites framework and generate mesopores during the surfactant-templating mesostructuring process. Different is the case of 10-membered rings channels such as in ZSM-5 zeolite, which are inaccessible to the surfactant. Evidences of mesoporosity were provided through N_2 adsorption desorption data where very different profiles have been found for parent and modified zeolites. Type I isotherm profiles have been found for parent zeolites while type IV for mesostructured samples. In addition, it has been observed for modified zeolites a type H4 hysteresis loop typical of mesoporous systems possessing a bimodal pore size distribution. This data of intracrystalline interconnectivity between meso- and micro-pores has been also confirmed by nitrogen adsorption and high resolution TEM analysis.

1.7 Ion exchange properties

The phenomenon of the ion exchange is thought to be the oldest physical process known to man. It is described in the bible and in Aristotele‘s writings. The ion exchange was the first property studied scientifically in the field of zeolites. Eichorn in 1858 [58] described the capability of natural zeolites such as chabazite and natrolite to perform a reversible cation exchange. This property allowed zeolites to be employed in domestic and industrial fields as water softeners. However, the first papers that described the ion exchange phenomenon arrived around 1970s [59]–[61]. The driving force behind these studies was the discovery of the introduction of different cations into a zeolite promoting catalytic and molecular sieving properties. Thermodynamically, the ion exchange phenomenon follows the statements listed below:

- The system is in a state of equilibrium.
- The exchange process is fully reversible. If the process is not reversible, the two different reaction are considered separately (forward exchange and reverse exchange).

For a binary ion exchange process, a cation (B^{zB}) present in the zeolite is exchanged with a cation (A^{zA}) present in the solution. This phenomenon can be written as:

$$Z_B A^{zA} + Z_A \bar{B}^{\overline{zB}} \leftrightarrow Z_B \bar{A}^{\overline{zA}} + Z_A B^{zB}$$

Where Z_A and Z_B are the valencies of the ions. Letters with bars as superscript represent cations inside the zeolite lattice.

If a zeolite interacts with a series of isonormal solutions containing different proportions of incoming and counter cations, it is possible to construct an isotherm at standard conditions of temperature and pressure. From this isotherm, it is possible to evaluate the distribution of cations between the zeolite and the solution phases when the equilibrium has been reached. Dyer et al. [62] as well as Townsend [63] show in their papers the proper experimental methodology to construct the isotherm. The isotherm is obtained from the quantities of the equivalent fraction of the incoming cation in solution (A_S) against the equivalent fraction in the zeolite ($\bar{A}_Z$).

These quantities are defined as:

$$A_S = Z_A m_A / (Z_A m_A + Z_B m_B) \qquad \bar{A}_Z = Z_A M_A / (Z_A M_A + Z_B M_B)$$

Where m_A, m_B and M_A, M_B are the cation concentrations (mol dm^{-3}) in solution and solid phases, respectively.

Figure 1.13 shows the idealised isotherm shape:

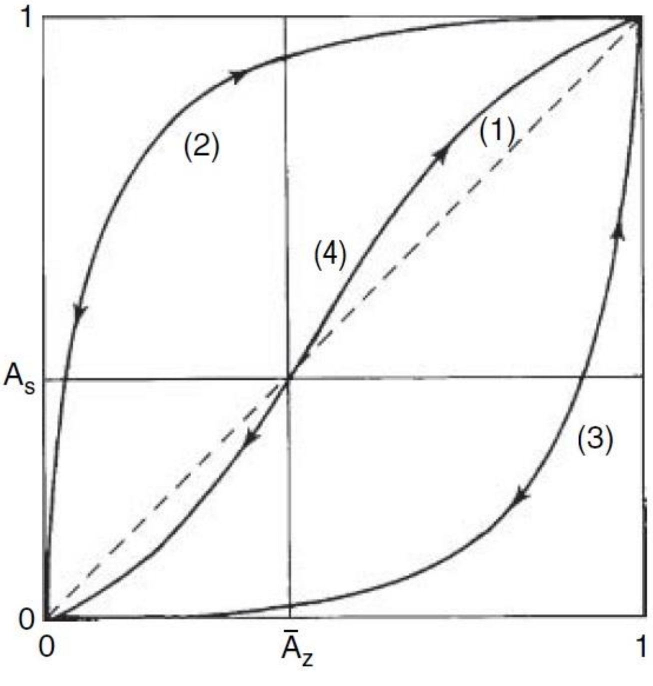

Figure 1.13: Idealised cation exchange isotherm. Picture adapted from reference [25]

The plot above gives a pictorial indication of the preferences of cations in both phases, solid and solution. The dotted isotherm (1) shows the case of a zeolite that has equal affinity for both cations. Isotherm (2) represents the case with cations A^{zA}

remaining in solution and that do not displace B^{zB} from the zeolite. Isotherm (3) is observed if the replacement of B^{zB} with A^{zA} occurs. The sigmoidal shape (4) represents a particular case when there is a change in selectivity. This case, under the concentration range studied, may indicate that there is a competition between cations in more than one exchange sites in the zeolite structure. Barrer and Klinowsky [64] in their paper described this selectivity testing zeolite A. They reported that, if there are different competing cations with different charges, as the dilution increases, the selectivity increases for the cation with greater valence.

1.8 Applications of zeolites

The introduction of zeolites into the market in 1950 generated a rapid increase in the production of these materials due to the demand for application in the industrial field as additives for detergents. Natural and synthetic zeolites play an active role in industrial processes as catalysts and this has generated an increasing worldwide demand that has continued to grow in the modern day industry. Natural zeolites found applications mainly in the construction products as well as components for building materials. Among their additional application fields animal feeding, horticulture and treatment of hard water can be listed. The largest consumers of natural zeolites are China and Cuba. It is reported that these countries use about 2.4 million tons per annum of zeolites to enhance the strength of cement [65]. US, Europe and Japan consume 0.15 million tons per annum of natural zeolites, particularly HEU- and CHA-type zeolite mineral in agriculture and horticulture. Also, these countries use these materials as ion exchangers to remove radioactive isotopes from ground water and reactor effluents [65]. The largest tonnage of commercial zeolite sold is LTA-type as water softener [65].

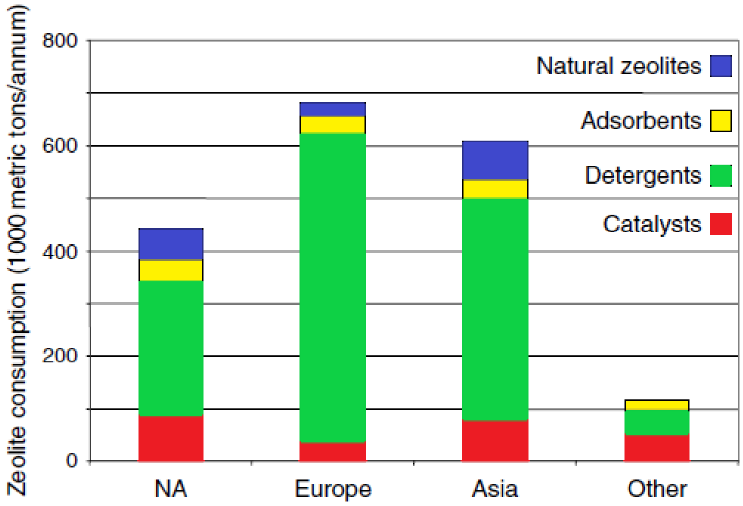

Figure 1.14: Estimated annual zeolite consumption excluding China's annual (>2.4 million metric ton consumption of natural zeolite). Adapted from ref. [25].

The largest market for synthetic zeolites is in catalysis. The least expensive synthetic zeolites is FAU-type and it accounts for more than 95% of the catalysis market [66]. This zeolite is in 2001 consumed in large quantities for oil refinery purposes to manufacture gasoline from crude oil.

The main application fields of zeolites are ion exchange, adsorption and separation and catalysis.

1.8.1 Ion exchange

Zeolites are utilized for their ion exchanging properties as additives in detergents. In this case, they act as water softener preventing carbonate precipitation. Zeolite A (LTA), for instance, exchanges calcium and NaX magnesium ions with sodium ions contained in zeolite framework. Behind this choice to use zeolites as detergent additive there is the need to solve issues related to environmental concerns. Detergents, which used phosphate builders as chelating agents, have been substituted with zeolites A and X. Both zeolites offer not only high ion exchanging capacities, but also because they are considered a good solution for environmental hazards such as eutrophication; this issue affects bodies water containing nitrate or phosphate due to discharge of detergents.

Because of their ion exchange capability, zeolites are also used to remove impurities in hemodialysis processes. The removal of NH_3, during the re-circulating dialysis stream in the development of portable hemodialysis systems, represents a great challenge. Zeolite F and Zeolite W represent the solution to this challenge due to their high ammonia ion exchange capacity applied to the hemodialysis system [67].

Another important application of zeolites is as radionuclide removals where they act as molecular sieves. Several natural zeolites have shown effectiveness in accepting some radionuclides such as ^{90}Sr, ^{137}Cs, ^{45}Ca and ^{60}Co. Mordenite for instance has shown its capacity to remove ^{137}Cs and ^{90}Sr found in contaminated soils [68] and waters. Zeolites and vermiculite have shown their effectiveness in removing ^{137}Cs from radioactive waters. This property has been very important to mitigate the consequences of Fukushima's events [69]. In that occasion, zeolites have been considered and proposed for the removal of radionuclides from water, used to cool down reactors, before releasing the treated water into the sea.

Heavy metals and organic poison represent a form of pollution that affects the food chain. Natural zeolites offer a solution to solve this issue. Cadmium ions, lead ions and copper ions are some examples of species that can be removed by these materials. Clinoptilolite has shown a great stability in acid environment and a great ability in removing heavy metals [70].

1.8.2 Adsorption and separation of gases

Zeolites are also used in separation applications in industry. They offer the potential of continuous separation for gas, vapour and liquid mixtures. The properties of zeolites are attractive for membrane applications due to pore sizes of molecular dimension, which enables the property of shape selectivity.

In agriculture, zeolites are used successfully as soil additives to improve the yield of agricultural products. They play the function of toxic substances removal. Some substances such as mercury, after being adsorbed by plants, bio-accumulates and entry in the food chain, however, their action can be restricted by using natural zeolites [71]. NaCl pre-treated pure eulandite crystals and NaCl pre-treated clinoptilolite have shown a remarkable rate of mercury removal from aqueous solutions. Mercury is used by many industries as catalysts in the pigment industry development as well in the battery industry. Materials, such as the Italian chabaziterich tuff zeolite [72], is used, for its capacity, to remove selectively high amounts of NH_4^+ from wastewater [73].

Because of their adsorption properties, zeolites also lead to potential applications in sensing technology. Zeolites such as LTL doped with iron nanoparticles have been used for the detection of CO_2 and O_2 in gas phase [74]. Zeolites such as MFI, LTA, MOR and FAU, have been also employed as H_2 selective separation membranes. Other applications include branched hydrocarbon separation as well as regular hydrocarbon separation. In addition, there are reports of application of zeolites for cations detection in water [75].

1.8.3 Catalysis

The introduction of zeolites in catalysis was in 1959 as hydrocarbon conversion catalysts by Union carbide. For the last 60 years, zeolites have been used as catalysts in many petrochemical processes. In 1992, zeolites were used as cracking catalysts by Mobil Oil [25].

From that moment, zeolites had a large economic impact, especially in industry and for fuel cracking processes. Shape selectivity, resulting from the well defined microporous structure, as well as the capacity to be resistant to heat represent the properties that play the most crucial role in catalysis. The shape selectivity imposes constraints on the reactants, on the transition states and on the products formed during catalytic transformations [76]. The thermal stability of zeolites allows these materials to be employed at high temperatures. FAU, for instance, represents one of the most important catalysts for fuel catalytic cracking due to its good octane booster capacity. Other zeolites, which play an important role in this field, are mordenite, zeolite Y and zeolite beta.

Zeolites are also important catalysts in hydrocracking. This process involves the conversion of higher paraffins over noble metal containing zeolite catalysts to yield distillate products. Zeolites have been also used as redox and environmental catalysts [77], [78].

1.9 Investigation techniques

1.9.1 Fourier transform infrared spectra (FTIR)

FTIR is a technique used to determine a variety of material properties including structural details and functional groups. In the field of zeolite studies it is used to identify acid sites, their distribution and strength. Infrared spectroscopy is the measurement of the wavelength and intensity of absorption in the mid-IR zone. The mid-IR range is 400 - 4000 cm^{-1}. This range is energetic enough to excite molecular vibration to higher energy levels. The wavelengths of IR absorption bands are characteristic of specific types of chemical bond. “Old fashioned” IR instruments are dispersive; they separate all frequencies of the energy emitted by IR the source (black-body) using a prism or a diffraction grating. The prism separates the light in several colours while a diffraction grating separates the frequencies with a better resolution. The instrument records the energy that passes through the material and the plot obtained is the absorbance or transmittance as a function of frequency, wavelength or wavenumber. Although this technique has been used for several years it has some disadvantages in terms of long scanning time and moderate sensitivity. An alternative is FTIR. This instrument shows better sensitivity, speed and accuracy compared to the ordinary IR instruments. In addition, a FTIR measures all frequencies simultaneously by using an optical device called interferometer, which generates one signal in which all IR frequencies are codified [79]. The picture below (Figure 1.15) shows how an FTIR spectrometer is made:

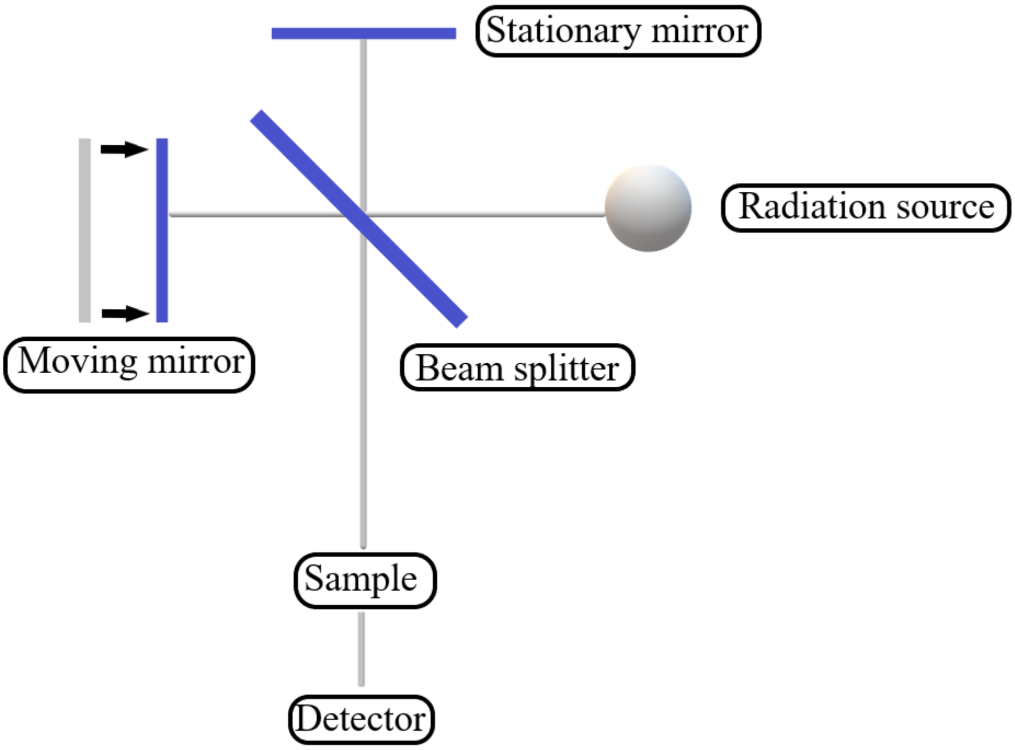

Figure 1.15: Scheme of a FTIR instrument.

When the IR radiation, which contains all frequencies, is passed through the beam splitter, it is divided into two beams. As one of them is reflected to a stationary mirror and the second to a moving mirror, both beams will have a different length path. The resulting signal of the two beams is called interferogram and it contains the information about all IR frequencies emitted from the source and all frequencies are measured at the same time. For this reason, the FT-IR is faster than a conventional IR. The interferogram is digitalised and through a Fourier transform converter, it is converted to a frequency spectrum of percent transmittance as a function of wavenumber.

The FT-IR is crucial for the investigation of acid properties of zeolites in this research project.

1.9.2 X-Ray diffraction

X-ray diffraction is a non-destructive characterisation technique used to determine the structure of a crystal. X-rays have a wavelength in the range of Ångström (Å) and in the same order of interatomic spaces within solids (10^{-10} m). This property makes XRD a powerful investigation technique to probe solids internal structure since the radiation is sufficiently energetic to penetrate these materials. The discovery of X-Rays was in 1895 by Wilhelm Röntgen during an experiment in a dark room where he observed that a shield of black paper, covered on one side with barium-platinum cyanide, was exhibiting a brilliant fluorescence when brought into the neighbourhood of the tube [80]. He termed this new form of radiation "X-Rays" using "X" to designate something unknown. Subsequently, he studied the ability of several materials and their ability to stop this new form of radiation. From one of these experiments, he generated the iconic picture of his wife's skeleton hand. In this "Röntgenogram", her hand was put in the path of the radiation and it showed a shadow, representing her bones with a darker shadow representing her ring and all surrounded by the penumbra representing the flesh.

A modern diffractometer consists of a tube envelope made under vacuum and made of glass or metal. The tube produces this form of radiation by heating a filament, which releases electrons by thermionic emission. The high voltage in the tube accelerates the electrons making them to collide to the focal spot of an anode in contact with a liquid coolant to improve the performance and heat conduction [81]. The X-rays are produced from the interaction on the anode. The quality of the X-radiation is controlled by adjusting the tube voltage (kV) which is the potential difference applied across the tube and the tube current (mA). There are two kind of X-Rays: Bremsstrahlung X-Rays and characteristic X-Rays. The first kind is the result of electrons that lose their kinetic energy as they pass through the atoms in the anode since they are attracted to the positively charged nuclei. The closer to the nuclei the electrons pass, the more energy they lose resulting in being deflected or stopped. Characteristic X-rays is observed as electrons eject orbiting electrons in the target atoms. This usually happens when the colliding electron has equivalent or greater energy compared to the target one. It is observed with inner electrons K-shell. The ejected electron is known as photoelectron and the vacancy is filled by an outer shell electron. The resulting electron transfer generates a form of radiation called characteristic X-rays because of the characteristic binding energies of that particular atom or material.

During XRD analysis, the X-rays are directed at the surface of the sample. While some of the X-rays pass through, part of the radiation is diffracted by the atoms in the periodic lattice of the sample. The scattered monochromatic X-rays that are in phase give a constructive interference. The detector records the pattern of diffracted X-Rays. In order to obtain a diffraction signal, the diffracted X-Rays must interfere constructively. The relationship between X-Ray wavelength, interatomic spacing and diffraction angle of constructive interference is described by the Braggs' law:

$n\,\lambda=2d\sin\theta$ where $n=1,2\ldots$

The path difference between X-rays scattered from adjacent crystal planes corresponds to $2d\sin\theta$. In order to obtain a constructive interference between the two scattered beams, the difference must be an integer multiple of the electron wavelengths $n\lambda$ (Figure 1.16).

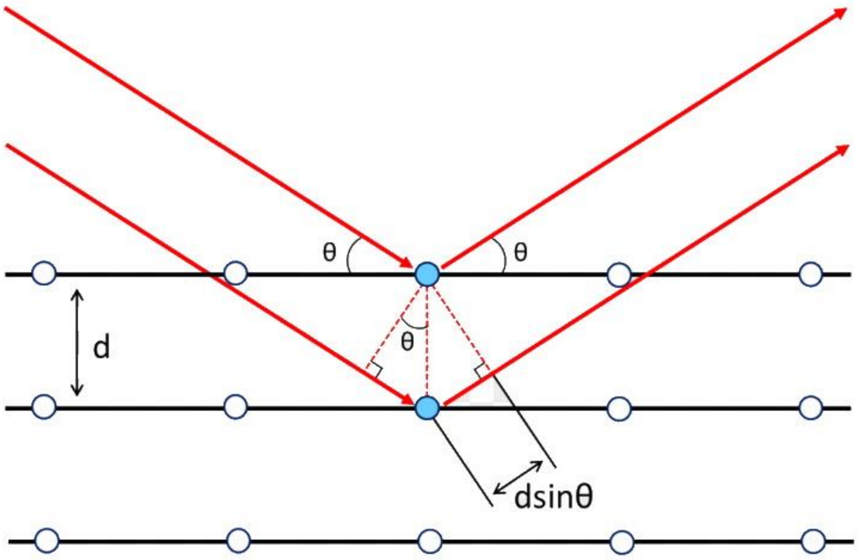

Figure 1.16: X-Ray diffraction graphic representation.

The intensity of the diffracted beam is scanned as a function of the angle 2θ between the incoming and the diffracted beams. When a powder sample is scanned, an image of diffraction lines is obtained. This occurs because a small fraction of powder particles will be oriented by chance at the angle with the incident beam of constructive interference. This technique is crucial not only to identify the material, since the XRD pattern represents its fingerprint, but also to obtain structural information and semiquantitative analysis. In order to identify the material, several parameters must be taken into account, for instance, peak positions which are related to the geometry of the cell, relative intensities which are determined by the type and position of the atoms in the unit cell and the widths of the peaks in the pattern, which give indication of the crystalline quality of the sample. Also in a powder pattern, the background plays a key role, as it indicates whether in the sample there is an amorphous component or not. In addition, the degree of crystallinity can be also obtained to determine information related to the presence of an amorphous phase.

1.9.3 Rietveld method

The first powder diffraction pattern recorded was reported over a century ago. A typical powder sample consists of microcrystalline powder where the crystallites are randomly oriented. When the sample encounters an incoming beam of X-ray wavelength (10^{-10}m), the radiation is diffracted in all directions by the crystallites in the sample itself resulting in diffraction cones. The intensity and distribution of the cones are measured on the 2θ axis of the powder pattern. The conversion of data from a three-dimensional reciprocal space to a one-dimensional generates a reduction of information and a systematic peak overlap. For many years, this problem affected the powder diffraction analysis representing a limit for the crystallographic research.

After 50 years, in 1969, Hugo Rietveld published an article, which revolutionized the modern chemistry and the structural sciences. In this paper, he described a technique for the characterisation of crystalline materials called Rietveld refinement [82]. This method offered a way to solve the overlap problem through modeling a calculated pattern described by a list of parameters such as crystal lattice and symmetry, crystal structure, microstructure, instrumental factors and others. At that time, data analysis was tedious since automated data collection was not common and Fourier maps were hand plotted. However nowadays, with modern software, users can refine any parameter simultaneously by the least squares method until a calculated pattern matches a collected one. The most important requirement for the Rietveld method, in order to be applied, is that the material must be crystalline. For this reason, this method is applicable to metals, inorganic compounds, and organic compounds of low molecular weights. Powder diffraction with neutrons or X-rays produces a pattern with reflections (intensity peaks) at certain locations. Many features of the crystalline material's structure can be determined by measuring the height, width, and position of these reflections. The method requires the application of complex mathematical approaches by using software that are designed for X-Ray, neutron and synchrotron powder diffraction studies. When applied to an experimental pattern, the Rietveld technique refines, through a reiterative procedure, a calculated pattern or a standard pattern from a database (C.O.D. [83], I.C.D.D. [84]), like it was a theoretical line curve, using a least-squares approach until it fits the measured curve. In this reiterative procedure, the result is the starting point for the next refinement. The Rietveld algorithm optimises the model function to minimize the weighted sum of squared differences between the observed and computed intensity values. The discrepancy index, called "R_{wp}%", displays the quality of the refinement [85]. This parameter is the result of the square root of the quantity minimized and scaled by the weighted intensities:

$$\mathbf{R^2_{wp} = \sum_i w_i(y_{C,i}-y_{O,i})^2/\sum_i w_i(y_{O,i})^2}$$ [85], [86]

Where:

- $\mathbf{y_{C,i}}$: intensity values simulated where C indicated they are computed from the model.
- $\mathbf{y_{O,i}}$: intensity values observed in experimental data.
- $\mathbf{\sum_i w_i(y_{C,i}-y_{O,i})^2}$: Weighted sum of squared differences between observed and computed intensity values.
- $\mathbf{w_i}$: is the weight and it is equal to $1/\sigma^2[y_{o,i}]$.

The whole pattern is analysed without separating peaks contained in it. The Rietveld method applies the data processing procedures on the aspects summarized below [87]:

- Separation of overlapping peaks in the pattern.

- Separation of characteristic $K_{\alpha}1$ and $K_{\alpha}2$ when using characteristic X-rays.
- Background subtraction.
- Refinement of lattice parameters, structure parameters (occupation factors, thermal displacement factors) [88].
- Correction of preferential orientation.
- Identification of phases and impurities peaks.
- Determination of integrated intensities, full widths at half-maximum intensities (FWHM).

1.9.4 N_2 adsorption desorption

Gas adsorption is one of the most used technique to characterise a wide range of solid porous material. Porous materials may have cavities and pores of several sizes of different shapes and interconnections. They are divided mainly in three categories: micro-, meso- and macro-porous materials where pores dimensions are respectively less than 2nm, between 2 and 50 nm and greater than 50 nm. The atoms on the surface of a material are characterised by coordinative unsaturation and thermodynamic metastability, so they may have chemical or physical interactions with other atoms or molecules of adsorptive gases. Among the many gases and vapour that can be used as adsorptives, nitrogen has remained the most preeminent. The earliest studies of nitrogen adsorption have been made by Dewar [89]. Years later, Langmuir, with his monumental work, gave his contribution to the interpretation of adsorbing data [90]. In his model, the adsorbent surface is represented by an array of equivalent sites where molecules are adsorbed in a random manner and it corresponds to a complete monolayer coverage as represented in type 1 isotherm. In the early 1930s it was realized that the interaction between N_2 and solid surfaces at temperature of 77K lead to the multilayer adsorption on the surface of the material. These phenomena are characterised by weak attractions such as van der Waals type.

In 1937, Brunauer and Emmet published a paper where they adopted gas adsorption to determine the surface area of various adsorbents [91]. They found that adsorption isotherms of nitrogen and other gases on iron-containing synthetic ammonia catalyst were showing a sigmoidal shape designated only later as Type II. One year later, along with Teller, they published the B.E.T. theory (Brunauer –Emmett –

Teller) which soon became the standard procedure to determine the surface area [92].

Nitrogen adsorption is used also for the pore size analysis and the first employment of this method is dated from 1940s. This method is based on the application of Kelvin equation with a correction of the multilayer thickness on pore walls. Computational methods were also proposed in the late 1940s but the most popular method for the determination of the pore size distribution remains the BJH method (Barrett – Joyner – Halenda) [93].

Although BET and BJH methods are still popular and used for the evaluation of surface area and pore size distribution, the recent development in computer simulation introduced new methods such as density functional theory (DFT) [94]. DFT and NLDFT methods have become important tools for the characterisation of porous materials.

Gas adsorption manometry is the method used for the determination of isotherms of nitrogen at 77K. The conventional technique consists of a discontinuous point by point method where successive amounts of nitrogen are introduced in a cell containing the sample at different stages. At each stage, the method allows the system to reach the equilibrium. Each of these steps corresponds to a single point in the adsorption isotherm [95] and the amount of gas adsorbed is generally evaluated by measuring the change of gas pressure.

The majority of physisorption isotherms may be grouped into six types (Figure 1.17).

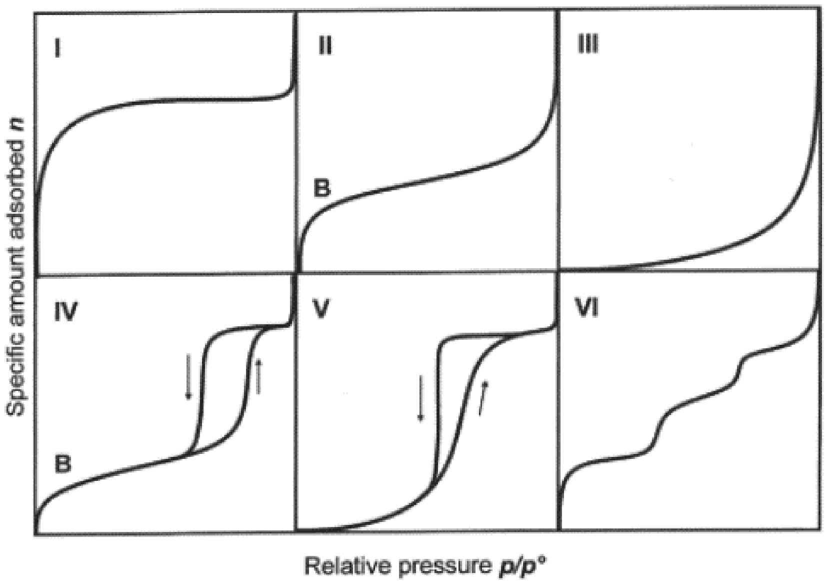

Figure 1.17: Types of isotherms (adapted from reference [18], [96]).

- Type I: this isotherm is typical of microporous solids with a relatively low external surface such as molecular sieves zeolites and activated carbon.
- Type II: It is obtained from non-porous or macroporous adsorbent materials. It represents unrestricted monolayer-multilayer adsorption. The point B is often taken to indicate the stage at which the monolayer coverage is complete and a multilayer adsorption about to begin.
- Type III: This is a convex isotherm over the entire range of the p/p° axis. It does not exhibit a point B. Such isotherms are shown by systems such as nitrogen and polyethylene.
- Type IV: this isotherm exhibits a hysteresis loop associated with capillary condensation taking place in mesopores. The initial part of the isotherm is attributed to monolayer-multiplayer adsorption. This isotherm is typical of mesoporous adsorbents.
- Type V: associated to weak adsorbent-adsorbate interaction shown by certain porous adsorbents.

- Type VI: this system describes a stepwise multilayer adsorption on a uniform non-porous surface. This isotherm is observed on systems such as argon or krypton on carbon at liquid nitrogen temperature.

Through mathematical modelling it is possible to evaluate the surface area. For type I, II and IV isotherms the surface area can be estimated using Brunauer - Emmett - Teller (BET) method.

Mesoporous materials show type IV isotherms. In this case, it is possible to see from the picture how desorption and adsorption curves do not coincide (Figure 1.18). This phenomenon is called hysteresis and through several theories researchers tried to find an explanation. It is generally associated with the filling and emptying of mesopores where the adsorbed gas condensates when its pressure is lower than its vapour pressure. However, the explanation of this phenomen called capillary condensation is not completely clear. Experimental evidences have also proposed that adsorption hysteresis at high p/p_0 may be generated by the contraction and slow re-expansion of the adsorbent [97].

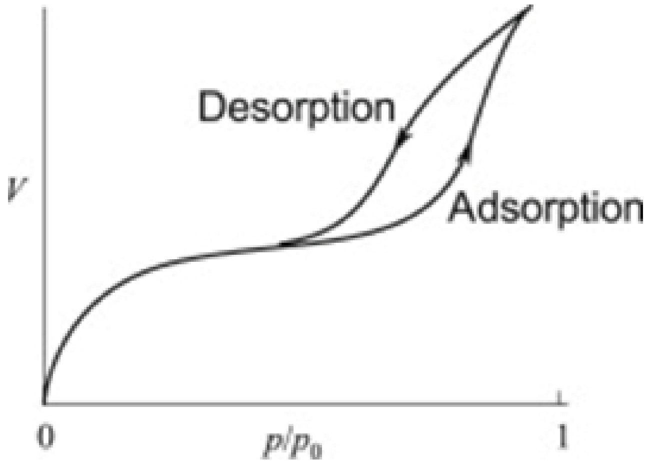

Figure 1.18: Type IV isotherm (adopted from reference [18]).

1.9.5 NH_3-TPD

Ammonia temperature controlled desorption (NH_3-TPD) is an investigation technique employed in catalysis to evaluate the acid strength of acid sites. The interest in evaluating the acid strength is also extended to zeolite science and zeolite catalysis since these materials are employed in this field as solid acid catalysts. The interaction of probe molecule towards catalysts is usually studied for the determination of the type of acid site: Brønsted or Lewis. The evaluation of the average adsorption heat or the activation energy of adsorbed ammonia give information about the acid sites strength and these aspects can be determined using NH_3-TPD. Information such as the temperature desorption rate and the temperature and the integrated area of the desorption peak are used as rough measure of the acid strength of the sorption sites. However, this method is affected by limitations because it does not allow distinguishing Brønsted acid sites from Lewis acid sites [98]. In addition, this method results in finding overlapping peaks since acids sites may desorb NH_3 simultaneously. This aspect adds some uncertainty in the process of evaluating sites with different acidity. Mass spectrometry is the analytical technique usually employed for these kind of experiments. This technique has many different applications and it is used in several fields such as forensic science, biochemistry and catalysis. In catalysis mass spectrometry is employed to monitor the ammonia desorbed from acid zeolites catalysts through the residual gas analysis. Residual gas analysis measures low levels of residual gas that remain in a vacuum chamber following pump down. Such gases may include residues from ambient air such as oxygen, nitrogen, water. They may also include reactants such as silane, organometallics, halides, etc., and reaction products such as ammonia, hydrogen, moisture, etc. Vacuum chambers can also contain contaminants due to system leaks and hydrocarbons that backstream into the process chamber from the pumping system. Reproducible process results from a vacuum process are only possible when the system is guaranteed to be leak-tight and when the kind and quantity of residual gases in the process system are known and accounted for in the process protocol. Residual gas analysers (RGAs) are a critical analytical tool for gaining this knowledge. Modern RGAs employs quadrupole mass spectrometry as their underlying operational principle. Quadrupole mass spectrometers (QMS) can monitor multiple gas-phase species in real-time. They have a wide dynamic range and can track gas-phase reactant, product and contaminant concentrations from ppb to % levels. A QMS detects and quantifies chemical species by first ionizing the molecules or atoms in a gas stream and then separating these ions by mass/charge (m/e) ratio. A quadrupole analyser requires high vacuum for operation since ions must pass freely through the analyser, affected by only the analyser field.

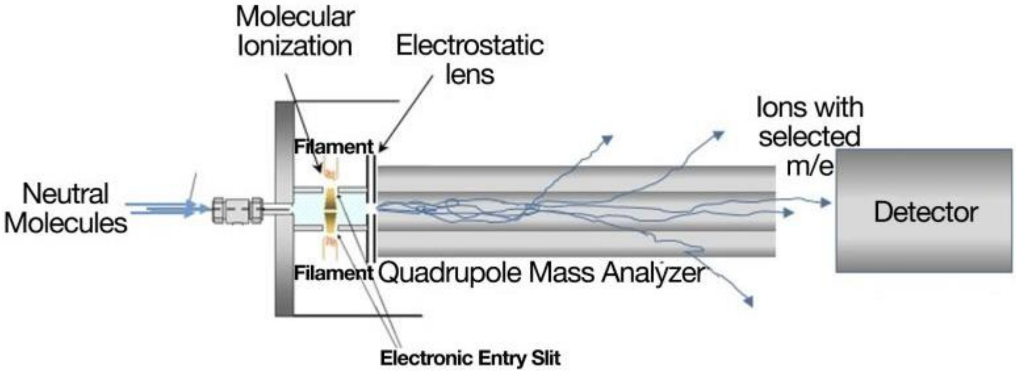

Figure 1.19: Functional components of a quadrupole mass spectrometer

A turbomolecular pumped vacuum system, usually on-board the RGA, ensures an operating pressure below 10^{-6} Torr [99]. Depending on the pressure of the system being analysed, the inlet to the QMS may be a simple vacuum connection (if the system being analysed is under medium to high vacuum) or a differentially pumped capillary tube (to limit the volume of gas entering the QMS and avoid raising the internal pressure of the RGA). When the RGA is in operation, a gas sample stream from the chamber being analysed enters the QMS at the ion source (from the left in figure 1.19). Various methods may be used to ionize the sample, with electron-impact ionization being the most common. Electrons emitted by a hot filament knock electrons off the incoming molecules and atoms to form positive ions. A quadrupole mass filter separates the ions according to their m/e ratio. Then, they are detected by a Faraday plate or secondary electron multiplier. All of the gas components are analysed within a single scan and the results of the analysis are displayed as a mass spectrum (plot of m/e versus peak intensity). The ionization process produces both parent ions (the original molecule with a positive charge) and ionized fragments of the original neutral molecules. The fragmentation pattern acts as a fingerprint that identifies the various neutral species that were present in the gas stream sample. If the identities of the major components are known, specific mass peaks can be monitored and calibration coefficients applied to derive the relative composition for each species present. Furthermore, because all species within a given sample are analysed, mass spectrometers can detect and highlight the presence of unexpected species or contaminants in a product gas stream. Some newer RGAs employ an ion trap as a mass analyser rather than a quadrupole. The theory of operation of these systems is quite complex.

1.9.6 Electron microscopy

Scanning electron microscopy is an investigation imaging technique invented in 1942 and used to scan samples and generate high magnification micrographs in the range 10-1000000X with high depth of field. Samples, in order to be analysed by this technique, should be conductive [100]. For non-conductive material may be deposited a very thin film made of carbon and in other cases of alloys [101], [102]. This technique is mainly used to investigate the morphology of the material. The surface of the samples is scanned by an electron beam, generated by heating a filament of tungsten at high voltage (40 kV), which can be used to create images of the distribution of the specimen. After the emission from the source, the electron beam is modified by apertures, magnetic lenses and electromagnetic coils. The electromagnetic coils reduce the beam diameter to scan the focused beam in a series raster (x-y) patterns [102]. The resulting images are displayed as variation in brightness on a computer monitor. The picture obtained shows the surface features of the sample. During the interaction of the beam with the specimen, two outgoing electron are generated:

- Backscattered electrons (BSEs): They are beam electrons emerged from the specimen with a large fraction of their energy after being scattered and deflected by the electric field of the atoms in the sample.
- Secondary electrons (SEs): These are electrons that escape the specimen surface after being ejected by beam electrons. The electrons in the sample atoms that leave their orbitals have sufficient energy to become secondary electrons.

The outgoing electrons signals are measured using one or more "Everhart-Thornley secondary electron" detectors, which are sensitive to both kind of electrons SEs and BSEs and a dedicated detector for back scattered electrons is also used.

The signals measured at each raster scan location are digitized and saved on a computer where they are subsequently displayed as variation in brightness on a monitor.

Interfacing this instrument with EDX allows to determine quantitative elemental composition of the material investigated. Electron in the beam with an energy equivalent or greater than the binding energy of an electron in the inner shell of an atom in the sample are likely to ejects the latter. When this condition is satisfied the ejection release a photoelectron. For the law of conservation of energy an outer shell electron fills the vacancy in the shell and this electron transfer process produces characteristic X-rays. This aspect can be used for element identification [102].

1.9.7 ICP-OES

Inductively coupled plasma optical emission spectroscopy is an analytical technique used to determine the atomic composition of an investigated sample. The principle behind this technique is to use the unique photophysical signals of each element to detect the element itself and its relative amount. ICP-OES is a powerful tool, which found its utility in several applications such as the analysis of trace elements in environmental, biological [103] and pharmaceutical field [104]. It is also employed in the analysis of drinking water, petrochemicals and complex samples [105].

Before to run an ICP-OES analysis, solid samples need to be digested in concentrated acid solutions (HNO_3, HCl). The obtained solutions and the multi-element standards are then transferred in plastic tubes and inserted in the racks of the instrument for the analysis. The system works by pumping a certain amount of a liquid sample into a nebulizer. The liquid is turned into a fine aerosol. This is achieved by the employment of a stream of a gas for instance Ar [106], N_2 [107] or a mixed gas composition [108]. The aerosol passes inside a spray chamber where the large droplets contained in it are removed. The remaining aerosol continues its journey to the plasma torch. The inductively coupled plasma torch (ICP) is the energy source of the analysis. It consists of three concentric glass tubes and it looks like a flame on a glass candle surrounded by a metal coil. The Ar, or the gas used, flows between two outermost tubes. The radio frequency energy is produced by generator and subsequently, the current passes through the coil around the glass torch. As result, a magnetic field is created and a spark, released into the stream of Ar, generates the plasma. A second stream of Ar carries the aerosol of the sample to the plasma torch, which evaporates the solvent contained in the sample. The heat generated by high temperatures at 7000K breaks the molecules of the sample into atoms and ions and simultaneously provides sufficient energy to excite the electrons, in both atoms and ions, to higher energy levels.

Once the excited electrons return to a lower energy level, depending on the element and on the energy level itself, an emission at a specific wavelength is recorded. In a real sample, since it contains many elements, several emissions with many different wavelengths will be observed. As result of the analysis, a wavelength spectrum is obtained. This spectrum shows a list of peaks which can be called analytical lines or emission lines and they are the result of the electrons movement between the energy levels. One element can also show more than one emission line and, in this case, it is usually selected the most intense. Signals of detected elements often overlaps and this significantly challenges the interpretation of the results. In order to address this issue, an optical grating device [109] may be used to separate the wavelengths that correspond to each element so that each of them can be individually detected.

The light emitted by atoms and ions is directed by mirrors and optical components to the spectrometer. Here, the emitted light is separated and the intensity is measured at very precise wavelengths by detector.

Nowadays detectors used in an ICP-OES are charge coupled devices (CCD) [110] and they look like computer chips and their surface is divided into pixels. Each of these pixels measures photons of light at different wavelengths. Specialized softwares calculates the concentration of each detected element in the sample. In order to achieve this, the instrument needs also to analyze a series of standard solutions to perform a calibration before the actual analysis of the sample is carried out.

1.9.8 Thermal analysis

Thermal methods of analysis are techniques where changes of physical and chemical properties of a sample are observed as a function of temperature as the sample undergoes to a heating program [111]. Termogravimetry (TGA) and differential thermal analysis (DTA) are important thermal analytical techniques.

Thermogravimetric analysis consists of the evaluation of the mass variation of a sample as function of time or temperature under controlled atmosphere conditions. Materials such as silica for instance adsorb an appreciable amount of water when they are exposed to the atmosphere and TGA can give information about the extent of adsorption. It is also possible to observe from the TG plot the weight loss of burned materials at corresponding temperatures ranges. This information can be useful to study the stability of materials such as organic matter anchored onto inorganic materials. The resulting plot of this analysis shows mass variation vs time or temperature [111].

Differential thermal analysis is an investigation technique used to study exothermic and endothermic transformations. It gives information about thermal stability against decomposition, fusion and phase changes. During the thermal scanning the temperature difference between the sample and the reference is recorded. In a differential thermal analysis, the heat flow is plotted against time or the temperature [111].

1.10 Zeolites as sensors

During the last 15 years, scientists have tested and modified electrode surfaces to regulate the electron transfer in heterogeneous electron transfer reactions. This phenomenon occurs when an electron moves between a chemical species, for instance in solution, and a solid-state electrode generating in a process called heterogeneous electron transfer [112]. The need to find materials able to control this phenomenon, without accepting passively electrons and accelerating the electron transfer process, pushed researches to a look for other solutions. This research lead scientists to the design of molecular structures on electrode surfaces. The primary requirement of a material on a modified electrode surface is the retaining of its molecular nature once immobilized as layer on the electrode substrate. The majority of research on modified electrodes employed organic and organometallic monomolecular or polymeric layers, which were adsorbed, deposited, covalently bonded as well as self-assembled on the surface of the electrode [113]–[115].

Only in the 80s, researchers started focussing on the use of inorganic and mineral structures and among them they used, as inorganic modifiers, materials such as clays [116], metal oxide particles [117] and zeolites [118]. These materials offer several advantages such as durability, a three dimensional template and molecular discrimination. Applications such as electrocatalysis, electrosynthesis and solid state sensors require a long term stability and endurance of the electrode once modified and used under reactive conditions. Inorganic lattices are durable as they are resistant to dissolution and to decomposition at high temperatures. Pore systems play a key role in these materials as they work as selective screens and differentiate species on the basis of molecular size, working as passive discriminators. Zeolites exhibit all these properties and can therefore be exploited for electrochemical applications. The cation exchange properties combined with the molecular sieving nature of zeolites made them suitable to study the vectorial electron transfers in experiments by Mallouk and co-workers experiments. They used these materials as a reactant support and as a size and charge filter to compose electron transport chains [119]. In their experiment, they studied the photo-initiated electron transfer between a molecule provided of a donor fraction ($Ru(bpy)_3^{2+}$) and an acceptor fraction ($diquat^{2+}$) in combination with a zeolite encapsulated secondary acceptor (benzylviologen, BV^{2+}). During the experiment it was noticed that the $diquat^{2+}$ portion could penetrate the zeolite whereas $Ru(bpy)_3^{2+}$ remained excluded and immobilized on the external surface of the zeolite. As result of the photo-electrochemical reaction, an oxidised Ru^{2+} and a reduced BV^{2+} (benzylviologen) were obtained. Zeolites are electronic insulators but can also provide a high ionic strength environment and in addition, they exhibit ionic conductivity. Their employability in electrochemistry was also demonstrated in battery science when Freeman in 1965 used zeolite X as an ionic host for the catholyte and used, as ionic separator, the ion exchanged form NaX [120]. As well as clays, zeolites have been employed as coatings in the preparation of electrodes and there are several methods have been used to retain the crystalline powder on the electrode surfaces. Since zeolites are electrical insulators, they need to be coupled with an electrical source to check their influence on the electrode. The majority of the approaches used to prepare zeolite modified electrodes consist of applying them as composites to form a coating on the electrode surface. Among the methods used there are:

- **Zeolite polymer suspension** [121]**:** Polystyrene is used to bind zeolites to electrode surfaces. A suspension of zeolites and of the dissolved polymer are used to cast the electrode. The solvent is evaporated and the polymer holds the zeolite on the coated surface. This method suffers from mechanical durability issues due to the poor adherence of the polymer to the zeolite.

- **Zeolite conductive powder mixture** [121]**:** This method is commonly used in the battery industry, and it consists of pressing the powder mixture onto an electrode grid. Organic oil can be added to the powder mixture, consisting of carbon paste and zeolite, to make a modified carbon paste electrode. Carbon paste is a good binder, which can be also reused if it loses reactivity by simply removing the outer layer.
- **Zeolite carbon polymer composites** [121]**:** This is a better solution than zeolites modified carbon paste electrodes is provided by copolymerisation of styrene, which binds zeolite with carbon powder [122]. The resulting electrode consists of a hard surface with an improved reproducibility and response time to electroactive solutes compared to zeolite modified carbon paste electrodes.
- **Coelectrodeposition** [121]**:** This is an electrochemical technology where an electrochemical reaction is used to produce a thin and uniform coating on a substrate electrode. The process is performed by passing a current through an electrochemical cell [123]. An attempt to perform coelectrodeposition was conducted using zeolite A with the polymer polypyrrole and to form a uniform particle polymer coating on a disc electrode [121], [124].
- **Dry Film/Pressed Pellet** [121]**:** In this case, dry films or pressed pellets of zeolites are compressed between planar electrodes. These electrodes are

typically characterised at high temperatures through voltammetric techniques.

Zeolite modified electrodes have found many uses such as in molecular recognition. In this case, their ability to discriminate between analytes is exploited. This feature is also used to preconcentrate and store suitably size molecules for electron transfer processes. These uses made zeolite suitable materials to be used as part of electrode components for batteries such as the catholyte. Their use also extends to analytical processes where they have found application in amperometry and potentiometry. With amperometry, zeolite modified electrodes have been used to detect ions in solution by evaluating the electrical current response. Examples of these applications are reported in ref [125], [126] where zeolite modified carbon pastes were used to sequester Hg^{2+} and Ag^{+} from aqueous solutions. In potentiometry, because of their cation exchange capacity, zeolites have found application in sensing science as component of membranes for doped ion selective electrodes, also called ion selective electrodes (ISE), for the equilibrium determination of cations concentration. ISE are used to detect specific ions in a solution. The activity of the species can be used to calculate the electrochemical potential since, according to the Nernst equation these two properties are dependent on one another. The response of ISE electrode, tested through potentiometry, represents the potential of the phase boundary between the solution and the sensing material in the electrode. Zeolites contribution in ISE is as ionophore, one of the most important examples being valinomicyn. The peculiarity of this molecule lies in its structure, which is strictly selective towards K^{+}, and it is able to exclude larger or smaller cations (e.g. Na^{+}, Rb^{+}). The employement of zeolites as part of an ion sensitive electrode started with Marshall in 1939 [127] and following this several explored the functionality of zeolites in this field [126], [128]–[134]. However, the selectivity of valinomicyn has not yet been matched. Examples of zeolites employed in ISEs are provided by Johansson at al. in which mordenite type zeolites were used, after being pressed with a low viscosity resin, for the selective detection of Cs^+ cations [134]. In this experiment, the membrane gave a near Nernstian response resulting in high selectivity towards Cs^+ over Ag^+, K^+, Na^+ and Li^+. However, the choice of the zeolite used in the membrane plays a key role since a different choice could show a different affinity towards other cations such as in the example of analcite zeolite which was more selective for Na^+ over Cs^+ [128] Another important aspect is the cation itself and its size that is taking part in the ion exchange as it affects the diffusion and transport of these species through the zeolite structure. Show et al. demonstrated in their experiment that smaller cations were more effective in replacing Cu(II) in zeolite Y. In this project, zeolite/graphite mixtures will be tested to evaluate their applicability as ion selective electrodes for cation detection in aqueous solutions through potentiometry, cyclic voltammetry and electrochemical impedance spectroscopy.

1.10.1 Potentiometry

Potentiometry is an analytical technique used in electrochemistry to measure the electrical potential of an electrochemical cell under static conditions like no current flow. This technique is also used to determine the activity of species in solution by evaluating the difference in potential between two electrodes (working and reference electrode). It can also be employed to evaluate other parameters such as pH and conductivity, and it can be coupled with other techniques such as liquid chromatography, since electrochemical detectors, compared to UV-vis and refractive index detectors, are more selective towards the analytes that do not absorb in the UV-vis region and they can provide a low detection limit [135]. The advantage of this technique is that it is cheap and fast. The equipment used to perform a potentiometric analysis consist of a potentiometer or electronic millivoltmeter connected to the two electrodes in contact with a solution containing the analyte. Any electrode possesses a potential difference between its surface and the solution region surface in which is immersed. The charge on the electrode surface consists of one layer of charge and a second layer, close to the electrode, of opposite polarity which acts as a second layer of charge and this representation is called "electrical double layer" [136]. The electrodes used are the reference electrode and a working electrode. Reference electrodes such as Ag/AgCl, are used because of their stable electrical double layer properties and in this way they keep a stable potential difference and the potential constant. This electrode consist of a Ag wire embedded in a glass capillary, coated with a thin layer of AgCl and in contact with a saturated solution of KCl Also, this electrode is equipped with a porous plug at the end of it which serves as salt bridge [136], [137]. Working or sensing electrodes establishes an equilibrium with the species as they diffuse in solution before they reach the surface of the electrode itself (description above). The resulting potential generated by the electrodes depends on the concentrations and on the activities of species in solution. The resulting potential from a potentiometric experiment is expressed as:

$\mathrm{EMF} = \mathrm{E}_{const} + \mathrm{E}_{mem}$ (eq. 1.1)

Where:

- EMF is the potential and response of the electrochemical cell.
- $\mathrm{E}_{\mathrm{const}}$ is the potential developed at the reference electrode.
- $\mathrm{E}_{\mathrm{mem}}$ is the potential developed at the membrane.

EMF, if the ion activity is assumed to be constant in the membrane phase, can be also expressed as:

$\mathrm{EMF} = \mathrm{E}^0 + \frac{RT}{ziF} \ln a_i$ (eq. 1.2)

Where:

- E^0 is the potential constant term at standard condition.
- z_i is the charge of the ion.
- a_i is the activity of an uncomplexed ion.
- F is the Faraday constant = 96485 C mol^{-1}.
- R is the universal gas constant = 8.314 JK^{-1} mol^{-1}.

For sensing applications with ion selective electrodes, the slope of a calibration curve obtained after the collection of the responses should be 59.2 mV/dec. This reference number is synonymous with good sensing properties of a material as the response is “Nernstian”. This would also suggest that the electron transfer from the solution to the membrane is fast.

1.10.2 Cyclic Voltammetry

Cyclic Voltammetry is an electrochemical technique used to investigate the reduction and oxidation processes of electrochemical reactions. This investigation technique is used to obtain information about the thermodynamics of the redox process and the kinetics of the electronic-transfer reactions. Since cyclic voltammetry allows for quick determination of these aspects, it is used as routinely technique to study redox properties of organic and inorganic compounds. In a typical cyclic voltammetry experiment, a solution with a redox couple is scanned linearly between potential (figure 1.20a).

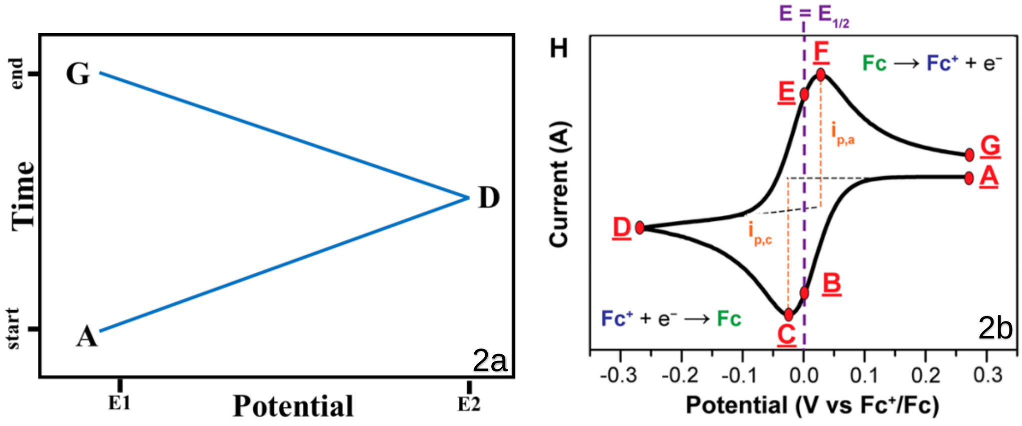

Figure 1.20: (a) Applied potential vs time of a generic CV experiment. A, D and G represent initial, switching, and end potentials respectively. (b) CV of the reversible redox couple Fc^+/Fc 1 mM, per formed at scan rate of 100 mV s−1. Figures adapted from ref. [138].

The solution, which is not stirred, contacts three electrodes (working electrode, reference electrode and counter electrode). The electrodes are connected to a potentiostat, which is used to linearly sweep the potential between the working and the reference electrodes and the current flows between the counter and working electrode. The analysis, which may consists of one or more cycles, runs until it reaches the preset potential and after that, it is swept back to the opposite direction. As result, the device measures the changing current between the working and the counter electrodes in real time and the response is displayed in terms of current vs potential.

This plot is called voltammogram (figure 1.20b) and it typically displays the applied potential (E) on the x-axis and the passed current (I), which represents the response, on the y-axis.

The two peaks in the voltammogram are the generated response of the equilibrium between two species, for instance ferrocenium (Fc^+) and ferrocene (Fc), during a scan. The equilibrium can be described by the Nernst equation. In this equation, the potential of an electrochemical cell (E) is related to the standard potential of a species (E^0) and to the relative activities of the oxidized (ox) and to the reduced (red) analyte in the system at the equilibrium.

$$E = E^0 + \frac{RT}{nF}\ln\frac{(\mathrm{Ox})}{(\mathrm{Red})} = E^0 + 2.3026\frac{RT}{nF}\log_{10}\frac{(\mathrm{Ox})}{(\mathrm{Red})}$$ [138] (eq. 1.3)

Where:

- F is the Faraday’s constant,
- R is the universal gas constant,
- n is the number of electrons
- T is the temperature.

For a generic one electron system such as the reduction of Fc^+ to Fc, the equation can be expressed in a different form by replacing the activities with concentrations and the standard potential with the formal potential ($E_{1/2}$):

$$E = E^{0\prime} + \frac{RT}{F}\ln\frac{[\mathrm{Fc}^+]}{[\mathrm{Fc}]} = E^{0\prime} + 2.3026\frac{RT}{F}\log_{10}\frac{[\mathrm{Fc}^+]}{[\mathrm{Fc}]}$$ [138] (eq. 1.4)

The Nernst equation represents a way to predict the response of a system as the concentrations of the species or the electrode potential change. For this system, if a potential of $E = E^{\circ\prime} \approx E_{1/2}$ is applied to the Fc^+ solution, the equation predicts that Fc^+ will be reduced to Fc until $[Fc^+] = [Fc]$, and equilibrium is achieved. The steps during a CV scan of an Fc^+ solution to negative potentials are displayed in figure 2b. In this figure Fc^+ is reduced to Fc at the working electrode. Point A in figure 2b displays the starting situation where only Fc^+ is in solution. During the scan at negative potentials from A to D, Fc^+ is depleted at the electrode and reduced to Fc. The point C represent the cathodic current ($I_{p,c}$). The current at this point is given by the delivery of Fc^+ species via diffusion from the solution to the electrode. As long as the scan continues, the diffusion layer at the surface of the electrode containing the reduced Fc is generated. The depletion of Fc^+ at the electrode due to growing diffusive layer limits transport and the current decreases for the reduction (from C to D) and, at more negative potentials, its rate of diffusion becomes slower generating a decrease of current. The resulting “duck” shape of the voltammogram depends on the nature of the diffusing species between the surface of the electrode to the bulk solution. At this point, the potential is switched to positive direction. In this case, the Fc is oxidized to Fc^+ as the potential becomes positive. B and E in figure 2b represent the steps where the concentrations of Fc and Fc+ are equal. Points C and F represent the $E^{0'}$, which is a straightforward way to estimate the reversibility of the electron transfer of a system. When a process is electrochemically reversible the difference between the two peaks at 25°C (2.22RT/F) is equal to 57mV. This is called the “peak to peak separation” (ΔEp). This information is useful to determine if the analyte is stable after reduction and if it can be re-oxidized. Electrochemical reversibility refers to the kinetics of the electron transfer between the electrode and the analyte. If the rate of electron transfer is high there will be high reversibility and the Nernstian equilibrium is established immediately upon any small change in applied potential. Systems that show this behavior are reversible. If the activation energy is high, the electron transfer will be slower and more negative potential required to observe oxidation or reduction and termed irreversible. Another important parameter during analysis is the scan rate. It determines how fast the applied potential is scanned. When scan rates are faster, the size of the diffusion layer is small and higher currents are observed [139]. The linear relationship between the peak current i_p (A) and the square root the scan rate ($V^{1/2}$ $s^{-1/2}$) can be described by the Randles –Sevcik equation:

$$i_p = 0.446nFAC^0\left(\frac{nF\upsilon D_o}{RT}\right)^{1/2}$$

[138] (eq. 1.5)

Where:

- n is the number of electrons transferred in the redox process.
- A (cm^2) is the electrode surface area usually treated as the geometric surface area.
- D_o (cm^2 s^{-1}) is the diffusion coefficient of the oxidized analyte.
- C^0 (mol cm^{-3}) is the bulk concentration of the analyte.

The calculation of diffusion coefficient by using this equation gives information whether the analyte is freely diffusing in solution. Since the analyte can adsorb on the surface of the electrode, it is important to make sure that it remains homogenous in solution before analyzing its reactivity.

1.10.3 Electrochemical impedance spectroscopy

According to Ohm’s law, the voltage or potential is directly proportional to the direct current (DC) that flows through a circuit and its resistance.

$E=IR$ (eq. 1.6) [139]

Where

- R is the resistance
- I is the current
- E is the voltage

In this law, the resistance represents the measure of the opposition to the flow of an electric current and it can be calculated by dividing the potential with the current.

$R = E/I$ (eq. 1.7)

The impedance (Z) represents a measure of the opposition to the flow of electrons, generated by a periodic electrical perturbation, that pass through a circuit [140]. The unit used to estimate this property is expressed in Ohm (Ω). Mathematically, impedance corresponds to the combination of resistance (a static property independent from the incident alternative current AC frequency) and (capacitive and inductive) reactance in a system such as a cell, a battery or a circuit and can be represented as:

$E = IZ$ (eq. 1.8) [139], [140]

where

- Z symbol represents the Impedance.

Or

$Z = E/I$ (eq. 1.9)

The technique used to evaluate the impedance in a system is called electrochemical impedance spectroscopy (EIS). In this technique, a periodic stimulation signal is applied to an electrochemical system using a potentiostat. This signal can be a sinuisoidal potential or a sinuisoidal current, which respectively give as output the measure of a sinuisoidal current or a sinuisoidal potential. If the output is the current then it is called potentiostatic EIS, while it is termed galvanostatic EIS if the output is the potential. In this research project, potentiostatic EIS was used.

Since the applied input is a voltage, this property can be written as oscillating voltage as:

$\mathbf{E(t) = |E|\sin(\omega t)}$ (eq. 1.10) [139], [140]

where

- $|E|$ is the amplitude of the voltage signal
- $\omega = 2\pi f$ is the angular frequency

The response will be the oscillating current with amplitude **|I|:**

$\mathbf{I(t) = |I|\sin(\omega t + \theta)}$ (eq. 1.11) [139], [140]

The current is shifted because of the impedance offered to the electron flow related to the electron flow by nature of the electrolyte, the diffusion and the electrode kinetics and the chemical reactions that are happening in the cell (figure 1.21).

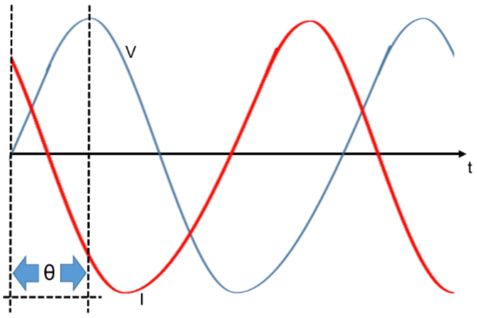

Figure 1.21: Phase lag between an AC voltage and the current response.

As result of these two equations, impedance can be expressed as:

$$Z = \frac{E(t)}{I(t)} = \frac{|E|\sin(\omega t)}{|I|\sin(\omega t+\theta)} = |Z|\,\frac{\sin(\omega t)}{\sin(\omega t+\theta)} \qquad \text{(eq. 1.12)}$$

Quantitatively, impedance corresponds to the ratio of the complex representation of the sinuisoidal voltage with the complex representation of the sinuisoidal current that flows in the considered system. Both properties, voltage and current, are considered as function of frequency. The relationship between E and I was traditionally represented with Lissajou curves obtained using oscilloscopes. Nowadays, other ways are used to represent impedance. One of them employs complex numbers.

Starting from Euler’s formula: **e^{jx} = cos(x) + jsin(x)** impedance can be re-written as:

$$Z = |Z|ej\theta = \frac{|E|e^{j\omega t}}{|I|e^{j\omega t} + \theta} \qquad \text{(eq. 1.13)}$$

And simplified as:

$$E = IZ = I|Z|^{j\theta} \qquad \text{[139]} \quad \text{(eq. 1.14)}$$

Where $j = \sqrt{-1}$

As displayed in the right hand side of the equation 1.13, the ratio of an oscillating voltage to an oscillating current corresponds to the impedance which includes magnitude |Z| and phase angle θ. Impedance spectroscopy uses the Cartesian complex plane representation. In this way, impedance can be considered the result of the contribution of two parts: a real part and an imaginary part as shown in equation 1.15:

Z = Z’ + jZ’’ (eq. 1.15)

The graphical representation of impedance is done in an Argand diagram or complex plane, which is the basis of the Nyquist plot, named by Harry Nyquist, a Swedish-American scientist. The Nyquist plot includes both parts of impedance, real and imaginary, and it displays a sequence of points where each of them corresponds to a different frequency (Figure 1.22).

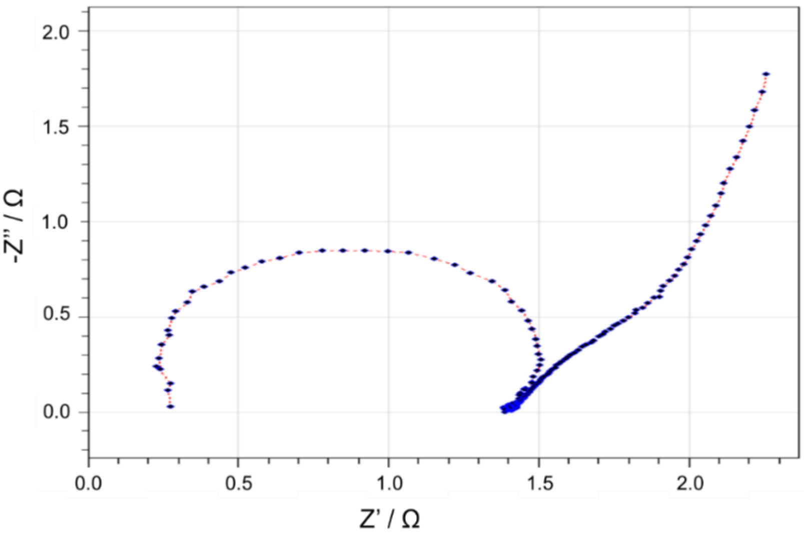

Figure 1.22: Example of Nyquist plot.

It is possible to recognize elements or a combination of them. However, there is a disadvantage: it does not give you information about the frequency associated to a certain point. In order to overcome this drawback, another way to represent impedance is through a Bode plot (figure 1.23). In this case, the plot displays the imaginary part or the phase angle against the frequency.

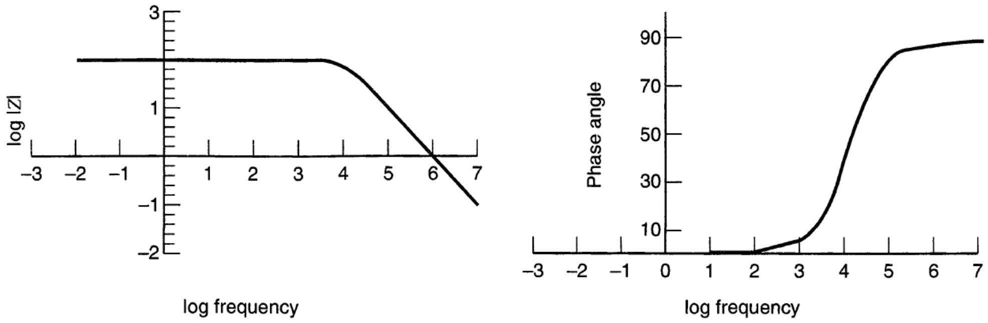

Figure 1.23: Examples of Bode plots. For a parallel RC circuit.

During EIS, the amplitude (voltage) is kept constant (5-10 mV) and only the frequency changes. The change of the frequency triggers processes where the electrons, as well as the ions, participate. Both, input and output signals, are converted through Fourier convert from the time domain to the frequency domain. Rather than plotting current (I) vs potential (E), in EIS, it is calculated the ratio of the frequencies potential dependent over the frequencies current dependent. As long as a pre-selected frequency range is scanned, many different processes will be detected in the system. Depending on the frequency system, some of these processes will be found at high frequencies and others at lower frequencies. Quicker processes, such as chemical reactions, occur at high frequencies whereas, at low frequencies, slower processes such as diffusion occur.

Once a Nyquist plot is obtained, the investigation of an inspected system by using EIS requires a certain knowledge of circuit elements. These components, once manually combined, compose the circuitry used to simulate the response displayed in the experimental Nyquist plot. This procedure is performed through softwares that include these design features. Among these circuits, component such as resistors, capacitors, inductors, memristor components, constant phase elements and Warburg elements can be listed. Each of these elements have their own contribution to the impedance.

The correct combination is crucial to evaluate the properties of the system under investigation. In addition, the above listed elements can be combined in series or in parallel and this increases the number of variables to take into account to obtain the right simulated circuit. Although this method might seem difficult, modern software can provide additional features enable simulations of equivalent circuits automatically, making this task simpler.

In order to evaluate the properties the operator is interested in, it is necessary to generate an equivalent calculated circuit, which could fit at its best the experimental plot. However, good fitting does not mean that the equivalent circuit correctly simulates the phenomena in the investigated material, especially when calculated circuits are complex and consist of many elements. Very often, it is not clear which circuit may work for the inspected system. Different equivalent circuits may fit the studied system and this is the reason why some scientists sometimes are skeptical about EIS. EIS, however, has a large number of applications such as the evaluation of passivation mechanism and corrosion, the evaluation of processes that occurs at different timescales, diagnosis of performance of fuel cells, capacitors, super capacitors and batteries. In this part of the project EIS was performed to evaluate the aspects related to the diffusivity of species in solution that migrate towards the materials included in the tested electrodes.

1.11 Research aim

The study in this PhD project can follow two potential directions. The first one has the interest to investigate structural and acidic properties of two particular zeolites: mazzite and LTL zeolite. Although these zeolites show significant similarities in terms of structure, they are characterized by a remarkable difference about their acid sites. Mazzite shows higher acidic properties compared to LTL zeolite. However, mazzite lacks in accessibility to these sites and this is due to the narrowness that characterizes its pore structure.

The properties of LTL and mazzite zeolites will be investigated through spectroscopic, solid state and electrochemical techniques. Spectroscopic techniques such as FTIR will be crucial to understand acidic properties. Solid state techniques such as X-ray diffraction will be employed to obtain information about structural aspects and electron microscopy such as SEM-EDX for morphology and composition. During the study of the properties of mazzite and LTL also, the ion exchange properties will be studied and investigated.

These aspects lead to a potential second direction which involves the use of electrochemical and potentiometric techniques. The aim of this part of the project will be to employ the ion exchange properties for applications in sensors technology and to develop electrodes for environmental application such as for cation detection in water. A further goal of this research is the enhancement of portability of devices for sensor technology that our research group wants to develop. The idea is to make a low cost system that can be used to carry out analyses in situ also characterised by a satisfactory level of selectivity towards species detected in water.

1.12 References

[1] A. F. Cronstedt, Natural zeolite and minerals, K. Sven. Vetenskapsakad. Handl, 19 (1756) 363.

[2] J. L. Schlenker, G. H. Kuhl, Proceedings from the 9th International Zeolite Conference, edited R. von Ballmoos, J. B. Higgins and M. M. J. Treacy, Butterworth-Heinemann, Stoneham, MA, 1 (1992) 3.

[3] A. F. Cronstedt, Försök till Mineralogie eller Mineral-Rikets Upställning, Stockholm: Wildiska, (1758) 99.

[4] E.M. Flanigen, in Introduction to Zeolite Science and Practice, 2nd edn., H. van Bekkum, E.M. Flanigen, P.A. Jacobs, J.C. Jansen (eds.), Elsevier, Amsterdam, Stud. Surf. Sci. Catal.137 (2001) 11.

[5] H. S. C. Deville, Reproduction de la Lévyne, C. R. Acad. Sci., 54, (1862) 324.

[6] G. Friedel, Zeolites and the substitution of various substances for the water which they contain. C. R. Acad. Sci., 122 (1896) 948.

[7] F. Grandjean, Optical study of the absorption of the heavy vapors by certain zeolites. C. R. Acad. Sci., 149 (1910) 866.

[8] O. Weigel, E. Steinhoff, Adsorption of organic liquid vapors by chabazite. Z. Kristallogr., 61 (1925) 125.

[9] J. W. McBain, The sorption of Gases and Vapors by Solids, Rutledge and Sons, (1932).

[10] R. M. Barrer, D. A. Ibbitson, Occlusion of hydrocarbons by chabazite and analcite. Trans. Farraday Soc., 40 (1944) 206.

[11] R. Barrer, Syntheses and reactions of mordenite, Journal of Chemical Society, (1948) 2158-2163.

[12] C. Baerlocher, L. B. McCusker, D. H. Olson, Atlas of Zeolite Framework types, Elsevier, (2007).

[13] R. M Barrer, C. Marcilly, Hydrothermal chemistry of silicates. Part XV. Synthesis and nature of some salt-bearing aluminosilicates. J. Chem. Soc. A Inorganic, Phys. Theor., (1970) 2735–2745.

[14] R. M. Milton, Molecular Sieve Science and Technology A Historical Perspective. ACS Symp. Ser., 398 (1989) 1.

[15] W. H. I. Taylor, The structure of analcite. Zeitschrift für Krist. - Cryst. Mater., 74 (1930) 1–19.

[16] D. S. Coombs, Recommended nomenclature for zeolite minerals: report of the subcommittee on zeolites of the International Mineralogical Association, Commission on new Minerals and Mineral names. Can. Mineral., 35 (1997) 1571–1606.

[17] L. Koopal, (2001), Definitions, Terminology and Symbols in Colloid and Surface Chemistry, internet version with annotations of D.H, Everett, Manual of Symbols and Terminology for Physicochemical Quantities and Units, Appendix II: Definitions, Terminology and Pure and Applied Chemistry, 31 (1972) 577.

[18] M. Thommes, K. Kaneko, A.V. Neimark, J.P. Olivier, F. Rodriguez-Reinoso, J. Rouquerol, K.S.W. Sing, Physisorption of gases, with special reference to the evaluation of surface area and pore size distribution, (IUPAC Technical Report), Pure and Applied Chemistry, 87 (2015) 1051–1069.

[19] J. Rouquerol, D. Avnir, C. W. Fairbridge, D. H. Everett, J. H. Haynes, N. Pernicone, J. D. F. Ramsay, K. S. W. Sing, K. K. Unger, Recommendations for the Characterization of Porous Solids (TechnicalReport), Pure and

Applied Chemistry, 66 (1994) 1739-1758.

[20] N. La-Salvia, J. J. Lovón-Quintana, A. S. P. Lovón, G. P. Valença, Influence of Aluminum Addition in the Framework of MCM-41 Mesoporous Molecular Sieve Synthesized by Non-Hydrothermal Method in an Alkali-Free System, Materials Research, 20 (2017) 1461-1469.

[21] R. Locus, D. Verboekend, R. Zhong, K. Houthoofd, T. Jaumann, S. Oswald, L. Giebeler, G. Baron, B. F. Sels, Enhanced Acidity and Accessibility in Al-MCM-41 through Aluminum Activation, Chemistry of Materials, 28 (2016) 7731-7743.

[22] S.A. Emami Moghaddam, R. Harun, M.N. Mokhtar, R. Zakaria, Potential of Zeolite and Algae in Biomass Immobilization, Biomed. Res. Int., 2018 (2018) 6563196.

[23] W.M. Meier, Zeolite structures and molecular sieves, Society of Chemical Industry, 10 (1968) 27.

[24] J. Čejka, R. E. Morris, P. Nachtigall (Eds.), RSC Catalysis Series No. 28 Zeolites in Catalysis: Properties and Applications, The Royal Society of Chemistry, (2017).

[25] J. Cejka, Introduction to Zeolite Science and Practice; 3rd Revised Edition; Studies in Surface Science and Catalysis, Elsevier, (2007) 168.

[26] A.J. Schwanke, R. Balzer, S. Pergher, Microporous and Mesoporous Materials from Natural and Inexpensive Sources, In Handbook of Ecomaterials, L.M.T. Martínez, O.V. Kharissova, B. Kharisov, Springer, (2017) 1–22.

[27] Database of zeolite structures: http://www.iza-structure.org/databases, as of May 2023.

[28] W. Löwenstein, The distribution of aluminum in the tetrahedra of silicates and aluminates, Am. Mineral., 39 (1954) 92–96.

[29] V. Inglezakis, A. Zorpas, Handbook of natural zeolites, Bentham Science Publishers, (2012).

[30] S. Mintova, N. Barrier, Verified synthesis of zeolitic materials Third revised edition, IZA Synthesis Commission, (2016) 215-221.

[31] D.W. Breck, Zeolite Molecular Sieves, Structure, Chemistry and Use, Wiley, (1974).

[32] W. Meise and F.E. Schwocho, Kinetic Studies on Formation of Zeolite-A, Adv. Chem. Ser. (1973) 169.

[33] B. Lu, T. Tsuda, H. Sasaki, Y. Oumi, K. Itabashi, T. Teranishi, T. Sano, Effect of Aluminum Source on Hydrothermal Synthesis of High-Silica Mordenite in Fluoride Medium, and It's Thermal Stability, Chem. Mater., 16 (2004) 286.

[34] A. Corma, F. Rey, J. Rius, M.J. Sabater, S. Valencia, Supramolecular self-assembled molecules as organic directing agent for synthesis of zeolites, Nature, 431 (2004) 287.

[35] H. Kacirek, H. Lechert, Rates of crystallization and a model for the growth of sodium-Y zeolites, J. Phys. Chem., 80 (1976) 1291.

[36] J. Ciric, Kinetics of zeolite A crystallization, J. Colloid Interface Sci., 28 (1968) 315.

[37] J.C. Cejka, A.S. Zone, Zeolite and Catalysis, Reactions and Application, John Willey and Sons inc., 6(3), (2010) 212-234.

[38] R. Xu, Q. Huo and W. Pang, in Proc. 9th Int. Zeolites Conf., R. von Ballmoos, J.B. Higgins, M.M.J. Treacy (Eds), Butterworth-Heinemann,

Montreal, (1992) 271.

[39] Q. Huo and R. Xu, Syntheses of AlPO4-5, AlPO4-11, and AlPO4-21 from non-aqueous systems, J. Chem. Soc., Chem. Commun., 783 (1990) 1987.

[40] E. R. Cooper, C. D. Andrews, P. S. Wheatley, P. B. Webb, P. Wormald, R. E. Morris, Ionic liquids and eutectic mixtures as solvent and template in synthesis of zeolite analogues, Nature, 430(7003) (2004) 1012-1016.

[41] R.M. Barrrer, Hydrothermal Chemistry of Zeolite. London Academic Press, 3(6), (1982) 235-242.

[42] I. Ekpe, Zeolite Synthesis, Characterisation and Application Areas: A Review, International Research Journal of Environmental Sciences, (2017).

[43] P. Cañizares, A. Durán, F. Dorado, M. Carmona, The role of sodium montmorillonite on bounded zeolite-type catalysts, Applied Clay Science, 16 (2000) 273–287.

[44] R. Ruiz, C. Blanco, C. Pesquera, F. Gonzalez, , I. Benito, J.L. Lopez, Zeolitization of a bentonite and its application to the removal of ammonium ion from waste water, Applied Clay Science, 12 (1997) 73-83.

[45] N. Moreno, X. Querol, F. Plana, J. Andrés, M. Janssen, H. Nugteren, Pure Zeolite Synthesis from Silica Extracted from Coal Fly Ashes. Journal of Chemical Technology and Biotechnology, 77, (2002) 274-279.

[46] G. Varga, The structure of kaolinite and metakaolinite, Epitoanyag - Journal of Silicate Based and Composite Materials, 59 (2007).

[47] C. A. Rios-Reyes, C. Denver-Williams, Ó. M. Castellanos, Reactivity Study of Kaolinite and Metakaolinite in Fluoride Media under Hydrothermal Conditions, Ingeniería y Universidad journal, 17(1) (2013) 183-203.

[48] M. Mohamed, E. Ahmed, Synthesis of Faujasite from Egyptian Clays:

Characterizations and Removal of Heavy Metals, Geomaterials, 5(2) (2015) 68-76.

[49] A. Dyer, An Introduction to Zeolite Molecular Sieves. xiii, Chichester, New York, Brisbane, Toronto, Singapore: John Wiley & Sons, Geological Magazine, 126(4) (1989) 446-447.

[50] C.L. Thomas, Chemistry of cracking catalysts, Ind. Eng. Chem., 41 (1949) 2564.

[51] T.H. Milliken, G.A. Mills, A.G. Oblad, The chemical characteristics and structure of cracking catalysts, Disc. Faraday Soc., 8 (1950) 279-290.

[52] K. Sadowska, K. Gora-Marek, M. Drozdek, P. Kustrowski, J. Datka, J. Martinez Triguero, F. Rey, Desilication of highly siliceous zeolite ZSM-5 with NaOH and NaOH/tetrabutylamine hydroxide, Microporous and Mesoporous Materials, 168 (2013) 195-205.

[53] D. Majda, K. Tarach, K. Gora-Marek, A. Michalik-Zym, S.D. Napruszewska, M. Zimowska, E.M. Serwicka, Thermoporosimetry of n-alkanes for characterization of mesoporous SBA-15 silicas - towards deeper understanding the effect of the probe liquid nature, Microporous and Mesoporous Materials, 226 (2016) 25-33.

[54] K. Tarach, J. Tekla, U. Filek, A. Szymocha, I. Tarach, K. Góra-Marek, Alkaline-acid treated zeolite L as catalyst in ethanol dehydration process, Microporous and Mesoporous Materials, 241 (2017) 132-144.

[55] X. Jia, W. Khan, Z. Wu, J. Choi, A. Yip, Modern synthesis strategies for hierarchical zeolites: Bottom-up versus top-down strategies, Advanced Powder Technology, 30 (2019) 467-484.

[56] V. Zholobenko, A. Al-Ani, J. Haslam, N. Mordvinova, O. Lebedev, A.

Vicente, C. Fernandez, Synthesis of Nanostructured Catalysts by Surfactant-Templating of Large-Pore Zeolites, Nanoscale Advances, 1 (2018) 310-318.

[57] T. Prasomsri, W. Jiao, S. Weng, J. García-Martínez, ChemInform Abstract: Mesostructured Zeolites: Bridging the Gap Between Zeolites and MCM-41, Chemical Communications, 51 (2015) 8900-8911.

[58] H. Eichhorn, J. C. Poggendorff's Annalen der Physik und Chemie, 4th series, Phys. Chem., Leipzig, 105 (1858) 26 (in German).

[59] E. Hoinkis and H.W. Levi, in Ion Exchange in the Process Industries, Soc. Chem. Ind., London, (1970) 339.

[60] L.V.C. Rees, N.M. Brooke, in Ion Exchange in the Process Industries, Soc. Chem. Ind., London, (1970) 352.

[61] A. Dyer, R.B. Gettins, in Ion Exchange in the Process Industries, Soc. Chem. Ind., London, (1970) 357.

[62] A. Dyer, H. Enamy, R.P. Townsend, The Plotting and Interpretation of Ion-Exchange Isotherms in Zeolite Systems, Sep. Sci. Tech., 16 (1981) 173-183.

[63] R. P. Townsend, Ion exchange in zeolites: some recent developments in theory and practice, Pure Appl. Chem., 58 (1986) 1358-1366.

[64] R.M. Barrer, J. Klinowski, Ion-exchange selectivity and electrolyte concentration, J. Chem. Soc. Faraday Trans., 70 (1974) 2080.

[65] D.H. Lauriente, Y. Inoguchi, The Chemical Economics Handbook - SRI Consulting, (2005) 599.

[66] H. Van Bekkum, E.M. Flanigen, P.A. Jacobs, J.C. Jansen (eds.), Introduction to Zeolite Science and Practice, Studies in surface and catalysis, Elsevier, 137 (2001) 1-8.

[67] J. F. Patzer 2nd, S. J. Yao, S. K. Wolfson Jr., Zeolitic ammonium ion

exchange for portable hemodialysis dialysate regeneration. ASAIO J. 41(2) (1995) 221-226.

[68] E. Valcke, M. Vidal, A. Cremers, J. Ivanov, G. Perepelyatnikov, The use of zeolites as amendments in radiocaesium- and radiostrontium-contaminated soils: A soil-chemical approach. Part III: A soil-chemical test to predict the potential effectiveness of zeolite amendments, Zeolites, 18 (1997) 218-224.

[69] N. Yamaguchi, A. Hikono, T. Saito, Effects of zeolite and vermiculite addition on exchangeable radiocaesium in soil with accelerated ageing, Journal of Environmental Radioactivity, 203 (2019) 18-24.

[70] L. Velarde, M. S. Nabavi, E. Escalera, M. L. Antti, F. Akhtar, Adsorption of heavy metals on natural zeolites: A review, Chemosphere, 328 (2023) 138508.

[71] C. Haidouti, Inactivation of mercury in Contaminated Soils by Natural zeolite, Science Total Environment, 208(1-2) (1997) 105-109.

[72] K. A. Carrado, P. K. Dutta, Handbook of Zeolite Science and Technology Edited by Scott M. Auerbach, Marcel Dekker, New York, (2003).

[73] G. Ferretti, G. Galamini, V. Medoro, M. Coltorti, D. Di Giuseppe, B. Faccini, Impact of Sequential Treatments with Natural and Na-Exchanged Chabazite Zeolite-Rich Tuff on Pig-Slurry Chemical Composition, Water, 12 (2020) 310.

[74] V. Georgieva, R. Retoux, V. Ruaux, V. Valtchev, S. Mintova, Detection of CO_2 and O_2 by iron loaded LTL zeolite films, Frontiers of Chemical Science and Engineering, 12 (2018) 94-102.

[75] N. Alireza, R. Gholamhosein, Modification of nanoclinoptilolite zeolite with hexadecyltrimethylammonium surfactant as an active ingredient of

chromate-selective membrane electrode, Journal of Chemistry, 2013(5) (2012) 1.

[76] V.L. Zholobenko, A.J. Evans, S.L.Y. Tang., Photocatalysis on zeolites and ordered mesoporous materials. “Nanoclusters and Nanocrystals” edited H.S. Nalwa, American Scientific Publishers, 6 (2003) 179-210.

[77] N. Y. Chen, W. E. Garwood, Industrial Application of Shape-Selective Catalysis, Catalysis Reviews, 28(2-3) (1986) 185-264.

[78] K. M. Minachev, Y. I. Isakov, Chemistry and Catalysis by Zeolites, edited by J. A. Rabo, American Chemical Society, 1 (1976) 552.

[79] R. Chang, Chimica Fisica Vol.2, Zanichelli, (2003)

[80] W. Roentgen, On a New Kind of Rays, Nature, 53 (1896) 274–276.

[81] T. Flohr, B. Ohnesorge, Springer-Verlag Berlin Heidelberg, Multi-Slice CT Technology. Multi-slice and Dual-source CT in Cardiac Imaging. Springer, (2007) 41-69.

[82] H H. M. Rietveld, A profile refinement method for nuclear and magnetic structures. J. Appl. Crystallogr., 2 (1969) 65−71.

[83] Crystallography Open Database, https://www.crystallography.net/cod/index.php

[84] The International Centre for Diffraction Data - ICDD, https://www.icdd.com/

[85] B. R. Toby, Factors in Rietveld analysis: How good is good enough?, Powder Diffraction, 21(1) (2006) 67-70.

[86] R. A. Young, Introduction to the Rietveld method, The Rietveld Method, edited by R. A. Young, Oxford University Press, Oxford, (1993) 1–38.

[87] F. Izumi, Chapter 7: The rietveld method and its applications to synchrotron

X-ray powder data, Editor(s): H. Saisho, Y. Gohshi, Analytical Spectroscopy Library, Elsevier, 7 (1996) 405-452.

[88] G. S. Pawley, Unit-cell refinement from powder diffraction scans, J. Appl. Crystallogr., 14 (1981) 357–361.

[89] J. Dewar, Studies with the Liquid Hydrogen and Air Calorimeters, Proceedings of the Royal Society of London. Series A, Containing Papers of a Mathematical and Physical Character, 76(510) (1905) 325–40.

[90] I. Langmuir, The constitution and fundamental properties of solids and liquids. Part 1. Solids, J. Am. Chem. Soc., 38 (1916) 222.

[91] S. Brunauer, P. H. Emmett, The Use of Low Temperature van der Waals Adsorption Isotherms in Determining the Surface Areas of Various Adsorbents, J. Am. Chem. Soc., 59 (12) (1937) 2682-2689.

[92] S. Brunauer, P. H. Emmett, E. Teller, Adsorption of gases in multimolecular layers, J. Am. Chem. Soc., 60(2) (1938) 309–319.

[93] E. P. Barrett, L. G. Joyner, P. P. Halenda, The Determination of Pore Volume and Area Distributions in Porous Substances. I, Computations from Nitrogen Isotherms, J. Am. Chem. Soc., 73 (1) (1951) 373-380

[94] F. Rouquerol, J. Rouquerol, K.S.W. Sing, Adsorption by Powders and Porous Solids, Academic Press, London, (1999).

[95] K. Sing, The use of nitrogen adsorption for the characterisation of porous materials, Colloids and Surfaces A: Physicochemical and Engineering Aspects, 187–188 (2001) 3-9.

[96] K. Sing, Reporting physisorption data for gas/solid systems with special reference to the determination of surface area and porosity (Recommendations 1984), Pure and Applied Chemistry, 57 (1985) 603-619.

[97] G. Reichenauer, Thermal aging of silica gels in water, Journal of Non-Crystalline Solids, 350 (2004) 189-195,

[98] F. Lónyi, J. Valyon, On the interpretation of the NH3-TPD patterns of H-ZSM-5 and H-mordenite, Microporous and Mesoporous Materials, 47(2) (2001) 293-301.

[99] E. De Hoffman, V. Stroobant, Mass spectrometry principles and Applications, Wiley, (2008).

[100] P. Echlin, Handbook of Sample Preparation for Scanning Electron Microscopy and Xray Microanalysis, Springer, (2009).

[101] W. D. Callister, Materials Science and Engineering: An Introduction, Edises, (2006).

[102] J. I. Goldstein, D. E. Newbury, J. R. Michael, N. W. M. Ritchie, J. H. J. Scott, D. C. Joy, Scanning Electron Microscopy and X-Ray Microanalysis, Springer, (2018).

[103] C. Grochowski, E. Blicharska, P. Krukow, K. Jonak, M. Maciejewski, D. Szczepanek, K. Jonak, J. Flieger, R. Maciejewski, Analysis of trace elements in human brain: its aim, methods, and concentration levels, Frontiers Chem., 7(115) (2019).

[104] A.J. Majumdar, N. Dubey, Applications of inductively coupled plasma-atomic emission spectrometry (ICP-OES) in impurity profiling of pharmaceuticals, Int. J. Pharmacy Life Sci., 8(1) (2017) 5420-5425.

[105] M. Resano, F. Vanhaecke, M.T.C. de Loos-Vollebregt, Electrothermal vaporization for sample introduction in atomic absorption, atomic emission and plasma mass spectrometry-a critical review with focus on solid sampling and slurry analysis, J. Anal. Atomic Spectrometry, 23(11) (2008) 1450-1475.

[106] D. Vogt, T. Vogt, B. Wolf, M. Neuroth, M. Otto, Direct determination of organic and inorganic oxygen in coals from the Argonne Premium Sample Program by solid sampling electrothermal vaporization inductively coupled plasma optical emission spectrometry, Fuel, 196 (2017) 185-194.

[107] A. Muller, D. Pozebon, V.L. Dressler, Advances of nitrogen microwave plasma for optical emission spectrometry and applications in elemental analysis: a review, J. Anal. Atomic Spectrometry, 35(10) (2020) 2113-2131.

[108] G.L. Scheffler, D. Pozebon, D. Beauchemin, Improving the analytical performance of electrothermal vaporization coupled to inductively coupled plasma optical emission spectrometry using a mixed-gas plasma, J. Anal. Atomic Spectrometry, 34(5) (2019) 891-898.

[109] J.W. Olesik, Echelle grating spectrometers for inductively coupled plasma-optical emission spectrometry. A review of basic equations and operating principles, Spectroscopy, 14(10) (1999) 36-41.

[110] T.W. Barnard, M.I. Crockett, J.C. Ivaldi, P.L. Lundberg, D.A. Yates, , P.A. Levine, D.J. Sauer, Solid-state detector for ICP-OES, Anal. Chem., 65(9) (1993) 1231-1239.

[111] A. W. Coats, J. P. Redfern, Thermogravimetric analysis. A review, Analyst, The Royal Society of Chemistry, 88(1053) (1963) 906-924.

[112] R. W. Murray, Chemically Modified Electrodes, Electroanalytical Chemistry, A. J. Bard, Ed., New York, 13 (1984) 191.

[113] R. W. Murray, A. G. Ewing, R. A. Durst, Chemically modified electrodes. Molecular design for electroanalysis, Anal. Chem. 59(5) (1987) 379.

[114] A. Merz, Chemically modified electrodes, In: Steckhan, E. (eds) Electrochemistry IV, Topics in Current Chemistry, Springer, Berlin,

Heidelberg, 152 (1990).

[115] D. M. Heard, A. J. J. Lennox, Electrode Materials in Modern Organic Electrochemistry, Angew. Chem. Int. Ed. Engl., 59 (2020) 18866.

[116] P. V. Kamat, Electrochemistry and photoelectro-chemistry of dye-incorporated clay-modified electrode, Journal of Electroanalytical Chemistry and Interfacial Electrochemistry, 163 (1984) 389.

[117] J. Zak, T. Kuwana, Electrooxidative catalysis using dispersed alumina on glassy carbon surfaces, Am. Chem. Soc., 104 (1982) 5514.

[118] C. G. Murray, R. J. Nowak, D. R. Rolison, Electrogenerated coatings containing zeolites, J. Electroanal. Chem. Interfacial Electrochem., 164(1) (1984) 205-210.

[119] J. S. Krueger, C. Lai, Z. Li, J. E. Mayer, T. E. Mallouk, Proceedings, 5th International Symposium, Inclusion Phenomena and Molecular Recognition, Orange Beach, Alabama, Springer, (1988).

[120] D. C. Freeman Jr, U.S. Patent 3,186,875 (1965); Br. Patent 999,948 (1965).

[121] D. R. Rolison, Zeolite-modified electrodes and electrode-modified zeolites, Chemical Reviews, 90 (1990) 867-878.

[122] B. R. Shaw, K. E. Creasy, Carbon composite electrodes containing alumina, layered double hydroxides, and zeolites, Journal of Electroanalytical Chemistry and Interfacial Electrochemistry, 243(1) (1988) 209-217.

[123] M. Jing, T. Wu, G. Zou, H. Hou, X. Ji, Chapter 9 - Nanomaterials for electrochemical energy storage, Editor(s): J. Andrew, E. Wain, J.F. Dickinson, Frontiers of Nanoscience, Elsevier, 18 (2021) 421-484.

[124] D. R. Rolison, R. J. Nowak, T. A. Welsh, C. G. Murray, Analytical implications of zeolites in overlayers at electrodes, Talanta, 38(1) (1991) 27-

35.

[125] P. Hernandez, E. Alda, L. Hernandez, Determination of mercury(II) using a modified electrode with zeolite, Fresenius' Zeitschrift für analytische Chemie, 327 (1987) 676-678.

[126] J. Wang, T. Martinez, Accumulation and voltammetric measurement of silver at zeolite-containing carbon-paste electrodes, Analytica chimica acta, 207 (1988) 95.

[127] C. E. Marshall, The use of zeolitic membrane electrodes, The Journal of Physical Chemistry, 43(9) (1939) 1155-1164.

[128] R. M. Barrer, S. D. James, Electrochemistry of crystal-polymer membranes, Part II, Membrane potentials, The Journal of Physical Chemistry, 64 (1960) 421–427.

[129] J. Wang, A. Walcarius, Zeolite containing oxidase-based carbon paste biosensors, Journal of Electroanalytical Chemistry, 404(2) (1996) 237–242.

[130] M. Demertzis, N. P. Evmiridis, Potentials of Ion-exchanged Synthetic Zeolite-Polymer Membranes. Journal of the Chemical Society, Faraday Transactions 1: Physical Chemistry in Condensed Phases, 82(12) (1986) 3647–3655.

[131] S. Matysik, F. M. Matysik, J. Mattusch, W. D. Einicke, Application of Zeolite- Polydimethylsiloxane Electrodes to Potentiometric Studies of Cationic Species, Electroanalysis, 10(2) (1998) 98–102.

[132] Walcarius, A. Zeolite-modified paraffin-impregnated graphite electrode, J. Solid State Electrochem., 10 (2006) 469–478.

[133] E. M. Maximiano, F. de Lima, C. A. L. Cardoso, G. J. Arruda, Modification of carbon paste electrodes with recrystallized zeolite for simultaneous

quantification of thiram and carbendazim in food samples and an agricultural formulation, Electrochimica Acta, 259 (2018) 66–76.

[134] G. Johansson, L. Risinger, L. Faelth, A cesium-selective electrode prepared from a crystalline synthetic zeolite of the mordenite type, Analytica Chimica Acta, 119 (1980) 25-32.

[135] R.L. Gil, C.G. Amorim, M.C.B.S.M. Montenegro, A.N. Araújo, Potentiometric detection in liquid chromatographic systems: An overview, J. Chromatogr. A., 1602 (2019) 326-340.

[136] S. Higson, Analytical chemistry, Oxford, Oxford University Press, (2003)

[137] Https://chem.libretext.org/Bookshelves/Analytical_Chemistry/Instrumental_Analysis_(LibreTexts)23%2A_Potentiometry/23.01%3A_Reference_Electrodes.

[138] N. Elgrishi, K. J. Rountree, B. D. McCarthy, E. S. Rountree, T. T. Eisenhart, J. L. Dempsey, A Practical Beginner's Guide to Cyclic Voltammetry, Journal of Chemical Education, 95(2) (2018) 197–206.

[139] A. J. Bard, L. R. Faulkner, Electrochemical Methods: Fundamental and Applications, 2nd ed., John Wiley & Sons, Hoboken, New York, (2001).

[140] A. I. Zia, S. C. Mukhopadhyay, Chapter 2: Impedance Spectroscopy and Experimental Setup, in Electrochemical Sensing: Carcinogens in Beverages, Springer, (2016).

Chapter 2

Structural and acidic properties of the LTL zeolite ion-exchanged with alkali metal cations

2.1 Abstract

Structural and acidic properties of a series of LTL zeolites exchanged with NH_4NO_3 and subsequently with alkali metal cations have been studied using Fourier transform infrared spectroscopy, X-ray powder diffraction, scanning electron microscopy, X-ray fluorescence and N_2 physisorption. It has been shown that up to 3 Cs^+ and Rb^+ cations per unit cell can be readily ion-exchanged into the LTL zeolite, replacing an equivalent number of K^+ cations in different locations within the structure. The cation migration mechanism has been evaluated by employing the Rietveld refinement method, which suggests that the larger cations access LTL structure through the main channels (*t-ltl* cages) and exchange K^+ in the 12MR. In addition, Cs^+ and Rb^+ can migrate into *t-ste* cages and ion-exchange K^+. By contrast, less than 1 Li^+ or Na^+ cation per unit cell can be introduced under similar conditions. Infrared spectra of the ion-exchanged zeolites show the presence of two intense bands of the bridging OH-groups: a narrow band at ~3640 cm^{-1}, which is attributed to Si(OH)Al groups freely vibrating in 12MR, and a rather broad band at ~3250 cm^{-1}, which is assigned to bridging OH groups forming hydrogen bond with neighbouring oxygen atoms, e.g. in 6-membered rings. It has been found that the concentration of Si(OH)Al groups in ion-exchanged NH_4-LTL with smaller cations (Li^+, Na^+) does not differ considerably from the concentration of Brønsted acid sites in the ammonium form of LTL. Lower concentrations of acid sites have been detected in the samples with Cs^+, Rb^+ and K^+. In addition, the acidic properties of the ion-exchanged LTL samples have been compared with a structurally related NH_4-MAZ zeolite.

2.2 Introduction

Linde type L zeolite (LTL) is a synthetic, crystalline aluminosilicate first synthesised in the 1950s [1], [2]. The framework Si/Al ratio is typically about 3.0 in this low silica zeolite [3]. The unit cell of LTL [4] is hexagonal (space group P6/mmm) with the lattice parameters a = 18.40 Å and c = 7.52 Å [2], [5]. LTL framework comprises polyhedral cancrinite (t-*can*) cages linked by double 6-rings (*d6r*) giving rise to the formation of *t-ste* and *t-ltl* cages and columns in the c-direction, thus leading to the formation of 12MR channels with a diameter of 7.1 Å, which allow access to the internal pore volume (figure 2.1) [6], [7].

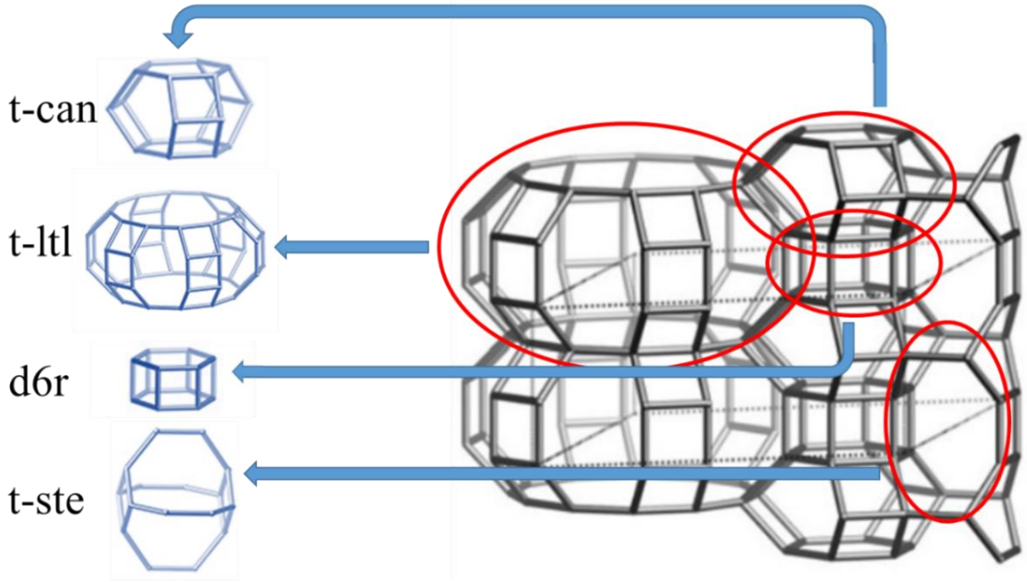

Figure 2.1: LTL structure: 12MR channel viewed normal to [001], adapted from reference [8].

As a large-pore zeolite, LTL is characterised by considerable sorption capacity. For instance, it has been utilised for the encapsulation of luminescent dyes [9]and in the field of optical sensing using lanthanide complexes [10]. More importantly, Pt-containing LTL has been employed in heterogeneous catalysis [4], [11], [12], e.g. in the aromatisation and dehydrogenation of n-hexane [13]–[16]. In this process, several factors have been considered to explain the exceptional catalytic properties of Pt/K-LTL, such as structural parameters of LTL in combination with the lack of acid sites [17]. Further, the presence of potassium cations, which neutralise acid sites, leads to an increase in the electron density on the Pt particles [12]. It is also reported that Pt/K-LTL catalytic activity is enhanced by Sn, used as a promoter, resulting in an improved catalytic performance of PtSn/K-LTL in n-hexane aromatisation [18]. In contrast, there are very few reports on the application of H-forms of zeolite LTL and its acidic properties [19], [20], which also highlight their potential for the future bio-refinery processes. For instance, the dehydration of ethanol opens a route to the production of ethylene from an alternative renewable feedstock, such as bioethanol [19], while aldol condensation reaction between furfural and ketones may be a conceivable route for the production of valuable compounds with longer carbon chains from short-chain biomass-derived molecules using either basic or acidic catalysts [20].

Zeolites LTL and MAZ show significant similarities in their structures and look analogous when viewed along the [001] axis [21] (figure 2.2a - b). Both materials have been investigated. However, in this chapter, more focus is given to K-LTL.

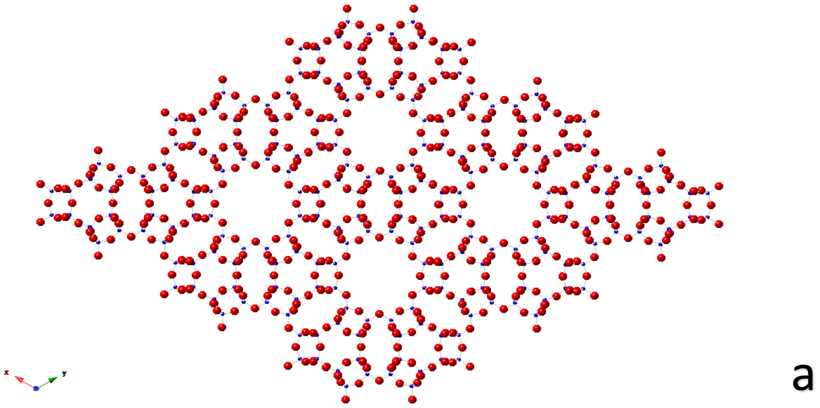

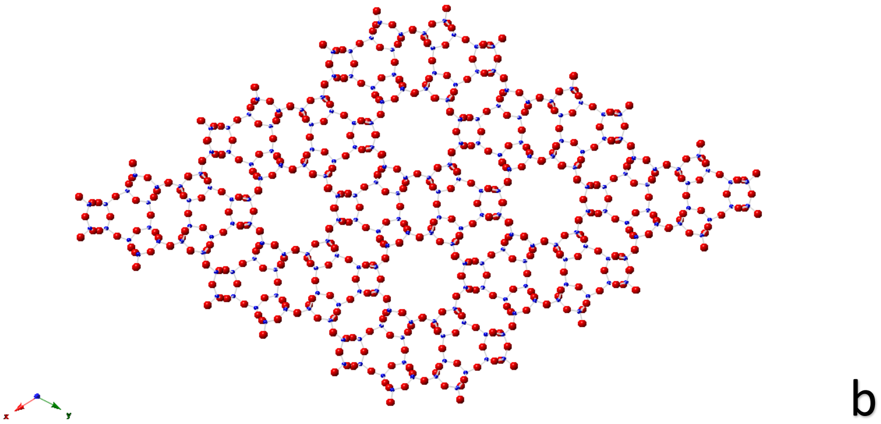

Figure 2.2: (a) Structure of zeolite K-LTL and (b) structure of MAZ viewed along the c-axis.

Hence, in this work, a series of ion-exchanged LTL samples is investigated and compared to MAZ with a major emphasis on the understanding of the nature of Brønsted acid sites (BAS) in these materials. This study has been carried out by employing Fourier transform infrared spectroscopy (FTIR), X-ray powder diffraction (XRD), scanning electron microscopy (SEM), X-ray fluorescence (XRF) and N_2 physisorption. Furthermore, the ion exchange in the LTL structure has been modelled using Rietveld refinement analysis in order to monitor the modifications of this zeolite and to define the cation location. In addition, temperature programmed desorption of ammonia (NH_3-TPD) has been carried out to examine the strength of the acid sites.

2.3 Experimental

2.3.1 Materials

The parent zeolite K-LTL was supplied by Tosoh. A sample of mazzite was prepared following the literature procedure [22]. Ammonium nitrate (99+%) and caesium chloride (99+%) were purchased from Acros Organic. Sodium nitrate (98+%) and potassium nitrate (99%) were purchased from Alfa Aesar. Rubidium chloride (99%) was supplied by Sigma-Aldrich and lithium nitrate (99%) by Timstar Laboratory Suppliers.

2.3.2 Materials preparation

Several series of materials were prepared using the parent K-LTL zeolite by ion-exchange of the ammonium form of the latter with metal alkali salt solutions. Specific preparation conditions for each sample are presented in table 2.1.

First, 10g of the parent K-LTL was three-fold ion-exchanged with 200ml of 0.5M NH_4NO_3. The zeolite and NH_4NO_3 solution were mixed and stirred for 90 minutes at 40°C. The solid was recovered, washed with deionised water and dried overnight at 90°C. This sample was designated NH_4-K-LTL.

Next, five series of M-NH_4-K-LTL samples (where M refers to Li, Na, K, Rb and Cs) were prepared. In each preparation, 1g of NH_4-K-LTL was ion-exchanged with an alkali metal salt solution. The procedure was performed up to four times at increasing concentrations (0.01-0.04 M) of the ion-exchange solution. Masses of K, Rb and Cs alkali salts, used to prepare solutions at the concentrations described above, were calculated to replace 33%, 66% and 100% of the NH_4^+ content in NH_4-K-LTL. An additional two-fold 100% ion exchange was performed as forth step. Masses of Li^+ and Na^+ salts were calculated to replace 100% and 200% of NH_4^+ in NH_4-K-LTL and a two-fold I.E. was carried out as the third and fourth steps.

The mixtures were stirred for 90 minutes at 40°C (Figure 2.3a). The recovered solids were washed with deionised water and dried overnight at 90°C (figure 2.3b).

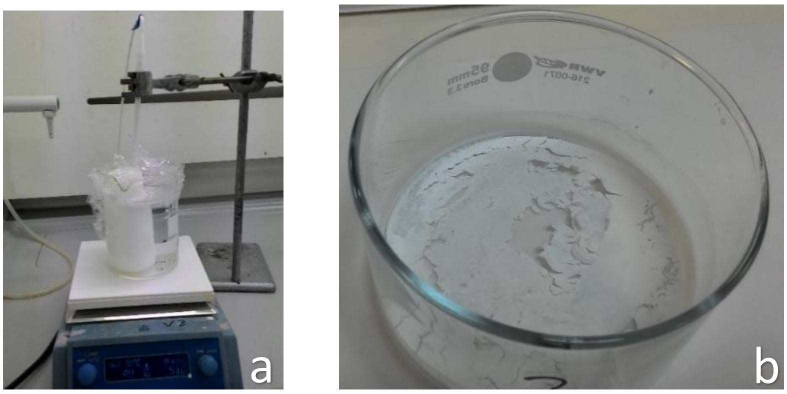

Figure 2.3: (a) Setup for ion exchange. (b) Dried ion exchanged sample.

Table 2.1: Preparation conditions for ion-exchanged samples obtained from the parent K-LTL zeolite.

Sample name	**Preparation conditions**
Parent K-LTL	
NH_4-K-LTL	Starting material: **Parent K-LTL**
NH_4-K-LTL-3	Three-fold ion exchange with 200 ml 0.5 M NH_4NO_3 at 40°C for 1:30h
Li-NH_4-K-LTL	Starting material: 1g **NH_4-K-LTL** in 150 ml **$LiNO_3$** aqueous solution.
Li-NH_4-K-LTL-1	Ion exchange with 0.023 mol/L of $LiNO_3$ at 40°C for 1:30h
Li-NH_4-K-LTL-2	Ion exchange with 0.045 mol/L of $LiNO_3$ at 60°C for 1:30h
Li-NH_4-K-LTL-3	Two-fold ion exchange with 0.023 mol/L of $LiNO_3$ at 60°C for 1:30h
Li-NH_4-K-LTL-4	Two-fold ion exchange with 0.045 mol/L of $LiNO_3$ at 60°C for 1:30h
Na-NH_4-K-LTL	Starting material: 1g **NH_4-K-LTL** in 150 ml **$NaNO_3$** aqueous solution.
Na-NH_4-K-LTL-1	Ion exchange with 0.033 mol/L of $NaNO_3$ at 40°C for 1:30h
Na-NH_4-K-LTL-2	Ion exchange with 0.045 mol/L of $NaNO_3$ at 40°C for 1:30h
Na-NH_4-K-LTL-3	Two-fold ion exchange with 0.033 mol/L of $NaNO_3$ at 40°C for 1:30h
Na-NH_4-K-LTL-4	Two-fold ion exchange with 0.045 mol/L of $NaNO_3$ at 40°C for 1:30h

K-NH$_4$-K-LTL	**Starting material: 1g NH$_4$-K-LTL in 150 ml KNO$_3$ aqueous solution.**
K-NH$_4$-K-LTL-1	Ion exchange with 0.008 mol/L of KNO$_3$ at 40°C for 1:30h
K-NH$_4$-K-LTL-2	Ion exchange with 0.015 mol/L of KNO$_3$ at 40°C for 1:30h
K-NH$_4$-K-LTL-3	Ion exchange with 0.023 mol/L of KNO$_3$ at 40°C for 1:30h
K-NH$_4$-K-LTL-4	Two-fold ion exchange with 0.023 mol/L of KNO$_3$ at 40°C for 1:30h
Rb-NH$_4$-K-LTL	Starting material: 1g **NH$_4$-K-LTL** in 150 ml **RbCl** aqueous solution.
Rb-NH$_4$-K-LTL-1	Ion exchange with 0.008 mol/L of RbCl at 40°C for 1:30h
Rb-NH$_4$-K-LTL-2	Ion exchange with 0.015 mol/L of RbCl at 40°C for 1:30h
Rb-NH$_4$-K-LTL-3	Ion exchange with 0.022 mol/L of RbCl at 40°C for 1:30h
Rb-NH$_4$-K-LTL-4	Two-fold ion exchange with 0.022 mol/L of RbCl at 40°C for 1:30h
Cs-NH$_4$-K-LTL	Starting material: 1g **NH$_4$-K-LTL** in 150 ml **CsCl** aqueous solution.
Cs-NH$_4$-K-LTL-1	Ion exchange with 0.008 mol/L of CsCl at 40°C for 1:30h
Cs-NH$_4$-K-LTL-2	Ion exchange with 0.015 mol/L of CsCl at 40°C for 1:30h
Cs-NH$_4$-K-LTL-3	Ion exchange with 0.022 mol/L of CsCl at 40°C for 1:30h
Cs-NH$_4$-K-LTL-4	Two-fold ion exchange with 0.022 mol/L of CsCl at 40°C for 1:30h

2.3.3 Material characterisation

The materials prepared by ion exchange were characterised using X-ray diffraction (XRD), Inductively coupled plasma atomic emission spectroscopy (ICP-OES), scanning electronic microscopy with energy-dispersive X-ray analysis (SEM-EDX), nitrogen adsorption-desorption and *in situ* FTIR spectroscopy.

ICP-OES. Inductively coupled plasma atomic emission spectroscopy was employed in conjunction with SEM EDX to evaluate the content of Li in the samples because Li characteristic radiation energy is very low and this makes its detection difficult by X-rays. The preparation of the samples for the analysis required to dissolve the powder of the material in HNO_3 (>65 %). 200 mg of each Li-NH_4-K-LTL (1 – 4) were dissolved in 20ml of NHO_3. Each sample was prepared in a separated vessel (figure 2.4b). Vessels were inserted in the carousel (figure 2.4b on the left) and positioned in the microwave (figure 2.4a) Samples were heated according to the following program:

Time, min	**T,°C**
10	180
240	180

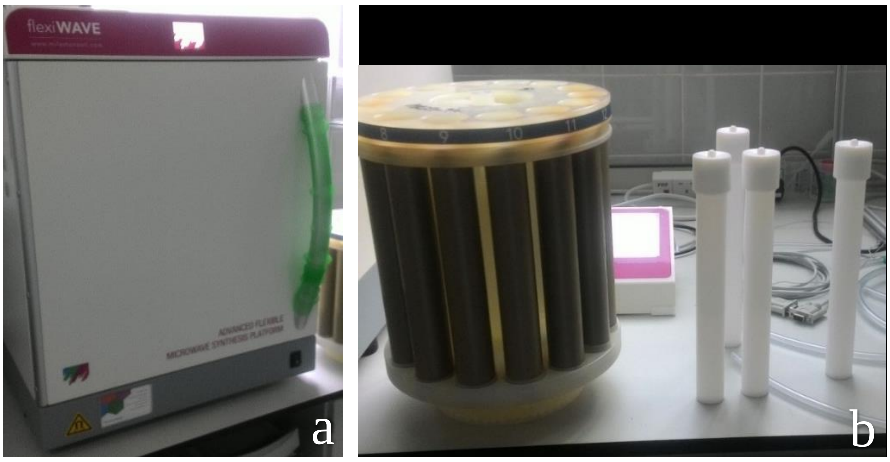

Figure 2.4: (a) Microwave and (b) carousel with vessels.

After the microwave step, solutions were diluted by adding 50ml of deionised water. ~10 ml of the solution were transferred from each vessel to a separated analysis tube and scanned at the ICP-OES (figure 2.5). The list of samples included also distilled water, blank and standards prepared at the follwing concentrations: 10 and 20 ppm.

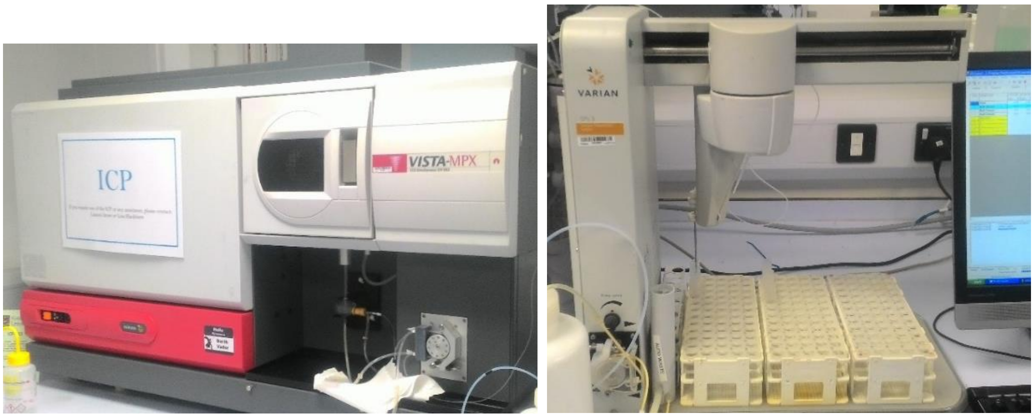

Figure 2.5: ICP-OES on the left and autosampler on the right hand side.

Chemical analysis. Elemental composition of zeolites was evaluated by SEM-EDX analysis using a Hitachi TM4000 plus II Tabletop electron microscope fitted with AZtec One EDS (Oxford Intruments), by X-ray fluorescence using a ThermoScientific ARL PERFORM’X with a 3.5kW Rh tube and by comparison with FTIR spectroscopy. Preparation of samples was performed by pressing few mg of powder sample (~10 – 15 mg) at the hydraulic press and depositing a fragment of it on an aluminium sample holder. The sample was then sticked on the surface of the sample holder using a conductive cement (Figure 2.6).

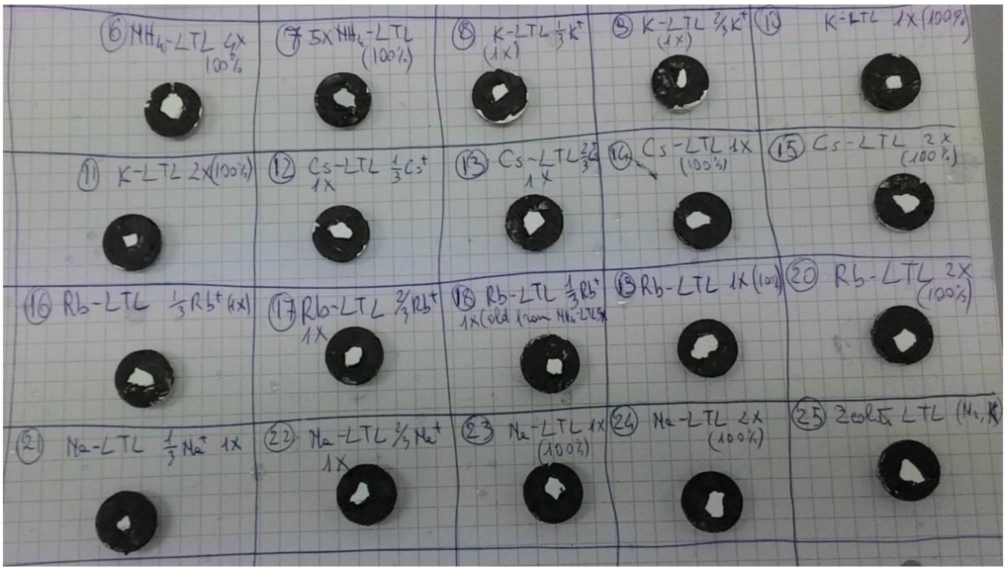

Figure 2.6: Samples ready for the SEM EDX analysis.

XRD. ~800 mg of sample was pressed in a plastic sample holder (figure 2.7a – b). X-ray powder diffraction patterns were recorded on a Bruker D8 Advance diffractometer (figure 2.8a - b), equipped with a LynxEye detector, using Cu Kα radiation at 40 kV and 40 mA at ambient temperature over the 2-theta angle range of 5-60° ($\lambda_{K\alpha 1}$=0.15406 nm and $\lambda_{K\alpha 2}$=0.15444 nm; Soller slit of 2.5°; step size of 0.02° scan duration of 4h, no monochromator was used). The crystalline phases were matched by comparing the XRD patterns of the catalysts with those reported in the literature. In addition, Bruker Diffrac.Eva v4.0, Vesta V3.5.7 [23], [24] and Maud V2.991 (L. Lutterotti) [25], [26] software packages were utilised for the analysis of the XRD data, including the Rietveld method, in order to investigate the structural features of the prepared LTL samples. The applied approach consisted of generating calculated XRD patterns through VESTA software. Cation locations in a "cif" file of K-LTL (parent zeolite) were edited, according to the elemental analysis data, by replacing K^+ with the cation of interest (NH_4^+ cations were also taken into account). The generated patterns were used for qualitative comparison with the experimental data. Next, the Rietveld analysis was carried out for selected samples using MAUD software.

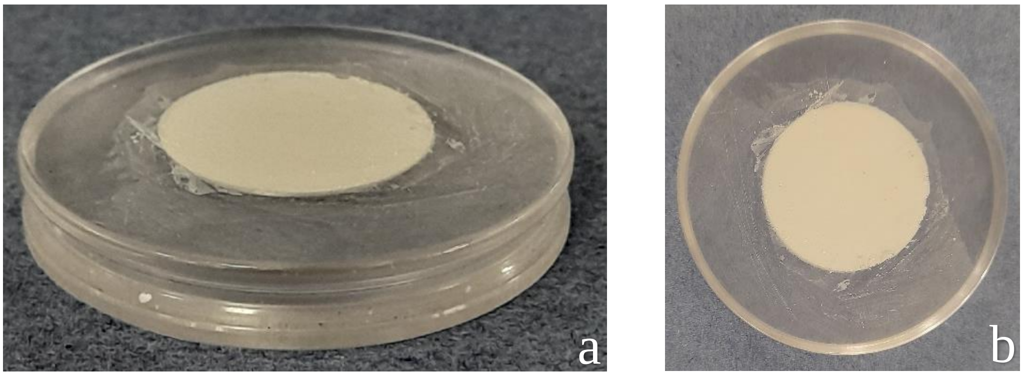

Figure 2.7: Sample ready for XRD analysis.

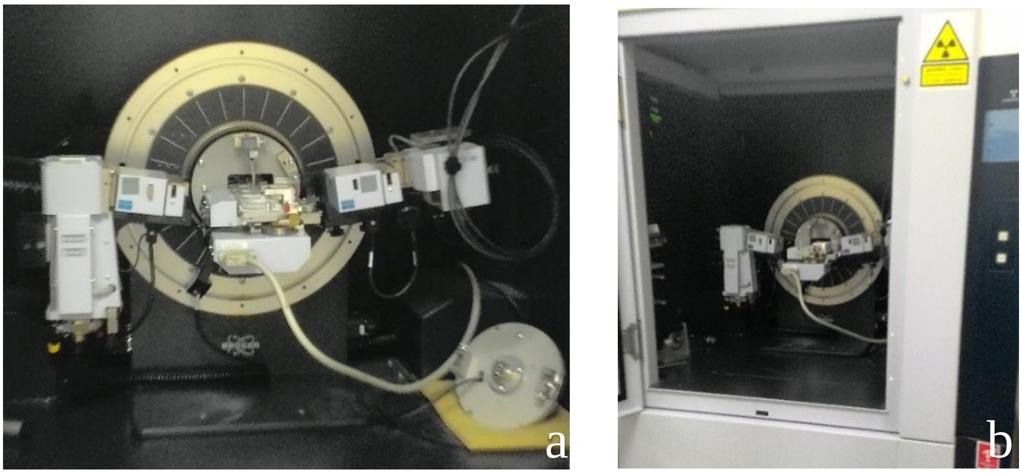

Figure 2.8: (a – b) Bruker D8 Advance diffractometer.

The Rietveld refinement used for the investigation of the zeolite materials presented in this work was applied through the use of MAUD software developed by L. Lutterotti et al. [25], [26]. In first instance, all patterns of the parent and ion exchanged zeolites were collected at the diffractometer. Next, each data set was loaded on MAUD software. In order to perform the Rietveld analysis the software needs a cif file as reference phase or as calculated pattern on which apply the modelling. Cif files detailing structural information of the reference materials, such as the occupancy and the coordinates of the atoms, have been downloaded from available databases [27], [28]. The parent zeolite used for this research was K-LTL, hence in order to perform the analysis, the extraframework cations included in the cif file were edited using MAUD software, e.g. Na cations were replaced by K cations. For all experimental patterns, this procedure was repeated, for instance, if a cif file including Cs and K was needed, then K in the cif files was replaced with Cs or a shared position with both species was generated. For the ion-exchanged materials with different cations, multiple shared positions were taken into account for some sites. Based on the edited cif files, simulated diffraction patterns were computed and compared with the experimental ones. The Rietveld refinement was performed with 21 iterations, optimising the occupancy of the extra-framework cations and their coordinate for each sample, and an additional set of 21 iterations was repeated if R% value was above 10%. All patterns showed an R% under ~8-10%.

FTIR. Comparative characterisation of the Brønsted and Lewis acid sites in zeolites, was carried out using transmittance FTIR experiments in an in situ IR cell (figure 2.9a) attached to a vacuum system (dynamic vacuum better than 10^{-5} mbar). The FTIR measurements were performed using a Thermo iS10 FTIR spectrometer (figure 2.10), equipped with a DTGS detector, in the range 6000–900 cm^{-1} at a spectral resolution of 1–8 cm^{-1} (typically 4 cm^{-1}, 0.96 cm-1 data spacing) and 64 scans in transmission mode utilising pyridine adsorption.

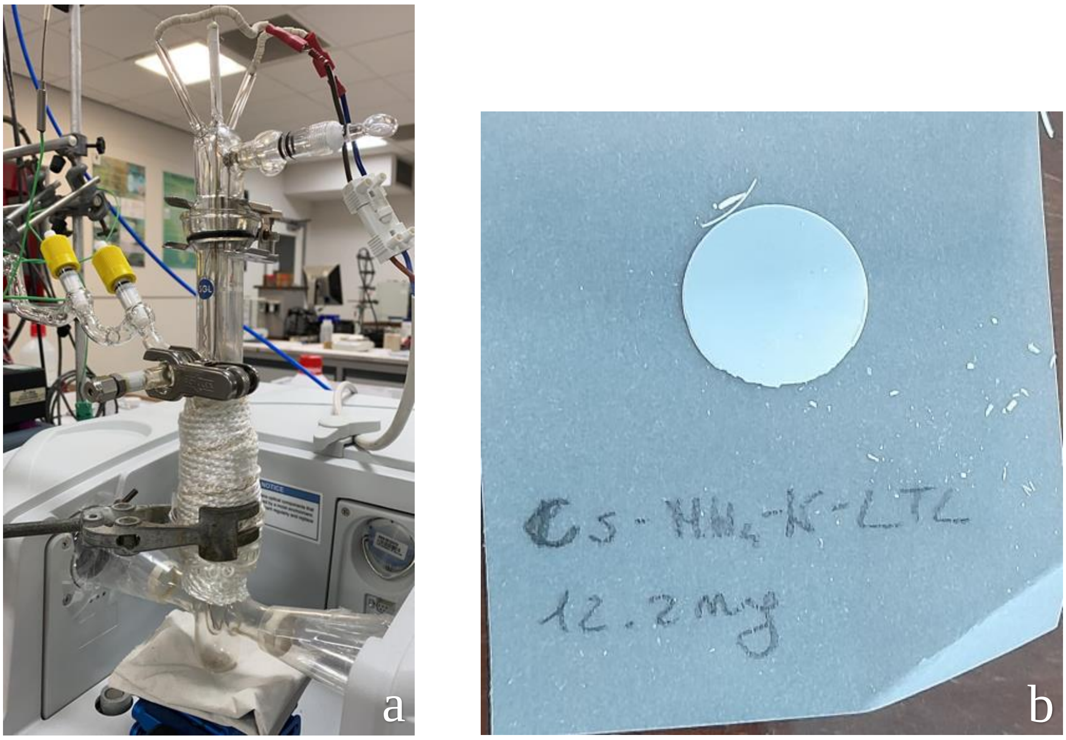

Figure 2.9: (a) IR cell attached to a vacuum system. (b) Sample disc of Cs-NH_4-K-LTL.

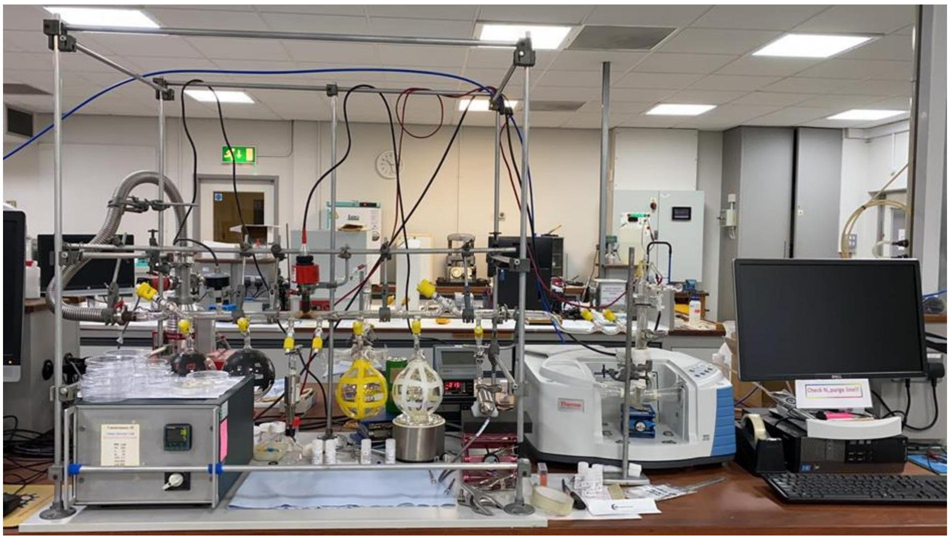

Figure 2.10: FTIR spectrometer setup and vacuum system.

Prior to recording the spectra, a self-supported sample disk (figure 2.9b) (1.3 cm in diameter, S = 1.3 cm^2; 1.5 to 30 mg/cm^2, but typically 7–10 mg/cm^2) was activated in the in situ vacuum cell typically at 450 °C (ramp 1 °C/min). After a period of 5 h at the selected activation temperature, the sample was cooled to the desired temperature (200 °C) in vacuum and its IR spectrum was collected. An excess of the probe molecule, Py (C_5H_5N, Acros Organics, 99.5%, dried over 3A molecular sieve), were admitted into the cell, usually at 200 °C in a stepwise manner. Physisorbed molecules were subsequently removed by evacuation at 200 °C for 20 min. Py adsorption-desorption was carried out typically at 200 °C. The FTIR spectra were collected at 200 °C. The obtained spectra were analysed, including integration, subtraction and determination of peak positions, using specialised Thermo software, Omnic 9.3. The following values of the molar absorption coefficients were applied: for Brønsted acid sites, ε(BAS)=1.61 cm μmol^{-1} (IR peak at ~1545 cm^{-1}) and for Lewis acid sites ε(LAS)=1.79 cm μmol^{-1} (IR peak at ~1455 cm^{-1}) [29]. The integration limits were 1565–1515 cm^{-1} for the Py-B peak and 1465–1535 cm^{-1} for the Py-L peak (±3 cm^{-1} depending on the nature of the sample and the temperature of the FTIR measurements). The error margin for the acid site quantification was estimated as ±5%.

NH_3-TPD. Ammonia desorption measurements on NH_4-K-LTL and NH_4-MAZ were carried out using a quadrupole mass-spectrometer MKS Cirrus (Figure 2.11). The samples (~40 mg) were loaded in a reactor tube furnace and activated at 150°C. Desorption of NH_3 was performed from 150 to 750°C with a temperature ramp of 10°C/min under He atmosphere with flow of 30 ml min^{-1} for both materials.

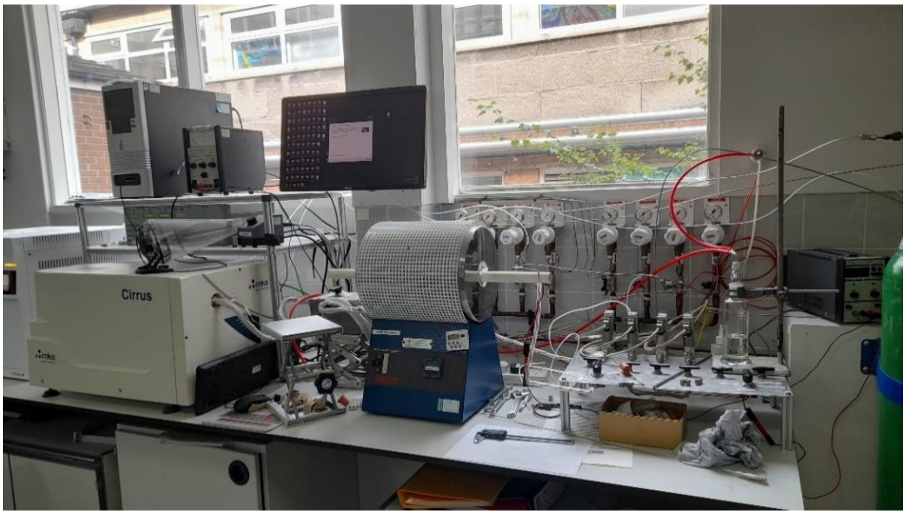

Figure 2.11: Quadrupole mass-spectrometer MKS Cirrus with furnace and gas line.

N_2 physisorption. Samples were prepared by weighing ~20 mg of the catalysts in a quartz cell (figure 2.12a). Samples were activated to remove the moisture and water according to the following program:

Target T, °C	Rate, ,°C /min	Soak time, min
30	1	30
450	1	300
100	5	500

After the activation step, the cell with the catalysts were connected to the stations in the second unit of the instrument to carry out the analysis. Analysis was performed with N_2 with a duration between 24h – 72h. The apparent surface areas of the catalysts was calculated using the BET model for the P/P_0 relative nitrogen pressure <0.1; their micropore volume and the pore size distribution were computed using the nonlinear density functional theory (NLDFT) model applied to the adsorption branch of the isotherms obtained from the nitrogen adsorption experiments carried out on a Anton Paar iQ Autosorb instrument (figure 2.12b). The total pore volume was determined at P/P_0 relative nitrogen pressure equal to 0.95.

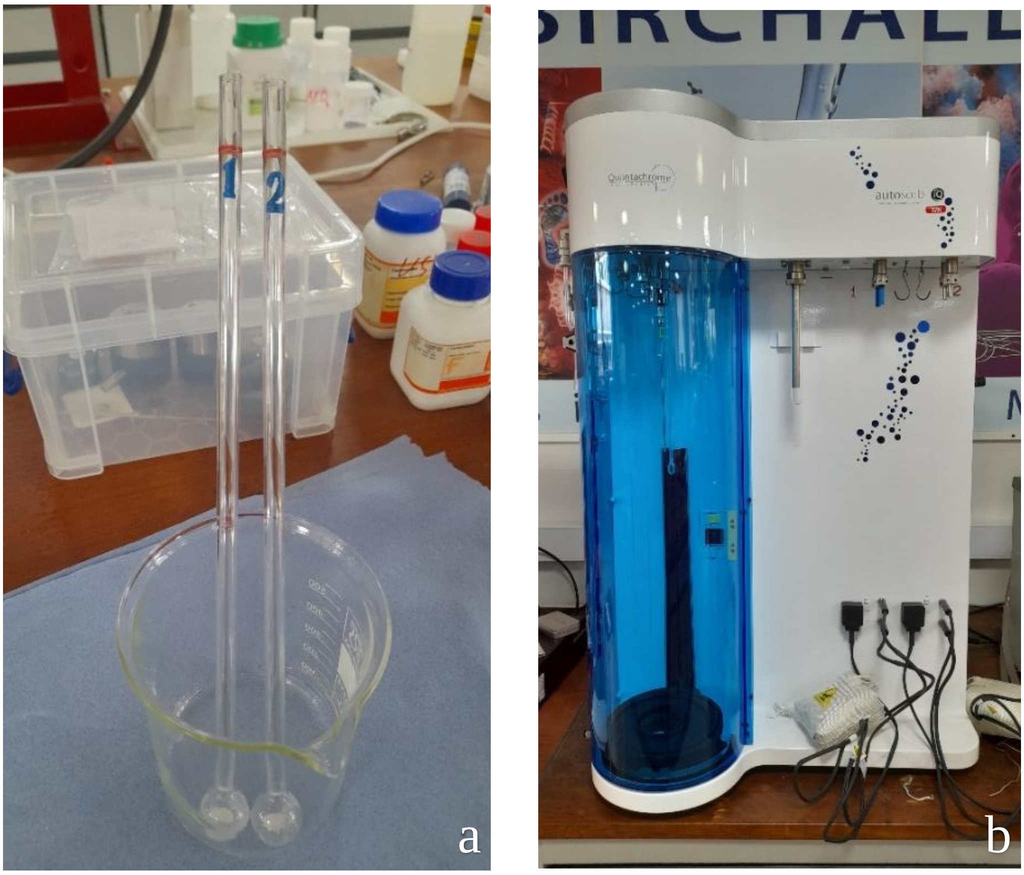

Figure 2.12: (a) Quartz cells with samples and rod. (b) Anton Paar iQ Autosorb instrument.

2.4 Results and discussion

2.4.1 SEM-EDX

The elemental analysis of the ion-exchanged zeolites was investigated using SEM-EDX. Table 2.2 and table 2.3 summarise chemical composition and textural data for the ion-exchanged LTL zeolites. The Si/Al ratio of the parent K-LTL zeolite is 3.2 and the starting K to Al ratio is 1:1. The elemental analysis results suggest that Cs^+, Rb^+ and K^+ cations are more easily introduced into the LTL structure (up to ~10 at%) compared to Li^+ and Na^+ (up to ~1-3 at%; see Figure 2.13).

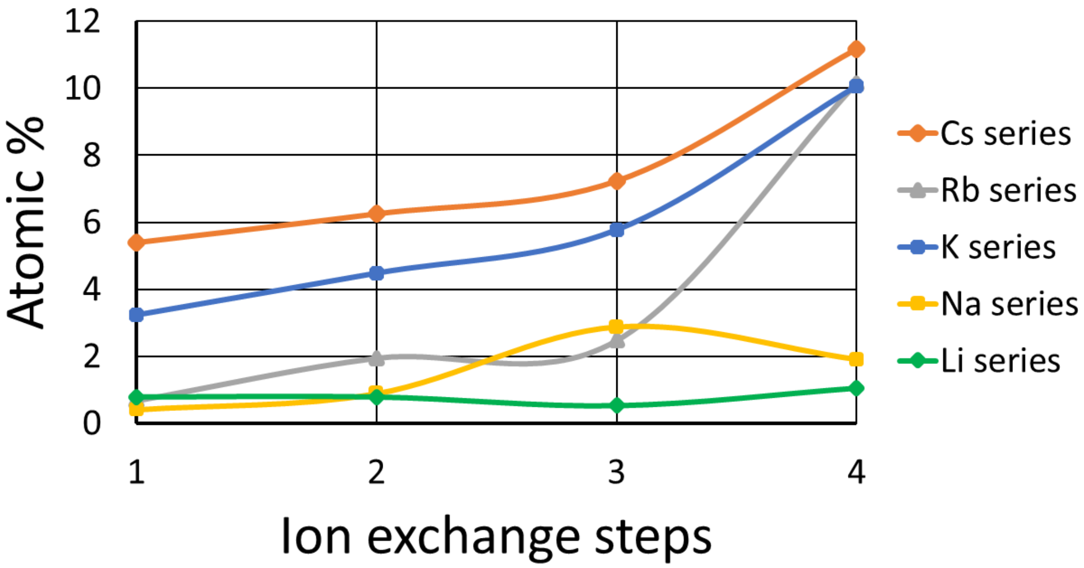

Figure 2.13: Atomic percentage of ion-exchanged cations in LTL samples as a function of ion exchange steps.

Table 2.2: Chemical composition and textural data for the ion-exchanged LTL samples and for NH_4-MAZ.

Sample	Composition	Crystallinity, %	S, $m^2\ g^{-1}$	V_{micro}, $cm^3\ g^{-1}$	S^a, $m^2\ cm^{-3}$	S^b, $m^2\ mmol^{-1}$
K-LTL	$K_{8.8}Al_{8.6}Si_{27.4}O_{72}$	92	346	0.12		
NH_4-K-LTL	$(NH_4)_{4.6}K_{4.0}Al_{8.6}Si_{27.4}O_{72}$	89	376	0.12		
Li-NH_4-K-LTL-4	$Li_{0.4}(NH_4)_{4.4}K_{3.8}Al_{8.6}Si_{27.4}O_{72}$	90	385	0.13	832	95
Na-NH_4-K-LTL-4	$Na_{0.8}(NH_4)_{4.0}K_{3.8}Al_{8.6}Si_{27.4}O_{72}$	88	357	0.12	843	93
K-NH_4-K-LTL-4	$(NH_4)_{2.2}K_{6.4}Al_{8.6}Si_{27.4}O_{72}$	87	332	0.12	823	92
Rb-NH_4-K-LTL-4	$Rb_{4.0}(NH_4)_{1.8}K_{2.8}Al_{8.6}Si_{27.4}O_{72}$	85	295	0.10	794	96
Cs-NH_4-K-LTL-4	$Cs_{4.6}(NH_4)_{1.4}K_{2.6}Al_{8.6}Si_{27.4}O_{72}$	84	266	0.09	806	99
NH_4-MAZ	$(NH_4)_{6.0}Al_{6.0}Si_{30.0}O_{72}$	82	317	0.14		

(a,b) corrected surface area taking into account the density change due to ion exchange.

This can be rationalised based on the size of hydrated ions and coulombic interactions between the hydrated cations and the framework oxygens. It should be noted that part of the initial percentage of potassium in NH_4-K-LTL represents potassium "locked" in the *t-can* cages that are neither be released into solution, nor exchanged with other species. At the same time, all cations can access the LTL structure, most likely, they are introduced through the *t-ltl* cages in the main channels. However, hydrated Li^+ and Na^+, because of steric constraint, do not have access to some parts of the structure, such as the *t-ste* cages, which are only accessible via 8-membered rings with the size of 7.5 Å x 4.7 Å [8] [27].

Table 2.3: Elemental analysis % results for the ion-exchanged LTL samples and for NH_4-MAZ.

Sample	%Si	%Al	%Li	%Na	%K	%Rb	%Cs	Si/Al
K-LTL	58.46	17.73			23.81			3.30
NH_4-LTL	71.03	20.04			8.86		0.05	3.54
Li-NH_4-K-LTL-1	68.91	23.86	0.79		7.00			2.89
Li-NH_4-K-LTL-2	69.31	24.04	0.79		6.51			2.88
Li-NH_4-K-LTL-3	68.81	23.90	0.53		7.06			2.88
Li-NH_4-K-LTL-4	69.28	23.90	1.05		6.42			2.90
Na-NH_4-K-LTL-1	70.91	20.10		0.41	8.57			3.53
Na-NH_4-K-LTL-2	70.00	19.84		0.89	9.27			3.53
Na-NH_4-K-LTL-3	66.14	22.93		2.87	8.06			2.88
Na-NH_4-K-LTL-4	65.46	22.44		3.40	8.71			2.92
K-NH_4-K-LTL-1	67.96	20.03			11.94			3.39
K-NH_4-K-LTL-2	66.93	19.85			13.19			3.37
K-NH_4-K-LTL-3	65.99	19.45			14.48			3.39
K-NH_4-K-LTL-4	61.91	19.32			18.77			3.20
Rb-NH_4-K-LTL-1	73.13	19.17			6.96	0.68		3.81
Rb-NH_4-K-LTL-2	72.88	18.42			6.75	1.95		3.96
Rb-NH_4-K-LTL-3	71.96	19.03			6.49	2.47		3.78
Rb-NH_4-K-LTL-4	64.29	19.23			6.34	10.14		3.34
Cs-NH_4-K-LTL-1	67.96	20.03			11.94		5.39	3.39
Cs-NH_4-K-LTL-2	66.93	19.85			13.19		6.25	3.37
Cs-NH_4-K-LTL-3	65.70	21.47			5.60		7.23	3.06
Cs-NH_4-K-LTL-4	62.45	20.26			6.12		11.18	3.08

Table 2.4: Actual K^+ content introduced during the ion exchange of NH_4-LTL with KNO_3.

Sample	Total %K^+	%K^+ in NH_4-LTL	%K^+ introduced in I.E.
K-NH_4-K-LTL-1	11.94	8.71	3.23
K-NH_4-K-LTL-2	13.19	8.71	4.48
K-NH_4-K-LTL-3	14.48	8.71	5.77
K-NH_4-K-LTL-4	18.77	8.71	10.06

It should be noted that part of the initial percentage of potassium in NH_4-K-LTL represents potassium "locked" in the *t-can* cages that can neither be released into solution, nor exchanged with other species. At the same time, all cations can access the LTL structure and most likely, they are introduced through the *t-ltl* cages in the main channels. However, hydrated Li^+ and Na^+, because of steric constraint, do not have access to some parts of the structure, such as the *t-ste* cages, which are only accessible via 8-membered rings with the size of 7.5 Å x 4.7 Å [8], [27]. Since Rb^+, Cs^+ and K^+ in their hydrated form can fit the 8MR of the *t-ste* cage, they can reach the inner cages. A slight increase in the Si/Al ratios suggests a loss of Al for the samples exchanged with Rb^+ and Cs^+, which can be explained by a partial dealumination of the zeolite, or by the removal of extraframework Al species during ion-exchange. Indeed, this is in agreement with the XRD data indicating a marginal decrease in crystallinity (see table 2.2) observed for these samples as compared to the Li-and Na-forms. In addition, AlOH groups and Lewis acid sites have been detected in the FTIR spectra (see FTIR section).

2.4.2 N_2 Physisorption

Nitrogen adsorption-desorption isotherms for K-LTL, NH_4-K-LTL and the ion exchanged forms with alkali metals samples are presented in Figure 2.14, 2.15 (a – b) and figure 6.1 (a – b), 6.2 (a - b) in figure 2A.1 (a – b) and 2A.2 (a – b) (Chapter 6 - appendix). The calculated values of the apparent BET area and the pore volume are presented in table 2.2 and Figure 2.16 (a – c). Results show an ~30% decrease in both the apparent surface area and pore volume measurements between Li- and Cs-exchanged zeolites, with Na-, K- and Rb-forms following the trend. This can be explained by the increasing size of the group 1 cations from Li to Cs. Indeed, considering that the diameter of Cs cations is ~0.34 nm and their concentration of 10 at%, caesium cations should occupy ~0.02 cm^3 per 1 g of the zeolite, which agrees well with the experimental value of 0.03 cm^3 g^{-1}. Results are shown in table 2.5. The data for the MAZ sample demonstrate considerably lower values of the surface area and the micropore volume, which is most likely due to the larger particle size of mazzite and the pore blockage.

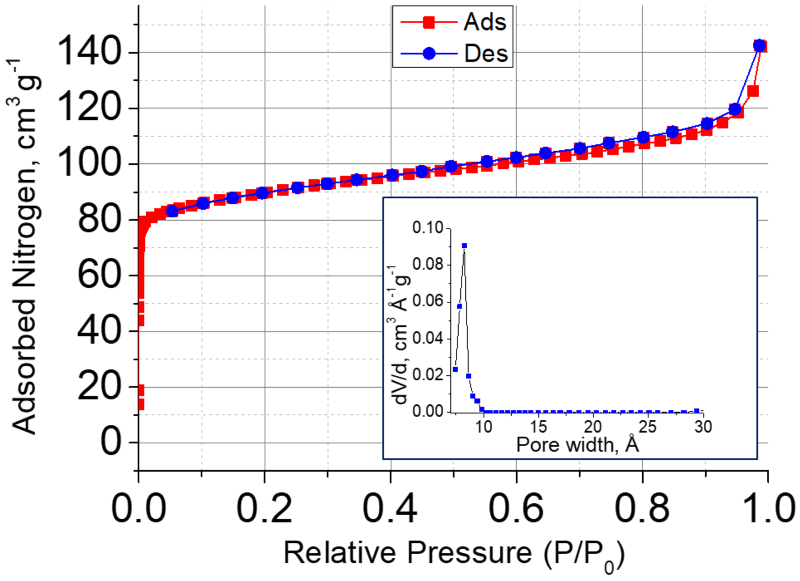

Figure 2.14: Nitrogen adsorption-desorption isotherms for K-LTL. The inserts show the pore size distributions for these materials.

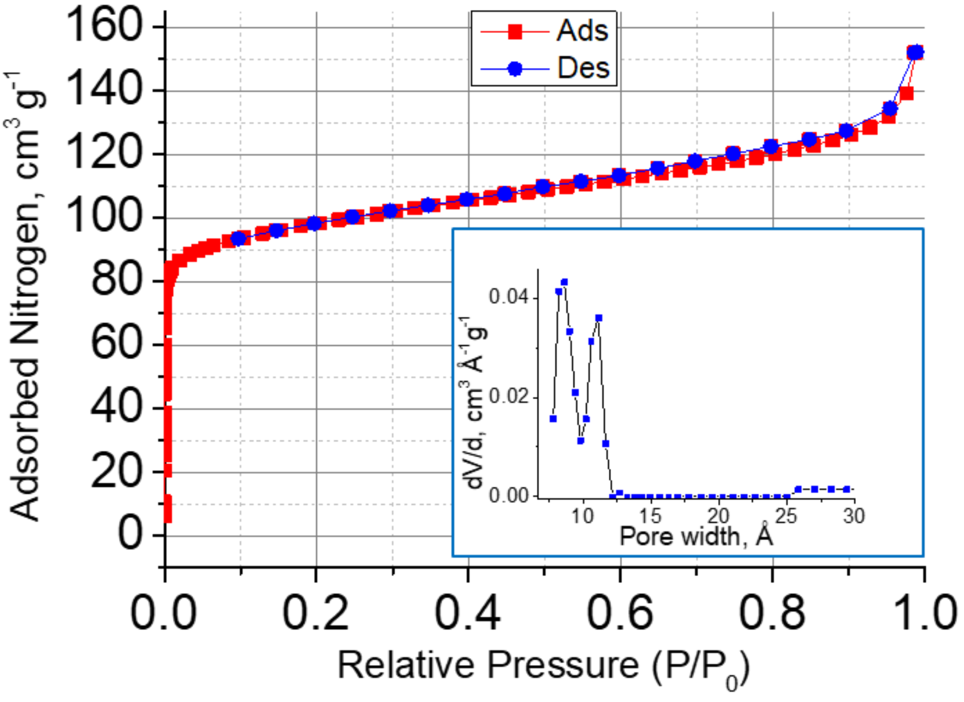

(a)

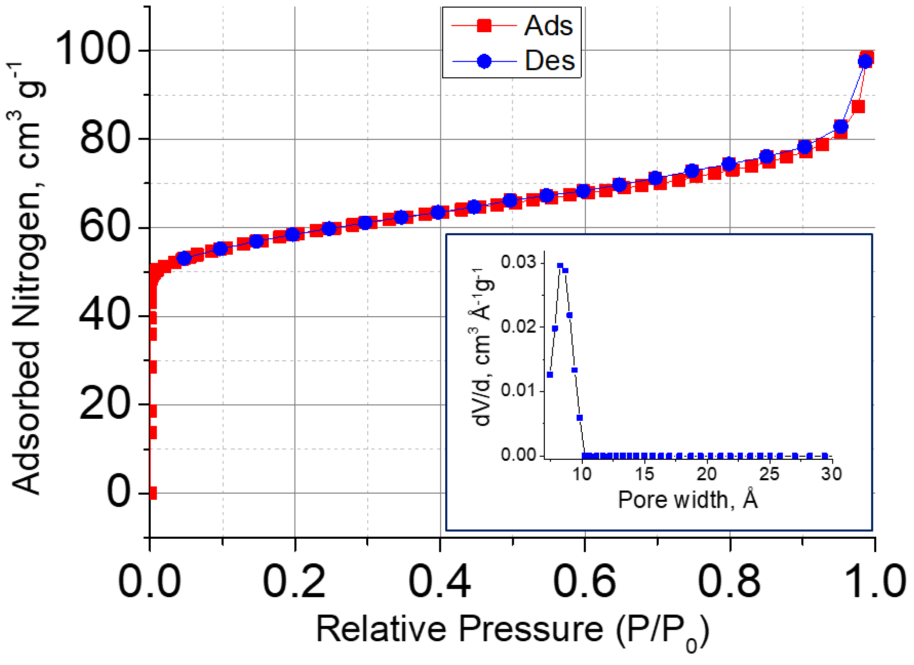

(b)

Figure 2.15 (a – b): Nitrogen adsorption-desorption isotherms for NH_4-K-LTL (a) and Cs-NH_4-K-LTL (b). The inserts show the pore size distributions for these materials.

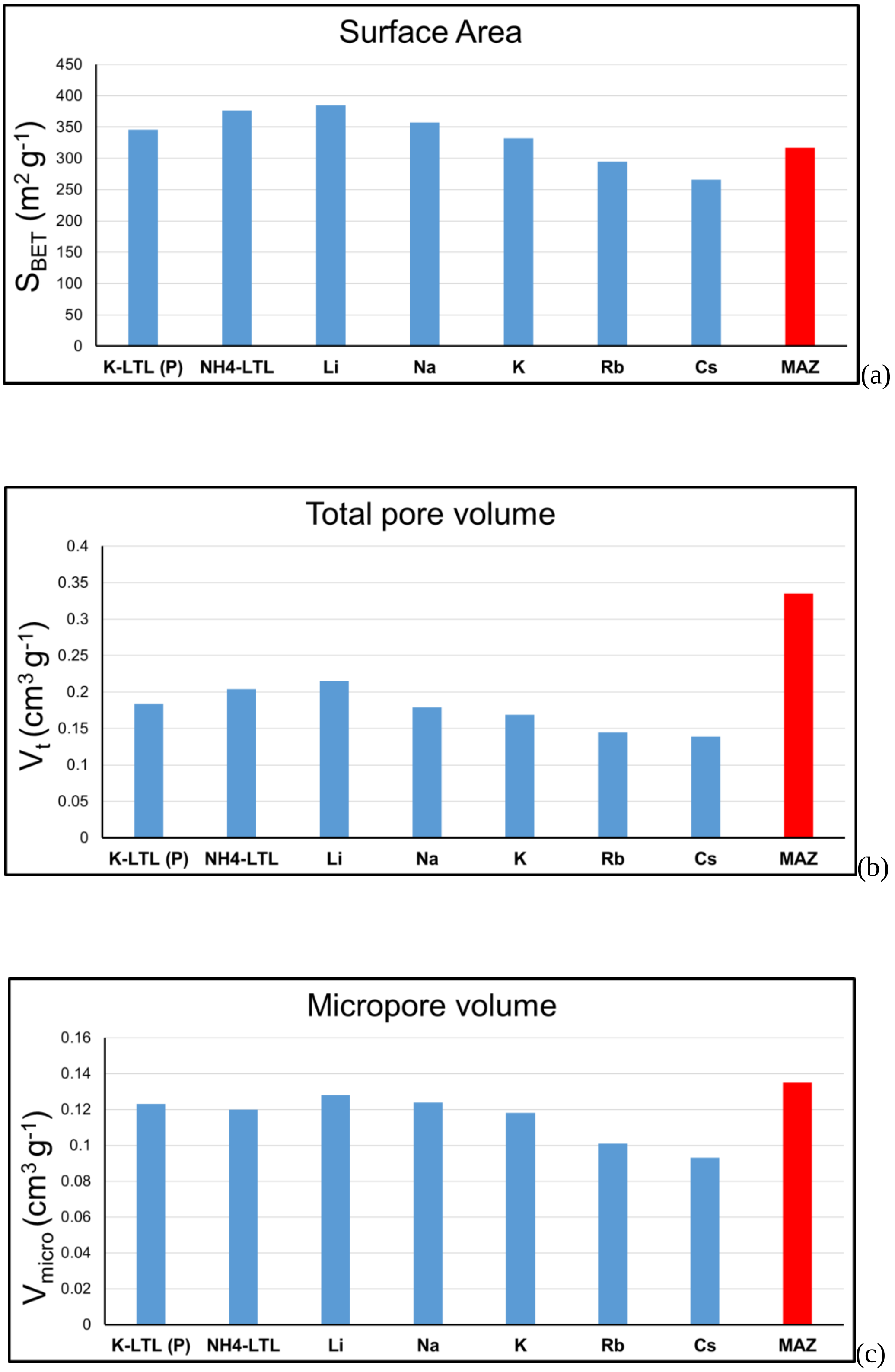

Figure 2.16: (a) Surface area, (b) total pore volume and (c) micropore volume of the ion-exchanged samples.

Table 2.5: Occupied volume and number of cations in the samples.

Cation	RMM, g per mol	Radius, cm	Volume, cm^3	wt.%	Number of mol per 1g	Number of atoms per 1g	V_{occ}, cm^3 g^{-1}
Li	6.9675	6.00E-09	9.04E-25	2.83	0.00407	2.447E+21	0.0022
Na	22.9897	9.50E-09	3.59E-24	8.78	0.00382	2.298E+21	0.0082
K	39.0983	1.33E-08	9.85E-24	14.06	0.00360	2.165E+21	0.0213
Rb	85.4678	1.48E-08	1.36E-23	26.34	0.00308	1.855E+21	0.0252
Cs	132.9054	1.69E-08	2.02E-23	35.74	0.00269	1.619E+21	0.0327

Unlike K^+, Rb^+ and Cs^+, a bimodal pore size distribution was observed for NH_4^+, Li^+ and Na^+ forms of LTL. Possible reasons for this behaviour might be related to the interaction between the adsorbed gases on the zeolite and the cations introduced with the ion exchange. Gases, such as nitrogen, because of their quadrupole moment, parameter that measure the deviation of the nuclear charge distribution from spherical symmetry, may show this behaviour. Another possible reason may be linked to the pore size calculation model employed by the software to characterise the materials prepared. Further investigation and additional analysis, for instance employing gases with no quadrupole moment such as Ar, are required to explain the pore size distribution results described in this paragraph.

2.4.3 XRD analysis

XRD studies have been employed to investigate structural modifications of parent zeolite and ion-exchanged materials. In general, all XRD patterns of the materials obtained through ion exchange show a profile typical of LTL. However, successive ion-exchanges have resulted in a gradual decrease in crystallinity from 92% for the parent K-LTL to 84% for the Cs-NH_4-K-LTL-4 sample. The presence of an amorphous phase has been evident in the XRD patterns between ~5 and 15 degrees 2theta (table 2.2, figure 2.17 and 2.18a - b). The experimental patterns show the same peak positions for all LTL pattern. However, the principal difference is in the peak intensities following ion-exchange of these materials. These differences are consistently observed in both experimental (Figure 2.17) and calculated patterns (Figure 2.18a – b).

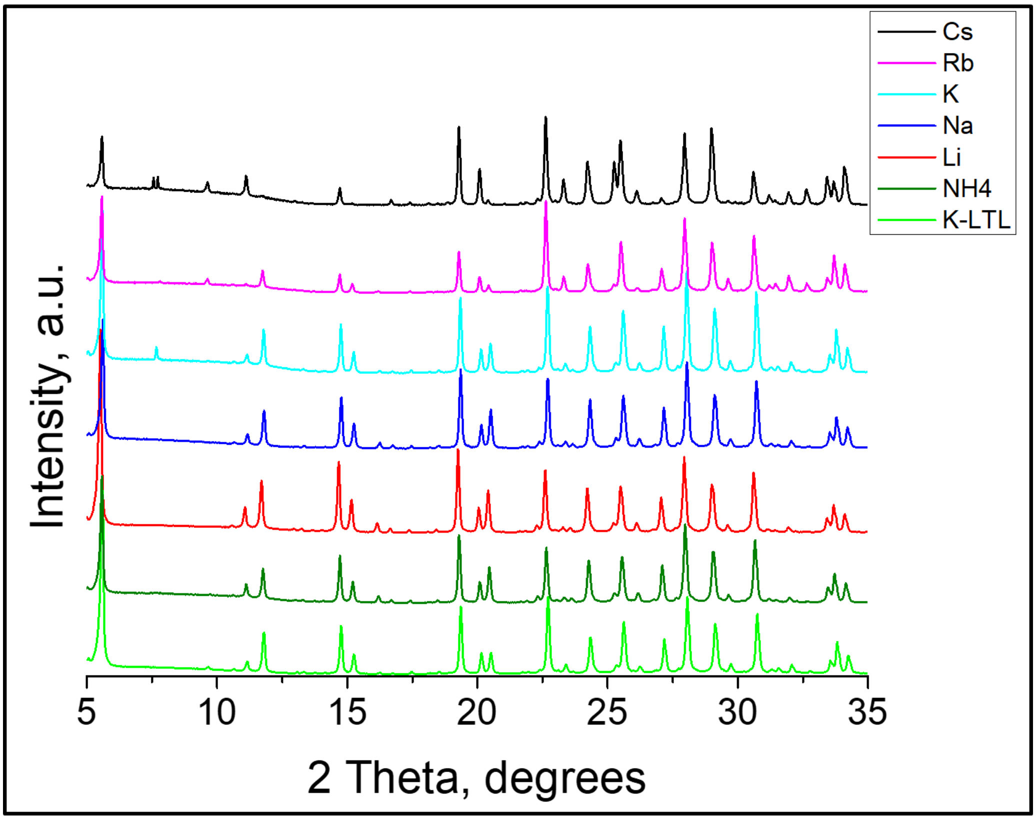

Figure 2.17: Experimental XRD patterns of the ion-exchanged LTL samples.

For instance, the peak at ~9.6 degrees for the parent K-LTL shows a very low intensity, but it is very prominent in the patterns of the Cs-exchanged material, whereas a reversed picture is observed for the peaks at ~15 degrees (Figure 2.17, 2.18 (a – b) and 2A.3 (a – b) – 2A.6 (a – b) in chapter 6 - appendix). A more detailed analysis of the XRD data has been carried out using Rietveld method (figure 2.19, top). Rietveld results shown in figure 2A.3 (a – b), 2A.4 (a – b), 2A.5 (a – b) and 2A.6 (a – b) (in chapter 6 - appendix) show agreement between experimental and computed patterns produced by software packages MAUD. Firstly, it reveals that the ion exchange affected the unit cell size of the exchanged LTL zeolites. In particular, for Cs-containing samples the lattice parameters increase [30] during all steps (see table 2.6 for more details).

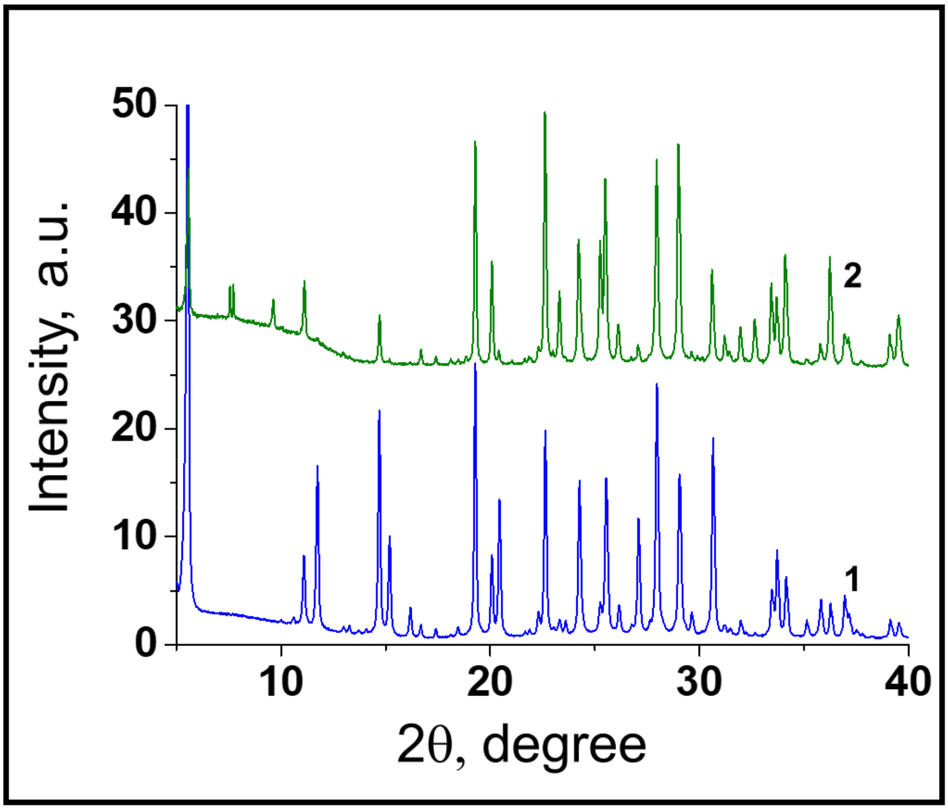

(a)

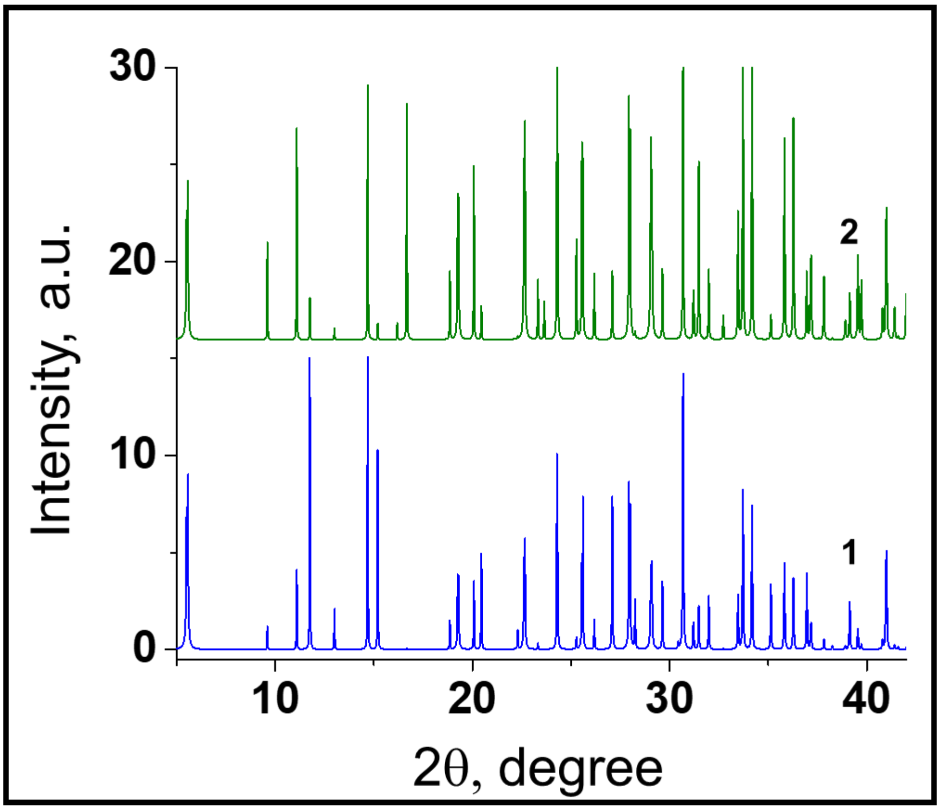

(b)

Figure 2.18 (a – b): Experimental (a) and simulated (b) XRD patterns of K-LTL (Tosoh) (1) and Cs-K-LTL (2).

Subsequent XRD data processing has been focused on computational modelling in order to understand the cation migration mechanism of the introduced species and their locations after each ion-exchange step. The results of our modelling are presented in table 2.6 and in figure 2.19 at the bottom using Cs^+ introduction into parent K-LTL during ion-exchange as an example.

Based on the site occupancy results, 1.8 Cs cations per unit cell are located in the *t-ltl* cages and 1.3 Cs cations are in the *t-ste* cages of the LTL structure. The data indicate that the preferential route is through the main channel 12MR of LTL and particularly through *t-ltl* cage. As the cation exchange continues, the exchanged species go through the 8MR *t-ste* cage. All these steps involve ion-exchange between K^+, already in the parent LTL, and Cs^+. Since *t-can* cage is not accessible to cations, the removal of K^+ from that location is not possible. According to the results of this work, Cs^+ and Rb^+ can enter the location in the centre of *t-ste* cage while cations such as Li^+ and Na^+, located in the main channel in the *t-ltl* cage, do not go any further (table 2.6 and table 2.7). It should be noted that most Cs cations, 1.8 per unit cell, are located in the main channels of LTL following the 4-stage ion-exchange.

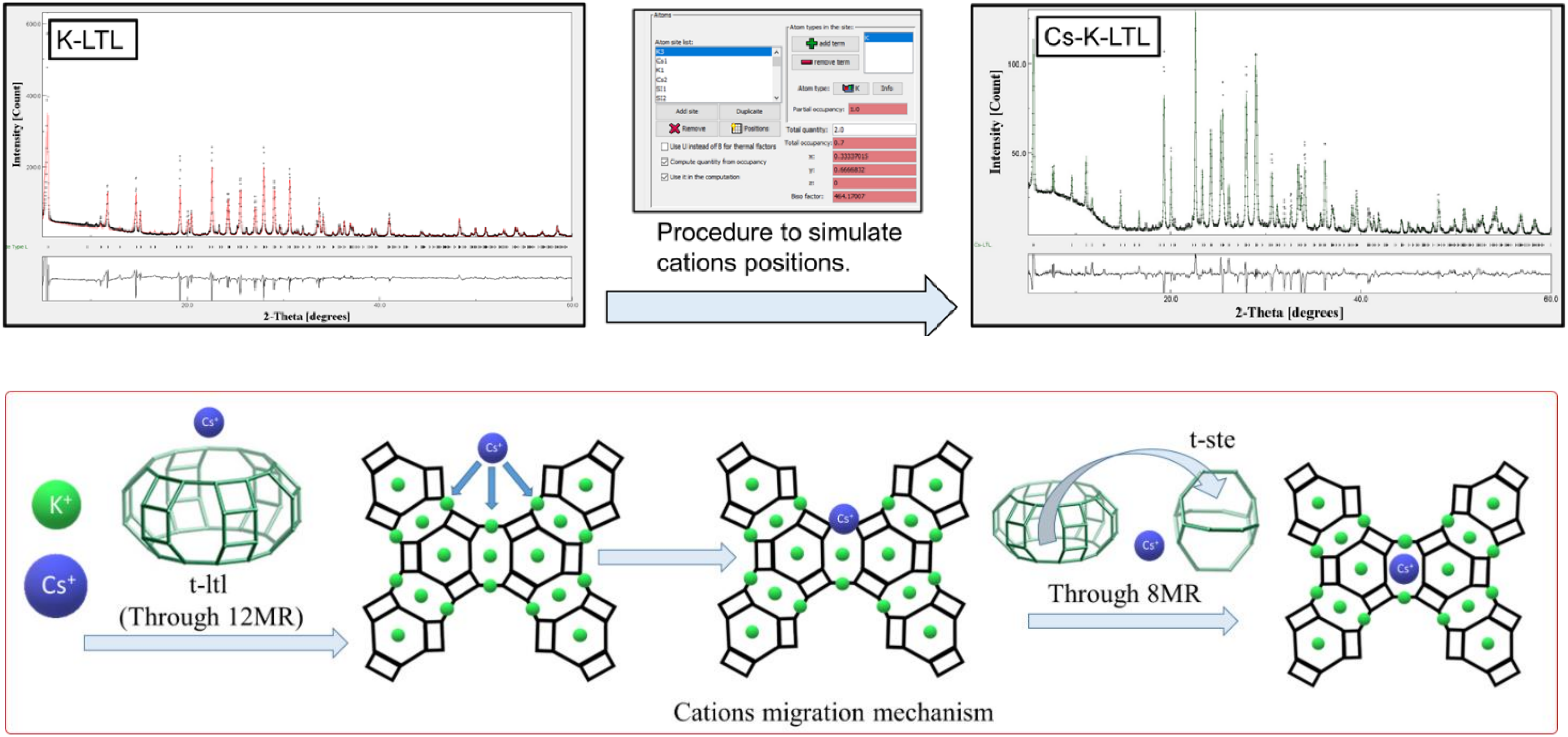

Atom site list: K3, Cs1, K1, Cs2, SI1, SI2

Atom type: K

Partial occupancy: 1.0

Total quantity: 2.0

Total occupancy: 0.7

x: 0.33337015

y: 0.6666832

z: 0

Biso factor: 464.17007

☐ Use U instead of B for thermal factors

☑ Compute quantity from occupancy

☑ Use it in the computation

Figure 2.19: (Top) Rietveld method and modelling. (Bottom) The cation migration mechanism of Cs+ species in K-LTL zeolite during ion-exchange.

Table 2.6: XRD analysis: lattice parameters and occupancies. The “Total occupancy per u.c.” is the total number of atoms (cations) per unit cell for a specific crystallographic position. “Site occupancy” is the occupancy of all atoms in a specific crystallographic position. Occupancies are defined in the original cif file. “Total occupancy per u.c.” is obtained by multiplying the “Site occupancy” by the number of specific sites (N.S.) present in a unit cell.

			can cage 6MR (top - bottom) (N.S.=2)		**ste cage (N.S.=3)**		**can cage (N.S.=2)**		**Main channel 12MR (N.S.=6)**	
	a=b, Å	**c, Å**	**Total occupancy per u.c.**	**Site occupancy M1 1**	**Total occupancy per u.c.**	**Site occupancy M2 0.9**	**Total occupancy per u.c.**	**Site occupancy M3 0.7**	**Total occupancy per u.c.**	**Site occupancy M4 0.6**
K-LTL	18.359	7.519	**1.544**	0.772	**2.844**	0.948	**0.892**	0.446	**3.600**	0.600
NH_4-K-LTL	18.411	7.536	**1.798**	0.899	**2.697**	0.899	**0.900**	0.450	**3.672**	0.612
Li-NH_4-K-LTL-1	18.394	7.532	**1.916**	0.958	**2.697**	0.899	**1.096**	0.548	**3.120**	0.520
Li-NH_4-K-LTL-2	18.393	7.532	**1.698**	0.849	**2.697**	0.899	**0.840**	0.420	**3.630**	0.605
Li-NH_4-K-LTL-3	18.393	7.531	**1.758**	0.879	**2.397**	0.799	**0.940**	0.470	**3.570**	0.595
Li-NH_4-K-LTL-4	**18.394**	**7.535**	**1.700**	**0.850**	**2.397**	**0.799**	**0.918**	**0.459**	**3.654**	**0.609**
Na-NH_4-K-LTL-1	18.407	7.538	**1.958**	0.979	**2.613**	0.871	**0.930**	0.465	**3.174**	0.529
Na-NH_4-K-LTL-2	18.401	7.537	**1.732**	0.866	**2.700**	0.900	**0.894**	0.447	**3.480**	0.580
Na-NH_4-K-LTL-3	18.393	7.533	**1.710**	0.855	**2.697**	0.899	**0.888**	0.444	**3.468**	0.578
Na-NH_4-K-LTL-4	**18.386**	**7.532**	**1.674**	**0.837**	**2.397**	**0.799**	**0.878**	**0.439**	**3.672**	**0.612**
K-NH_4-K-LTL-1	18.374	7.530	**1.748**	0.874	**2.397**	0.799	**1.366**	0.683	**3.234**	0.539
K-NH_4-K-LTL-2	18.383	7.530	**1.912**	0.956	**2.097**	0.699	**1.190**	0.595	**3.690**	0.615
K-NH_4-K-LTL-3	18.378	7.521	**1.796**	0.898	**2.710**	0.903	**0.880**	0.440	**3.594**	0.599
K-NH_4-K-LTL-4	**18.388**	**7.546**	**1.796**	**0.898**	**2.397**	**0.799**	**0.880**	**0.440**	**3.738**	**0.623**
Rb-NH_4-K-LTL-1	18.401	7.536	**1.690**	0.845	**2.187**	0.729	**1.086**	0.543	**3.768**	0.628
Rb-NH_4-K-LTL-2	18.405	7.540	**1.942**	0.971	**2.103**	0.701	**1.190**	0.595	**3.576**	0.596
Rb-NH_4-K-LTL-3	18.417	7.543	**1.682**	0.841	**2.391**	0.797	**1.302**	0.651	**3.606**	0.601
Rb-NH_4-K-LTL-4	**18.420**	**7.549**	**1.866**	**0.933**	**2.397**	**0.799**	**0.708**	**0.354**	**3.642**	**0.607**
Cs-NH_4-K-LTL-1	18.419	7.544	**1.690**	0.845	2.226	0.742	**0.720**	0.360	4.163	0.694
Cs-NH_4-K-LTL-2	18.424	7.547	**1.902**	0.951	**1.878**	0.626	**1.108**	0.554	**3.971**	0.662
Cs-NH_4-K-LTL-3	18.425	7.548	**1.822**	0.911	**2.094**	0.698	**1.378**	0.689	**3.618**	0.603
Cs-NH_4-K-LTL-4	**18.431**	**7.557**	**1.572**	**0.786**	**2.397**	**0.799**	**1.074**	**0.537**	**3.600**	**0.600**

Table 2.7: XRD analysis: occupancies of individual cations per crystallographic position.

	can cage 6MR (top - bottom)	**ste cage**	**can cage**	**Main channel 12MR**
	M1	**M2**	**M3**	**M4**
K-LTL	1.54 K	2.84 K	0.89 K	0.6 K
NH_4-K-LTL	1.80 K	2.34 N + 0.36 K	0.90 K	1.79 N + 1.88 K
Li-NH_4-K-LTL-1	1.92 K	0.56 N + 2.14 K	1.09 K	0.12 Li + 1.26 N + 1.74 K
Li-NH_4-K-LTL-2	1.69 K	0.30 N + 2.40 K	0.84 K	0.66 Li + 1.44 N + 1.53 K
Li-NH_4-K-LTL-3	1.76 K	0.30 N + 2.09 K	0.94 K	0.58 Li + 0.76 N + 2.24 K
Li-NH_4-K-LTL-4	**1.70 K**	**0.68 N + 1.72 K**	**0.92 K**	**0.71 Li + 1.50 N + 1.44 K**
Na-NH_4-K-LTL-1	1.96 K	0.08 N + 2.53 K	0.93 K	0.18 Na+ 1.46 N+ 1.53 K
Na-NH_4-K-LTL-2	1.73 K	0.14 N + 2.56 K	0.894 K	0.78 Na + 0.88 N +1.82 K
Na-NH_4-K-LTL-3	1.71 K	0.72 N + 1.97 K	0.88 K	0.77 Na + 1.75 N + 0.942 K
Na-NH_4-K-LTL-4	**1.67 K**	**0.39 N + 2.00 K**	**0.88 K**	**0.98 Na + 1.41 N +1.28 K**
K-NH_4-K-LTL-1	1.75 K	1.203 N + 1.19 K	1.36 K	0.78 K + 0.23 N + 2.22 K
K-NH_4-K-LTL-2	1.91 K	1.07 N + 1.03 K	1.19 K	1.44 K + 0.09 N + 2.16 K
K-NH_4-K-LTL-3	1.79 K	1.28 K + 0.01 N + 1.42 K	0.88 K	1.42 K + 2.35 K
K-NH_4-K-LTL-4	**1.79 K**	**1.09 K +1.29 K**	**0.88 K**	**2.35 K + 0.74 N + 0.64 K**
Rb-NH_4-K-LTL-1	1.65 K	0.67 N + 1.51 K	1.28 K	0.42 Rb + 0.17 N + 3.18 K
Rb-NH_4-K-LTL-2	1.94 K	0.27 N + 1.83 K	1.19 K	0.72 Rb + 0.28 N + 2.58 K
Rb-NH_4-K-LTL-3	1.68 K	0.74 Rb + 1.65 K	1.30 K	1.32 Rb + 0.01 N + 2.28 K
Rb-NH_4-K-LTL-4	**1.86 K**	**0.49 Rb + 1.91 K**	**0.71 K**	**1.72 Rb + 0.65 N + 1.28 K**
Cs-NH_4-K-LTL-1	1.69 K	1.40 N + 0.82 K	0.72 K	1.01 Cs + 0.01 N + 3.14 K
Cs-NH_4-K-LTL-2	1.90 K	1.20 N + 0.68 K	1.11 K	1.21 Cs + 0.11 N + 2.75 K
Cs-NH_4-K-LTL-3	1.82 K	0.94 Cs + 1.15 K	1.38 K	1.70 Cs + 0.024 N + 1.90 K
Cs-NH_4-K-LTL-4	**1.57 K**	**1.29 Cs + 1.11K**	**1.07 K**	**1.70 Cs + 0.61 N+ 1.29 K**

2.4.4 FTIR

FTIR spectra of K-LTL, NH_4-K-LTL and Cs-NH_4-K-LTL zeolites are presented in Figure 2.20. In addition to the SiOH groups vibrating at 3745 cm^{-1}, Na- and K-containing samples show low intensity bands at ~3720 and 3670 cm^{-1}, which can be attributed to defect sites, namely internal silanols and AlOH groups, respectively. These are weakly acidic hydroxyls originating from a minor degradation of the zeolite structure during ion-exchange.

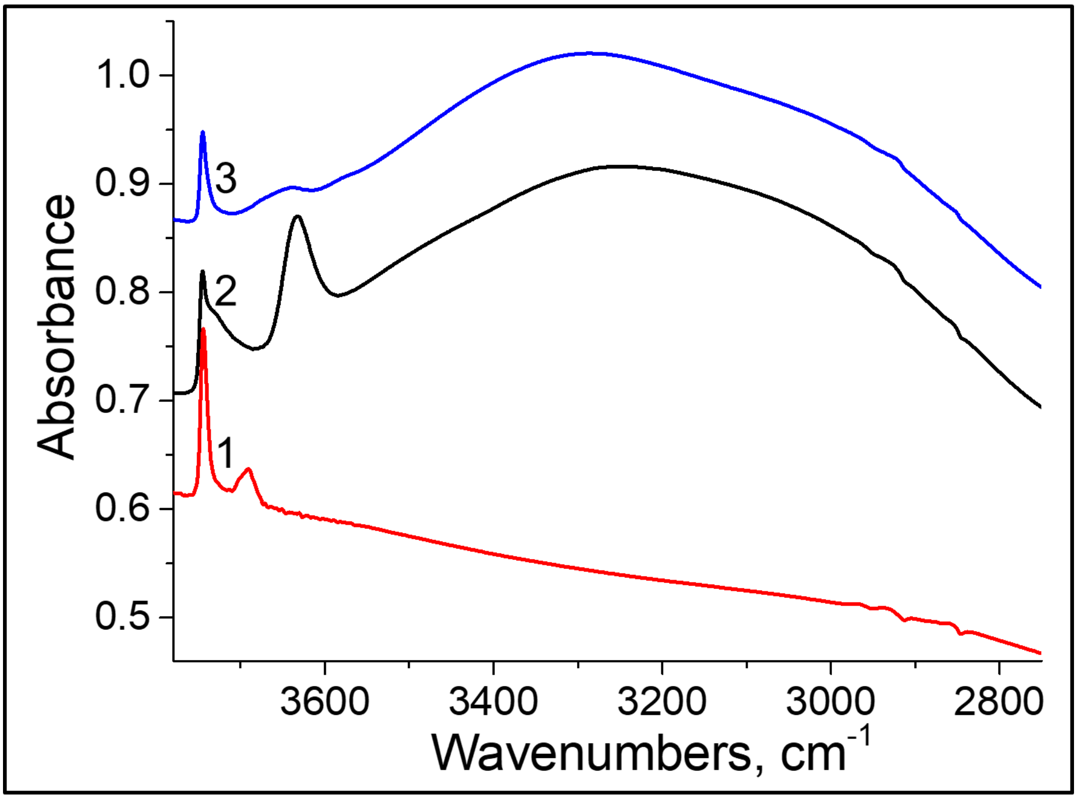

Figure 2.20: The OH region of the FTIR spectra for (1) K-LTL (parent), (2) NH_4-K-LTL and (3) Cs-NH_4-K-LTL. Spectra are offset for clarity.

An important feature in the FTIR spectra of ion-exchanged zeolites is the presence of two intense bands of the bridging OH-groups: at 3640 cm^{-1}, this is attributed to SiOHAl groups freely vibrating in 12MR, and at ~3250 cm^{-1}, which is very broad and hence is assigned to bridging OH groups forming hydrogen bond with neighbouring oxygen atoms, e.g. in 6-membered rings (6MR).

Similar phenomena have been reported for MFI, FAU, MOR and LTL zeolites [19], [29], [31], [32], and some representative examples are shown in Figure 2.21.

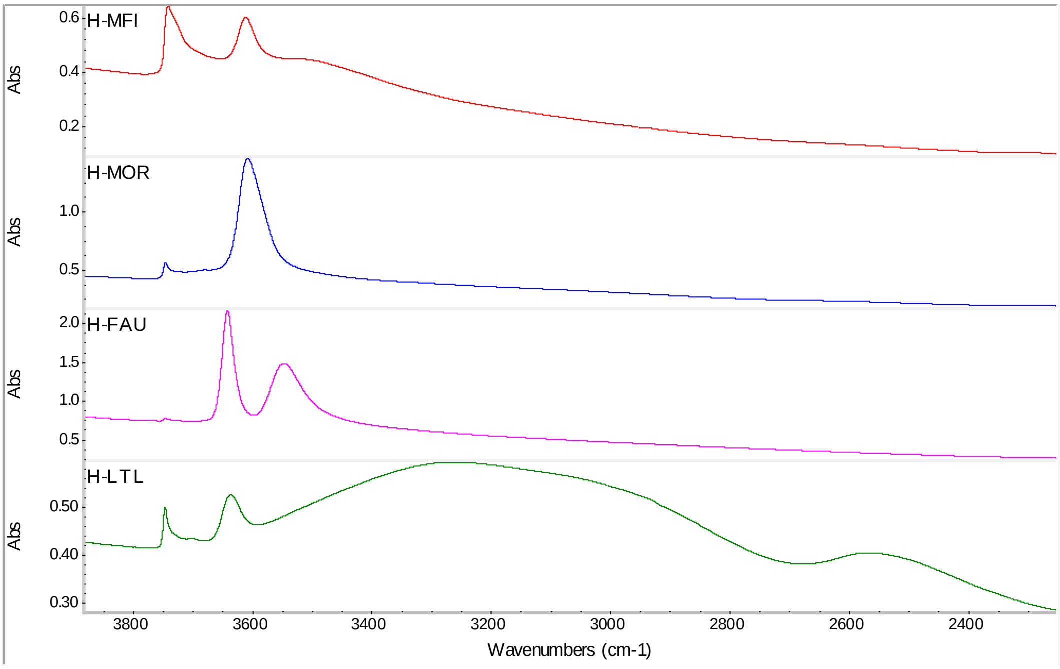

Figure 2.21: Experimental FTIR spectra of H-forms of MFI, MOR, FAU and LTL zeolites. The narrow OH peaks at ~3600 cm^{-1} are indicative of isolated Al(OH)Si groups; broad bands at low frequencies represent H-bonded OH-groups.

It should be noted that all these samples have been activated at 450°C prior to the IR measurements and no residual NH_3 or NH_4^+ species have been detected (figure 2.22).

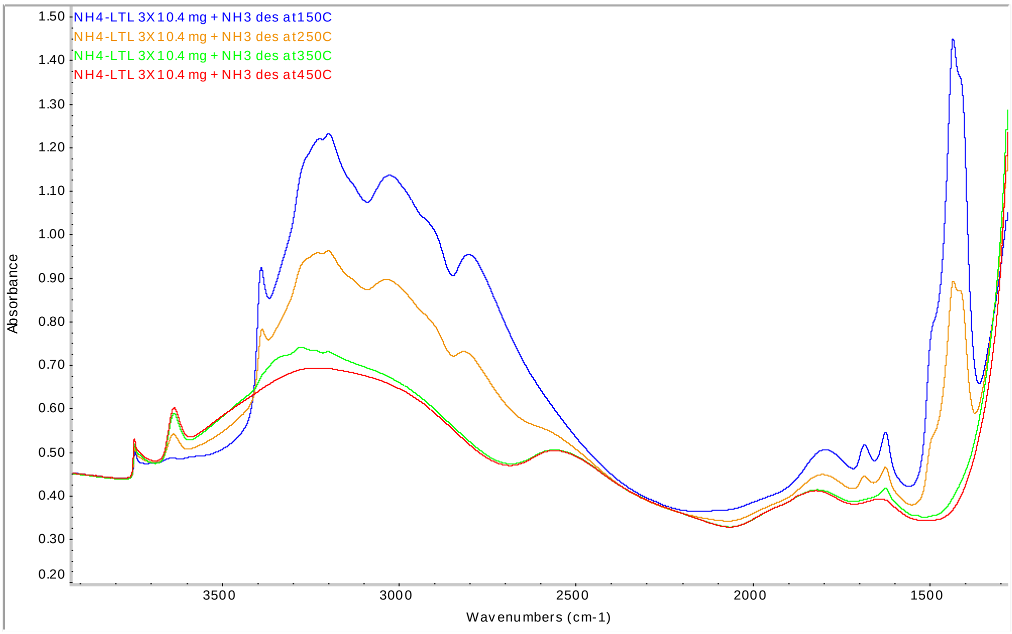

Figure 2.22: Experimental FTIR spectra of NH_4-K-LTL zeolite following stepwise ammonia desorption at 150-450°C.

Recent computational studies of H-bound bridging OH-groups in HZSM-5 (Figure 2.23, left) have demonstrated that as the H --- O distance (H-bond length) reaches 1.85 Å (while the O-H bond length in the bridging OH-group is 0.985 Å), the OH band shifts to ~3250 cm^{-1}, its full width at half-maximum reaches ~175 cm^{-1} and its intensity increases by almost an order of magnitude [33].

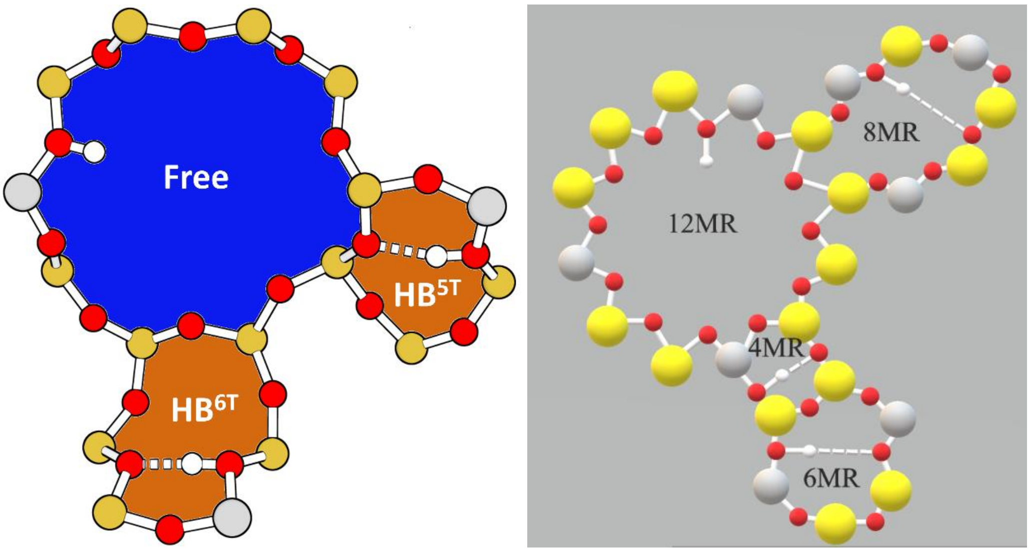

Figure 2.23: (Left) H-bound bridging OH-groups in HZSM-5 and (right) in LT

Applying these findings to our experimental spectra, one can conclude that there is a significant number of bridging OH-groups in the LTL zeolites that are H-bound to the neighbouring oxygen atoms with the hydrogen bond length shorter than 1.85 Å (LTL zeolite presents a rather extreme manifestation of this spectroscopic effect) (figure 2.23, right). Such H-bound SiOHAl groups are located in the 6-, and possibly 4-MR, of the LTL structure. Among the samples reported, the peak intensity ratio of the bands at 3640 and 3250 cm^{-1} is ~2 for Na-NH_4-K-LTL and K-NH_4-K-LTL, ~3 for Rb-NH_4-K-LTL and ~18 for Cs-NH_4-K-LTL samples (table 2.9).These results suggest that SiOHAl groups in 12-MR of the main channels can be selectively "poisoned" using ion-exchange with Cs^+ cations. Acidic properties of ion exchanged LTL have been investigated using pyridine as a probe molecule (Figure 2.23 and 2A.7, 2A.8 and 2A.9 in chapter 6 - appendix). The difference spectra following Py adsorption for both NH_4-K-LTL and Cs-NH_4-K-LTL show two major negative peaks at 3640 and ~3250 cm^{-1}, corresponding to the free and H-bound bridging OH-groups, confirming their acidic nature. In contrast, only one negative peak attributed to the free (isolated) bridging OH-groups interacting with Py has been detected for NH_4-MAZ (Figure 2.24).

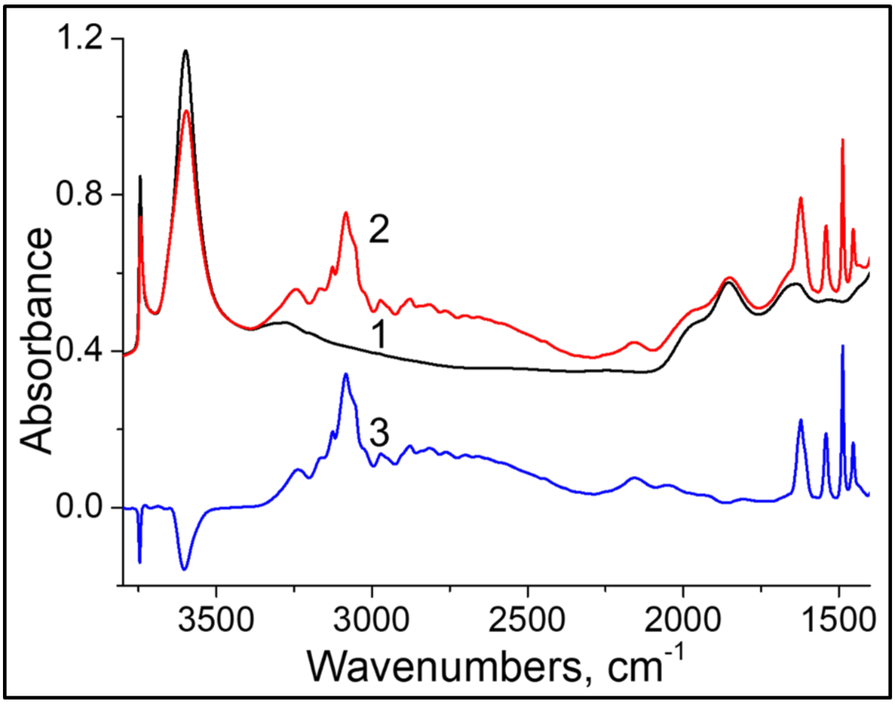

Figure 2.24: FTIR spectra of (f) NH4-MAZ: (1) - the material before Py adsorption, (2) - the material after Py adsorption at 200ºC and (3) - the difference spectrum.

The data on the number of accessible to Py Brønsted and Lewis acid sites in the ion-exchanged LTL zeolites are provided in table 2.8 and figure 2.25.

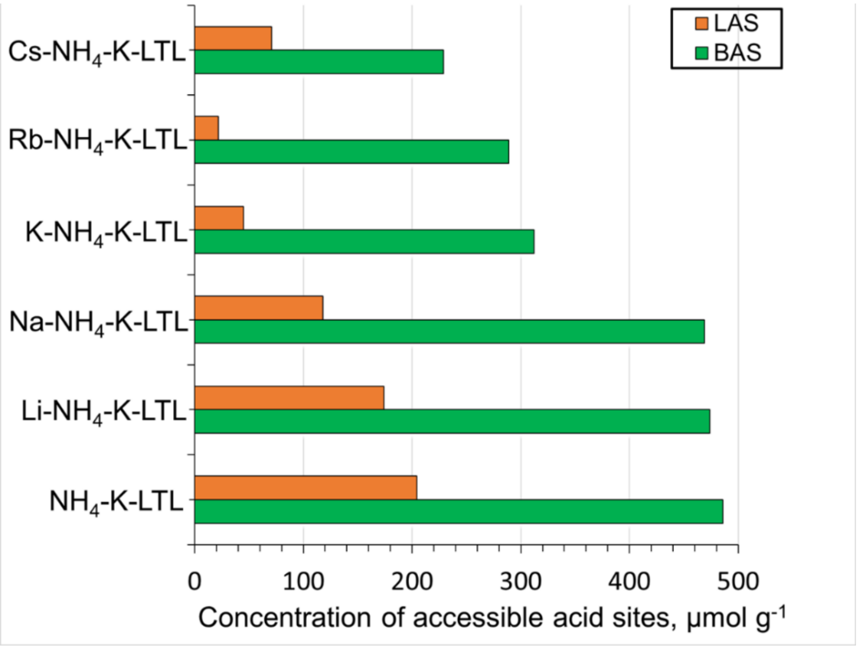

Figure 2.25: Concentration of Brønsted and Lewis acid sites in the ion-exchanged LTL samples.

Table 2.8: XRD crystallinity % and FTIR data for the ion-exchanged LTL samples and for NH_4-MAZ.

Sample	Crystallinity, %	BAS, µmol g^{-1}	LAS, µmol g^{-1}
NH_4-MAZ	82	183	88
K-LTL	92	0	8
NH_4-K-LTL	89	486	204
Li-NH_4-K-LTL-4	90	474	174
Na-NH_4-K-LTL-4	88	469	118
K-NH_4-K-LTL-4	87	312	45
Rb-NH_4-K-LTL-4	85	289	34
Cs-NH_4-K-LTL-4	84	229	71

A clear trend among the ion exchanged zeolites can be seen as the number of Lewis acid sites decreases with the increased size of the exchanged cation, indicating that alkali metal cations not only neutralise the zeolite acid sites, but also facilitate the removal of some of the Lewis acid sites, probably associated with extra-framework Al. Cs-NH_4-K-LTL is the only exception, which may be linked to the more basic properties of the ion-exchange solution that could result in some structural degradation. Indeed, this sample shows the lowest crystallinity among the studied materials (Table 2.2). The number of Brønsted acid sites is also declining following ion-exchange, with a particularly significant decrease detected for K-, Rb- and Cs-exchanged samples.

Table 2.9: Additional peak intensity ratios of all ion exchanged samples.

Samples	**Peak height ratio (I_{3250}/I_{3640})**
NH_4-K-LTL	
NH_4-K-LTL 13.5mg	2.2
Li-LTL	
Li-NH_4-K-LTL-1 12.2mg	1.8
Li-NH_4-K-LTL-2 10.3mg	1.4
Li-NH_4-K-LTL-3 11.7mg	1.9
Li-NH_4-K-LTL-4 14.0mg	1.7
Na-LTL	
Na-NH_4-K-LTL-1 12.5mg	1.9
Na-NH_4-K-LTL-2 13.6mg	1.6
Na-NH_4-K-LTL-3 12.4mg	1.9
Na-NH_4-K-LTL-4 10.9mg	1.6
K-LTL	
K-NH_4-K-LTL-1 10.9mg	2.4
K-NH_4-K-LTL-2 11.1mg	2.1
K-NH_4-K-LTL-3 9.5mg	1.8
K-NH_4-K-LTL-4 11.1mg	1.1
Rb-LTL	
Rb-NH_4-K-LTL-1 10.6mg	3.2
Rb-NH_4-K-LTL-2 11.1mg	3.2
Rb-NH4-K-LTL-3 13.1mg	3.1
Rb-NH_4-K-LTL-4 11.7mg	2.3
Cs-LTL	
Cs-NH_4-K-LTL-1 10.6mg	6.4
Cs-NH_4-K-LTL-2 11.7mg	9.9
Cs-NH_4-K-LTL-3 12.4mg	8.5
Cs-NH_4-K-LTL-4 11.8mg	18.3

2.4.5 NH_3-TPD

TPD of ammonia has been carried out to evaluate the strength of acid sites in NH_4-K-LTL in comparison with NH_4-MAZ. The data presented in figure 2,26 demonstrate that the apparent strength of acid sites in MAZ is greater as compared to that for the LTL zeolite. Indeed, the NH_3 desorption peak is shifted for the mazzite sample to a higher temperature by ~75°C. However, this can be related to the restricted ammonia desorption in MAZ associated with the transport limitations owing to the micropore blockage in this zeolite.

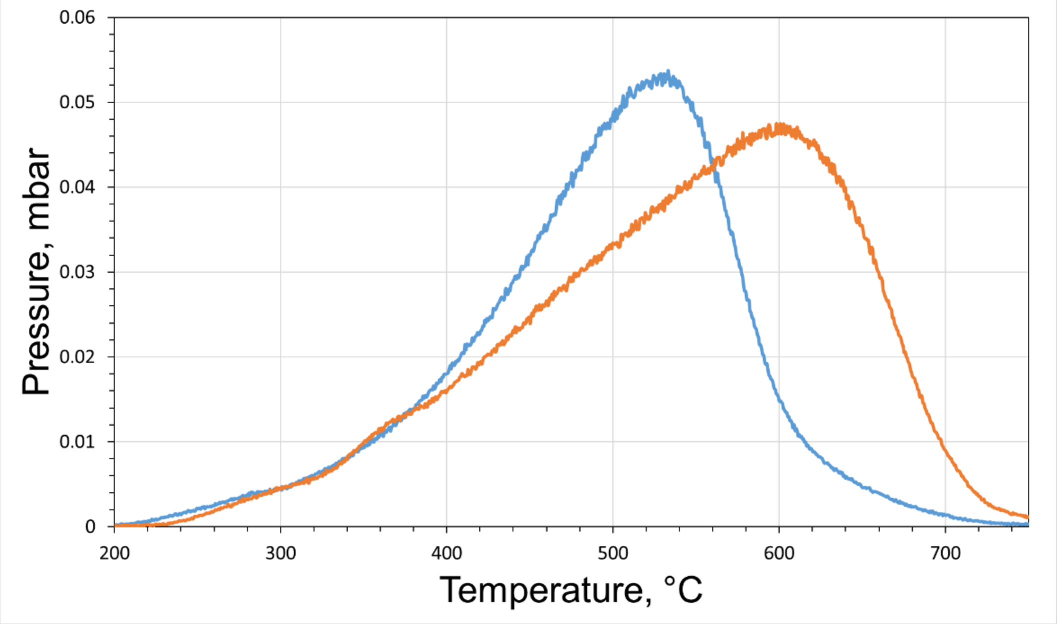

Figure 2.26: NH_3-TPD data for NH_4-LTL (blue) and NH_4-MAZ (orange).

2.5 Conclusions

A series of ion-exchanged LTL zeolites has been prepared, and their structural and acidic properties have been studied using FTIR, XRD, SEM-EDX, XRF and N_2 physisorption. According to the elemental analysis, the larger alkali metal cations, in particular Cs^+, can replace almost 40% of the exchangeable species (K^+ and NH_4^+), whereas Li^+ and Na^+ can be introduced only in small quantities. The X-ray diffraction analysis and the Rietveld method show that all cations can migrate through the LTL structure via the 12MR *t-ltl* cage. At higher concentrations of alkali metals, only larger cations such as Cs^+, Rb^+ and K^+ can access to the smaller 8MR *t-ste* cage, while the *t-can* cages are inaccessible at the condition employed and no cations have been introduced in them except for the original K^+ present in the parent zeolite K-LTL. Infrared spectra of the ion-exchanged zeolites show the presence of two bands of the bridging OH-groups: a narrow band at ~3640 cm^{-1}, which is attributed to the isolated SiOHAl groups in the main channels (12MR), and a broad band at ~3250 cm^{-1} assigned to bridging OH groups forming hydrogen bond with neighbouring oxygen atoms in the 4- or 6-membered rings. The concentration of Brønsted acid sites has been monitored using pyridine adsorption. Only a slight decrease in the BAS concentration is observed for the Li and Na ion-exchanged samples as compared with the starting NH_4-K-LTL. The introduction of Cs^+, Rb^+, and K^+ cations results in up to 50% decrease in the concentration of BAS and LAS. Furthermore, ion-exchange with the larger cations, in particular Cs, can be used to selectively remove isolated acidic SiOHAl groups in the 12MR of the main channels. In comparison with NH_4-K-LTL, the number of acid sites in NH_4-MAZ accessible to Py is significantly lower. At the same time, the effective strength of acid sites, measured using ammonia TPD, in NH_4-MAZ is greater than that in NH_4-

K-LTL. Both results are associated with the transport limitations due to the micropore blockage in the structure of mazzite.

2.6 References

[1] D.W. Breck, E.M. Flanigen, Molecular Sieves, Society of Chemical Industry, London, (1968) 47.

[2] D.W. Breck, N.A. Acara, US Patent 2,711,565, 1958.

[3] P. Pichat, C. Franco-Parra, D. Barthomeuf, Infrared structural study of various type L zeolites, Journal of the Chemical Society, Faraday Transactions 1: Physical Chemistry in Condensed Phases, 71 (1975) 991-996.

[4] R R.M. Barrer, H. Vllliger, The crystal structure of the synthetic zeolite L, Zeitschrift Fur Kristallographie - New Crystal Structures, 128 (1969) 352-370.

[5] T. Ohsuna, Y. Horikawa, K. Hiraga, O Terasaki, Surface Structure of Zeolite L Studied by High-Resolution Electron Microscopy, Chemistry of Materials, 10 (1998) 688–691.

[6] S.S. Hassani, F. Salehirad, H.R. Aghabozorg, Z. Sobat, Synthesis and morphology of nanosized zeolite L, Crystal Research and Technology, 45 (2010) 183-187.

[7] J.M. Newsam, M.T. Melchior, H. Malone, Full profile analysis of the ^{29}Si NMR spectra of LTL-framework zeolites, Solid State Ionics, 26(2) (1988) 125-131.

[8] L.B. McCusker, D.H. Olson, C. Baerlocher, Atlas of Zeolite Framework Types, Elsevier (2007).

[9] P. Li, Y. Wang, H. Li, G. Calzaferri, Luminescence Enhancement after

Adding Stoppers to Europium(III) Nanozeolite L, Angewandte Chemie Interantional Edition, 53 (2014) 2904-2909.

[10] Y. Wang, H. Li, L. Gu, Q. Gan, Y. Li, G. Calzaferri, Thermally stable luminescent lanthanide complexes in zeolite L, Microporous Mesoporous Materials, 121 (2009) 1-6.

[11] S.D. Bhat, P.S. Niphadkar, T.R. Gaydhankar, S.V. Awate, A.A. Belhekar, P.N. Joshi, High temperature hydrothermal crystallization, morphology and yield control of zeolite type K-LTL, Microporous Mesoporous Materials, 76 (2004) 81-89.

[12] L.J. Garces, V.D. Makwana, B. Hincapie, A. Sacco, S.L. Suib, Selective N,N-methylation of aniline over cocrystallized zeolites RHO and zeolite X (FAU) and over Linde type L (Sr,K-LTL), Journal of Catalysis, 217 (2003) 107−116.

[13] J. Song, H. Ma, Z. Tian, L. Yan, Z. Xu, Q. Liu, W. Qu, The effect of Fe on Pt particle states in Pt/KL catalysts, Applied Catalysis General, 492 (2015) 31−37.

[14] E. G. Derouane, D. J. Vanderveken, Structural recognition and preorganization in zeolite catalysis: Direct aromatization of n-hexane on zeolite L-based catalysts, Applied Catalysis, 45 (1) (1988) 15-22.

[15] G. Larsen and G. L. Haller, Metal-support effects in Pt/L-zeolite catalysts, Catalysis Letters, 3 (1989) 103−110.

[16] J.R. Bernard, D.W. Ward, 5th Interantional Conference on Zeolites, Heyden, London, (1980) 686-695

[17] Besoukhanova, C., Guidot, J., and Barthomeuf, Platinum-zeolite interactions in alkaline L zeolites. Correlations between catalytic activity and platinum state, Journal of the Chemical Society, Faraday Transactions 1: Physical Chemistry in Condensed Phases, 77 (1981) 1595-1604.

[18] S.J. Cho, R. Ryoo, Characterization of PtSn narioparticles in KL zeolite and n-hexane aromatization activity, Catalysis Letters, 97 (2004) 71-75.

[19] K. Tarach, J. Tekla, U. Filek, A. Szymocha, I. Tarach, K. Góra-Marek, Alkaline-acid treated zeolite L as catalyst in ethanol dehydration process, Microporous and Mesoporous Materials, 241 (2017) 132−144.

[20] A. Al-Ani, C. Freitas, V. Zholobenko, Nanostructured large-pore zeolite: The enhanced accessibility of active sites and its effect on the catalytic performance, Microporous and Mesoporous Materials, 293 (2020).

[21] L. B. McCusker, C. Baerlocher, S. T. Wilson, R. W. Broach, Synthesis and Structural Characterization of the Aluminosilicate LZ-135, a Zeolite Related to ZSM-10, Journal of Physical Chemistry, 113 (2009) 9838-9844

[22] A.M. Goossens, E.P. Feijen, G. Verhoeven, B.H. Wouters, P.J. Grobet, P.A. Jacobs, J.A. Martens, Crystallization of MAZ-type zeolites using tetramethylammonium, sodium and n-hexane derivatives as structure- and composition-directing agents, Microporous and Mesoporous Materials, 35-36 (2000) 555-572.

[23] K. Momma and F. Izumi: VESTA: a three-dimensional visualization system for electronic and structural analysis, J. Appl. Crystallogr., 41 (2008) 653-658.

[24] K. Momma and F. Izumi: VESTA 3 for three-dimensional visualization of crystal, volumetric and morphology data, J. Appl. Crystallogr., 44 (2011) 1272-1276.

[25] L. Lutterotti, S. Matthies, H. R. Wenk, MAUD (Material Analysis Using Diffraction): a user friendly java program for Rietveld texture analysis and more. Proceeding of the Twelfth International Conference on Textures of Materials (ICOTOM-12) , (1999) 1599-1604.

[26] L. Lutterotti, Maud: A Rietveld Analysis Program Designed for the Internet and Experiment Integration, Acta Crystallographica Section A - ACTA CRYSTALLOGR A. 56 (2000).

[27] Database of zeolite structures: http://www.iza-structure.org/databases, as of May 2023.

[28] The International Centre for Diffraction Data - ICDD, https://www.icdd.com/.

[29] V. Zholobenko, C. Freitas, M. Jendrlin, A. Travert, P. Bazin, F. Thibault-Starzyk. Quantitative characterisation of zeolite acidity using pyridine: an AGIR study. Journal of Catalysis, 385 (2020) 52-60.

[30] D. Seoung, Y. Lee, S. J. Kim, H. H. Lee, D. Ahn, N. S. Shin, T. Vogt, Pressure-induced hydration and cation migration in a Cs^+ exchanged gallosilicate zeolite LTL: Synchrotron X-ray powder diffraction study at ambient and high pressures, Microporous and Mesoporous Materials, 136(1-3) (2010) 75-82.

[31] V.L. Zholobenko, L.M. Kustov, V.Yu. Borovkov, V.B. Kazansky. A new

type of acidic hydroxyl groups in ZSM-5 zeolite and in mordenite according to diffuse reflectance IR spectroscopy, Zeolites, 8, (1988) 175-178.

[32] V.L. Zholobenko, M.A. Makarova, J. Dwyer. Inhomogeneity of Broensted acid sites in mordenite, J. Phys. Chem., 97 (1993) 5962-5964.

[33] H. Windeck, F. Berger, J. Sauer, Spectroscopic Signatures of Internal Hydrogen Bonds of Brønsted-Acid Sites in the Zeolite H-MFI, Angewandte Chemie International Edition, 135(25) (2023)

Chapter 3

Synthesis and characterisation of the structural and acidic properties of the MAZ zeolite

3.1 Abstract

In first instance, the synthesis of mazzite zeolite was performed. In the first attempt a multiphase system consisting of mazzite, sodalite, faujasite and gmenilite was obtained. During the next attempts, the amount of some of the reactants was variated on purpose. Variation of the amount of NaOH allowed to obtain purer mazzite with no additional extraphases or impurities. This was achieved with ~2g of NaOH. Synthesised mazzite was analysed by SEM-EDX, XRD, N_2 adsorption desorption and FTIR. Subsequently, a range of modified MAZ and LTL zeolites have been prepared and ion-exchanged with a series of alkali metal cations. It has been shown that K^+, Rb^+ and Cs^+ can be readily introduced into the MAZ structure with ~2 cations ion-exchanged per unit cell. In contrast, less than 1 cation of Li^+ or Na^+ per unit cell has been introduced under similar conditions. Ion-exchanged zeolites have been characterised using Fourier transform infrared spectroscopy, X-ray powder diffraction, scanning electron microscopy, X-ray fluorescence and N_2 physisorption in order to gain a better understanding of their structural and acidic properties. The FTIR data indicate considerable heterogeneity of the bridging OH groups in mazzite. The concentration of both Brønsted and Lewis acid sites detected in MAZ using Py as a probe molecule is lower than expected from its chemical composition, with the relative accessibility of the bridging OH-groups varying from 16% for H-MAZ to 28% for K-exchanged samples. This is in agreement with the N_2 adsorption-desorption data showing a rather low micropore volume for the ion-exchanged materials and with the NH_3-TPD results implying considerable transport limitations. This work demonstrates that the channel structure of mazzite is partially blocked resulting in a decreased micropore volume and limited access to the acid sites. In addition, optimisation of the synthesis procedures and the development of

post-synthesis treatments are required in order to generate effective catalysts for the conversion of hydrocarbons based on MAZ and LTL zeolites.

3.2 Introduction

Mazzite was probably first obtained in 1966 by Flanigen and Kellberg [1] (their patent No. 4241036, applied for in 1975, granted and published in 1980, refers to the abandoned applications 569805 and 655318 submitted in 1966 and 1967) under the name of zeolite omega. Around this time, Ciric also reported the preparation and application of a synthetic mazzite named ZSM-4 [2] (his patent No. 3923639, applied for in 1972, granted and published in 1975, refers to the abandoned application 509568 as well as 722149 submitted in 1965 and 1968). In 1972, mazzite was identified in basaltic rocks from Mont Semiol in France. The crystalline structure of mazzite was resolved in 1974-1975 by Galli [3], [4]and Rinaldi et al. [5].

Because of its structure, characterized by a hexagonal symmetry, Mazzite belongs to the category of highly acidic zeolites with broad pores and unidirectional porosity. These properties make mazzite suitable and advantageous for applications in catalysis such as for the conversion of hydrocarbons. According to Flanigen's information contained in her patent (U.S. Pat. No. 4,241,036), omega zeolite has a structure common to all type of mazzites such as ZSM-4 and MZ-34 for example. However, although all mazzites may show similarities about their structure, they can be distinguished from one another by their specific synthetic routes. In addition, zeolites which belong to this category show different properties and physical characteristics such as Si/Al ratio.

3.3 Structure

Zeolites of the mazzite family (Framework Type MAZ [6] Figure 3.1) are microporous crystalline aluminosilicates characterised by a structure with a tubular 12-membered ring channel system (Figure 3.2b). The framework of type of zeolites consists of columns of gmelinite cages linked through oxygen bridges which gives to the 12-MR pores a diameter of 0.74 nm. Parallel to the 12-MR channel, there is a secondary channel system comprised of distorted 8-MR with the size of 0.31x0.31 nm.

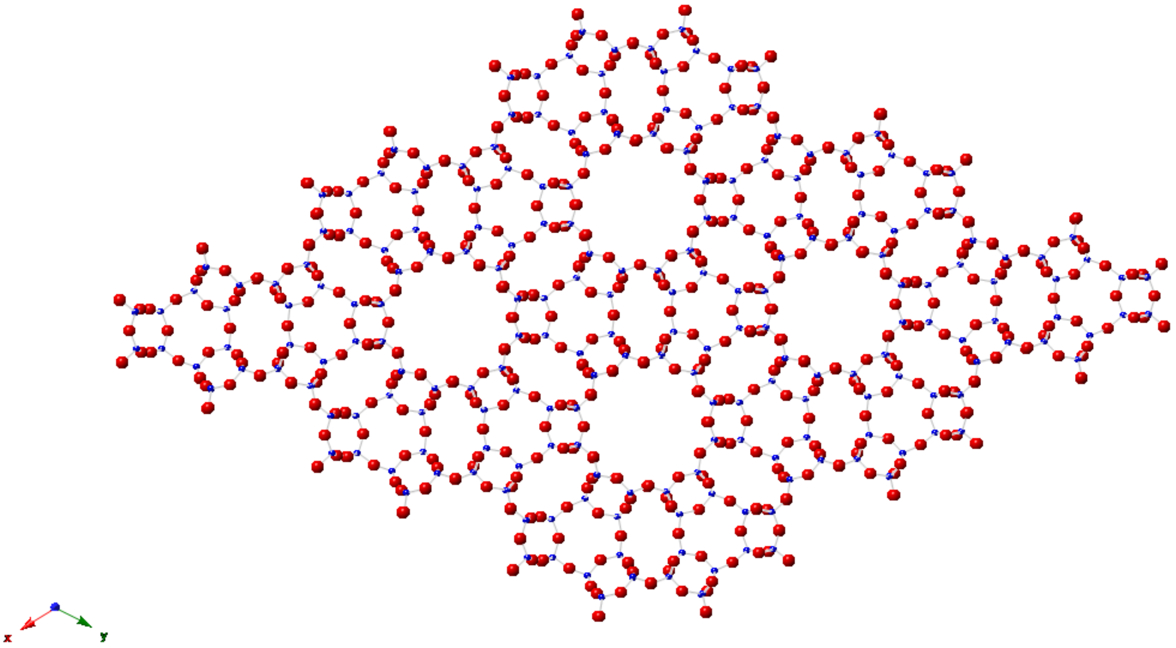

Figure 3.1: Structure of mazzite viewed along c-axis.

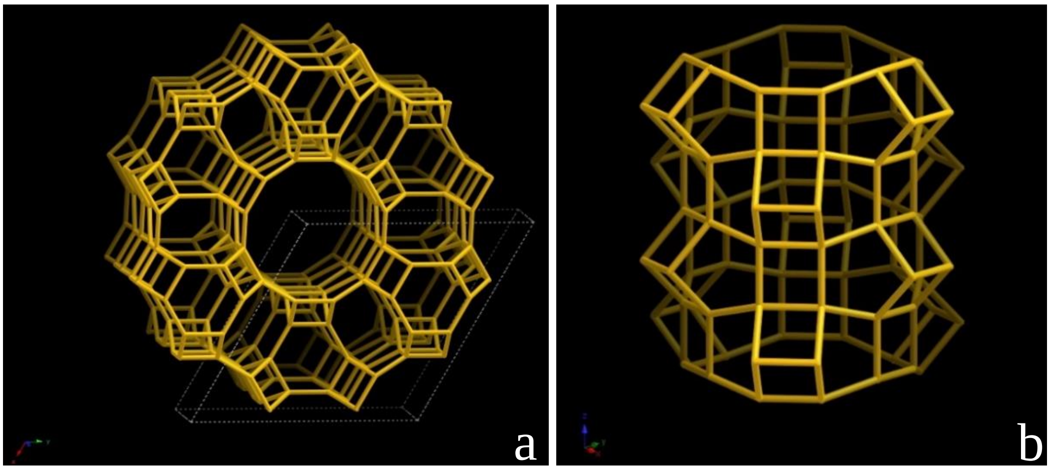

Figure 3.2: (a) Framework type MAZ. Projection of MAZ topology along [001] axis. (b) Tubular 12-MR channel system. Pictures adapted from “Database of zeolites structures” (http://www.iza-structure.org/databases/).

The lattice is characterised by two crystallographically non-equivalent tetrahedral sites called T1, located in the 4-MRs of gmelinite cages, and T2 in the 6-MRs channels (Figure 3.3). There are 24 T1 sites and 12 T2 sites per unit cell.

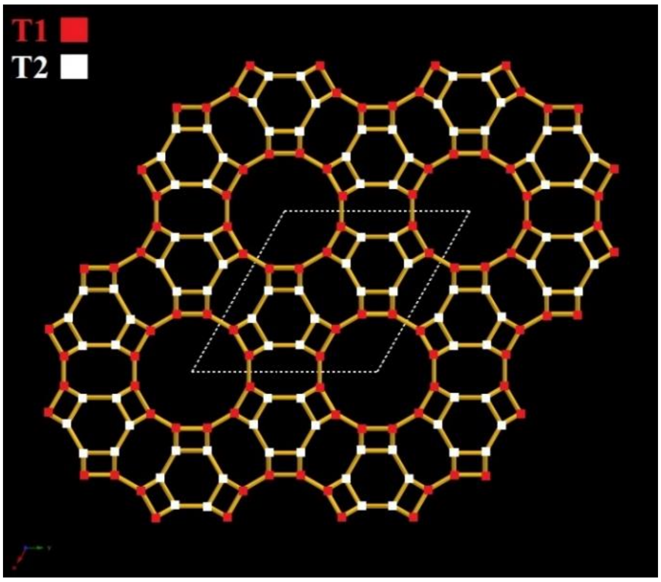

Figure 3.3: Framework type with T1 and T2 sites. Projection of MAZ topology along [001] axis. Picture adapted and modified from “Database of zeolites structures” (http://www.iza-structure.org/databases/)

3.4 Synthesis

The synthesis procedure of mazzite involves the preparation of hydrogels, which contain a trivalent alumium source, a silicon source, alkali metal cation or alkaline earth metal cation in the hydroxide form, water and structure agents. The hydrogel is obtained as result of a polycondensation of aluminosilicate polyanions directed by structure directing agents (SDA) or templates.

Templates can be neutral or charged as well as organic or inorganic molecules. Their function is to alter the gel chemistry in order to form oligomers in solution. The condensation of these oligomers leads to the formation of a specific framework and a micropore systems. The oligomers are able to stabilize the framework through electrostatic and dispersive interactions. It should be pointed out that the variation of the stoichiometry of constituents, subsequently of the gel and then of the hydrothermal treatment, the latter necessary for the crystallisation, may result in zeolites that show differences from mazzite (MAZ) such as offretite (OFF) or Zeolite L (LTL) [7].

There are several synthetic routes to prepare mazzite. According to the reference [8] mazzite type zeolite was synthetized by preparing a solution consisting of precipitated silica and sodium aluminate with NaOH, TMA-Cl and TMA-OH. This mixture was homogenized by stirring and crystallized in an autoclave for 43 hours at 100°C. Subsequently, the product was filtrated, washed and dried. This protocol allowed to obtain high alumina mazzite with Si/Al=3.1.

The method described in A. M. Gossens et al. [9] represents a good approach to obtain a product with high purity. In this synthesis procedure a solution consisting of gibbsite or sodium aluminate, which represent the aluminium source, is prepared by dissolving them in an aqueous mixture of NaOH and TMAOH. This solution is stirred and then a second solution consisting of Ludox HS-40 as silica source and water is added. The gel obtained is aged for 3 days at room temperature and then crystallized for 10 days at the temperature of 100° C in an oven. The final product was filtered, washed with deionised water and dried.

3.5 Crystallisation mechanism of Mazzite

In the mechanism of mazzite synthesis described, TMA cations have been occluded inside gmelinite cages during the crystallisation process because of their inability to diffuse through 12 MRs, 8MRs, 6MRs channels. TMA cations act as structure directing agent during MAZ-type structure formation and growth. During the crystal growth, TMA cations are not sufficient to balance the entire charge of the anionic lattice and this is why Na^+ are added to achieve electro-neutrality.

A templating effect is originated from the affinity between TMA cations and the interior of gmenilite cages. Unfortunately, this mechanism is still debated and partially unknown. It should be noticed that, without TMA, the formation of MAZ-type zeolites is inhibited and a FAU-type zeolite is obtained instead. It seems that behind this mechanism there is the action of a common precursor for MAZ and FAU which might correspond to a 12T atom unit as suggested by Vaughan [10].

In order to build a FAU-type zeolite, the hexagonal prism and sodalite cage are required as secondary building units. If TMA is excluded from the synthesis, the sodalite cage is formed which leads to FAU formation. When TMA is involved in the synthesis, the 12T atom precursor can form a double-saw chain which consist of five side-shared 4-MRs. The three by three link in these chains develop one complete and one partial gmelinite cage. The success of this condensation is promoted by the occlusion of TMA cations in the complete cage. Na cations participate to the formation and orientation of the “teeth” of the double saw chains during the formation of gmenilite cages.

During the synthesis procedure described [9], several attempts to produce mazzite zeolite have been carried out with and without employing the three different n-hexane derivatives. It should be pointed out the importance of TMA cations presence due to their structural directing agent function. However, although some attempts to synthesize mazzite zeolite have been successful without employing n–hexane derivatives in other case they played a key role in order to obtain a purer product.

The aspects about purity and morphology have been revealed through the characterisation on the material obtained which highlighted the influence of these derivatives as well as the molar gel composition.

3.6 Acidic properties

One of the major areas of interest in the field of zeolites is catalysis. Through patents and papers, literature offers several examples and results, which highlight how zeolites and their acid properties play a key role in catalysis.

As zeolites are solid acids, both Brœnsted and Lewis acid sites are present. Brœnsted acid sites are bridging hydroxyl groups, such as SiOHAl groups, that transfer protons with strong bases. Lewis acid sites are electron pair acceptor sites, which can be trigonal aluminium cations. They can be coordinatively unsaturated metal cations such as Al^{3+} in extraframerwork positions, Al oxide clusters or metal cations in exchangeable positions (e.g. Na^+, Ca^{2+}).

In order to differentiate Brœnsted from Lewis sites, basic molecules such as pyridine can be used. The frequency of the ring deformation vibration helps to understand if pyridine is adsorbed on Bronsted sites (as pyridium ion) or coordinatively adsorbed Lewis sites.

The channel system in the structure of a zeolite is a crucial feature in catalysis as it acts as the "access route" to acid sites for molecules and species. However, reduced dimensions of the channels may limit the accessibility to the acid sites.

In general, this problem can be solved through specific chemical procedures, which involves structure modification.

Several research groups had investigated the acid properties in mazzite. Since the accessibility to acid sites by molecules and species in unmodified mazzites is limited, post synthetic treatments, such as dealumination, play a crucial role in catalysis since they improve pore sizes. In reference [11], the authors have investigated mazzites samples with different Si/Al ratios such as 4.4 (MAZ4.4) for the parent, 10 (MAZ10) and 30 (MAZ30) for the modified samples. The accessibility of acid sites, before and after dealumination, was evaluated through N_2 adsorption. N_2 adsorption-desorption isotherms revealed that the accessibility of micropores in MAZ4.4 was poor and the pore volume was low. In the other case, the pore volume of dealuminated mazzites was greater (Si/Al ratio10 and 30), indicating an improved degree of accessibility has been observed (table 3.1).

Table 3.1: Pore volumes (cm^3 g^{-1}) of different mazzites (adapted and from reference [11]).

Sample	Total, cm^3 g^{-1}	Micropore, cm^3 g^{-1}	Mesopore, cm^3 g^{-1}
MAZ4.4	0.076	0.045	0.032
MAZ10	0.274	0.143	0.131
MAZ30	0.313	0.182	0.132

These results suggested how the dealumination process can be effective in opening pores and in reaching acid sites inaccessible in an ordinary mazzite.

Infrared investigation also has been carried out on mazzite samples by adsorption of probe molecules such as ammonia and pyridine in order to identify acid sites [11]. Concentration, strength and types of acid sites were determined in this investigation. Two types of OH groups were observed using IR spectroscopy namely Si-OH groups and Si-OH-Al groups. Their intensities increased passing from non dealuminated samples to dealuminated samples. The experiments with ammonia and pyridine as probe molecules have shown different results.

Ammonia has reacted with most of the sites as seen from the spectra. However, some bands suggested that some hydroxyl groups were not affected by the probe molecule as they might be not acid or not accessible.

In the case of pyridine used as probe molecule, it has been observed that for MAZ4.4 only some acid sites adsorbed it while many of them were not accessible [11]. A different situation has been observed for dealuminated mazzites, which have shown in MAZ30 for instance that most of sites reacted with pyridine (table 3.2).

Table 3.2: Concentration of Bronsted and Lewis sites determined by ammonia and pyridine adsorption (adapted and from reference [11]).

	Brœnsted sites/u.c		Lewis sites/u.c
Sample	NH_3	Py	
MAZ4.4	7.59	1.60	0.09
MAZ10	2.30	1.05	0.19
MAZ30	1.05	0.63	0.08

McQueen et al. [12] also investigated mazzite sample emphasising the influence of framework and non-framework species, the nature, strength and accessibility of acid sites on parent and dealuminated mazzite sample. Through IR investigations, they identified three families of sites: very strong Lewis sites, structural Bronsted sites and Lewis and Bronsted sites with weak and medium strength. The amount of acid sites, titrated by ammonia, has been evaluated through TPD analysis (table 3.3). It revealed that the number of strong sites remained constant in dealuminated mazzites (MAZ(2) to MAZ(5) series). On the basis of this observation, they reported that the number of strong acid sites in dealuminated mazzite were associated to framework Al and weak acid sites to non-lattice Al.

Table 3.3: Absolute and relative amounts of acid sites titrated with ammonia using temperature programmed adsorption of ammonia (adapted and from reference [12]). [a] Determined by ^{29}Si NMR and infrared spectroscopy.

	Si/Al[a]	Total		Strong	
Sample		meq/g	N/Al	meq/g	N/Al
MAZ(1)	15	0.68	0.59	0.40	0.35
MAZ(2)	20	0.71	0.29	0.20	0.08
MAZ(3)	20	0.64	0.33	0.26	0.13
MAZ(4)	22	0.47	0.53	0.32	0.36
MAZ(5)	23	0.40	0.67	0.32	0.54

IR analysis carried out the evaluation of the nature of sites on dealuminated mazzite using pyridine adsorption. This analysis highlighted the improved accessibility to acid sites after dealumination confirming the results reported in reference [11]. Furthermore, they found increased acid strength of Lewis sites due to the significant portion of pyridine that remained adsorbed on the surface after adsorption.

As seen in reference [11], mazzite has been tested as catalyst by comparing it to mordenite [12]. Mazzite, also in this case, has shown a better performance for the conversion of n-hexane and has also shown lower reaction temperatures.

Shigeishi et al. [13] have evaluated the strength of Bronsted and Lewis acid sites by microcalorimetry. They carried out this analysis with the adsorption of CO at different coverages on samples of parent (Si/Al ratio 3.2) and on dealuminated mazzite (Si/Al ratio 9 and 14). Lewis sites have been generated by outgassing the samples above 400°C. Compared to Bronsted sites, Lewis sites were lower in amount. In addition, they have shown stronger acidity, especially for framework Al species rather than non-framework Al species which contributed to weaker acidity. This aspect is in agreement with reference [12]. Furthermore, they found evidences of a synergic effect between Bronsted and Lewis sites. When Lewis sites interact with Bronsted sites a bathochromic shift is observed for OH peak positions in the IR spectra. They called this phenomenon superacidity and sites involved “superacid sites”. These sites were detected when low doses of CO adsorb on Lewis sites [13]. As the CO coverage increases and Lewis sites are filled, their interaction with Bronsted sites decreases this synergic effect between the two sites with a reversion of OH peaks bands to their initial values [13]. The catalytic performance of dealuminated mazzite was compared to that of mordenite and HZSM-5. According to the results reported, mazzite was more effective than mordenite in isomerising n-butane and more selective towards isobuthane than HZSM-5.

The superacidity of MAZ is of significant interest showing how mazzite zeolites can be effective in acid catalysed reactions.

3.7 Experimental

3.7.1 Materials

Ammonium nitrate (99+%) and caesium chloride (99+%) were purchased from Acros Organic. Sodium nitrate (98+%) and potassium nitrate (99%) were obtained from Alfa Aesar. Rubidium chloride (99%) was supplied by Sigma-Aldrich and lithium nitrate (99%) by Timstar Laboratory Suppliers. NaOH was provided by Fisher, $NaAlO_2$ (53% Al_2O_3), TMA-OH (25% solution) and LUDOX (40% SiO_2) by Sigma Aldrich. For the ion-exchange experiments, H-MAZ zeolite with Si/Al=5 was provided by Johnson Matthey. The parent zeolite K-LTL (Si/Al=3.1) was supplied by Tosoh.

3.7.2 Materials preparation

Mazzite synthesis and experimental setup

The syntheses were carried out in polypropylene bottles using two separate solutions with varied amounts of NaOH (1.25 to 4.0 g). In a typical preparation, the first solution containing NaOH (1.25 g), H_2O (14.50 g), $NaAlO_2$ (3.10 g), TMA-OH (2.80 g) it was stirred until the mixture became clear. Next, the second solution containing LUDOX (24.20 g) was added as the silica source. The resulting mixture, with the molar composition of 1 Al_2O_3 : 4.8 NaOH : 0.48 TMA-OH : 10 SiO_2 : 110 H_2O, was stirred for 30 minutes so that a homogenous gel was formed. Subsequently, the bottle was sealed and aged at room temperature for 3 days. After the aging step, the mixture was crystallised under static conditions at 100 °C for 12 days. Finally, the solid was separated, washed with distilled water (pH<10), dried overnight at 90 °C and calcined at 500^{o}C for 5 hours. The samples prepared were designated MAZ-S1, MAZ-S2, MAZ-S3 and MAZ-S4.

The ammonium forms of both MAZ-S2 (2g) was prepared via three-fold ion-exchange with 200 mL of 0.5 M NH_4NO_3. The zeolites and NH_4NO_3 solution were mixed and stirred for 90 minutes at 40 °C. The solids recovered were washed with deionised water and dried overnight at 90 °C. This sample was designated NH_4-MAZ-S2.

<u>Ion exchanged MAZ samples preparation</u>

Several series of materials were prepared using the parent H-MAZ zeolite by ion-exchange with metal alkali salt solutions. Specific preparation conditions for each sample are presented in table 3.4.

In each preparation, 1g of H-MAZ was ion-exchanged with 100 ml of an alkali metal salt solution obtaining M-H-MAZ (where M refers to Li, Na, K, Rb and Cs). The procedure was performed up to two times at increasing concentrations (0.2-0.4 M) of the ion-exchange solution. The mixtures were stirred for 90 minutes at 40°C. The recovered solids were washed with deionised water and dried overnight at 90°C.

Table 3.4: Preparation conditions for ion-exchanged samples obtained from the parent H-MAZ zeolite.

Sample name	**Preparation conditions**
Parent H-MAZ	
Li-H-MAZ	Starting material: 1g **H-MAZ** in 100 ml **$LiNO_3$** aqueous solution.
Li-H-MAZ-1	Ion exchange with 0.02 mol/L of $LiNO_3$ at 40°C for 1:30h
Li-H-MAZ-2	Two-fold ion exchange with 0.04 mol/L of $LiNO_3$ at 40°C for 1:30h
Na-H-MAZ	Starting material: 1g **H-MAZ** in 100 ml **$NaNO_3$** aqueous solution.
Na-H-MAZ-1	Ion exchange with 0.02 mol/L of $NaNO_3$ at 40°C for 1:30h
Na-H-MAZ-2	Two-fold ion exchange with 0.04 mol/L of $NaNO_3$ at 40°C for 1:30h
K-H-MAZ	Starting material: 1g **H-MAZ** in 100 ml **KNO_3** aqueous solution.
K-H-MAZ-1	Ion exchange with 0.02 mol/L of KNO_3 at 40°C for 1:30h
K-H-MAZ-2	Two-fold ion exchange with 0.04 mol/L of KNO_3 at 40°C for 1:30h
Rb-H-MAZ	Starting material: 1g **H-MAZ** in 100 ml **RbCl** aqueous solution.
Rb-H-MAZ-1	Ion exchange with 0.02 mol/L of RbCl at 40°C for 1:30h
Rb-H-MAZ-2	Two-fold ion exchange with 0.04 mol/L of RbCl at 40°C for 1:30h
Cs-H-MAZ	Starting material: 1g **H-MAZ** in 100 ml **CsCl** aqueous solution.
Cs-H-MAZ-1	Ion exchange with 0.02 mol/L of CsCl at 40°C for 1:30h
Cs-H-MAZ-2	Two-fold ion exchange with 0.04 mol/L of CsCl at 40°C for 1:30h

3.8 Material characterisation

The materials prepared by ion exchange were characterised using scanning electronic microscopy with energy-dispersive X-ray analysis (SEM-EDX), inductively coupled plasma atomic emission spectroscopy to investigate the elemental composition (ICP-OES), X-ray diffraction (XRD), nitrogen adsorption-desorption and *in situ* FTIR spectroscopy.

ICP-OES. Like for LTL samples, inductively coupled plasma atomic emission spectroscopy was employed in conjunction with SEM EDX to evaluate the content of Li in the samples for the same reasons described in the previous chapter. The preparation of the samples for the analysis required to dissolve the powder of the material in HNO_3 (>65 %). 200 mg of each Li-H-MAZ (1 – 2) were dissolved in 20ml of HNO_3. Each sample was prepared in a separated vessel and inserted in the carousel, which was then positioned in the microwave. Samples were heated according to the following program:

Time, min	**T,°C**
10	180
240	180

After the microwave step, solutions were diluted by adding 50ml of deionised water. ~10 ml of the solution were transferred from each vessel to a separated analysis tube and scanned at the ICP-OES. The list of samples included also distilled water, blank and standards prepared at the follwing concentrations: 10 and 20 ppm.

Chemical analysis. Elemental composition of zeolites was evaluated by SEM-EDX analysis using a Hitachi TM4000 plus II Tabletop electron microscope fitted with AZtec One EDS (Oxford Intruments), by X-ray fluorescence using a ThermoScientific ARL PERFORM'X with a 3.5kW Rh tube and by comparison with FTIR spectroscopy. Preparation of samples was performed by pressing few mg of powder sample (~10 – 15 mg) at the hydraulic press and depositing a fragment of it on an aluminium sample holder. The sample was then sticked on the surface of the sample holder using adhesive pads.

XRD. ~800 mg of sample was pressed in a plastic sample holder. X-ray powder diffraction patterns were recorded on a Bruker D8 Advance diffractometer, equipped with a LynxEye detector, using Cu Kα radiation at 40 kV and 40 mA at ambient temperature over the 2-theta angle range of 5-60^o ($\lambda_{K\alpha1}$=0.15406 nm and $\lambda_{K\alpha2}$=0.15444 nm; Soller slit of 2.5^o; step size of 0.02^o scan duration of 4h, no monochromator was used). The crystalline phases were matched by comparing the XRD patterns of the catalysts with those reported in the literature. In addition, Bruker Diffrac.Eva v4.0, Vesta V3.5.7 [14], [15] and Maud V2.991 (L. Lutterotti) [16], [17] software packages were utilised for the analysis of the XRD data including the Rietveld method, in order to investigate the structural features of the prepared samples. The applied approach consisted of generating calculated XRD patterns using VESTA software. Cation locations in a cif file of the parent zeolite were edited, according to the elemental analysis data. The generated patterns were used for semi-quantitative comparison with the experimental data. The Rietveld refinement in this work was carried out using MAUD software and the cif files detailing structural information of the reference materials, such as the occupancy and coordinates of the atoms, were downloaded from available databases [18], [19].

The parent zeolite used for this research was H-MAZ, hence in order to perform the analysis, the extraframework cations included in the cif file were edited, then simulated diffraction patterns were computed and compared with the experimental ones.

FTIR. Comparative characterisation of the Brønsted and Lewis acid sites (BAS and LAS) in zeolites was carried out using transmittance FTIR measurements in the 6000-900 cm^{-1} spectral range utilising pyridine adsorption (Acros Organics, 99.5%). FTIR analyses were performed at ~80 °C using self-supported disks activated in an *in situ* IR cell at 450 °C for 5 h in vacuum (10^{-5} Torr, the temperature ramp was 1 ^{o}C/min). FTIR spectra were collected using a Thermo iS10 spectrometer at a 4 cm^{-1} resolution (0.96 cm^{-1} data spacing). An excess of Py was admitted into the transmittance cell at 200 °C in a stepwise manner. The saturated sample was then evacuated for 20 min at 200 °C to remove physically adsorbed Py. The following values of the molar absorption coefficients were applied: for Brønsted acid sites, ε(BAS)=1.34 cm μmol^{-1} (IR peak at ~1545 cm^{-1}) and for Lewis acid sites ε(LAS)=1.79 cm μmol^{-1} (IR peak at ~1455 cm^{-1}) [20]. The integration limits were 1565 to 1515 cm^{-1} for the Py-B peak and 1470 to 1435 cm^{-1} for the Py-L peak (±2 cm^{-1} depending on the nature of the sample). The spectra were analysed using specialised Thermo software, Omnic 9.3. The error margin for the acid site quantification was estimated as ±5%.

NH_3-TPD. Ammonia desorption measurements were carried out using a quadrupole mass-spectrometer MKS Cirrus. The samples (~40 mg) were loaded in a reactor tube furnace and activated at 150°C. Desorption of NH_3 was performed from 150

to 750°C with a temperature ramp of 10°C/min under He atmosphere with flow of 30 ml min^{-1} for both materials.

N_2 physisorption. MAZ samples were prepared by weighing ~20 mg of the catalysts in a quartz cell. Samples were activated to remove the moisture and water according to the following program:

Target T, °C	**Rate, ,°C /min**	**Soak time, min**
30	1	30
450	1	300
100	5	500

After the activation step, the cell with the catalysts were connected to the stations in the second unit of the instrument to carry out the analysis. Analysis was performed with N_2 with a duration between 24h – 72h. The apparent surface areas of the catalysts was calculated using the BET model for the P/P_0 relative nitrogen pressure <0.15; their micropore volume and the pore size distribution were computed using the nonlinear density functional theory (NLDFT) model applied to the adsorption branch of the isotherms obtained from the nitrogen adsorption experiments carried out on a Anton Paar iQ Autosorb instrument. The total pore volume was determined at P/P_0 relative nitrogen pressure equal to 0.95.

3.9 Results and discussion (Synthesis of mazzite)

3.9.1 XRD analysis

The XRD patterns of selected mazzite samples synthesised using different amounts of NaOH are presented in Figure 3.4, and their phase composition is summarised in table 3.5. A single mazzite phase with no impurities, has been obtained for the preparations with the lower amount of NaOH in the synthesis gel, MAZ-S1 and MAZ-S2. As the amount of NaOH is increased, additional phases are detected, including sodalite, faujasite and gmelinite. For MAZ-S4, FAU is present as the dominant phase with MAZ and SOD as minor phases, which is in agreement with the literature data [7], [8], [10] Indeed, the excessive presence of sodium cations promotes the formation of hexagonal prism and sodalite cage which are the building blocks of the FAU and SOD structures. When TMA is involved in the synthesis, a double sawtooth chain can form, which consists of five side-sharing 4-MRs. Next, gmelinite cages are developed via linking of these chains. This process is promoted by the occlusion of TMA cations in the complete *t-gme* cage. The synthesised pure mazzite samples (MAZ-S1 and MAZ-S2) have a Si/Al ratio of 3.5 (table 3.6). The SEM images display elongated crystals (~5 micron in length) of MAZ-S3 with a rough surface and an anhedral form, and smaller crystals (1-2 microns) of MAZ-S2 with particles of a spherulitic morphology. From the nitrogen adsorption-desorption data for the NH_4-MAZ-S2 sample, the calculated values of the apparent BET area, 105 $m^2\ g^{-1}$, and the micropore volume, 0.02 $cm^3\ g^{-1}$, are considerably lower than those for the NH_4-K-LTL zeolite (376 $m^2\ g^{-1}$ and 0.12 $cm^3\ g^{-1}$), which is probably due to the pore blockage in the MAZ structure.

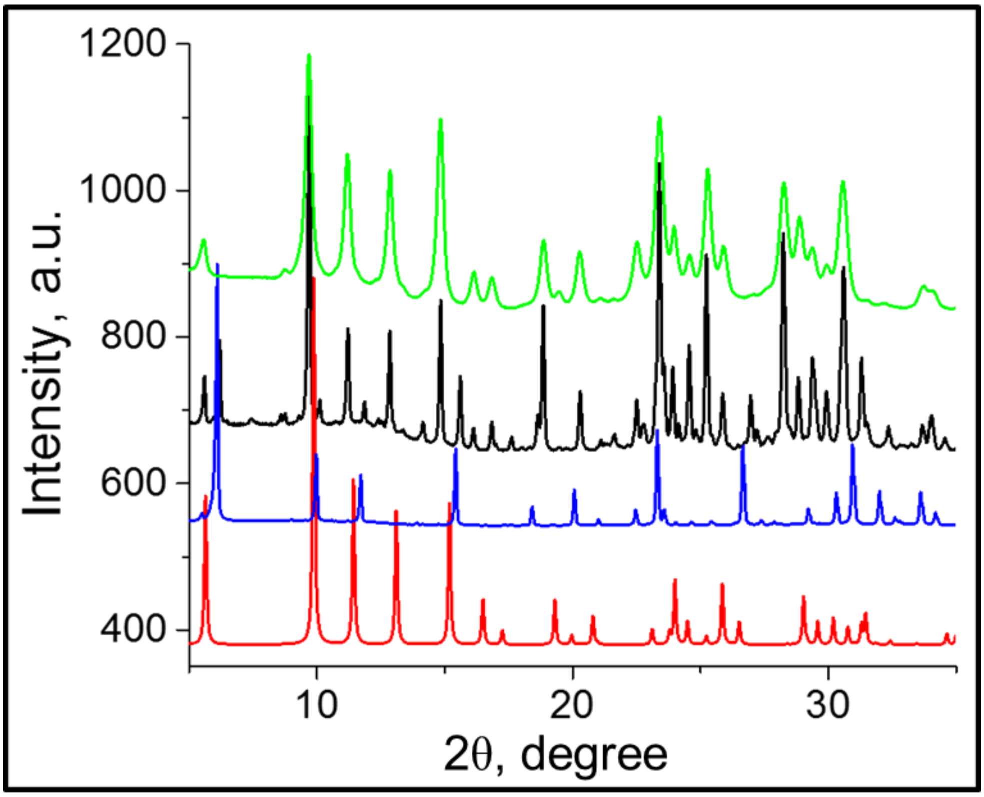

Figure 3.4: Top to bottom: experimental XRD patterns of MAZ-S2 (green) and MAZ-S3 (black), and calculated patterns of FAU (blue) and MAZ (red). Patterns are offset for clarity.

Table 3.5: XRD data for synthesized mazzite samples.

Sample	Amount of NaOH in the synthesis gel, g	Phase composition	Crystallinity, %
MAZ-S1	1.25	MAZ	83.9
MAZ-S2	2.0	MAZ	92.3
MAZ-S3	3.0	MAZ with (SOD, FAU and GME)	86.6
MAZ-S4	4.0	FAU with (MAZ and SOD)	85.8

3.9.2 SEM-EDX

The chemical composition on synthesized mazzite samples was investigated using SEM/EDX. Si/Al ratio for mazzite, as reported in literature, is 3.1. Zeolites synthesized in this work showed a Si/Al ratio of 3.3 for the first attempt and 3.5 for the remaining attempts except for the synthesis with 3 g where a ratio of 2.74 was recorded. table 3.6 shows the results of all samples.

Table 3.6: elemental composition of mazzite samples

Sample	Si	Al	Na	Si/Al
MAZ-S1	68.49	21.00	10.51	3.30
MAZ-S2	64.87	18.58	16.55	3.49
MAZ-S3	57.74	21.06	21.20	2.74
MAZ-S4	61.31	17.66	21.04	3.47

The purity of the synthesized mazzites are confirmed in the SEM pictures (figure 3.5 a-b).

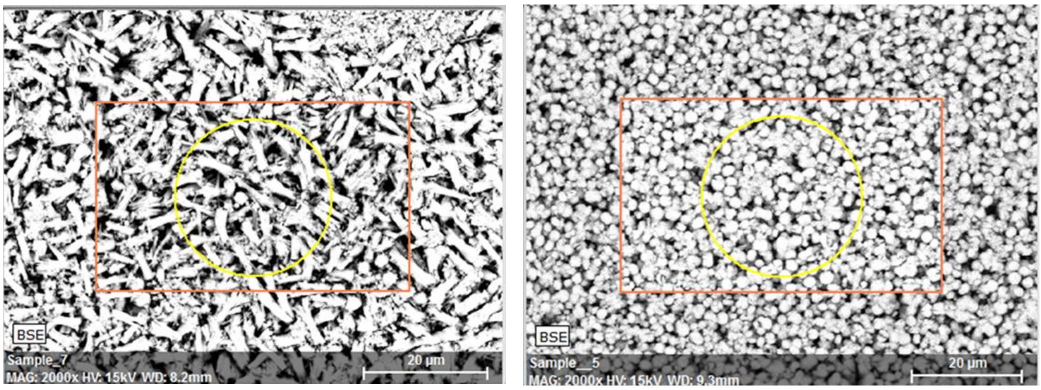

Figure 3.5: MAZ-S3 (mazzite prepared with 3g of NaOH) (left), MAZ-S2 (mazzite prepared with 2g of NaOH) (right).

Figure 3.5 (left) shows the synthesis attempt of a mazzite prepared with 3g of NaOH. Particles displayed show crystals with a rough surface and an anhedral form. Unlike this case, crystals of mazzite prepared with 2g of NaOH, exhibited particles with a spherulitic morphology but rough surfaces were found even in this case.

3.9.3 N_2 Physisorption

Nitrogen adsorption-desorption isotherms for mazzite synthesized with 2g of NaOH is presented in Figure 3.6. The calculated values of the apparent BET area and the pore volume are presented in table 3.7. The data for the MAZ sample demonstrate considerably lower values of the surface area and the micropore volume if compared to LTL results, which is most likely due to the larger particle size of mazzite and the pore blockage.

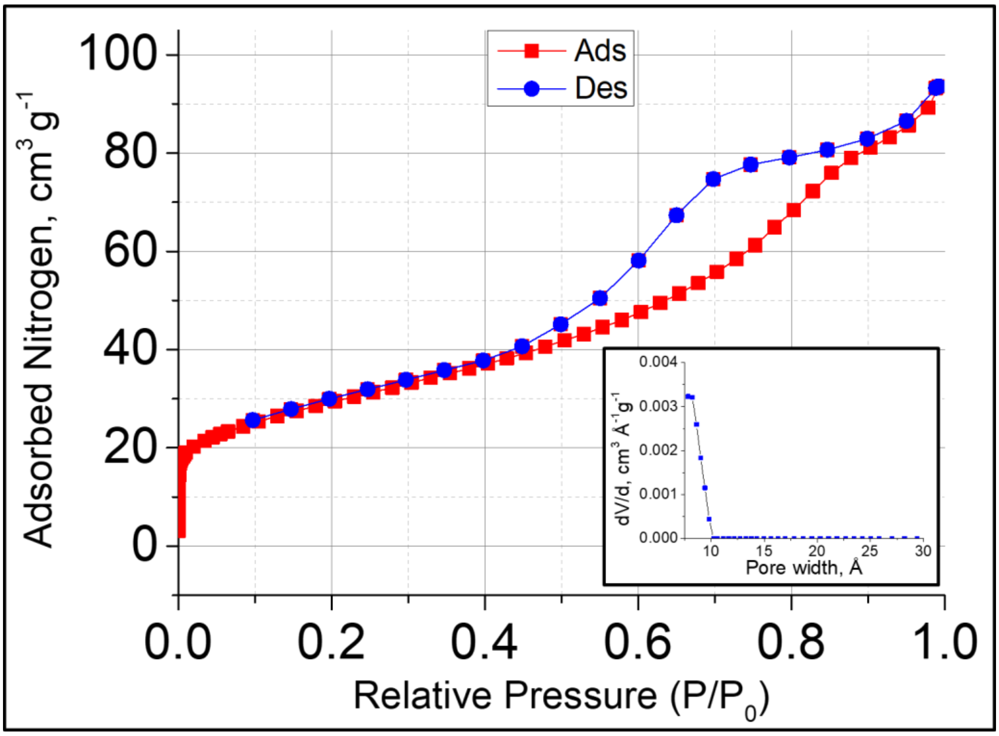

Figure 3.6: Nitrogen adsorption-desorption isotherms for synthesized MAZ-S2. The inserts show the pore size distributions for these materials.

Table 3.7: Surface area and micropore volume of synthesized mazzite.

Sample	S, m^2 g^{-1}	V$_{micro}$^{c}, cm^3 g^{-1}
Mazzite (2g)	105	0.02

3.9.4 FTIR

Acidic properties of the synthesised mazzite have been investigated using pyridine as a probe molecule (Figure 3.7). The difference spectrum (blue) following Py adsorption for mazzite shows one negative peaks, attributed to the bridging OH-groups at 3610 cm^{-1} interacting with Py has been detected for NH_4-MAZ-S2. However, infrared data indicate that no more than 3% of acid sites in this sample are accessible to Py, unlike for NH_4-K-LTL, which can be explained by the pore blockage in the MAZ structure.

Therefore, a commercial sample of mazzite (H-MAZ) was utilised for further evaluation of its acid sites.

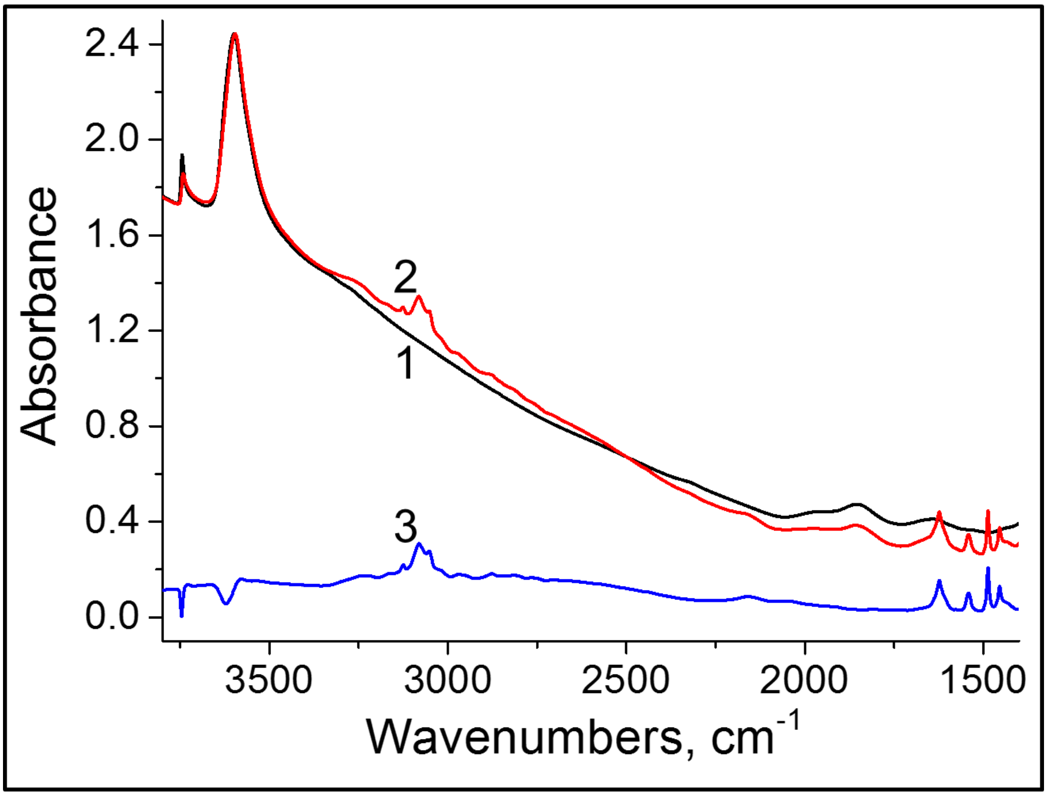

Figure 3.7: NH_4-MAZ-S2 - (1) - material before Py adsorption at 200 °C, (2) - material after Py adsorption and (3) - the difference spectrum.

3.10 Results and discussion (Ion exchange of a commercial mazzite)

3.10.1 SEM-EDX

SEM-EDX analysis was employed to investigate the elemental analysis of ion exchanged MAZ samples. The chemical composition and the textural data of the observed samples is shown in figure 3.8 and in table 3.9. The Si/Al ratio for the parent zeolite H-MAZ is 4.58. For the ion exchanged samples is around 5 for Li-H-MAZ but 5.24 according to XRF data. Si/Al ratio is ~5.5 for Na-H-MAZ and it decreases up to ~5 with Cs in Cs-H-MAZ-2. The elemental analysis (figure 3.8) results suggest that MAZ shows a similar trend seen in LTL and FAU [21], as the number of introduced cations per unit cell increases from ~0.2 for Li to ~1.9 for Cs (a relatively low value for Rb could be associated with the overlap of the Si and Rb signals in SEMEDX and XRF analysis). A slightly lower crystallinity for Cs-H-MAZ-2 sample as compared to the parent material may indicate partial structural damage during the ion-exchange.

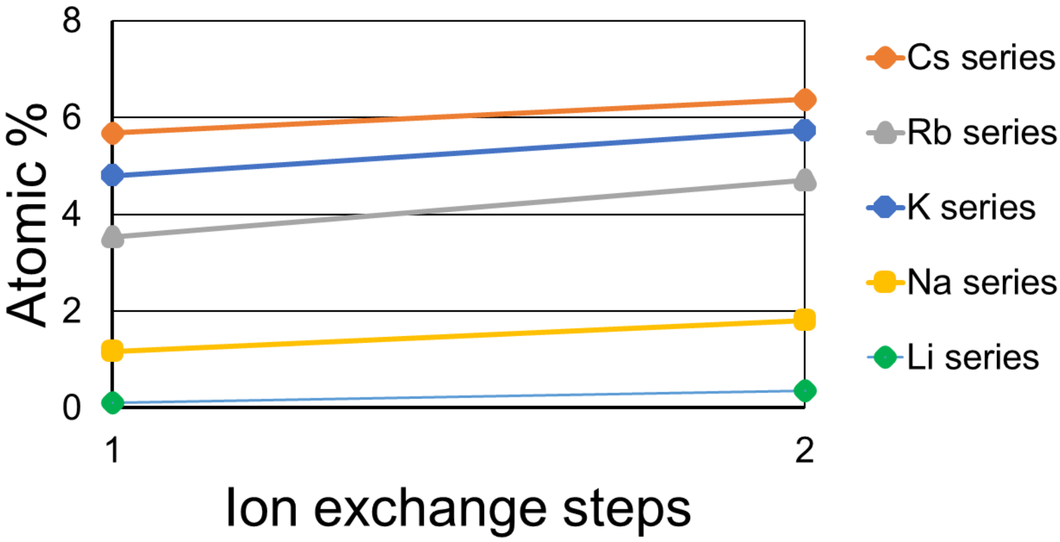

Figure 3.8: Atomic percentage of ion-exchanged cations in MAZ samples as a function of ion exchange steps.

Table 3.8: Chemical composition and textural data for the ion-exchanged MAZ samples.

Sample	Composition [a]	Crystallinity [b], %	S, $m^2\ g^{-1}$	V_{micro} [c], $cm^3\ g^{-1}$	S^d, $m^2\ cm^{-3}$	S^e, $m^2\ mmol^{-1}$
H-MAZ	$H_{6.0}Al_{6.0}\ Si_{30.0}O_{72.0}$	82	372	0.10		
Li-H-MAZ-2	$Li_{0.2}H_{5.8}Al_{6.0}Si_{30.0}O_{72.0}$	82	369	0.10	760	135
Na-H-MAZ-2	$Na_{0.6}H_{4.4}Al_{6.0}Si_{30.0}O_{72}$	82	344	0.09	716	131
K-H-MAZ-2	$K_{1.7}H_{4.3}Al_{6.0}Si_{30.0}O_{72}$	81	254	0.05	572	101
Rb-H-MAZ-2	$Rb_{1.5}H_{4.5}Al_{6.0}Si_{30.0}O_{72}$	82	205	0.05	582	91
Cs-H-MAZ-2	$Cs_{1.9}H_{4.1}Al_{6.0}Si_{30.0}O_{72.0}$	78	189	0.04	592	93

Notes: (a) estimated experimental error is ~0.2 atoms per u.c.; (b) estimated by the Diffrac.Eva software; (c) estimated error is 0.01 $cm^3\ g^{-1}$; (d,e) corrected surface area taking into account the density change due to ion exchange.

Table 3.9: Elemental analysis at% results for the ion-exchanged MAZ.

Sample	%Si	%Al	%Li	%Na	%K	%Rb	%Cs	Si/Al
H-MAZ	82.08	17.92						4.58
Li-H-MAZ-1	83.17	16.73	0.10					4.97
Li-H-MAZ-2	82.93	16.71	0.36					4.96
Na-H-MAZ-1	83.28	15.1		1.17	0.45			5.52
Na-H-MAZ-2	82.3	15.05		1.81	0.84			5.47
K-H-MAZ-1	80.58	14.63			4.8			5.51
K-H-MAZ-2	79.68	14.59			5.73			5.46
Rb-H-MAZ-1	81.55	14.93				3.53		5.46
Rb-H-MAZ-2	80.31	14.98				4.71		5.36
Cs-H-MAZ-1	78.75	15.58					5.68	5.05
Cs-H-MAZ-2	78.02	15.61					6.37	4.99

Results of H-MAZ ion exchanged with $LiNO_3$ were obtained from ICP-OES analysis since Li^+ is not detectable at the SEM-EDX for the same reasons explained in chapter 2. A lower crystallinity (table 3.8) for MAZ samples compared to LTL samples may suggest partial structural damage during the ion exchange, which increases from Li to Cs.

3.10.2 N_2 Physisorption

Nitrogen adsorption-desorption analysis was performed to evaluate surface area and pore volume of parent MAZ and ion exchanged samples. Isotherms are presented in figure 3.9a – b and in figure 3A.1 and 3A.2 in chapter 6 – appendix. Calculated values of BET and pore volume are in table 3.8 and in figure 3.10a - c. Like for LTL, MAZ shows a decreasing trend for surface area and pore volume. Apparent surface area from Li to Na decreases of ~7%, between Na and K ~26% and ~20% from K to Rb and to Cs. Pore volume decreases of ~4.5% from Li to Na and from Na to K ~13%, from K to Rb ~20% and ~2% from Rb to Cs. Interestingly, the micropore volume is decreasing significantly from 0.1 $cm^3\ g^{-1}$ for Li-H-MAZ to 0.04 $cm^3\ g^{-1}$ for the Cs-form of mazzite. This cannot be accounted for solely based on the size of Cs cations, as even following a complete ion-exchange they would occupy ~0.03 $cm^3\ g^{-1}$. Most likely, Cs cations create additional restrictions for the adsorption of nitrogen in the already partially blocked pore system of the MAZ structure. Table 3.10 summarises the calculated occupied volumes for these samples, which are lower than the results obtained for LTL: this aspect can be explained by a more limited pore accessibility of MAZ.

Table 3.10: Occupied volume and number of cations in the MAZ samples.

Cation	RMM, g per mol	Radius, cm	Volume, cm^3	wt.%	Number of mol per 1g	Number of atoms per 1g	Vocc, $cm^3\ g^{-1}$
Li	6.9675	6.00E-09	9.04E-25	**1.91**	0.00274	1.647E+21	**0.0015**
Na	22.9897	9.50E-09	3.59E-24	**6.01**	0.00262	1.574E+21	**0.0057**
K	39.0983	1.33E-08	9.85E-24	**9.81**	0.00251	1.511E+21	**0.0149**
Rb	85.4678	1.48E-08	1.36E-23	**19.21**	0.00225	1.353E+21	**0.0184**
Cs	132.9054	1.69E-08	2.02E-23	**27.00**	0.00203	1.223E+21	**0.0247**

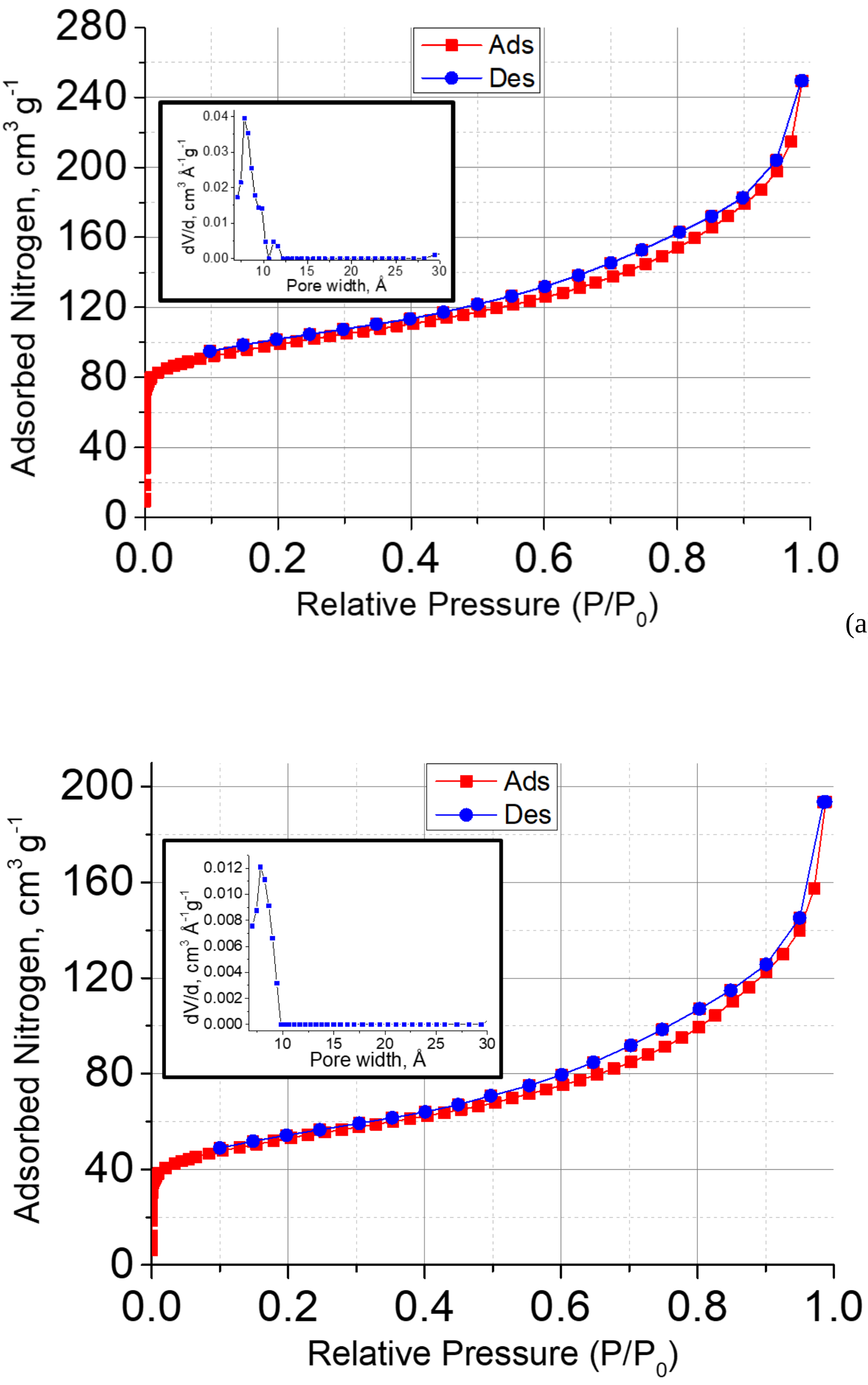

(a)

(b)

Figure 3.9: Nitrogen adsorption-desorption isotherms for for Li-H-MAZ (a) Cs-H-MAZ (b).

The inserts show the pore size distributions for these materials.

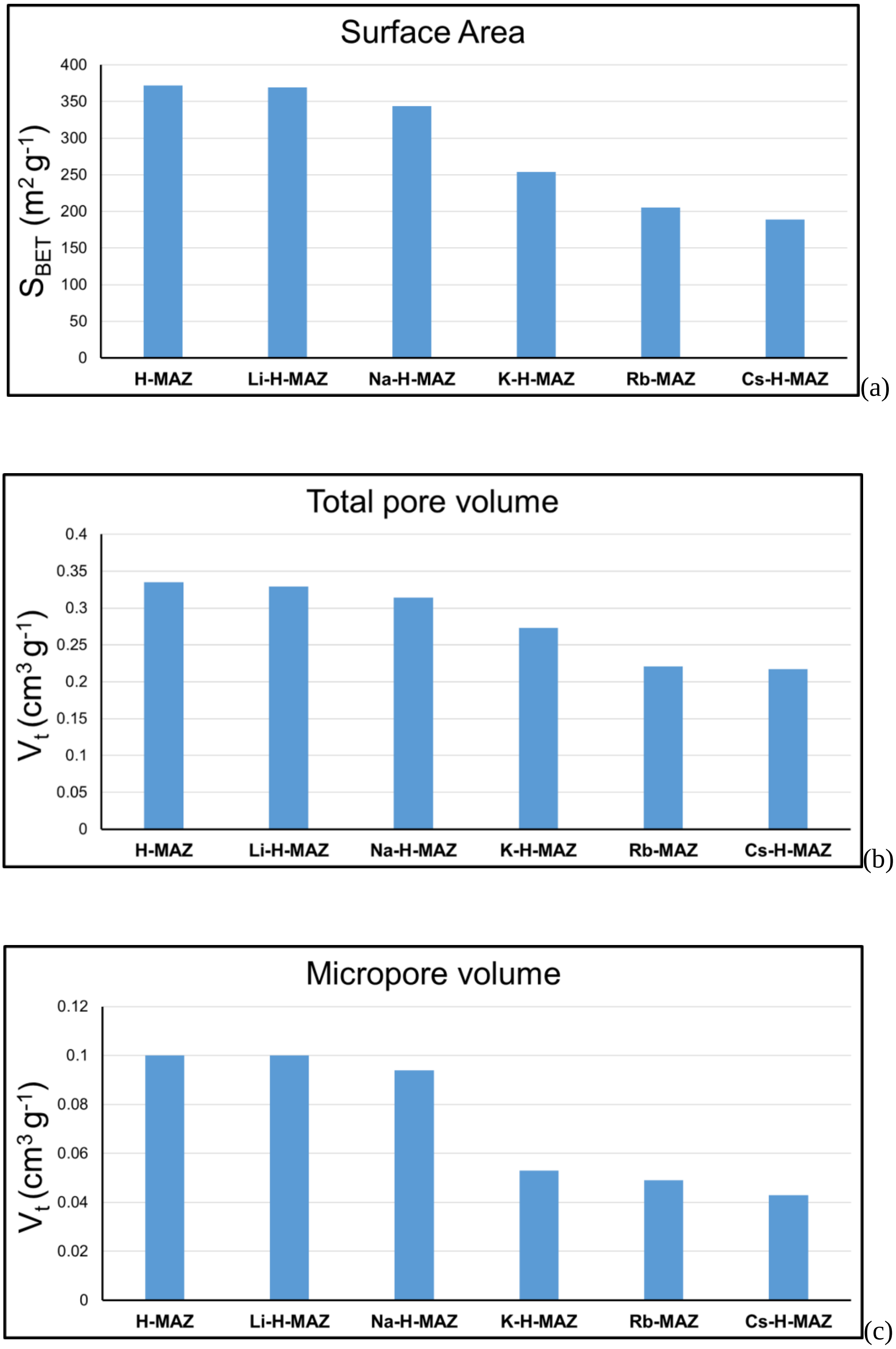

Figure 3.10: (a) Surface area, (b) total pore volume and (c) micropore volume of the ion-exchanged MAZ samples.

3.10.3 XRD analysis

Parent MAZ and ion exchanged MAZ samples were investigated by XRD analysis to observe the structural aspects. Experimental patterns are shown in figure 3.11. No other crystalline phases are present and in terms of peaks position. Ion exchanged samples show a similar the pattern seen in the parent H-MAZ except for peaks at 16.9 and 19 degrees in 2theta, which decrease their intensities from Li until Cs where they almost disappear. As long as the ion exchange continues, patterns collected showed a general decrease in terms of peak intensities. Unlike LTL samples, for MAZ no impurities were found at low angles. The trend of a gradual decrease of crystallinity can be noted from the parent MAZ to the Cs- ion exchanged sample (table 3.8). Differences among experimental patterns were observed through the Rietveld method to investigate the structural changes as result of the ion exchange steps. Experimental and calculated pattern, produced by software packages MAUD, showed in figure 3.12a-b and 3A.3 (a – b) and 3A.4 (a – b) in chapter 6 - appendix. Rietveld results showed a good agreement between experimental and calculated patterns. The samples recorded similar lattice parameters from H-MAZ to K-H-MAZ a clear trend with a slight increase from K-H-MAZ to Cs-H-MAZ.

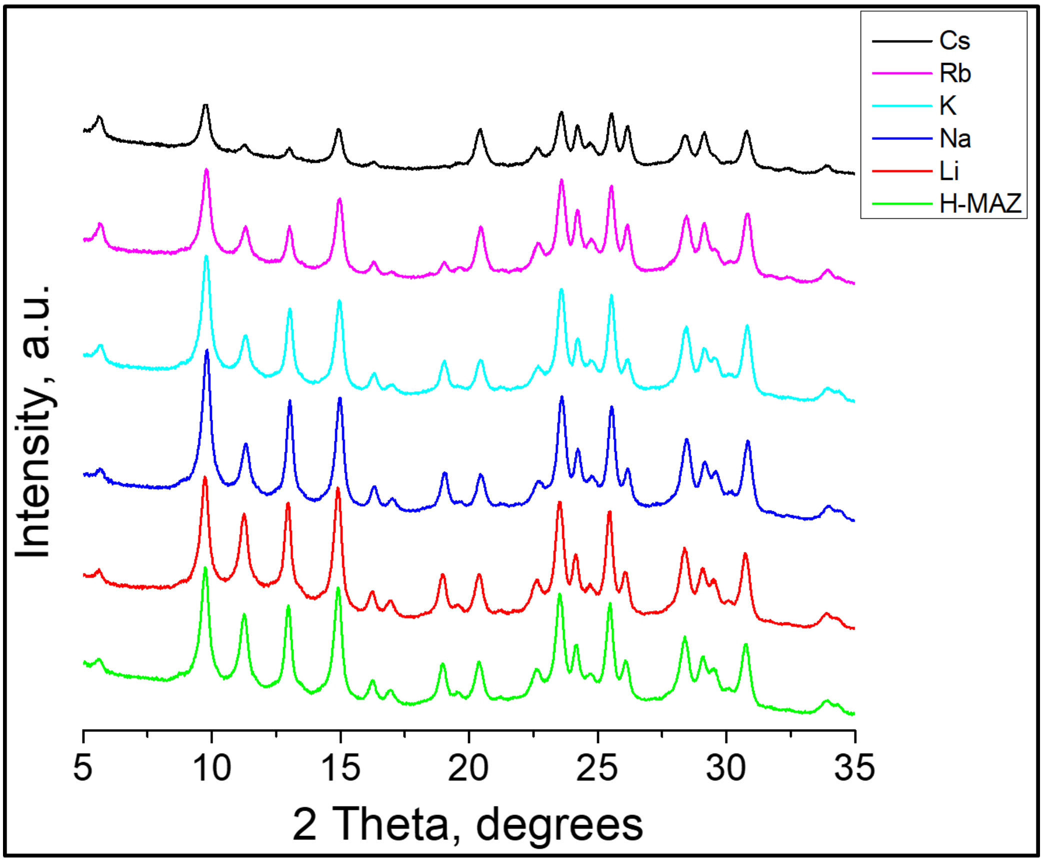

Figure 3.11: Experimental XRD patterns of the parent and the ion-exchanged MAZ samples.

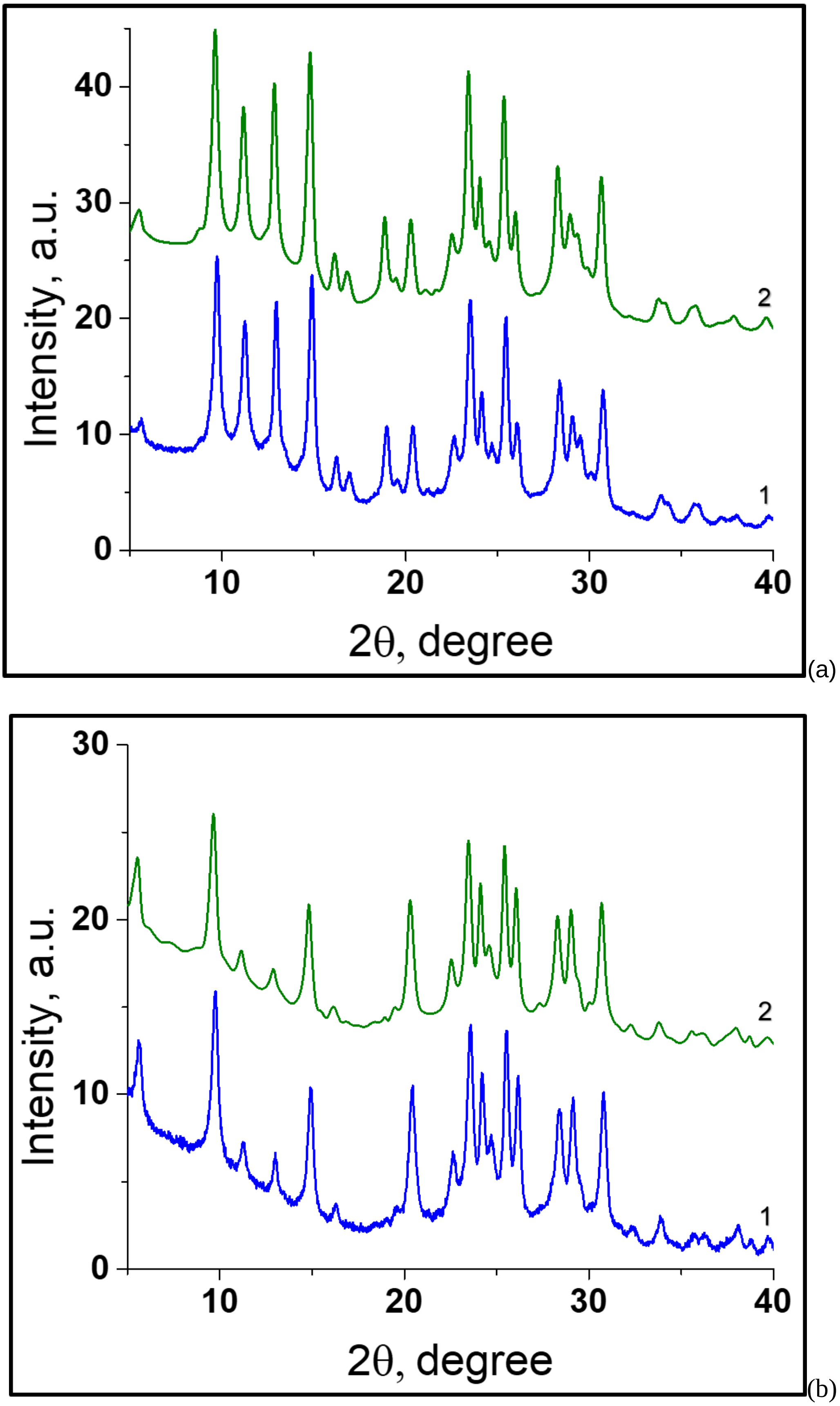

Figure 3.12: Experimental (1) and simulated (2) XRD patterns of Li-H-MAZ (a) and Cs-H-MAZ (b).

MAZ is characterised by a structure consisting of 12MR cages, the so-called *t-maz* (figure 3.13a), which are connected to 6 *t-kaj* (figure 3.13b) cages through 5MR, and which share 8MR with gmelinite cages, *t-gme* (figure 3.13c). Based on the modelling, it can be concluded that cations are located in the 12 MR of the *t-maz* cage, up to 2 cations per unit cell for K, Rb and Cs (table 3.11 and table 3.12). Considering its small size, hydrated alkali metal cations cannot reach the *t-kaj* cage through the 5MR, hence, this window prevents the migration of hydrated cations towards the gmelinite cage. Access to the mazzite pore system via the 0.31x0.31 nm 8MR channels for the hydrated alkali metal cations is also unlikely. Although some Cs^+, Rb^+ and K^+ might be able to enter the *t-kaj* cages if sufficient defects are present in the material providing a possible pathway into the smaller cages of the mazzite structure. These results are in agreement with the data reported in ref. [22], [23], indicating that only following activation at 450^{o}C of the Cu-exchanged zeolite omega (Cu-MAZ), Cu ions are found in the 8MR rings of the gmelinite cages. It should be noted that the calculated lattice parameters show a slight increase for the studied zeolites, from the K- to Cs-form (table 3.11).

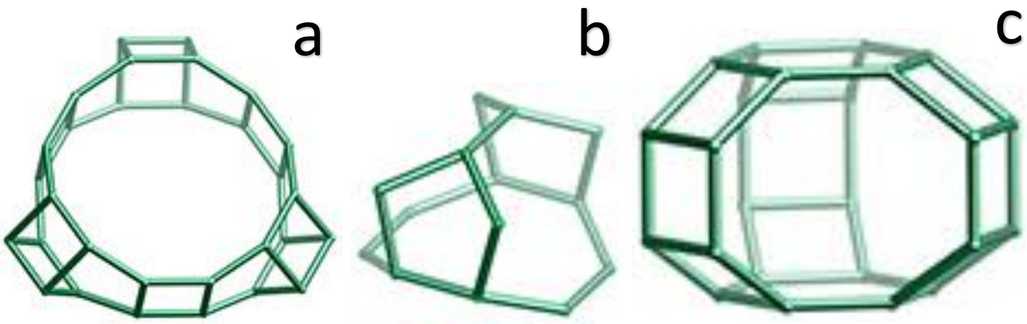

Figure 3.13: Cages that compose MAZ structure: (a) *t-maz* cage, (b) *t-kaj* cage and (c) *t-gme* or gmelinite cage.

Table 3.11: Table of occupancies and lattice parameters of parent MAZ and ion exchanges samples.

			***t-kaj* cage**		***t-gme* cage**		**Main channel 12MR**	
	a=b, Å	**c, Å**	**Total occupancy per u.c.**	**Site occupancy M1 6**	**Total occupancy per u.c.**	**Site occupancy M2 2**	**Total occupancy per u.c.**	**Site occupancy M3 4**
H-MAZ	**18.19**	**7.59**	**5.874**	**0.979**	**0.790**	**0.395**	**3.988**	**0.997**
Li-H-MAZ-1	**18.18**	**7.59**	**5.844**	**0.974**	**0.800**	**0.400**	**4.000**	**1.000**
Li-H-MAZ-2	**18.19**	**7.60**	**5.898**	**0.983**	**0.630**	**0.315**	**4.000**	**1.000**
Na-H-MAZ-1	**18.18**	**7.59**	**5.850**	**0.975**	**0.514**	**0.257**	**4.000**	**1.000**
Na-H-MAZ-2	**18.19**	**7.59**	**5.886**	**0.981**	**0.348**	**0.174**	**4.000**	**1.000**
K-H-MAZ-1	**18.18**	**7.59**	**5.370**	**0.322**	**0.161**	**0.320**	**4.000**	**1.000**
K-H-MAZ-2	**18.19**	**7.59**	**5.444**	**0.907**	**0.336**	**0.168**	**4.000**	**1.000**
Rb-H-MAZ-1	**18.20**	**7.60**	**5.490**	**0.915**	**1.892**	**0.946**	**4.000**	**1.000**
Rb-H-MAZ-2	**18.21**	**7.59**	**5.554**	**0.926**	**1.989**	**0.995**	**4.000**	**1.000**
Cs-H-MAZ-1	**18.22**	**7.58**	**1.200**	**0.200**	**1.017**	**0.509**	**4.000**	**1.000**
Cs-H-MAZ-2	**18.22**	**7.58**	**1.598**	**0.266**	**1.145**	**0.572**	**4.000**	**1.000**

Table 3.12: Table of specific occupancies for each extra framework cation.

	***t-kaj* cage**	***t-gme* cage**	**Main channel 12MR**
	M1	**M2**	**M3**
H-MAZ	**5.87 H**	**0.79 H**	**3.98 H**
Li-H-MAZ-1	**5.84 H**	**0.80 H**	**0.00003 Li + 3.96 H**
Li-H-MAZ-2	**5.89 H**	**0.63 H**	**0.001 Li + 3.96 H**
Na-H-MAZ-1	**5.85 H**	**0.51 H**	**0.01 Na + 3.96 H**
Na-H-MAZ-2	**5.89 H**	**0.38 H**	**0.20 Na + 3.80 H**
K-H-MAZ-1	**5.37 H**	**0.32 H**	**1.60 K + 2.36 H**
K-H-MAZ-2	**5.44 H**	**0.34 H**	**1.68 K + 2.32 H**
Rb-H-MAZ-1	**5.49 H**	**1.89 H**	**1.16 Rb + 2.80 H**
Rb-H-MAZ-2	**5.55 H**	**1.98 H**	**1.34 Rb + 2.66 H**
Cs-H-MAZ-1	**1.20 H**	**1.02 H**	**1.84 Cs + 2.12 H**
Cs-H-MAZ-2	**1.59 H**	**1.15 H**	**1.96 Cs + 2.04 H**

3.10.4 FTIR

The acidic properties of H-MAZ and the ion-exchanged zeolites have been evaluated using FTIR spectroscopy with pyridine as a probe molecule. FTIR spectra are shown in figure 3.14, figure 3.15, figure 3.16 and in figure 3A.5 and 3A.6 in chapter 6 - appendix. The spectra of the analysed materials show two major OH bands, one typical of the silanol groups at 3745 cm^{-1}, and the other attributed to the bridging Si(OH)Al groups at 3600 cm^{-1} for H-MAZ, 3610 cm^{-1} for Na-H-MAZ and 3620 cm^{-1} for Cs-H-MAZ. The shift in the band position can be explained by the heterogeneity of the bridging hydroxyls or by the effect of the alkali metal cations on the vibrational frequency of the OH-groups. Following the Py adsorption for parent and ion-exchanged zeolites, a negative peak at 3605 cm^{-1} is observed in the difference spectra, which corresponds to the acidic OH-groups interacting with Py. Using the intensity of this peak, relative accessibility of the bridging OH-groups has been calculated, which varies from 16% for the parent H-MAZ to 26-28% for K- and Rb-exchanged samples. In the Py region of the spectra, two peaks at 1545 and 1455 cm^{-1} have been utilised to monitor the concentration of accessible Brønsted and Lewis acid sites in the ion-exchanged MAZ zeolites in table 3.13 and figure 3.17.

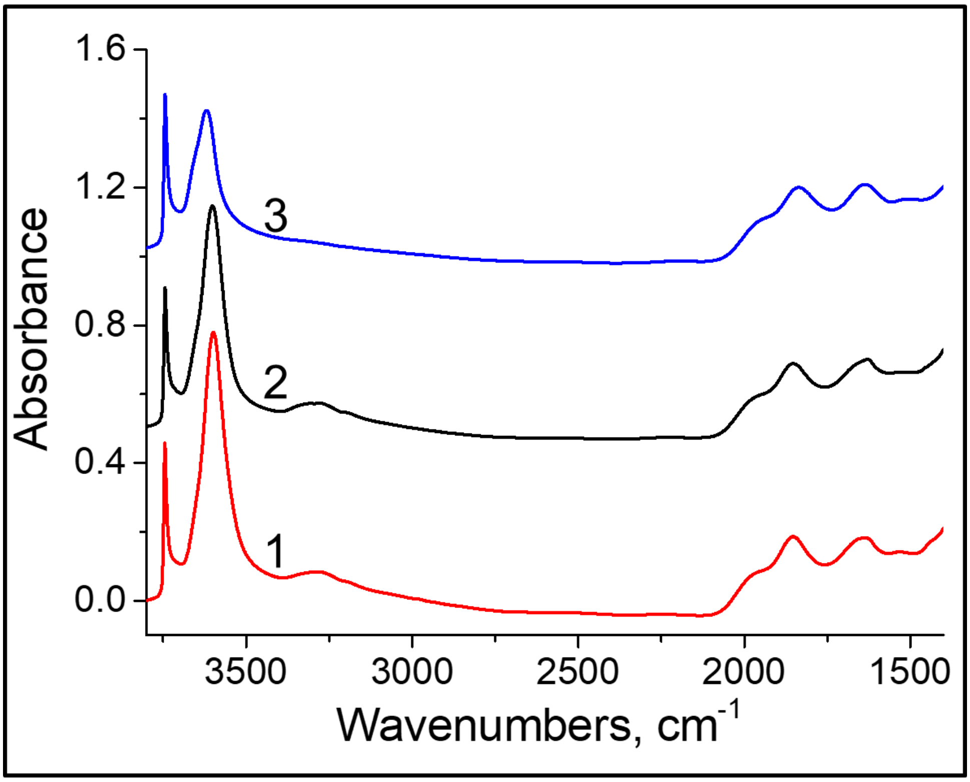

Figure 3.14: The OH region of the FTIR spectra for (1) H-MAZ, (2) Li-H-MAZ and (3) Cs-H-MAZ. Spectra are offset for clarity.

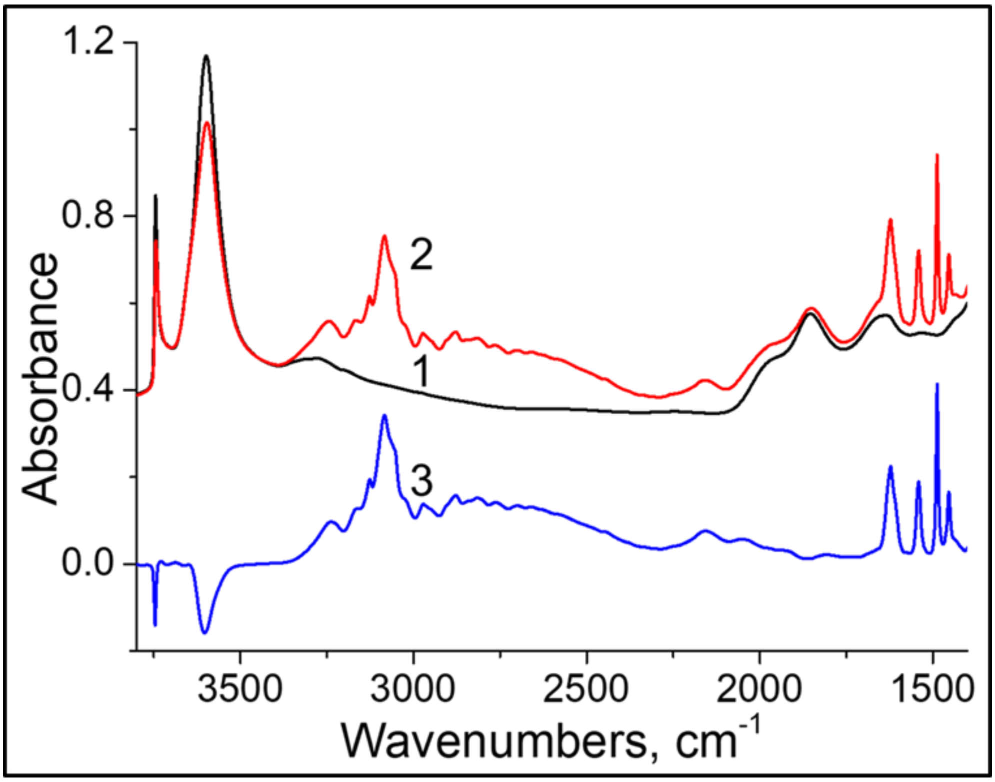

Figure 3.15: FTIR spectra of H-MAZ. (1) - the material before Py adsorption, (2) - the material after Py adsorption at 200°C and (3) - the difference spectrum.

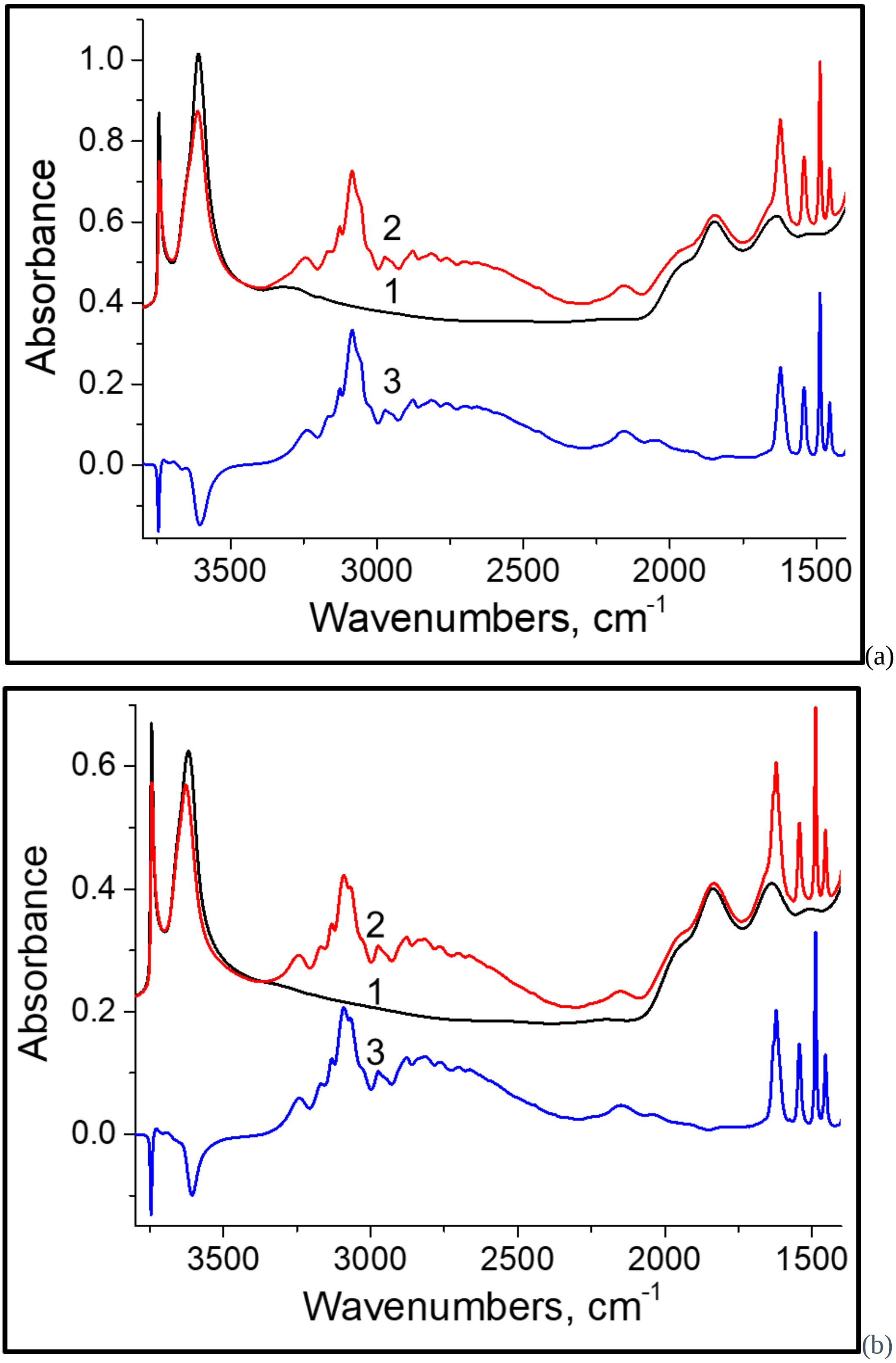

Figure 3.16: FTIR spectra of (a) Na-H-MAZ and (b) Cs-H-MAZ. (1) - the material before Py adsorption, (2) - the material after Py adsorption at 200°C and (3) - the difference spectrum.

Table 3.13: FTIR data for the ion-exchanged MAZ samples.

Sample	Concentration of BAS, μmol g^{-1}	Accessibility of BAS, %	Concentration of LAS, μmol g^{-1}
H-MAZ	220	16	88
Li-H-MAZ-2	192	18	75
Na-H-MAZ-2	188	24	78
K-H-MAZ-2	186	28	74
Rb-H-MAZ-2	148	26	68
Cs-H-MAZ-2	141	25	65
NH_4-K-LTL	486	100	204

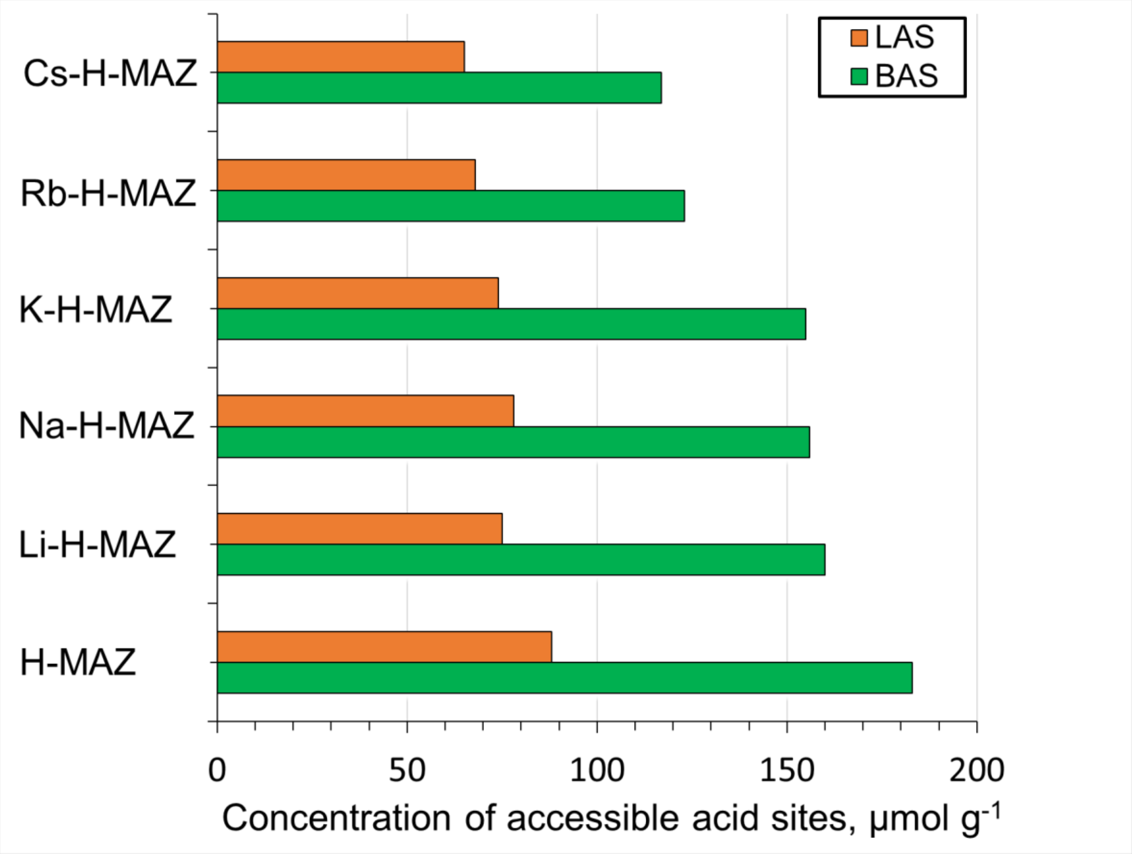

Figure 3.17: Concentration of Brønsted and Lewis acid sites in the ion-exchanged MAZ samples.

The trend visible in figure 3.17 suggests that the ion exchange affected mainly the nature of Brønsted acid sites. BAS decrease slowly compared to the behaviour seen for LTL but their concentration decreases gradually as they are increasingly neutralised by larger alkali metal cations. For the parent MAZ and ion exchanged samples, Lewis acid sites concentration is also decreasing during ion-exchange, probably due to the removal of some extra-framework Al species. Considering the structural similarity, elemental composition and the secondary building units present in MAZ and LTL, one could expect comparable acidic properties for these two zeolites. However, significant differences are observed: (i) in addition to the acidic hydroxyls in the 12MR channels, there is a large number of H-bound Si(OH)Al groups in LTL probably located in the 4- and 5MR, whereas bridging OH-groups in MAZ are probably sited only in 12- and 8MR; (ii) FTIR characterisation indicates that only around 20% of Brønsted acid sites in MAZ are accessible to Py. These differences can be associated with a preferential distribution of Al in LTL structure and considerable pore blockage in the MAZ zeolite.

3.10.5 NH_3-TPD

NH_3-TPD data comparing the strength of acid sites in NH_4-MAZ-S2 and NH_4-K-LTL already presented in chapter 2 in figure 2.26 demonstrate that the effective strength of acid sites in MAZ is greater than that for the LTL zeolite as the ammonia desorption peak is shifted for the mazzite sample to a higher temperature by ~75°C. The asymmetrical shape of the TPD peaks for both zeolites may be indicative of the heterogeneity of their acid sites. At the same time, both effects could be linked to the transport limitations during ammonia desorption from MAZ due to the micropore blockage in this material. The data presented make it evident that the channel structure of mazzite is severely disrupted, therefore, access to its active sites in the micropores is restricted, a limitation that can be overcome by generating secondary mesoporosity by a post-synthesis treatment (dealumination, desilication, etc.) or by nanostructured synthesis, as has been previously suggested for a number of zeolites, such as FAU, BEA, LTL, MFI and MOR [24]–[26].

3.11 Conclusions

The effect of ion exchange with alkali metals on MAZ in comparison with LTL was investigated. The elemental analysis revealed that larger cations have easier access to MAZ structure with ion exchange percentages that reached 40% for Cs followed by 39% for K and 31% for Rb. Lower quantities were found for Na and Li, respectively 12% and 1.2%. The ion exchange effect was also studied through FTIR which confirmed the presence of one narrow band related to the isolated SiOHAl groups in the main channels (12MR) at ~3640 cm^{-1}. BAS detection by pyridine confirmed a decreasing trend in terms of concentrations of these acid sites from Li to Cs. In general, the concentration range found for MAZ is narrower in comparison with the correspondent ion exchanged LTL. In addition, ion exchanged mazzite samples showed a decreased concentration of BAS such as 50% lower for Cs and 34% for Li suggesting a lower acidic nature of MAZ. However, N_2 adsorption desorption data revealed that the high transport limitations may be due to the low micropore volume of MAZ samples. This aspect may also suggest a limited accessibility of pyridine to the acid sites during FTIR analysis. NH_3-TPD for NH_4-K-LTL compared with NH_4-MAZ confirmed this limited accessibility due to pore blockage and the higher strength of MAZ acid sites. A cation migration mechanism was provided also for MAZ. Through X-Ray powder diffraction and Rietveld refinement was shown that all cations migrate through the main channel *t-maz* cage. However only large cations are able to access to the cage *t-kaj*. This cage represents the bottleneck in the cation migration path of cations because of the restricted window size of the 5MR that connects this cage to the *t-maz*. According to the Rietveld results only high ion exchanged MAZ with K, Rb and Cs were able to reach *t-kaj* cage in minor quantities. Gmelinite cage resulted to be inaccessible to all the extraframework cations.

3.12 References

[1] E. Flanigen, E. R. Kellberg, Synthetic crystalline zeolite and process for preparing same, US Patent No. 4241036 (1980).

[2] J. Ciric, Converting hydrocarbons with zeolite ZSM-4, US Patent No. 3923639 (1975).

[3] E. Galli, Mazzite, a zeolite, Crystal Structure Communications, Vol. 3, No. 2, p. 339-344, 1974.

[4] E. Galli, E. Passaglia, D. Pongiluppi, R. Rinaldi, Mazzite, a new mineral, the natural counterpart of the synthetic zeolite Ω, Contributions to Mineralogy and Petrology, 45 (1974) 99-105.

[5] R. Rinaldi, J. J. Pluth, J. V. Smith, Crystal structure of mazzite dehydrated at 600°C, Acta Crystallographica, Section B, 31 (1975) 1603-1608.

[6] L.B. McCusker, D.H. Olson, C. Baerlocher, Atlas of Zeolite Framework Types, Elsevier (2007).

[7] S. Ernst, J. Weitkamp, Synthesis of large pore aluminosilicates, Catalysis Today, 19 (1994) 27–60.

[8] M. Gackowski, Ł. Kuterasiński, J. Podobiński, A. Korzeniowska, B. Sulikowski, J. Datka, Hierarchical zeolite mazzite: Physicochemical properties and α-pinene isomerization, Applied Catalysis A: General, 578 (2019) 53-62.

[9] A. Goossens, E. Feijen, G. Verhoeven, B. Wouters, P. Grobet, & J. Pierre, J. Martens, Crystallization of MAZ-type zeolites using tetramethylammonium, sodium and n-hexane derivatives as structure- and composition-directing

agents, Microporous and Mesoporous Materials, 35(6) (2000) 555-572.

[10] D.E.W. Vaughan, in: G. Ohlmann, H. Pfeifer, R. Fricke (Eds.), Catalysis and Adsorption by Zeolites, Studies in Surface Science and Catalysis, Elsevier, 65 (1991) 275.

[11] M. Guisnet, P. Ayrault, C. Coutanceau, M. Alvarez, J. Datka, Acid properties of dealuminated beta zeolites studied by IR spectroscopy, Journal of The Chemical Society, Faraday Transactions, 93 (1997) 1661-1665.

[12] D. McQueen, B. Chiche, F. Fajula, A. Auroux, C. Guimon, F. Fitoussi, P. Schulz, A Multitechnique Characterization of the Acidity of Dealuminated Mazzite, Journal of Catalysis, 161 (1996) 587-596.

[13] R. Shigeishi, B. Chiche, F. Fajula, CO adsorption on superacid sites on dealuminated mazzite, Microporous and Mesoporous Materials, 43 (2001) 211-226.

[14] K. Momma, F. Izumi: VESTA: a three-dimensional visualization system for electronic and structural analysis, J. Appl. Crystallogr., 41 (2008) 653-658.

[15] K. Momma, F. Izumi: VESTA 3 for three-dimensional visualization of crystal, volumetric and morphology data, J. Appl. Crystallogr., 44 (2011) 1272-1276.

[16] L. Lutterotti, S. Matthies, H. R. Wenk, MAUD (Material Analysis Using Diffraction): a user friendly java program for Rietveld texture analysis and more. Proceeding of the Twelfth International Conference on Textures of Materials (ICOTOM-12) , (1999) 1599-1604.

[17] L. Lutterotti, Maud: A Rietveld Analysis Program Designed for the Internet

and Experiment Integration. Acta Crystallographica Section A - ACTA CRYSTALLOGR A. 56 (2000).

[18] Database of zeolite structures: http://www.iza-structure.org/databases, as of May 2023.

[19] The International Centre for Diffraction Data - ICDD, https://www.icdd.com/.

[20] V. Zholobenko, C. Freitas, M. Jendrlin, A. Travert, P. Bazin, F. Thibault-Starzyk. Probing the acid sites of zeolites with pyridine: Quantitative AGIR measurements of the molar absorption coefficients. J. Catalysis, 385 (2020) 52-60.

[21] H.S. Sherry, The Ion-Exchange Properties of Zeolites. I. Univalent Ion Exchange in Synthetic Faujasite, Journal of Physical Chemistry, 70 (1966) 1158–1168.

[22] J. Wieser, A.J. Knorpp, D.C. Stoian, P. Rzepka, M.A. Newton, JA. van Bokhoven. Assessing the Productivity of the Direct Conversion of Methane-to-Methanol over Copper-Exchanged Zeolite Omega (MAZ) via Oxygen Looping. Angewandte Chemie International Edition, 62 (2023).

[23] A. J. Knorpp, A. B. Pinar, C. Baerlocher, L. B. Mccusker, N. Casati, M. A. Newton, S. Checchia, J. Meyet, D. Palagin, J. A. Van Bokhoven, Paired Copper Monomers in Zeolite Omega: The Active Site for Methane-to-Methanol Conversion, Angewandte Chemie International Edition, 60 (2021) 5854–5858.

[24] S. Mintova, N. Barrier, Verified synthesis of zeolitic materials Third revised

edition, IZA Synthesis Commission, (2016) 215-221.

[25] A. Al-Ani, C. Freitas, V. Zholobenko, Nanostructured large-pore zeolite: The enhanced accessibility of active sites and its effect on the catalytic performance, Microporous Mesoporous Materials, 293, (2020).

[26] T. Prasomsri, W. Jiao, S. Weng, J. García-Martínez, Mesostructured Zeolites: Bridging the Gap Between Zeolites and MCM-41, Chemical Communications, 51 (2015) 8900-8911.

Chapter 4

Preparation and characterization of zeolite-modified electrodes for sensing applications

4.1 Abstract

A series of membranes were prepared employing mixtures of zeolites and graphite and depositing the resulting material on substrates obtained from strips of PET sheets. The aim behind this part of the research was to test the application of these mixtures for sensing applications. Zeolites used for this purpose were NaX, NaA and K-LTL. Each of these materials was ball milled with graphite and pressed to obtain a pellet. The resulting material was used like a pencil and deposited on an etched PET substrate by friction. Electrodes were tested by using potentiometry, cyclic voltammetry and electrochemical impedance spectroscopy. No Nernstian responses were found for the tested materials through potentiometric tests in standard solution of KCl at different concentrations. Among the zeolites used, only K-LTL gave a close to Nernstian response with 44.53 mV/decade during the first test and 41.67 mV/decade after drying over night and after a second test. NaX and NaA gave responses under 18 mV/decade and no improvement was seen after drying them over night for a second test. Cyclic voltammetry was used on the redox system $[Fe(CN)_6]^{4-} \rightleftharpoons [Fe(CN)_6]^{3-} + e^-$. The data obtained were used to investigate the reversibility of this system. According to the tested electrodes the system did not show reversible behavior in contrast with prior literature. The analysis showed hand-drawing methods were limited by the zeolites themselves, since they are not electroactive materials, for which the surface of the formed membranes did not display active sites for reduction or oxidation. Electrochemical impedance spectroscopy was employed to study diffusivity aspect related to the migration of cations that migrate from solution through the electrode surface material. Tests underlined high resistance resulting from the preparation method that negatively affected the reading of the response. This issue was not simply related to the

presence of the non-electroactive component zeolite, but it was also due to the high resistance generated by the interaction between the substrate and the electroactive component, graphite.

4.2 Introduction

Zeolites are a class of three-dimensional inorganic and crystalline materials characterized by micropore systems with high surface areas due to the interconnection of AlO_4 and SiO_4 tetrahedra. Their structural features reflect properties such as porosity, high surface area, absorptivity and ion exchange ability. These aspects make zeolite good candidates in many applications such as ion exchange, adsorption and separation of gases and catalysis. Zeolites are also employed for gas sensing [1] and they can be used as main element of a sensor and as an auxiliary component [2], [3]. Zeolites have also been utilized for sensing of species dissolved in aqueous systems [4]. Sensors used for these purposes are called zeolite- modified electrodes (ZMEs) [4]–[6] and they represent a subclass of chemical modified electrodes (CME). ZME can be divided in two subclasses: zeolite conductive polymer membranes [7]–[10] and zeolite graphite matrices [11]–[14], of which the latter class includes zeolite modified carbon paste electrodes. It is reported in literature that zeolites have the capacity to detect a large range of species such as pesticides [15], [16], detergents [17], vitamins [18]–[20] and inorganic cations [20]–[27]. In literature FAU (NaX) framework was extensively used for electrochemical studies [7], [17], [19] as well as LTA (NaA) [28]. In this part of the project, NaX and NaA zeolites along with K-LTL, were investigated as a potential catalyst in the previous chapters, were tested for electrochemical applications. This chapter aims to illustrate the results of this challenging task and it represents an attempt to employ zeolites for cation detection in aqueous solutions exploiting their ion exchange properties. However, since zeolites are not electroactive and their contribution is given by their ability to immobilize species, an electroactive counterpart was required and for this, graphite was employed. The idea of using zeolites and graphite comes from the attempt of mimicking the action of valinomicin as ionophore and polymer porous matrixes such a PVC and polyurethanes. The main challenge of this project was to develop an inexpensive, highly selective sensors also employable by non-professional operators. In this research, zeolites work as “ionophores” by taking cations from solutions they are in contact with and used with graphite in substitution of the polymer matrix.

The electrochemical response of zeolite containing electrodes consisting of NaX, NaA and K-LTL to monovalent cation K^+ was observed by potentiometric and voltammetric studies. Additional studies with electrochemical impedance spectroscopy were attempted.

4.3 Experimental

4.3.1 Materials

Graphite powder (particle size <20µm, synthetic), potassium ferrocyanide ($K_4[Fe(CN)_6]$), potassium chloride (KCl) and sodium chloride (NaCl) were purchased from Sigma-Aldrich. Zeolite NaX (Si/Al=1.3) was purchased from Riogen. Zeolite NaA (Si/Al=1.0) was purchased from Crosfield. K-LTL (Si/Al+3.1) was supplied by Tosoh Japan. Caesium chloride (99+%) were purchased from Acros Organic. Sodium nitrate (98+%) and potassium nitrate (99%) were purchased from Alfa Aesar. Rubidium chloride (99%) was supplied by Sigma-Aldrich and lithium nitrate (99%) by Timstar Laboratory Suppliers.

4.3.2 Ion selective pencil (ISP) preparation

The sensors used in this study were prepared according the method used by Jendrlin et al. [29]. Binary mixtures consisting of zeolite and graphite in powder form were ball milled in 40:60 ratio for 30 minutes until homogenous mixing was achieved. The solid mixture of both components was transferred in pellet die and then pressed using a hydraulic press by applying pressure from 1 to 4 tons and keeping the mixture under pressure for 5 seconds during each pressing step. The obtained pellet was crushed in a mortar and ground with pestle and pressed one more time in the hydraulic press following the same procedure described above. Obtained pellets were the starting point in making ion selective electrodes. The substrate used to make the electrodes consisted of stripes (dimension: 23mm x 39mm) of PET sheets. The surface of the substrate was preliminary etched by using sandpaper of aluminium oxide (grit 240) in order to increase the adsorption surface for the mixture zeolite/graphite. Pellets were used to draw by abrasion a line of the material across the PET substrate and sticky tape was used in the midsection to insulate the electrode (figure 4.1 left). The measured resistance was lower than 3 kΩ.

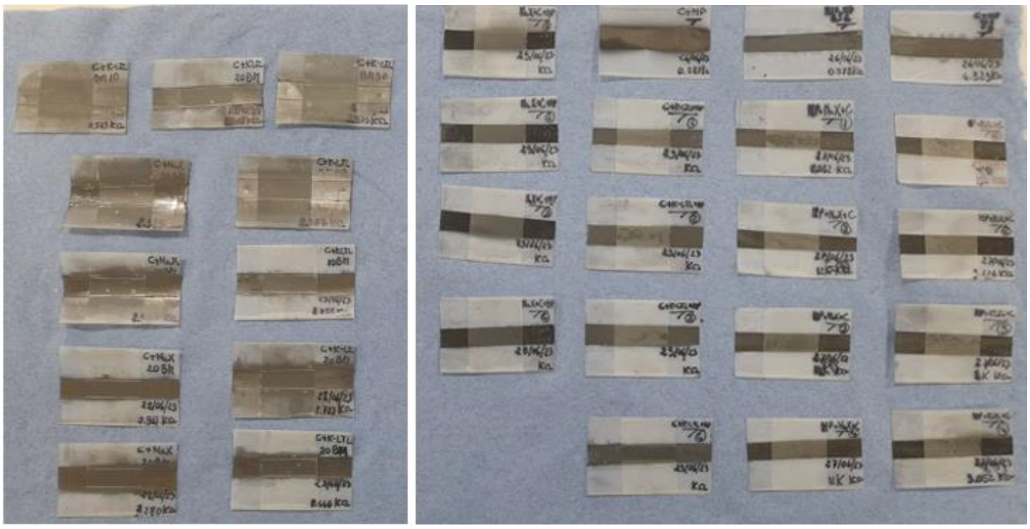

Figure 4.1: Electrodes tested in this study. Electrodes prepared using (left) the hand drawn method and (right) using the airbrush method.

An additional preparation method was employed which involved the preparation of an ink based on the method described in reference [30]. Initially, the mixture consisting of zeolite and graphite (40:60 ratio) was ball milled for 30 minutes. Next, the powder mixture was dispersed in a solution of nail polish with acetone and treated at the ultrasound bath for 30 minutes. Ink is shown in figure 4.2 (left).

Figure 4.2: (left) Ink, (right) airbrush used to deposit ink on the substrate.

PET was used as the substrate. The substrate was etched with sandpaper of aluminium oxide (grit 240). 2ml of the obtained ink were transferred with a pipette to the cup of an airbrush (figure 4.2 right) and deposited on the substrate. Electrodes obtained using this method are shown in figure 4.1 (right).

4.4 Material characterisation

X-Ray powder Diffraction. Mixture of zeolite K-LTL and graphite were investigated by XRD analysis after ball milling them for 10, 20 and 30 minutes. Single components were scanned. K-LTL was scanned 5-60 ^{o} 2theta and graphite 5-90^{o}. Both samples were prepared by pressing the powders in a plastic sample holder and XRD patterns were recorded on a Bruker D8 Advance diffractometer, equipped with a LynxEye detector, using Cu Kα radiation at 40 kV and 40 mA at ambient temperature (λKα1=0.15406 nm and λKα2=0.15444 nm; Soller slit of 2.5o; step size of 0.02^{o} scan duration of 30 min, no monochromator was used).

Potentiometry. Electrodes were evaluated by employing a potentiometer Lawson Labs Inc. 16-channel EMF-16 interface. Each of the tested electrodes was connected to a single channel and immersed in a stirred solution of 200 mL of deionised water in a crystallisation dish. As reference electrode a double-junction Ag/AgCl reference electrode with a 1.0 M of LiOAc bridge electrolyte (Fluka) was used. The measurement of the electrodes response was performed by adding standards of known concentration. During this experiment four amounts of KCl 0.1 M were added (20µL, 100µL, 1000µL, and 10000µL) to distilled water. The first amount of KCl (20µL) was added after 180 seconds in order to let the electric recorded signal stabilize. Subsequently, each amount of KCl was added at regular steps of 120 seconds. The experiment was stopped after 120 seconds from the last addition. Recorded potential response EMF and activities were used to obtain calibration curves employing the Nikolsky-Eisenman equation and activity coefficients from the Debye-Hückel method. Tests on electrodes were performed at least three times, and each time, the electrode was rinsed and dried with paper before repeating the above described analysis procedure. Additional tests involved drying the electrodes overnight.

Cyclic voltammetry. CV was used to test the employment of these materials to study redox processes. An Ivium CompactStat.h potentiostat was used to record voltammograms with of a glassy carbon rods used as counter electrode, an Ag/AgCl double junction electrode as reference electrode and the mixture zeolite/graphite on the PET substrate as working electrode. Materials were scanned in 80 mL, 5 mM $K_4[Fe(CN)_6]$ and the scanning potential range employed was between -0.5V and 0.9 V at a scan rate of 5 mV/s. Analysis and data treatment was conducted using IVIUM software.

Electrochemical impedance spectroscopy. EIS of the produced electrodes was evaluated using an Ivium CompactStat.h potentiostat combined with a multiplexer depending on the necessity to run multiple analysis simultaneously (figure 4.3, left). The setup used for the EIS experiment consisted of a glassy carbon rod used as counter electrode, an Ag/AgCl double junction electrode as reference electrode and the mixture zeolite/graphite on a strip of PET sheet (23mm x 39mm) as working electrode (figure 4.3, right). Analysis and data processing was conducted using IVIUM software. Scan were run in 80mL 0.1M of KCl solutions for NaX, NaA and K-LTL zeolites mixed with graphite. Additional scans with solutions of alkali metals in the concentration range 0.1 – 0.001M were run for K-LTL. Constant potential settings in a frequency range between 2.4kHz – 0.1Hz with amplitude 10 mV were employed.

Figure 4.3: (left) Ivium potentiostat model CompactStat.h (bottom), multiplexer (top). (right) Setup adopted for EIS experiment.

4.5 Results and discussion

4.5.1 XRD

Patterns of K-LTL and graphite as single component as well as ball milled samples were collected through powder X-Ray diffraction. XRD patterns are displayed in figure 4.4. K-LTL was scanned in the 2theta range 5-60° while graphite from 5 to 90°. Two different mixtures were prepared with both ball milled component K-LTL and graphite to check structural changes. One mixture consisting of both components was prepared by simply adding and manually mixing K-LTL and graphite (700g, 40:60) in the same container; no ball milling was performed in this case. A second sample was prepared by ball milling of K-LTL and graphite (700g, 40:60) in the same container for 30 minutes with 10 spheres (0.4g each) of zirconia.

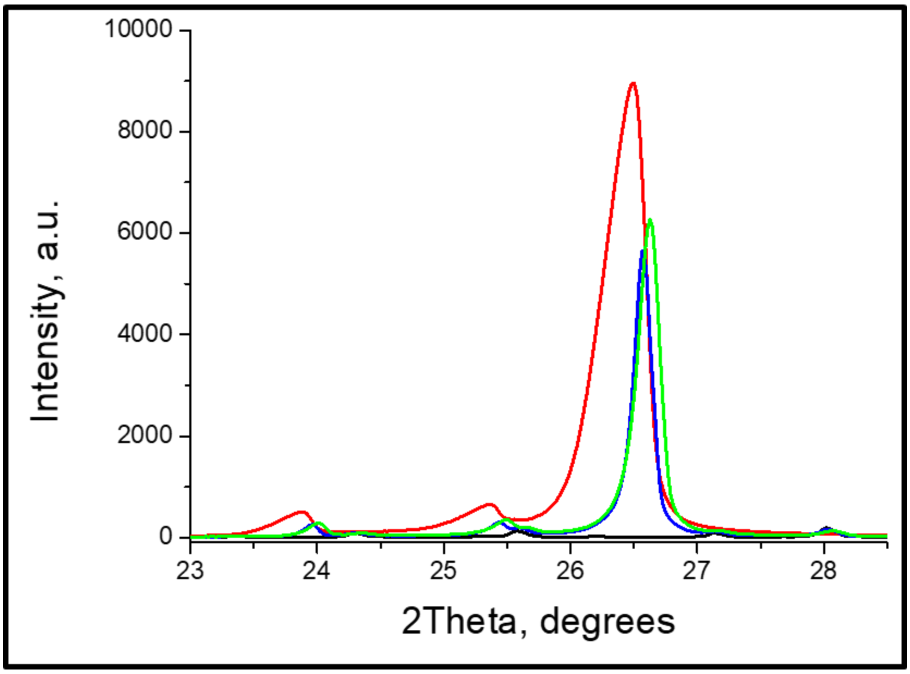

Figure 4.4: Pattern of K-LTL (black), graphite (red), manually mixed sample of K-LTL and graphite and (green) and ball milled mixture of K-LTL and graphite (blue). Patterns are shown in the 2theta range 23 to 28.5° for clarity.

Peaks in the manually mixed sample appear offset and slightly shifted to higher angles in 2theta compared to the ball-milled mixture. This aspect may be attributed to a distortion of the lattice or of the plains of the graphite. In addition, an increased peak intensity can be noticed in the manually mixed sample. Compared to graphite as the single component, both mixtures showed a decrease in terms of intensity for peaks at 26.3 (002), 44.4 (101) degrees as well as 50.6 (102), 54.6 (004) and 59.8 (003) degrees in 2theta. This phenomenon is due to the sliding in an in-plane direction between graphene layers in graphite as result of the ball milling procedure [31].

4.5.2 Potentiometry

The potentiometric response of zeolite modified electrodes of graphite and NaA and graphite with NaX were tested in deionized water with 0.1 KCl standard. Two electrodes were prepared from each zeolite. Electrodes of the same zeolite were prepared with a different thickness by attempting to deposit a double amount of material on the substrate. Final resistance of the prepared electrodes was under 3KΩ. An estimation of the electrodes thickness can be determined using the following equation:

$$d = V/A = m/ \rho a$$

Where d is the thickness [μm], V is the volume [cm^3], A is the surface of the layer [cm^2], m is the mass [g] and ρ is the density of the layer [$g\ cm^{-3}$]. The density was calculated from the mass and the volume of the starting pellet. Final thickness of the membranes are shown in table 4.1

Table 4.1: Thickness of the prepared electrodes.

Zeolite	d, μm
NaA d1	1.0
NaA d2	1.8
NaX d1	2.4
NaX d2	3.9

The potentiometric response of the all the electrodes is displayed in figure 4.5 and in table 4.2. Responses for NaA electrodes recorded slopes around 13 mV/decade for both thicknesses resulting far from Nernstian response. A similar result was recorded for both NaX electrodes and 16.23 mV/decade for thickness1 and 12.17 mV/decade for thickness 2 was found. Since zeolites are hydrophilic, a second test was done on the same electrodes after drying them overnight. However no improvement was obtained and all the electrodes showed again slopes far from Nernstian response. A common problem seen in both analysis was the presence of leaching. This represents the drawback of the hand-drawn preparation method especially for the electrodes with double thickness. Indeed, the additional layers of material deposited on the first one, which is in contact with the substrate, are easily removed once in the solution. This not only does not guarantee the durability of the membrane for additional tests but also contaminates the sample under investigation.

Table 4.2: Slopes of electrodes with NaA and NaX at different thickness.

ZME	Slope, mV/decade
NaA d1	13.23
NaA d2	13.26
NaX d1	16.23
NaX d2	12.17

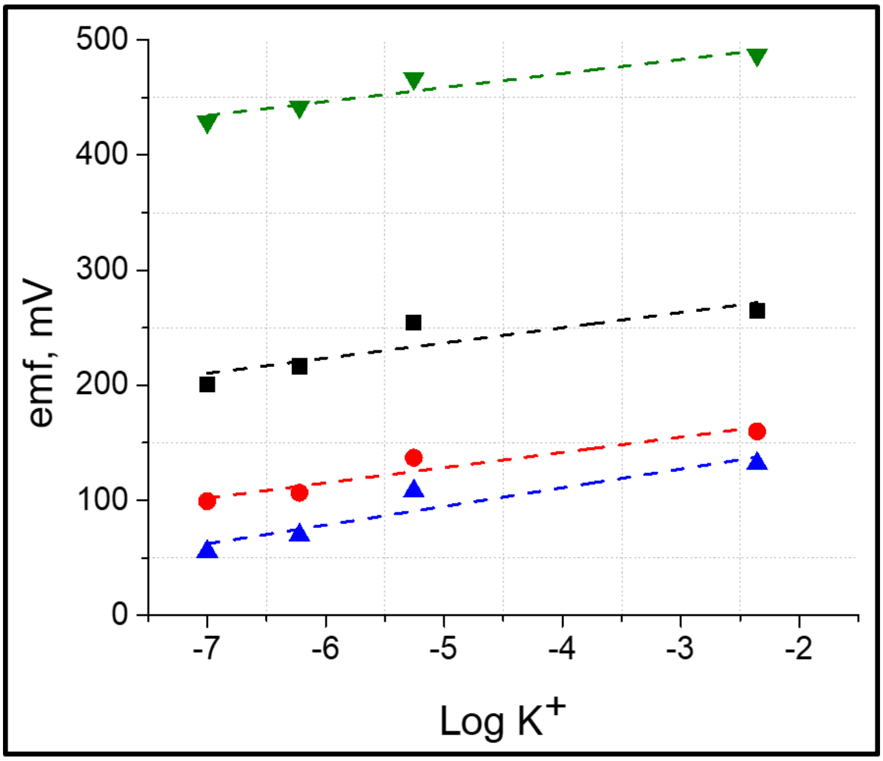

Figure 4.5: Potentiometric response and slopes of the electrodes: NaA d1 (black), NaA d2 (red), NaX d1 (blue) and NaX d2 (green).

An attempt with a different zeolite was performed. Following the same preparation method described and used for NaX and NaA, zeolite K-LTL was ball milled with graphite and tested with KCl 0.1M in deionized water. In order to limit leaching of material, which affected membranes with NaA and NaX in the previous experiment, for K-LTL, only one layer of material was deposited until resistance was under 3KΩ. The potentiometric response obtained showed 44.53 mV/decade for the fresh electrode with K-LTL and graphite after the first test. The same electrode was rinsed with deionized water, dried with paper and tested a second time. Even in this case, leaching was observed as well as a lower response after the test in a fresh solution. A slope of 36.57 mV/decade was obtained after this test. The electrode was then dried overnight and tested one more time obtaining a response of 41.67 mV/decade.

Potentiometric responses for mixture K-LTL with graphite are displayed in figure 4.6 and in table 4.3.

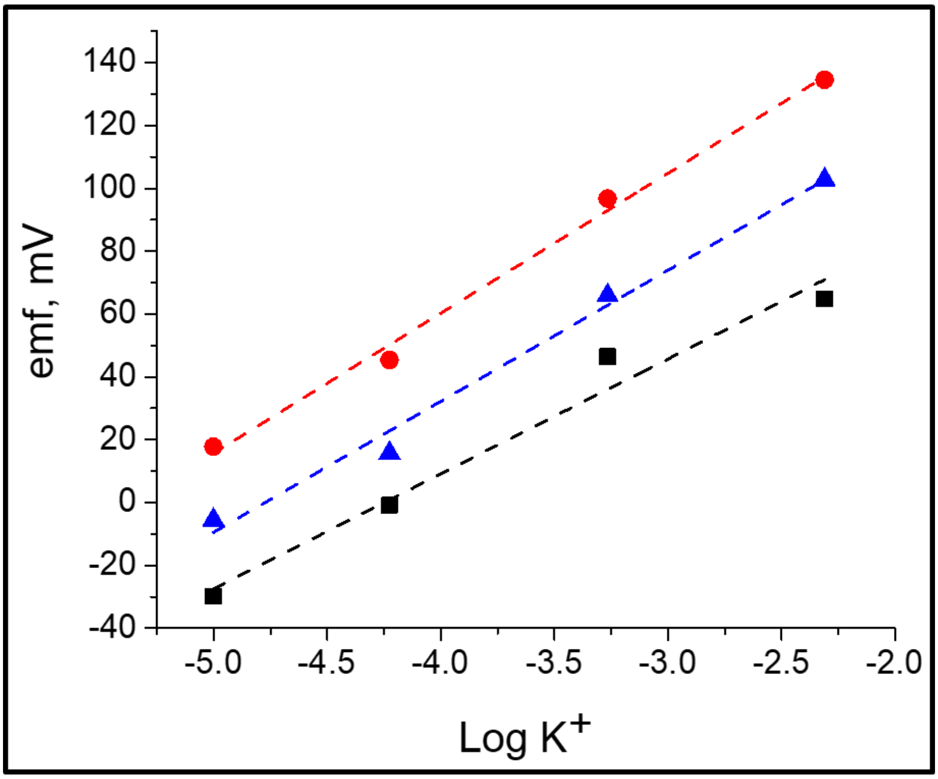

Figure 4.6: Potentiometric response and slopes of K-LTL and graphite electrodes to K^+ using a fresh electrode (red), same electrode rinsed and tested (black) and after drying it overnight (blue).

Table 4.3: Slopes of K-LTL and graphite electrodes: (red) fresh electrode, (black) rinsed and tested electrode, (blue) dried overnight and tested electrode.

ZME	Slope, mV/decade
Red	44.53
Black	36.57
Blue	41.67

The loss of response during the second test (black) and the increase after drying the same membrane may represent the confirmation of the hydrophilic nature of zeolites. Although even these results do not match with the Nernstian response of 59.2 mV/decade, K-LTL resulted to be a more promising material to be employed for sensing applications compared to NaX and NaA. However, even in this case, the resulting difference in potential between working and reference electrodes was not proportional to the concentration of the ion in solution to achieve the Nernstian response. Leaching phenomenon and loss of response was observed even in this case. This aspect does not make the membranes made with the hand-drawing method suitable for long use and does not make the electrodes easily reproducible. Although, the described method is inexpensive and, after disposal, the electrode can be easily reprepared, these aspects do not balance the disadvantages described above. An alternative method to make electrodes involving the preparation of an ink was attempted and tested. The ball milled mixture of K-LTL and graphite in 40:60 ratio, was dispersed in a solution of nail polish used as binding agent: 300 mg of binary miture (K-LTL and graphite) were added to 300 mg of nail polish (50%:50% m m^{-1}). 1.5 ml of acetone used as solvent were added during the preparation for its ability to dissolve nail polish particles. Next the mixture was treated in an ultrasonic bath for 30 minutes. The electrode was dried overnight at 60°C. The obtained ink was deposited on the PET substrate by using an airbrush. The potentiometric response to K^+ in this case was 22.52 mV/decade and it is shown shown in figure 4.7.

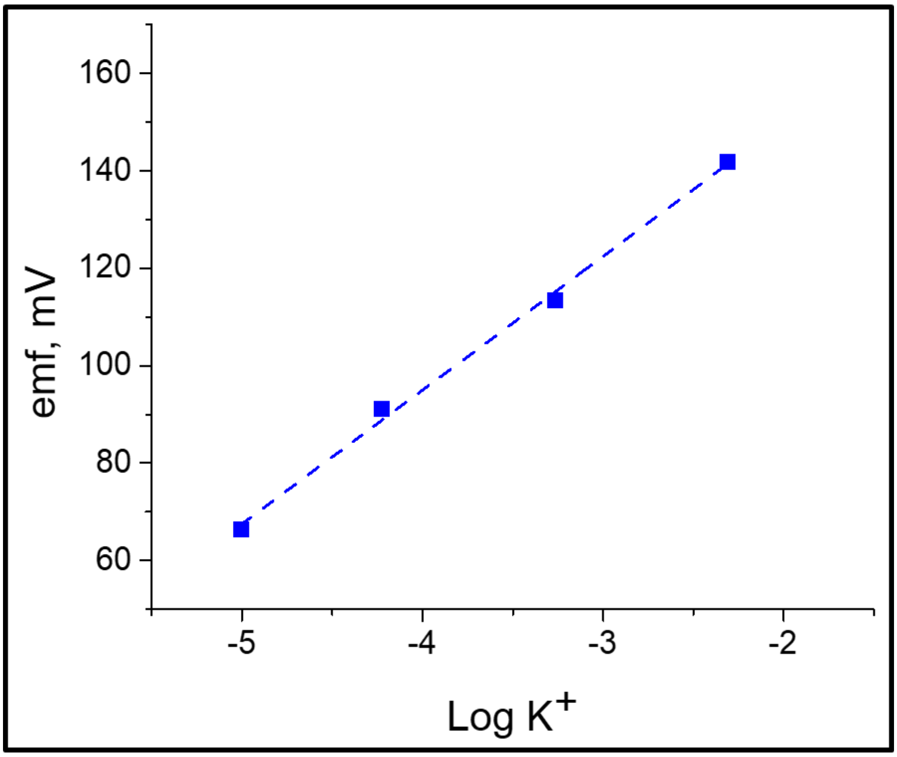

Figure 4.7: Potentiometric response of the ink (K-LTL + graphite) in nail polish and acetone.

The result obtained does not represent an improvement compared to the hand drawn method with K-LTL because of the lower slope recorded but it confirms that K-LTL is more prone to accept K^+ than NaA and NaX. The probable reasons behind the unsuccessful test can be attributed to several aspects. Depositing the ink in a homogeneous way on the substrate does not make this preparation method reproducible and this may be caused by the manual use of the airbrush. Indeed, the distance and the angle between the nozzle and the substrate plane affect how the inkjet is deposited: the bigger the distance the more diluted the ink will be deposited on the substrate. Another reason may be attributed to the ratio between power mixture and nail polish. All this aspect require further investigation to improve the method.

4.5.3 Cyclic voltammetry

The electrochemical behavior of membranes prepared with three different zeolites NaX, NaA and K-LTL and mixed with graphite was investigated by cyclic voltammetry using a well-known reversible redox system such as potassium ferrocyanide in KCl solution. Figure 4.8 shows the cyclic voltammograms collected at 5 mV s^{-1} in 5 mM ferrocyanide in 0.1M KCl at zeolite/graphite electrodes. Each electrode was tested three times.

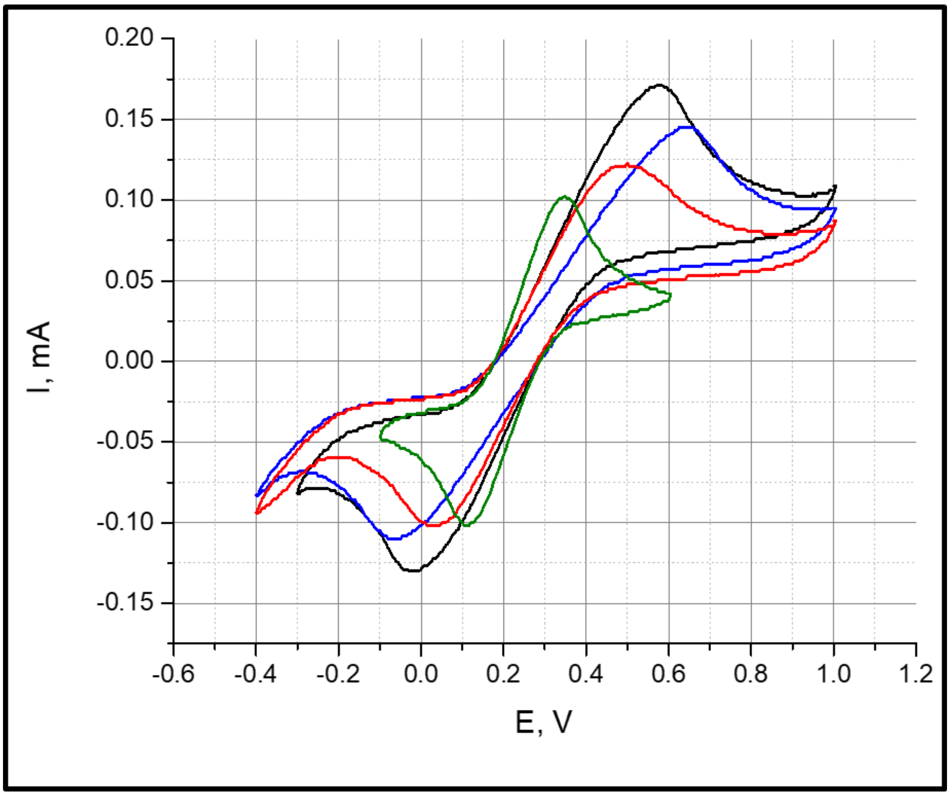

Figure 4.8: Cyclic voltammograms of 5mM ferrocyanide in 0.1 M KCl obtained at (black) a NaX/graphite, (blue) a NaA/graphite, (red) a K-LTL/graphite and (green) a graphite electrode. The scan rate is 5 mV s^{-1}.

The obtained voltammograms show the typical "duck shape" with both reduction and oxidation peaks present. The presence of a return peak in cyclic voltammetry allows to determine parameters such as formal potential for the redox couple, by averaging both peak potentials, and the separations between the two peak potential obtained from the subtraction of the anodic and cathodic potentials. Additional information can be obtained from anodic and cathodic peak currents. In particular, if their ratio is equal to 1 this may suggest that the product is stable on the time scale of the experiment and that the electron transfer reaction is reversible in both directions. Peak currents and peak potentials were determined for all voltammograms and are shown in table 4.4. The reversibility of the studied system on the tested electrodes was investigated.

Table 4.4: Peak currents, peak potentials, separation of the two peak potentials, current ratios and formal potential of the redox couple of the tested electrodes.

NaX	**Ipa, A**	**Ipc, A**	**Ea, V**	**Ec, V**	**Δep, mV**	**Ipa/Ipc**	**E°'**
	1.16E-04 ± 7.79E-06	-9.68E-05 ± 1.18E-06	0.572 ±0.002	-0.035 ± 0.004	607± 6	1.20 ± 0.09	0.268 ± 0.001
NaA	**Ipa, A**	**Ipc, A**	**Ea, V**	**Ec, V**	**Δep, mV**	**Ipa/Ipc**	**E°'**
	8.25E-05 ± 9.20E-06	-7.71E-05 ± 5.35E-07	0.647± 0.002	-0.067 ± 0.002	713 ±2	1.07 ±0.12	0.290 ± 0.002
K-LTL	**Ipa, A**	**Ipc, A**	**Ea, V**	**Ec, V**	**Δep, mV**	**Ipa/Ipc**	**E°'**
	9.02E-05 ± 4.55E-06	-8.31E-05 ± 9.98E-07	0.493 ± 0.005	0.027 ± 0.002	467 ± 6	1.09 ± 0.07	0.260 ± 0.002
C	**Ipa, A**	**Ipc, A**	**Ea, V**	**Ec, V**	**Δep, mV**	**Ipa/Ipc**	**E°'**
	8.45E-05 ± 3.38E-06	-8.11E-05 ±2.10E-06	0.348 ± 0.002	0.108 ± 0.002	240 ± 4	1.04 ± 0.02	0.228 ± 0.001

Results show an increasing “peak to peak separation” (Δep) from the electrode with just graphite to NaA with graphite. Electrodes of K-LTL and NaX, respectively with graphite, appear in between. Although the electrode with graphite shows the lowest Δep, the obtained result is greater than the theoretical value of 58 mV for 1 electron transfer process. This aspect suggests the presence of an irreversible process for the redox system: $[Fe(CN)_6]^{4-} \rightleftharpoons [Fe(CN)_6]^{3-} + e^-$. Addition of zeolites to graphite makes the studied system even less reversible, since more negative and positive potentials are required to complete the redox cycle. The electrodes evaluation suggests that this is synonym of a system characterised by a high activation energy with a low electron transfer which is in contrast with the reported highly reversible nature of $[Fe(CN)_6]^{4-} \rightleftharpoons [Fe(CN)_6]^{3-} + e^-$. The described irreversibility is also confirmed by the Ipa/Ipc ratio, which is greater than 1 for the electrode with just graphite and increases for the electrodes that employ zeolites. The addition of a zeolite pushes peak potentials towards greater negative reduction and oxidation currents. The current increase is the result of the diffusion layer growing at the surface of the electrode during oxidation and reduction steps. However, the main difference between the response of electrodes that employs mixtures and electrodes with just graphite may be due to a more extended reduction and oxidation process where species are not converted on the electrode surface. This is mainly due to two reasons: the first one is related to the non-homogenous distribution of the mixed material on the substrate and the second is strictly related to the presence of zeolites, which are not electroactive. These aspects represent an additional drawback of the hand-drawn preparation method of these electrodes because there is no control in achieving a homogeneous distribution of graphite and zeolite on the substrate. The presence of a zeolite does not help the conversion of the species interacting with the surface electrode since this material is neutral and represents an obstacle for the redox process. For the studied redox system, porosity of zeolites does not represent the answer since there are steric factors that affect the diffusion from the solution to the pores of the material. Although the presence of a limiting pore size, there would not be a way to perform reduction or oxidation within the zeolite structure but only in correspondence of graphite. A possible improvement might be represented by the employment of active species such as silver and copper introduced by ion exchange in the zeolite structure. Similar cases are reported in literature [32] and may represent a path to follow for further investigation and additional tests on these materials.

4.5.4 Electrochemical impedance spectroscopy

EIS (Electrochemical Impedance spectroscopy) analysis was performed to investigate the ion diffusion process in four electrodes, one consisting of pure graphite and three prepared using a mixture of graphite and NaX, NaA and K-LTL zeolites. Each electrode was tested three times. The electrode with graphite was used to run a preliminary test. Nyquist plots of the tested electrodes are shown in figure 4.9, 4.11, 4.12 and 4.13. K-LTL in alkali metal solutions spectra are shown in figure 4A.1 – 4A.15 in chapter 6 - appendix).

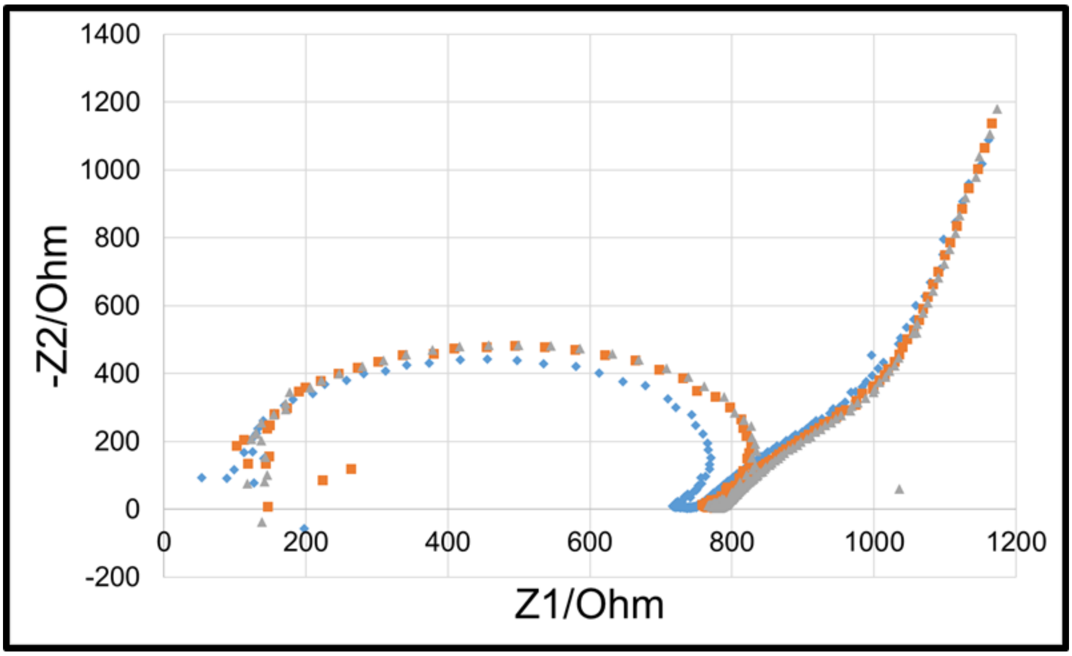

Figure 4.9: EIS spectrum of graphite electrode.

From a visual inspection of the spectra for the electrode with graphite in figure 4.9, it can be deduced that the response differs greatly from that expected for graphite. Nyquist plot of the electrode with graphite displayed a semicircle in the high frequency region associated with the resistance of the membrane. Expected response of graphite should be similar to the response of a capacitor. The response of an ideal capacitor with zero resistance is shown in figure 4.10a.

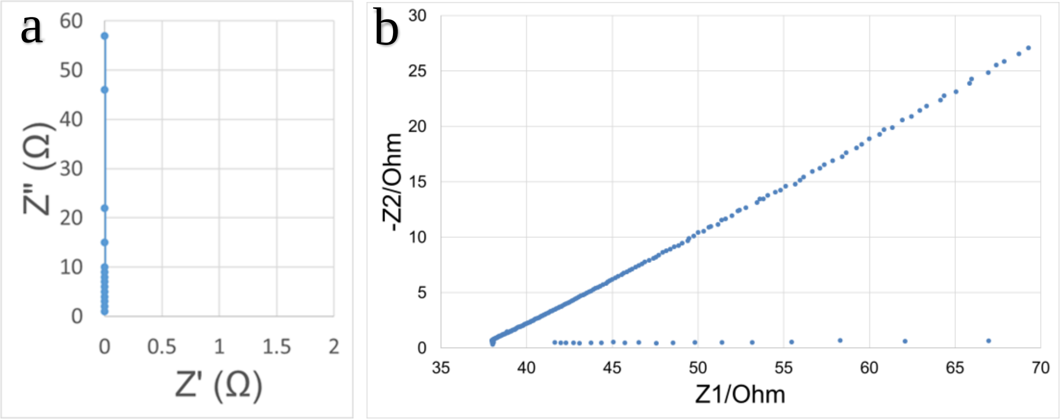

Figure 4.10: (a) Nyquist plot of the typical response of a capacitor. (b) Response of pellet of graphite.

For this reason, an additional test on a pellet of graphite was conducted. The Nyquist plot of pure graphite is shown in figure 4.10b. This response does not depict perfectly the ideal scenario shown in figure 4.10a. Indeed, the presence of smaller resistance in the high frequencies region as well as the presence of a pseudo capacitance in the low frequency region was found. This result points out that the substrate used may limit the performance of graphite due to the high resistance caused by its interaction with the membrane.

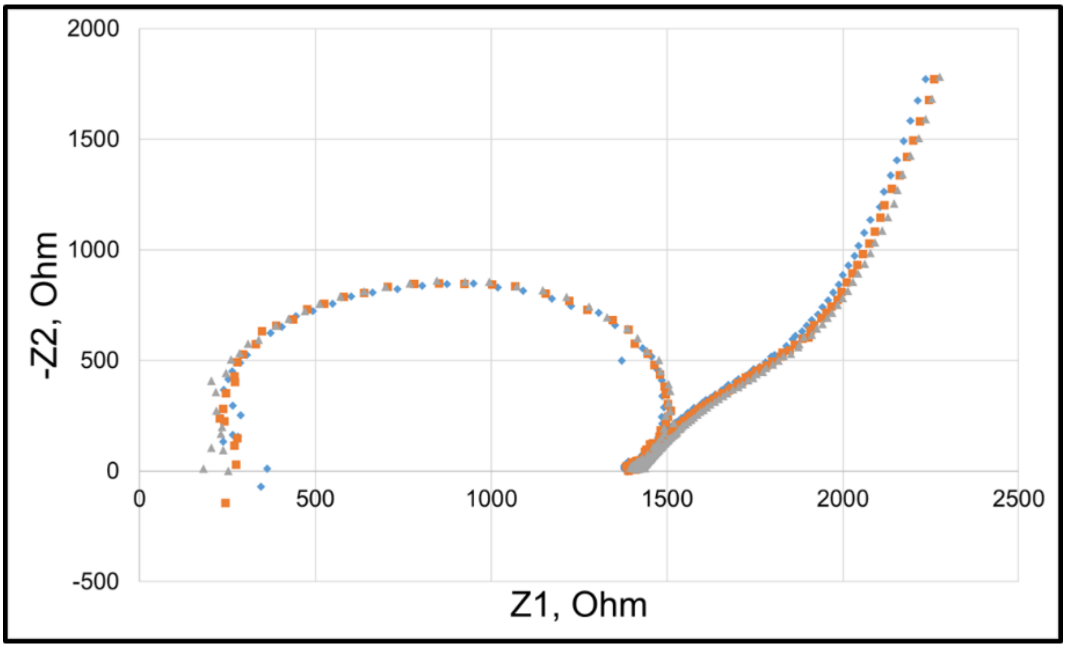

Figure 4.11: EIS spectrum of NaX/graphite electrode.

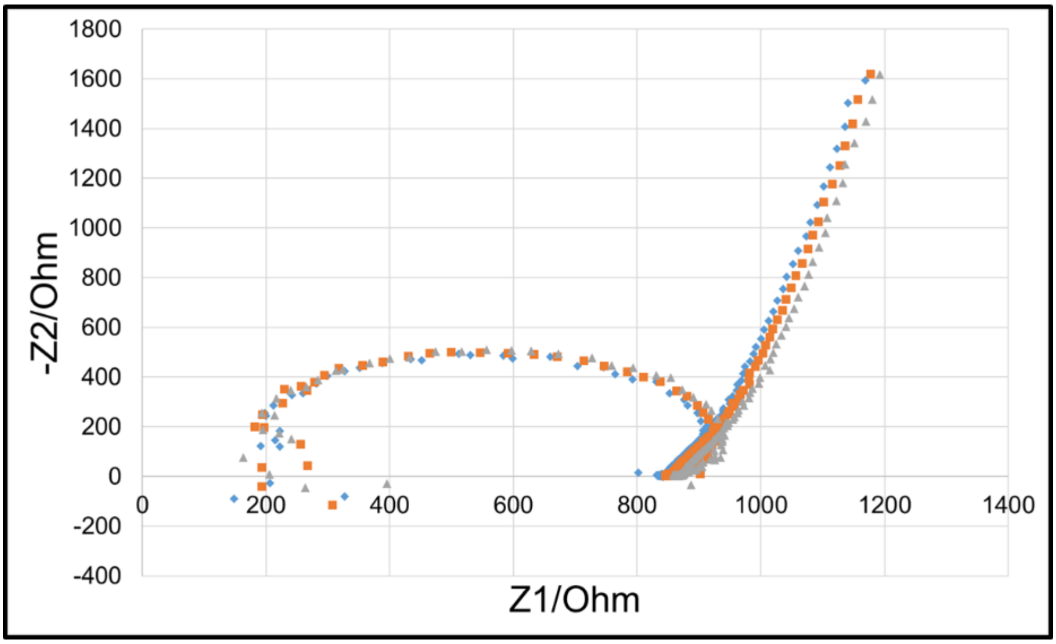

Figure 4.12: EIS spectrum of NaA/graphite electrode.

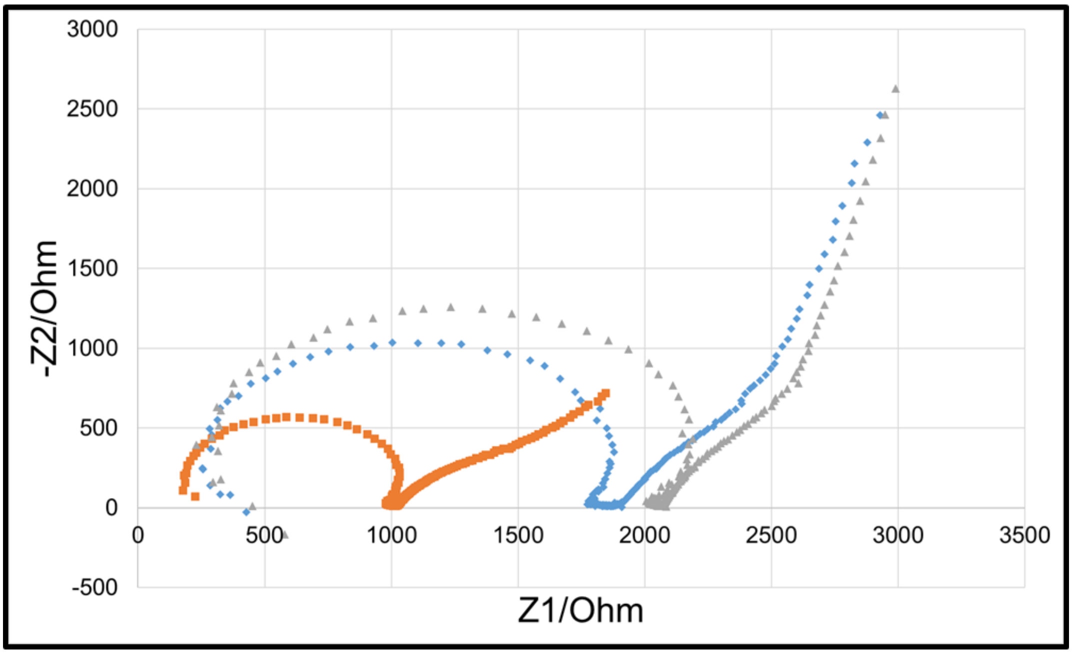

Figure 4.13: EIS spectrum of K-LTL/graphite electrode.

The same scenario was found for all the membranes made using graphite and the other zeolites (figure 4.11, 4.12, 4.13). The addition of zeolites did not improve the response, and even higher resistance values in the high frequency region were found and capacitance in low frequencies region. The low frequency semicircle may be attributed to the charge transfer resistance between the substrate and the material and the double layer capacitance at high frequency regions may be originated from the material/solution interface. Based on obtained data, a fit procedure by producing a circuit (figure 4.14, left insert) on the EIS profiles was attempted by using IVIUM software. However, the choice of the components might not be correct since the results were affected by error of several orders of magnitude (figure 4.14, right insert).

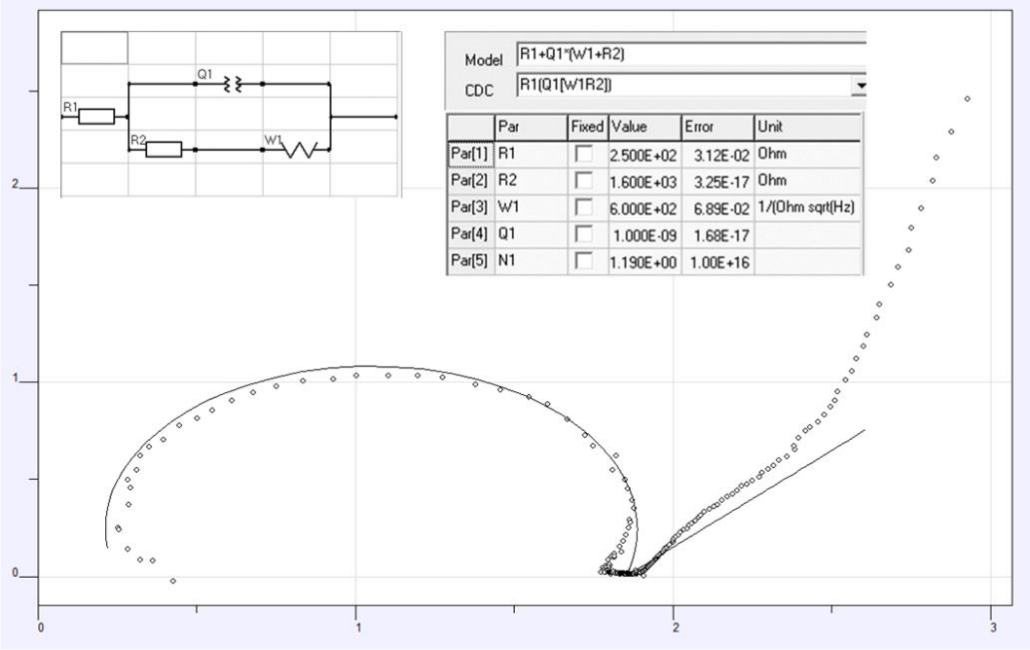

Model R1+Q1*(W1+R2)
CDC R1(Q1[W1R2])

	Par	Fixed	Value	Error	Unit
Par[1]	R1	☐	2.500E+02	3.12E-02	Ohm
Par[2]	R2	☐	1.600E+03	3.25E-17	Ohm
Par[3]	W1	☐	6.000E+02	6.89E-02	1/(Ohm sqrt(Hz)
Par[4]	Q1	☐	1.000E-09	1.68E-17	
Par[5]	N1	☐	1.190E+00	1.00E+16	

Figure 4.14: EIS spectrum of K-LTL (as example). The inserts (left) represent the circuit used for the simulation of the system and (right) the results obtained from the fitting procedure.

4.6 Conclusions

The hand-drawn method used in these studies represents a cheap way to make electrodes that combines two very low cost materials: graphite and zeolites. Although the preparation is very simple, the resulting electrodes show several disadvantages such as leaching with the consequent changes in concentration. The hand drawn method does not ensure reproducibility during the preparation of the electrodes and it is unpredictable how the material will be deposited on the substrate making the sensing part a mix of active and inactive regions due to the properties of the materials involves. The choice of the substrate needs further investigation since PET impart the high electrodes resistance as seen from the EIS results. Zeolites remain an interesting addition for sensing analysis as seen in literature however, their employment did not succeed in any of the performed tests in this study. Properties such as ion exchange and porosity that these materials offer may be exploited for cation detection of species in solution but since zeolites do not offer selectivity, the detection is difficult to perform as well as the quantification of the species using potentiometry. If porosity may offer a solution in potentiometry, it results not relevant for cyclic voltammetry were in the presented test the scanned systems and the correspondent species cannot access zeolite pores for steric constraint. Redox processes occur on the surface of the electrode where only graphite, the electroactive component, is present leaving inactive the electrode areas were only zeolite is deposited. The employment of active species such as silver and copper introduced in zeolite structures by ion exchange may represents a possible solution that deserves to be mentioned. Although it may be expensive, interesting results are provided in literature and this method might represent another attempt to integrate zeolites in sensing applications.

4.7 References

[1] X. Xu, J. Wang, and Y. Long, Zeolite-based materials for gas sensors, Sensors, 6 (2006) 1751–1764.

[2] K. Sahner, G. Hagen, D. Schönauer, S. Reiß, R. Moos, Zeolites - Versatile materials for gas sensors, Solid State Ionics, 179 (2008) 2416–2423.

[3] S. N. Talapaneni, J. Grand, S. Thomas, H. A. Ahmad, S. Mintova, Nanosized Sn-MFI zeolite for selective detection of exhaust gases, Mater. Des., 99 (2016) 574–580.

[4] A. Walcarius, Zeolite-modified electrodes in electroanalytical chemistry, Anal. Chim. Acta, 384 (1999) 1–16.

[5] D. R. Rolison, Zeolite-Modified Electrodes and Electrode-Modified Zeolites, Chem. Rev., 90 (1990) 867–878.

[6] A. Walcarius, Zeolite-modified paraffin-impregnated graphite electrode, J. Solid State Electrochem., 10, (2006) 469–478.

[7] A. Walcarius, V. Ganesan, O. Larlus, V. Valtchev, Low temperature synthesis of zeolite films on glassy carbon: Towards designing molecularly selective electrochemical devices, Electroanalysis, 16 (2004) 1550–1554.

[8] G. Johansson, L. Risinger, A cesium-selective electrode prepared from a crystalline Synthetic zeolite of the mordenite type, Anal. Chim. Acta, 119 (1980) 25–32.

[9] M. L. Hamlaoui, K Reybier, M Marrakchi, N Jaffrezic-Renault, C Martelet, R Kherrat, A. Walcarius, Development of a urea biosensor based on a polymeric membrane including zeolite, Anal. Chim. Acta, 466 (2002) 39–

45.

[10] R. M. Barrer and S. D. James, Electrochemistry of Crystal-Polymer Membranes Part I. Resistance Measurements, J. Electrochem, 960 (1959).

[11] S. Kilinc Alpat, U. Yuksel, H. Akcay, Development of a novel carbon paste electrode containing a natural zeolite for the voltammetric determination of copper, Electrochem. commun., 7 (2005) 130–134.

[12] M. Mazloum-Ardakani, Z. Akrami, H. Kazemian, H. R. Zare, Preconcentration and electroanalysis of copper at zeolite modified carbon paste electrode, Int. J. Electrochem. Sci., 4 (2009) 308–319.

[13] J. Wang, A. Walcarius, Zeolite-modified carbon paste electrode for selective monitoring of dopamine, J. Electroanal. Chem., (1996).

[14] C. Bing, L. Kryger, Accumulation and voltammetric determination of complexed metal ions at zeolite-modified sensor electrodes, Talanta, 43(1) (1996) 153–160.

[15] A. Walcarius, P. Mariaulle, L. Lamberts, Use of a zeolite-modified electrode for the study of the methylviologen-sodium ion-exchange in zeolite, Y. J. Electroanal. Chem., 463 (1999) 100–108.

[16] L. R. Siara, F. De Lima, C. A. L. Cardoso, G. J. Arruda, Electrochemically pretreated zeolite-modified carbon-paste electrodes for determination of linuron in an agricultural formulation and water, Electrochim. Acta, 151 (2015) 609–618.

[17] S. Matysik, F. M. Matysik, J. Mattusch, W. D. Einicke, Application of Zeolite-Polydimethylsiloxane Electrodes to Potentiometric Studies of

Cationic Species, Electroanalysis, 10 (1998) 98–102.

[18] T. Rohani, M. A. Taher, A new method for electrocatalytic oxidation of ascorbic acid at the Cu(II) zeolite-modified electrode, Talanta, 78 (2009) 743–747.

[19] A. Walcarius, L. Lumberts, E. G. Derouane, Cation determination in aqueous solution using the methyl viologen-doped zeolite-modified carbon paste electrode, Electroanalysis, 7 (1995)120–128.

[20] D. R. Rolison, R. J. Nowak, T. A. Welsh, C. G. Murray, Analytical implications of zeolites in overlayers at electrodes, Talanta, 38 (1991) 27–35.

[21] S. Senthilkumar, R. Saraswathi, Electrochemical sensing of cadmium and lead ions at zeolite-modified electrodes: Optimization and field measurements. Sensors Actuators, B Chem., 141 (2009) 65–75.

[22] L. Cao, J. Jia, Z. Wang, Sensitive determination of Cd and Pb by differential pulse stripping voltammetry with in situ bismuth-modified zeolite doped carbon paste electrodes, Electrochim. Acta, 53 (2008) 2177–2182.

[23] J. Wang, T. Martinez, Accumulation and voltammetric measurement of silver at zeolite-containing carbon-paste electrodes, Anal. Chim. Acta, 207 (1988) 95–102.

[24] A. Walcarius, V. Vromman, J. Bessiere, Flow injection indirect amperometric detection of ammonium ions using a clinoptilolite-modified electrode, Sensors Actuators, B Chem., 56 (1999) 136–143.

[25] B. Kaur, R.Srivastava, B. Satpati, Ultratrace detection of toxic heavy metal

ions found in water bodies using hydroxyapatite supported nanocrystalline ZSM-5 modified electrodes, New J. Chem., 39 (2015) 5137–5149.

[26] C. E. Marshall, The use of zeolitic membrane electrodes, J. Phys. Chem. 43(9) (1939) 1155-1164.

[27] M. Arvand-Barmchi, M. F.Mousavi, M. A. Zanjanchi, M. Shamsipur, A PTEV-based zeolite membrane potentiometric sensor for cesium ion, Sensors Actuators, B Chem., 96 (2003) 560–564.

[28] M. D. Baker, C. Senaratne, J. Zhang, Effects of Supporting Electrolyte and Zeolite Co-cations on the Electrochemical Response of Zeolite-modified Electrodes, J. Chem. Soc. Faraday trans., 88 (1992) 3187-3192.

[29] M. Jendrlin, S. Khumngern, A. Numnuam, P. Thavarungkul, P. Kanatharana, D. Kirsanov, V. L. Zholobenko, L. Mendecki, A. Radu, Ion sensing pencil: Draw your own sensor, Sensors and Actuators B: Chemical, 337 (2021) 129751

[30] A. E. Ferreira Oliveira, A. C. Pereira, Development of a Simple and Cheap Conductive Graphite Ink, Journal of The Electrochemical Society, IOP Publishing, 168(8) (2021) 087508

[31] DW. Jung, JH. Jeong, BC. Cha, JB Kim, Effects of ball-milled graphite in the synthesis of SnO_2/graphite as an active material in lithium ion batteries. Met. Mater. Int. 17 (2011) 1021–1026.

[32] A. Walcarius, T. Barbaise, J. Bessi, Factors affecting the analytical applications of zeolite-modified electrodes preconcentration of electroactive species, Analytica Chimica Acta, 340 (1997) 61-76.

Chapter 5

Conclusions and future work

5.1 Conclusions

Aim of this project was to prepare, characterize and study acidic and structural properties of LTL and MAZ zeolites after ion exchange with alkali metals (Li, Na, K, Rb and Cs). In addition, the synthesis of mazzite according to our methodologies was performed. Commercial ion exchanged LTL and MAZ zeolites were prepared by mixing solutions of known and increasing concentrations of alkali metals with the parent zeolites. The obtained samples were extensively characterized by, SEM EDX, ICP-OES, XRD, FTIR, N_2 adsorption-desorption, NH_3-TPD. SEM EDX and ICP-OES were used to evaluate the cation-loading of species introduced via ion exchange. Data revealed that both zeolites were more prone to accept Cs^+ among all alkali metals. In terms of comparison between the two employed zeolites, LTL showed for all alkali metals cations a greater degree of ion exchange. A clear increasing loading trend was found for LTL and MAZ, which followed the periodic table order: Li^+, Na^+, K^+, Rb^+, Cs^+. Atomic percentages also revealed a certain preference towards K^+, more emphasized in LTL than MAZ where the latter showed a slight evidence of this aspect. LTL and MAZ results showed that the size of hydrated cations and the coulombic interactions with the framework oxygens played a key role in the ion exchange process justifying the observed trend. N_2 adsorption-desorption allowed to find additional information and evidence that exposed some of the structural aspects that influenced the diffusion of cations through both zeolites. If for LTL, a high atomic percentage of introduced cations was found, for MAZ, the pore narrowness and pore blockage worked as a bottleneck. Observed surface area as well as the total and the micropore volume for the parent and ion exchanged LTL samples were greater than the corresponding ion exchanged MAZ materials.

X-Ray diffraction analysis was employed to inspect additional structural aspects and to observe each pattern at the several ion exchange steps and at different concentrations. The Rietveld method revealed details of the ion exchange steps by observing the structural modifications in the samples that occurred during the ion exchange. In addition, this allowed us to understand the path followed by the introduced species through the units that build the framework of the studied zeolites. Based on the Rietveld method findings cation migration was studied. The method required working on the editing of cif files of parent zeolites, which represented the starting point of the process. This step, depending on the material, involved to edit the information included in these files such as the Si/Al ratio, the extraframework species and their occupancies. The information received from the elemental analysis was taken into account to generate the used cif files. Cif files were generated by employing additional software packages, such as Vesta, in order to simulate XRD patterns and to have a visual comparison of the patterns and MAUD to apply the Rietveld method. For LTL samples the introduction of the ion exchanged species showed an increase in the lattice parameters from NH_4^+ to Cs^+. In LTL, migration of cations in low concentrations occurred through the *t-ltl* cage that represents the main channel of the framework (12MR) but only for Cs^+, Rb^+ and K^+ was possible to replace NH_4^+ and K^+ already in that location. At higher concentrations, data revealed that only Cs^+, Rb^+ and K^+ can migrate through the 8MR that works as link between *t-ltl* cage and *t-ste* cage. This position is inaccessible to Li^+ and Na^+ because of the steric constraint that affects these hydrated species. Only K was found in *t-can* cage, which was inaccessible to all introduced species because of the narrower 4MR and 6MR. The employed methodology, taking Cs^+ as example, showed an occupancy correspondent to 1.8

cations in *t-ltl* cage and 1.3 cations in *t-ste* cages per unit cell. For MAZ, Rieveld showed a different scenario and suggested that cations at low concentrations access the main channel (12MR) *t-maz* cage, but only Cs^+, Rb^+ and K^+ can ion exchange almost 2 cations per cell. Despite the structural similarities with LTL, the cage linked to *t-maz* by a 5MR, called *t-kaj*, did not give access to the cations in this position limiting their further migrations. However, for MAZ additional investigation are recommended since in some cases good agreement between experimental and calculated patterns with cations in *t-kaj* cage was found. This cannot be excluded because of the possibility of structural defects, which would allow the migration of cations in the other sites.

Along with the structural aspects, also the acidic properties of ion exchanged LTL and MAZ were investigated. From the FTIR results of parent and ion exchanged zeolites it can be noticed that both materials show two different kinds of spectra with two bands in common. Both zeolites show one band at ~3745 cm^{-1} typical of the silanol groups and a second band around 3600 - 3640 cm^{-1} for the bridging Si(OH)Al groups. Compared to MAZ samples, LTL spectra present one additional broad band at ~3250 cm^{-1} indicating the presence of bridging OH groups, which establish hydrogen bonds with neighbouring oxygen atoms in the 4- or 6-membered rings. Higher concentrations of Brønsted and Lewis acid sites were found for ion exchanged LTL samples. The accessibility of the acid sites towards pyridine adsorption in MAZ samples was ~20% and this may be due to the limited accessibility towards the probe molecule. This aspect is in agreement with the N_2 adsorption-desorption results and confirms the low accessibility to BAS due to the narrowness of the porous systems in MAZ samples.

In addition to the ion exchanged zeolites characterisation, the synthesis of mazzite was performed. Four syntheses were attempted by varying the amount of NaOH in the preparation mixture. It was observed that the increasing amount of NaOH affected the purity of the product. From the XRD analysis of samples at higher amounts of NaOH (3g), additional phases where detected such as sodalite, faujasite and gmelinite while, with 4g of NaOH, sodalite was found as the dominant phase. With lower amounts of NaOH (1g and 2g) a purer product was obtained. The presence of Na cations plays an important role. An excess of it generates hexagonal prisms and sodalite cages and the consequent formation of FAU and SOD. The presence of TMA in the synthesis, which is essential, generates double sawtooth chains, and from their links, gmelinite cages are developed where TMA cations are occluded. The obtained products was also evaluated by SEM. Mazzite prepared with 2g of NaOH showed crystals of 1-2 microns and particles of spherulitic morphology. By contrast, less pure mazzites showed rough surfaces and anhedral crystals. Pure mazzite sample was analysed with N_2 adsorption-desorption, which pointed out the narrowness of the porous system and the low surface area typical of this zeolite. NH_3-TPD was employed to characterize the strength of acid sites of this mazzite sample and it was compared with LTL zeolite. Data revealed the higher acidity of mazzite acid sites, however the results suggest evidence of transport limitations during ammonia desorption due to pore blockage confirming the pore narrowness seen in the N_2 adsorption-desorption results.

Another part of this PhD project was focused on the employment of zeolites for sensing purposes. This work represents the prosecution of a previous research where the intention was to illustrate the tests performed and the results obtained. In this work, mixtures of graphite and zeolites ball milled in 40:60 ratio were prepared and pressed as pellets to be used like pencils to make electrodes. The developed procedure called the “hand drawn” method consisted of depositing by abrasion the material contained in the pellet on an acetate stubastrate previously etched with sand paper. Several mixtures were prepared where in each of them a different zeolite was used. Employed zeolites were NaX, NaA and K-LTL. Resistance of the electrodes was measured and values under 3kΩ only were accepted. The electrodes were tested by using electrochemical investigation techniques such as potentiometry, cyclic voltammetry and electrochemical impedance spectroscopy. Each technique was used to investigate a specific aspect of the employed materials in contact with aqueous solutions. Potentiometry was used to obtain the activity coefficients to produce calibrations curves. This was done by adding standards at known concentrations containing K^+ to a starting volume of deionised water. The response of the electrodes in contact with this solution and their capability to detect concentrations close to Nernstian response were tested. From the first attempts, the “hand drawn” method showed its limits such as leaching in the solutions in contact with the electrodes. Among the zeolite components, only K-LTL showed the closest result to the Nernstian response to K^+ cations with slopes of 44.53 mV/decade for the fresh electrode and 41.67 mV/decade for the overnight dried and re-tested electrode. This aspect confirmed the hydrophilic nature of zeolites, however it may represent a drawback for a second use of the same electrode. Although the sensor may recover its response after drying it, operation which would take hours, the leaching phenomenon would increasingly affect the response after each additional use forcing the operator to prepare a new electrode. In order to avoid the leaching phenomenon, an alternative preparation method was attempted mixing graphite and K-LTL with nail polish 50%:50% m m^{-1} to make an ink. The obtained material was deposited on the previously etched acetate substrated with an airbrush. Although no leaching was observed, a potentiometric response of 22.52 mV/decade to K^+ was recorded. The employment of this method showed several difficulties related to the deposition procedure of the ink where the manual skills play a key role. Cyclic voltammetry pointed out the limiting nature of zeolites in employing the tested electrodes made with the "hand drawn" method to study redox systems. Indeed, since zeolites are not electroactive, their presence hinders the electrochemical conversion of species on the surface of the mixed material, possible only when in contact with graphite. In addition, the non-homogenous distribution of the mixed material represents one of the main drawbacks of these electrodes with cyclic voltammetry. Greater peak currents for reduction and oxydation were observed a consequence of the in-homogeneous. Electrochemical impedance spectroscopy pointed out the presence of high resistance between the substrate and the material deposited with the "hand drawn" method. This was observed with only deposited graphite and suggests that there is not a proper flow of electrons between the two components.

This work shows the differences between LTL and MAZ, two zeolites employed in catalysis that share similarities in terms of structure but differences in terms of acidic properties. Although the high acidic nature of MAZ is reported in literature, the investigated MAZ samples did not show great evidence of this behaviour. The work also exploits X-Ray diffraction and Rietveld method to shed light on the migration of cations during the ion exchange and gives a general idea of the "journey" of these species through the zeolite structures. The employment of zeolites mixed with grahite for sensing purposes showed several limitations, hence, the employed methodologies require further research.

5.2 Future recommendations

5.2.1 LTL and MAZ, the acidic and structural properties

- Additional tests of ion exchanged materials of these zeolites should be performed. The ion exchange preparation described in this work followed by calcination should be investigated since the contribution of high temperatures might allow cations to reach inner cages in the studied zeolite structures giving the chances for instance to Cs^+ to reach cancrinite cage in LTL. The same conditions should be employed for MAZ to observe the difference in terms of amount of introduced cations with the hydrated samples. Also, post-synthetic treatments should be investigated as well as the consequent evaluation of introduced species with ion exchange.
- Quantitative analysis of the chemical composition for instance using XRF should be carried out. Moreover, further work is required for the optimisation of the mazzite synthesis.
- XRD patterns recorded at longer scanning time are recommended for the prepared materials. This might improve the results obtained through the Rietveld refinement and it may be beneficial for a better understanding of the extra peaks found at low angles in LTL samples. The employment of different software packages to perform the Rietveld method would be recommended not only for results comparison but also to find better solutions for limitations that affect some software packages. The cation migration mechanism needs more investigation and improvements. For MAZ and ion exchanged samples additional tests are required due to results where a good agreement between experimental and calculated patterns were introduced cations were found in unexpected locations such as *t-kaj* cage.

- More tests are recommended for NH_3-TPD since very few samples were investigated. Ion exchanged samples should be investigated to understand how the introduction of extra framework cations affects the desorption of ammonia. These tests should be extended to ion exchanged LTL and MAZ zeolites.
- The employment of the studied LTL and MAZ zeolites for catalytic evaluation would be recommended. Tests of these materials and applications for hydrocarbon conversion would be a great addition to the present research.

5.2.2 Electrochemistry

- Based on the results reported in chapter 4, further research is recommended to find an alternative substrate material to reduce the resistance with the sensing mixture. The employment of zeolites requires more tests as well since their use as simple addition exploiting their ion exchange and porosity properties did not give the expected results. Modifications and alternative procedures are recommended as well. A suggestion would be to perform the ion exchange on these zeolites with active species such as copper or silver. Also, alternative materials different than zeolites are suggested. An interesting addition to the study might be to test carbon materials such as CMK-3 that offer (meso) porosity and may work as electroactive component simultaneously mimicking the combined aspects zeolites and graphite reducing also the resistance generated from the combination of particles of two different materials.

Chapter 6

Appendix

6.1. List of figures

Chapter 1

Chapter 2

Chapter 2 Appendix figures list

Chapter 3

Chapter 3 Appendix figures list

Chapter 4

Chapter 4 Appendix figures list

6.2 List of tables

Chapter 2

Chapter 3

Chapter 4

Chapter 6

Appendix figures

Chapter 2

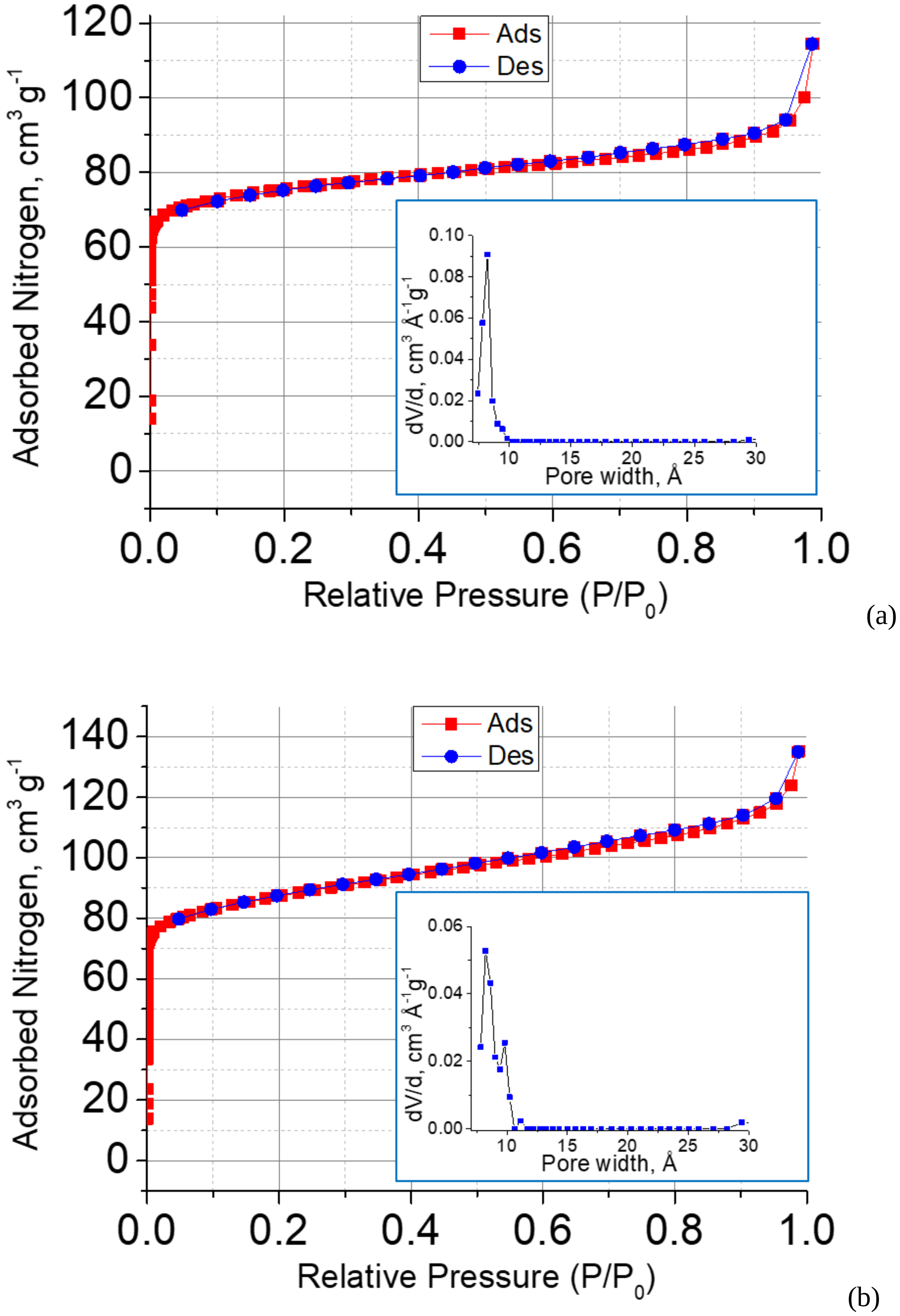

Figure 2A.1 (a – b): Nitrogen adsorption-desorption isotherms for Rb-NH_4-K-LTL (a) and K-NH_4-K-LTL (b). The inserts show the pore size distributions for these materials.

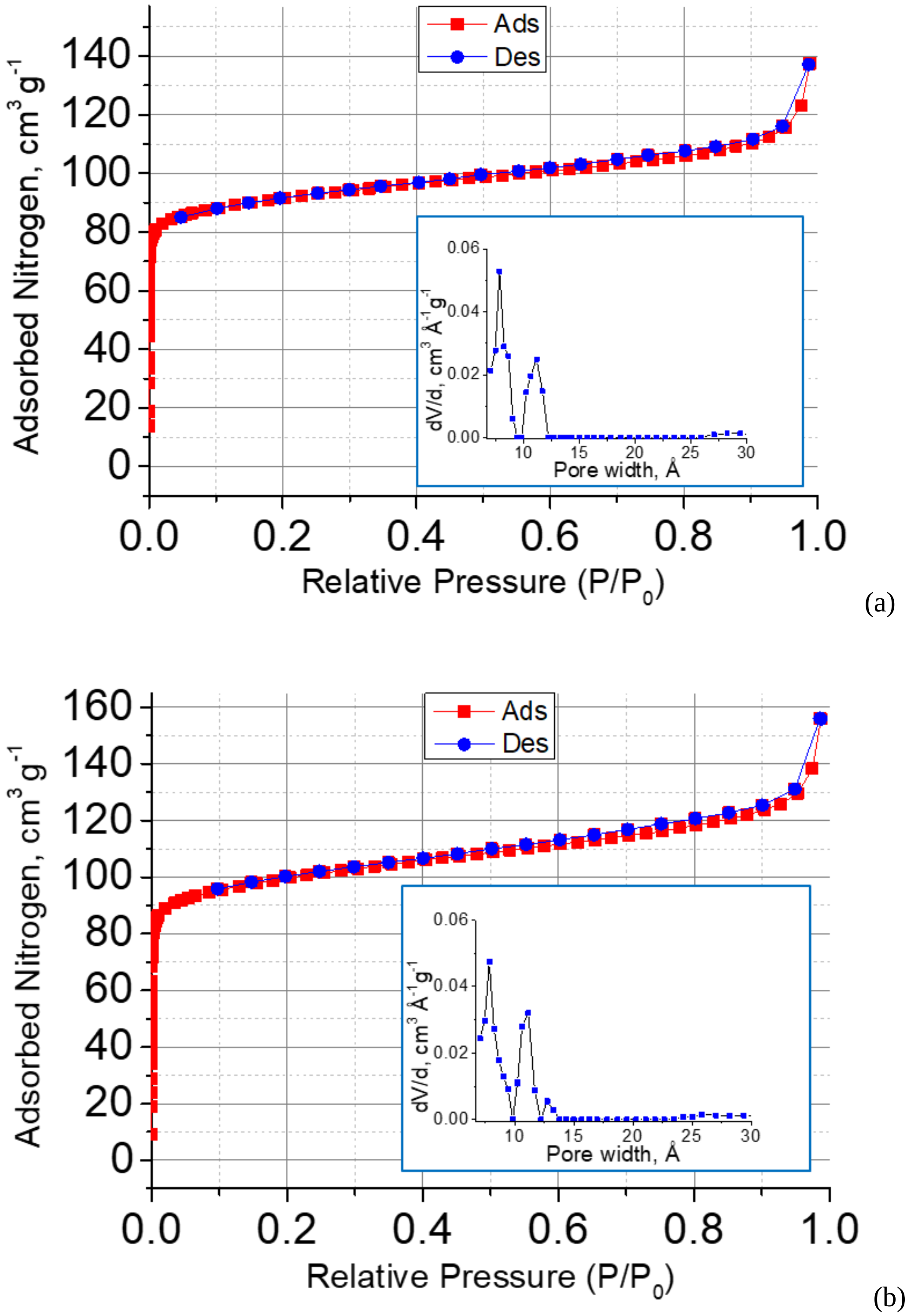

Figure 2A.2 (a – b): Nitrogen adsorption-desorption isotherms for Na- NH_4-K-LTL (a) and Li-NH_4-K-LTL (b). The inserts show the pore size distributions for these materials.

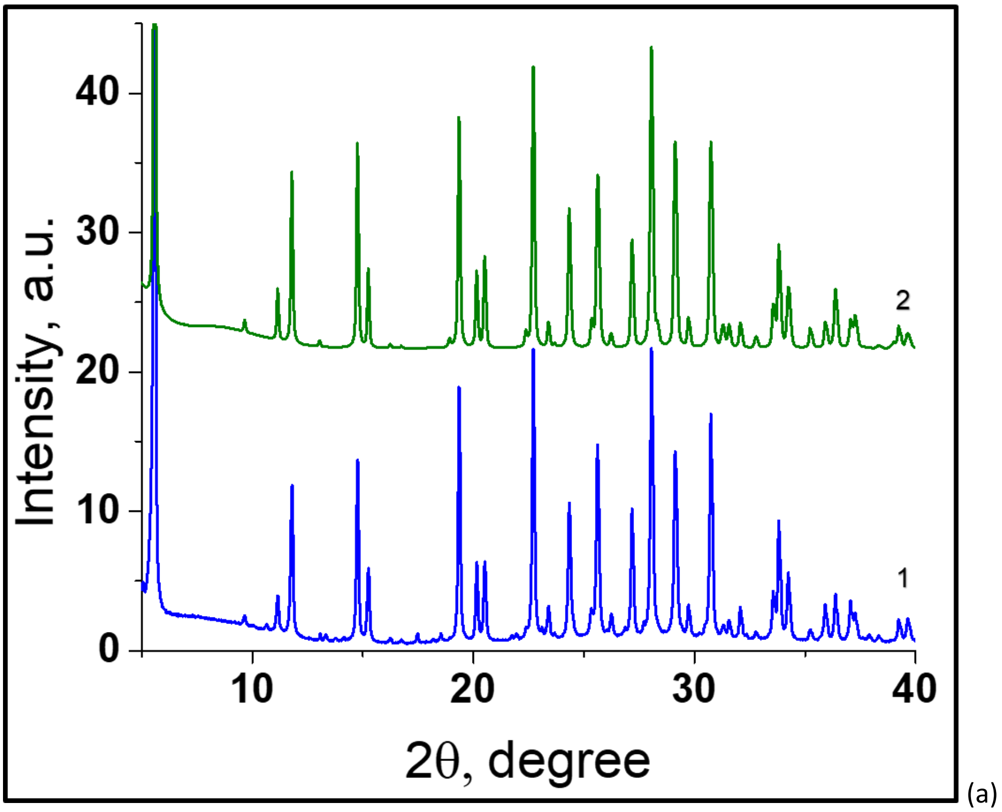

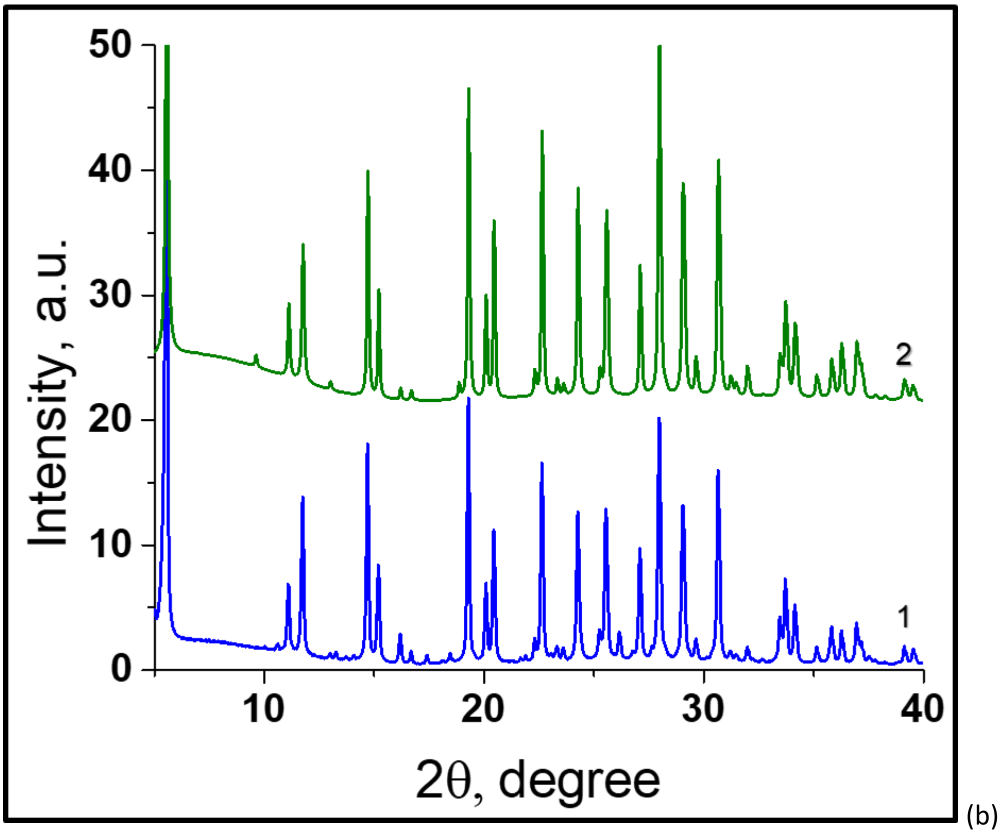

Figure 2A.3 (a – b): Experimental (1) and simulated (2) XRD patterns of K-LTL (Tosoh) (a) and NH_4-K-LTL (b).

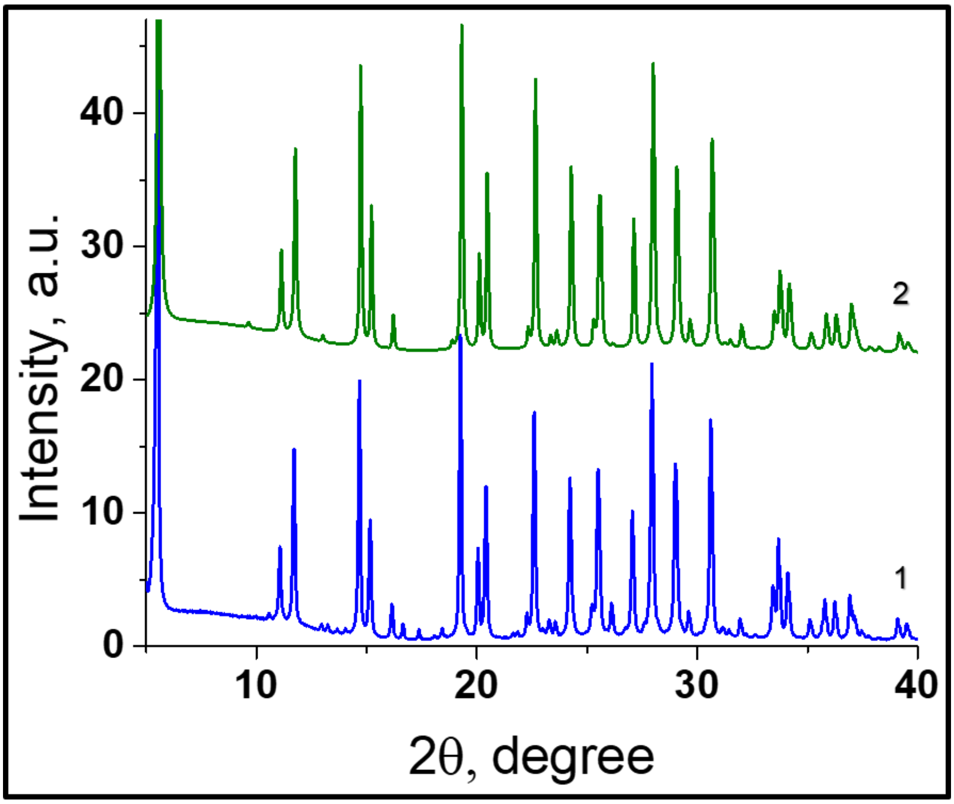

(a)

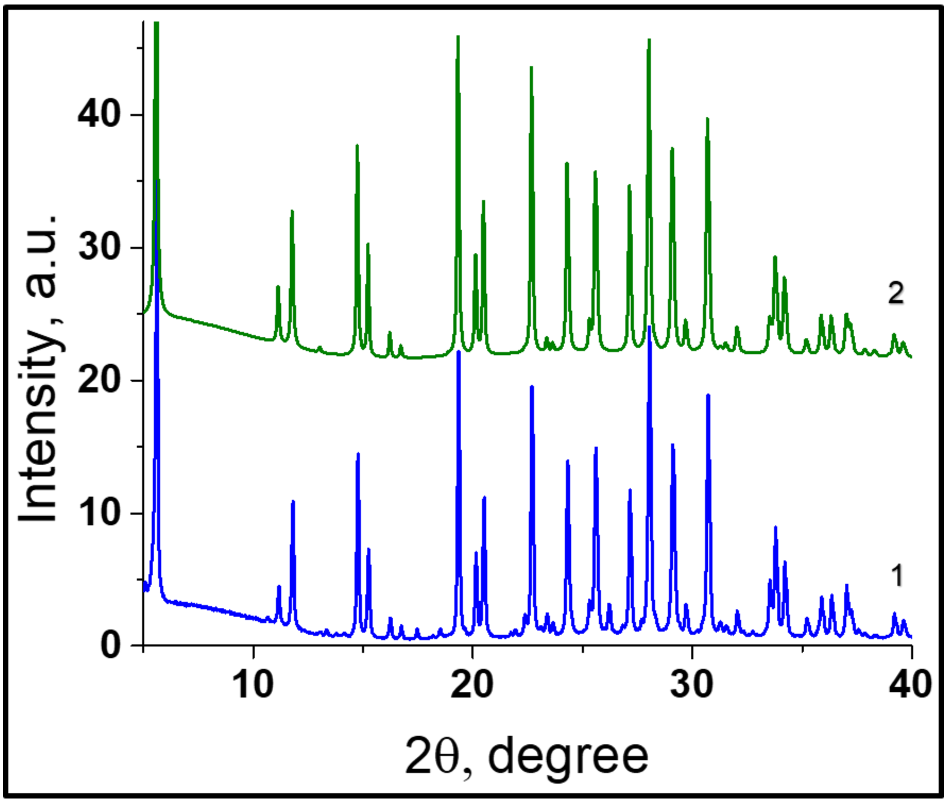

(b)

Figure 2A.4 (a – b): Experimental (1) and simulated (2) XRD patterns of (a) Li-NH_4-K-LTL-4 (Tosoh) and (b) Na-NH_4-K-LTL-4.

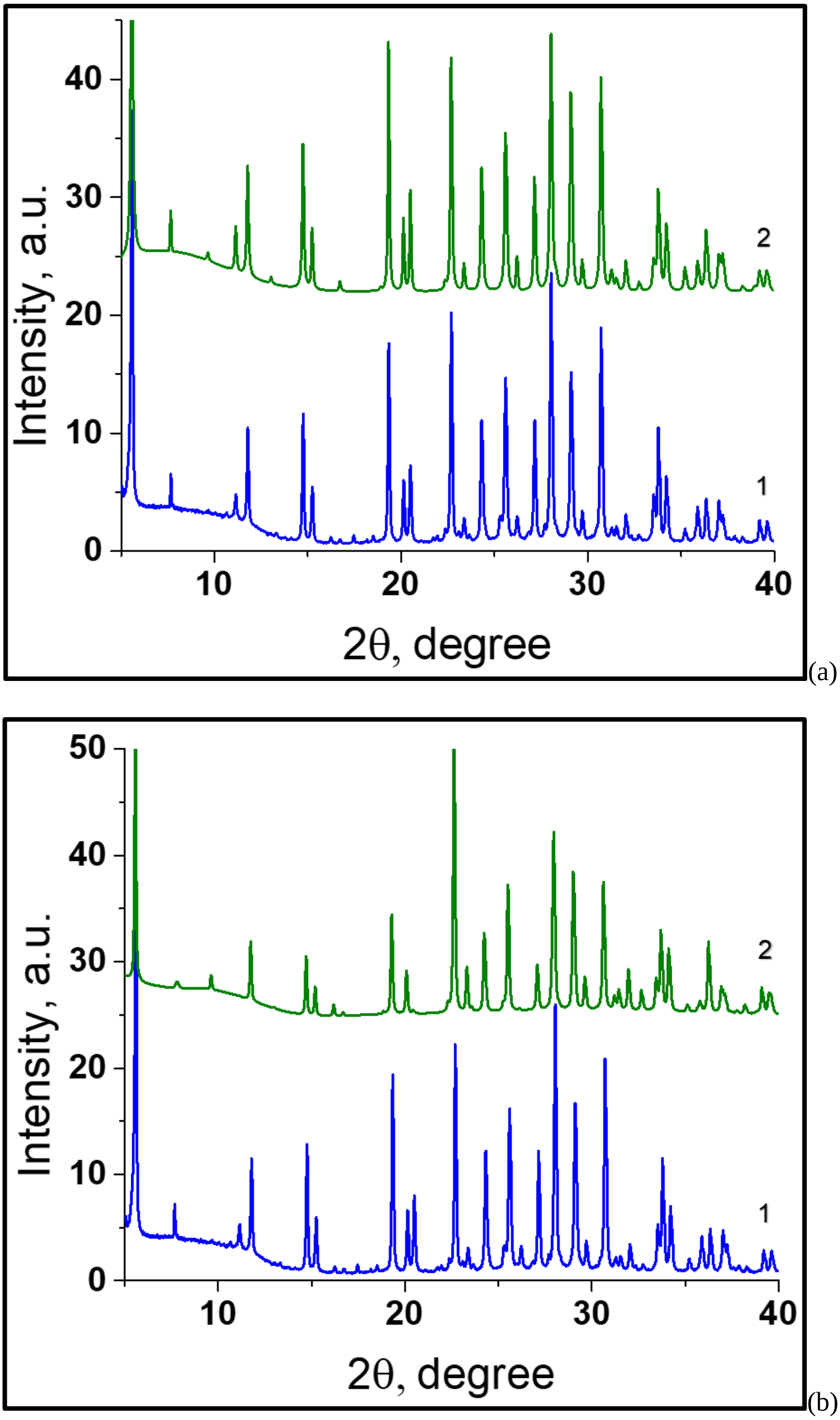

Figure 2A.5 (e – f): Experimental (1) and simulated (2) XRD patterns of (a) K-NH_4-K-LTL-4 and (b) Rb-NH_4-K-LTL-4.

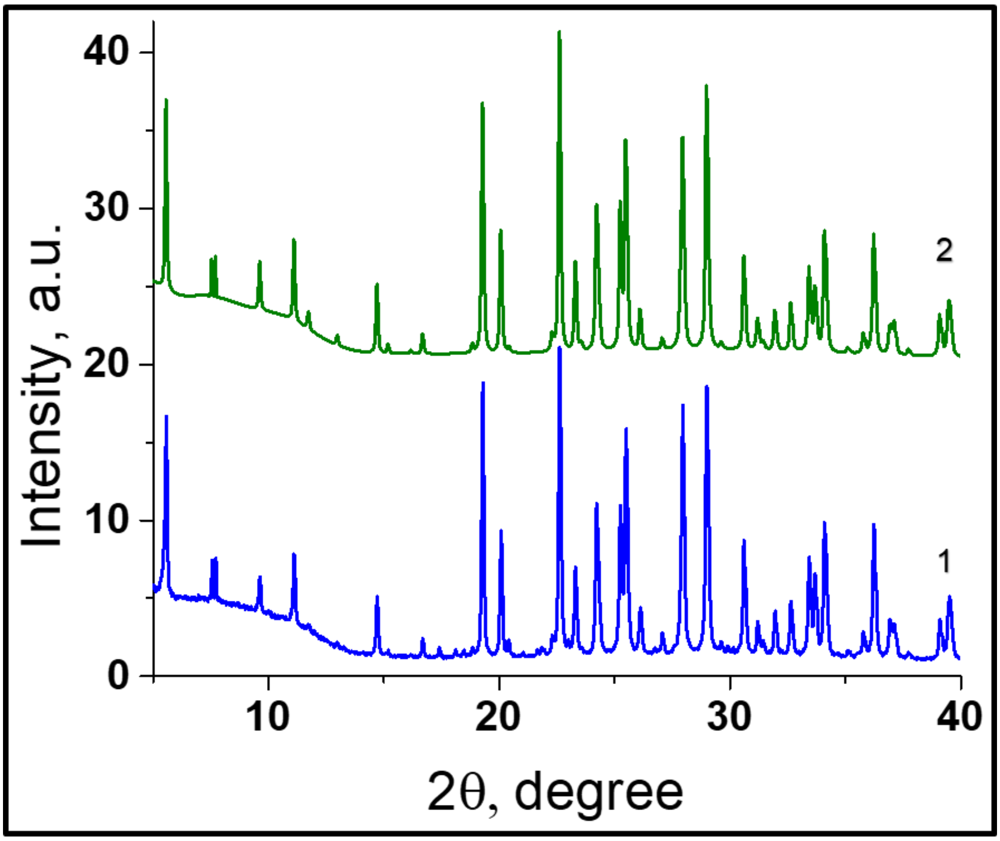

Figure 2A.6: Experimental (1) and simulated (2) XRD patterns of Cs-NH_4-K-LTL-4.

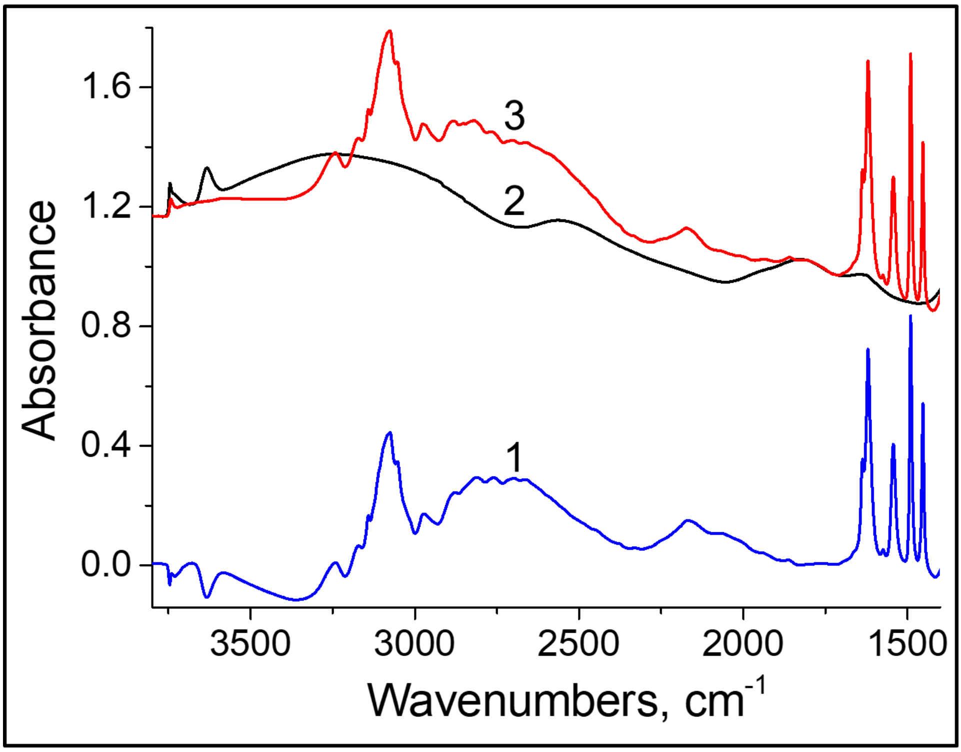

(a)

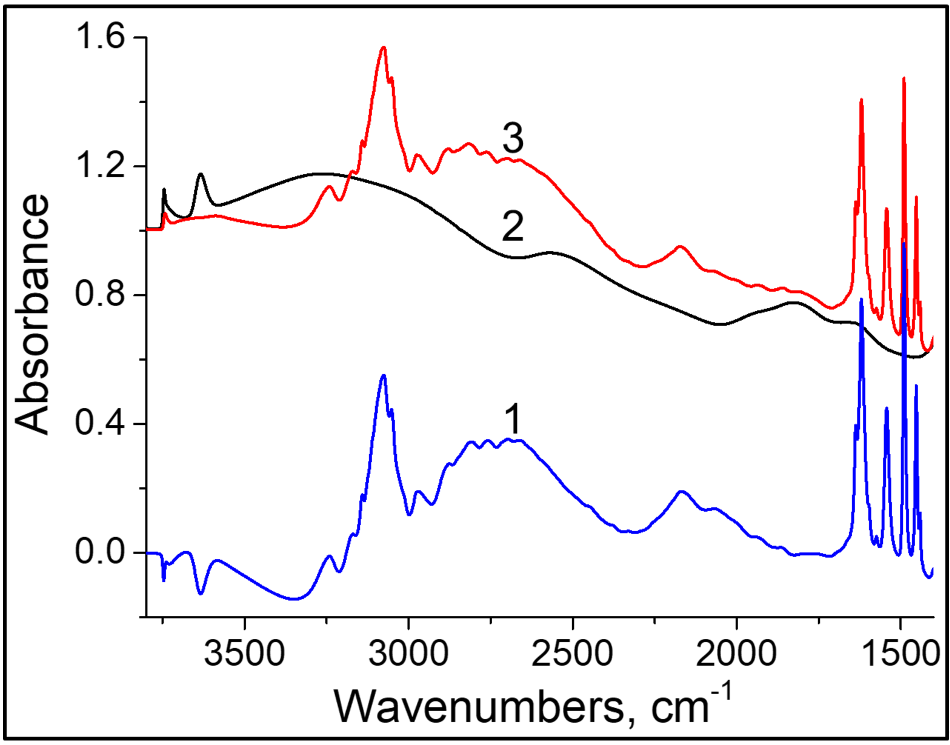

(b)

Figure 2A.7 (a – b): FTIR spectra of (a) NH_4-K-LTL (b) Li-NH_4-K-LTL: (1) - the material before Py adsorption, (2) - the material after Py adsorption at 200°C and (3) - the difference spectrum.

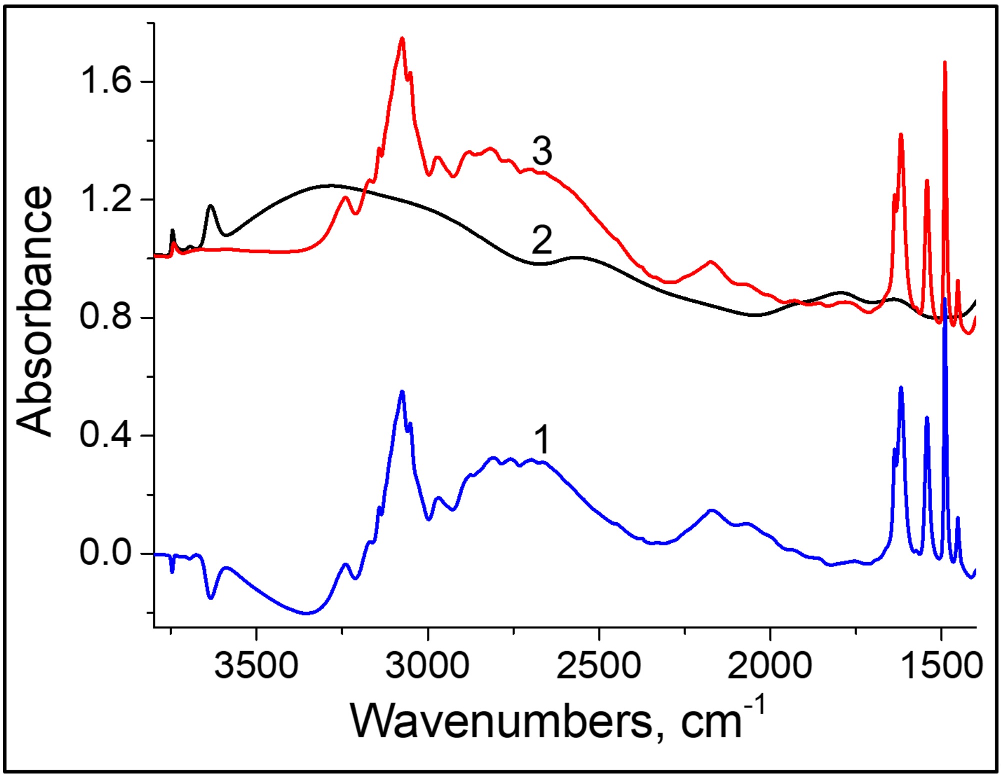

(a)

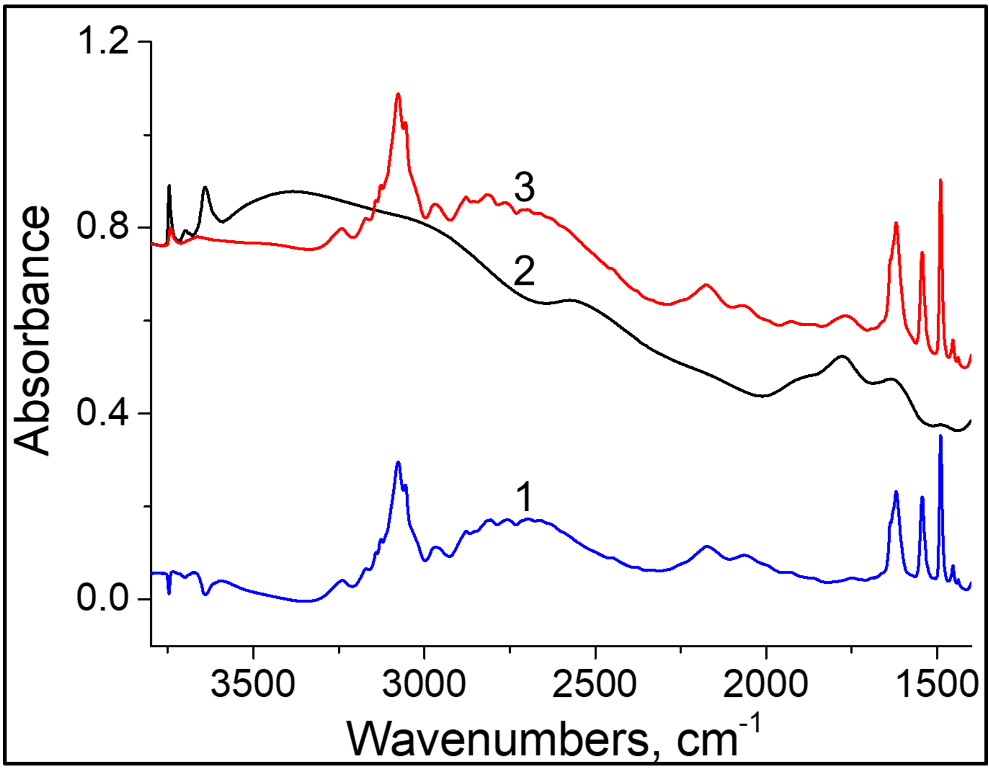

(b)

Figure 2A.8 (a - b): FTIR spectra of (a) Na-NH_4-K-LTL and (b) K-NH_4-K-LTL: (1) - the material before Py adsorption, (2) - the material after Py adsorption at 200°C and (3) - the difference spectrum.

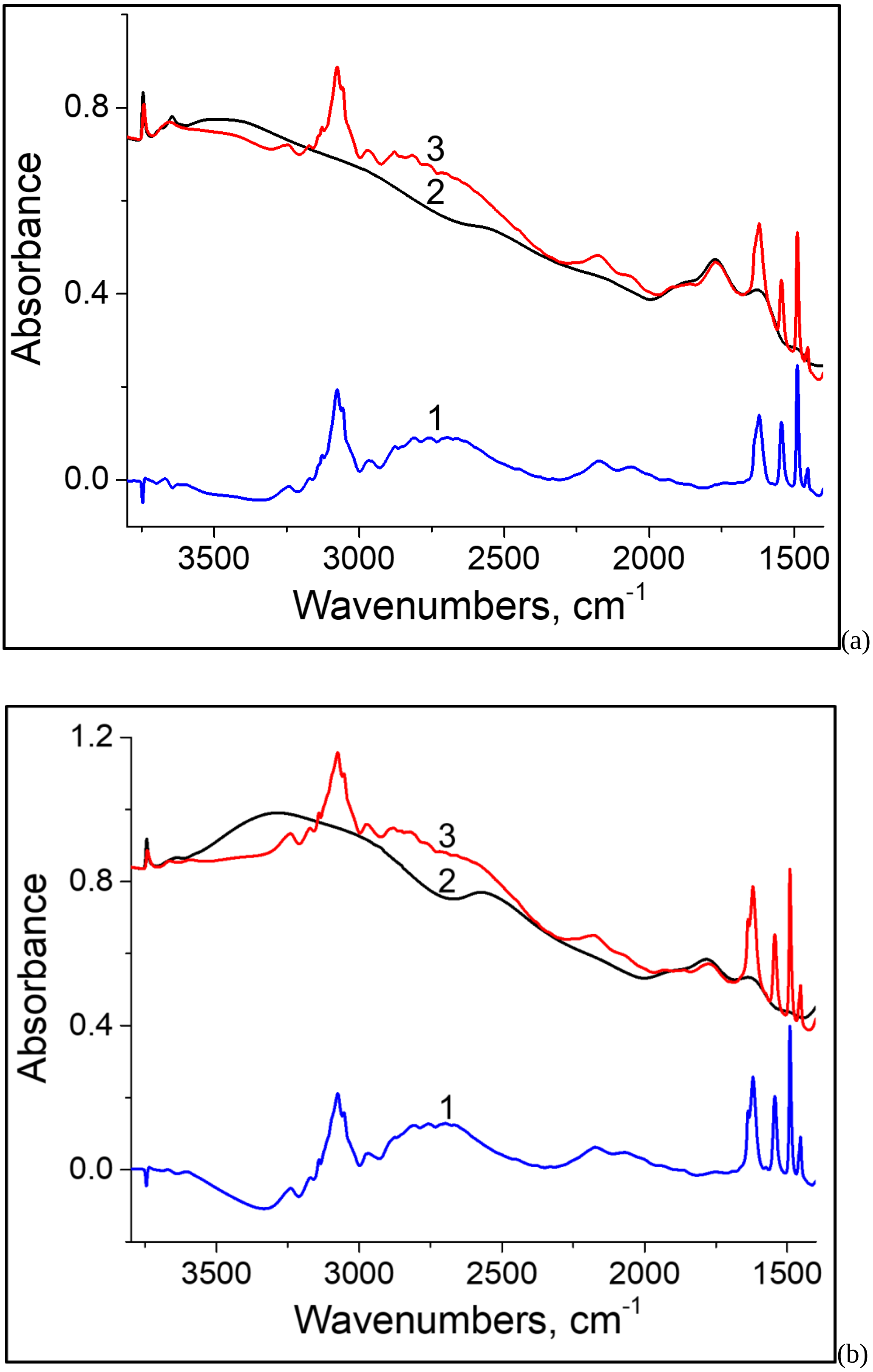

Figure 2A.9 (a - b): FTIR spectra of (a) Rb-NH$_4$-K-LTL and (b) Cs-NH4-K-LTL: (1) - the material before Py adsorption, (2) - the material after Py adsorption at 200°C and (3) - the difference spectrum.

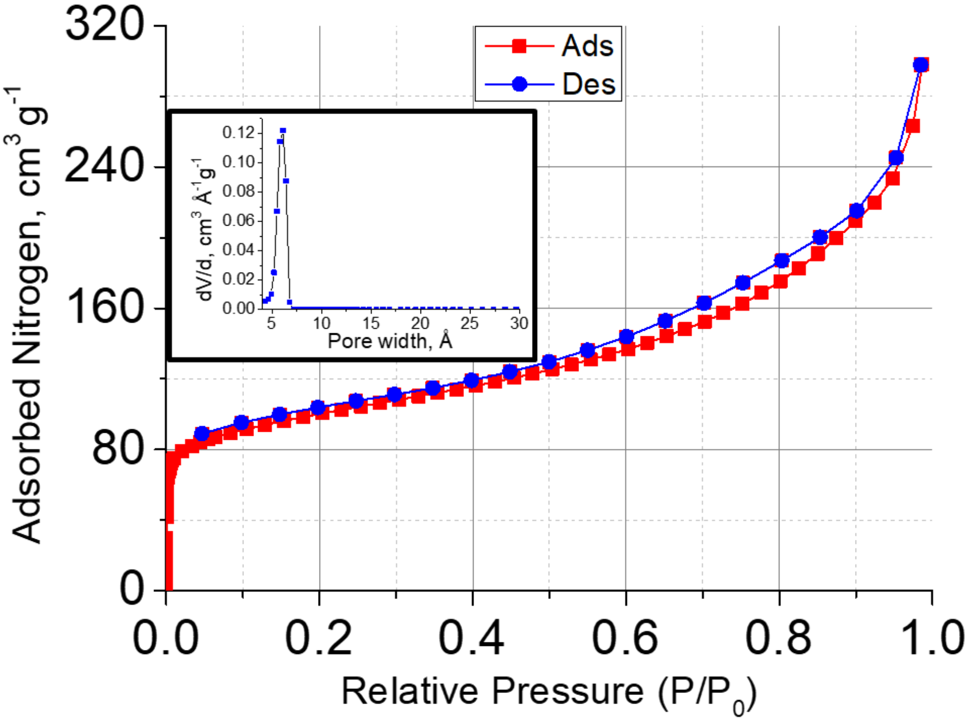

(a)

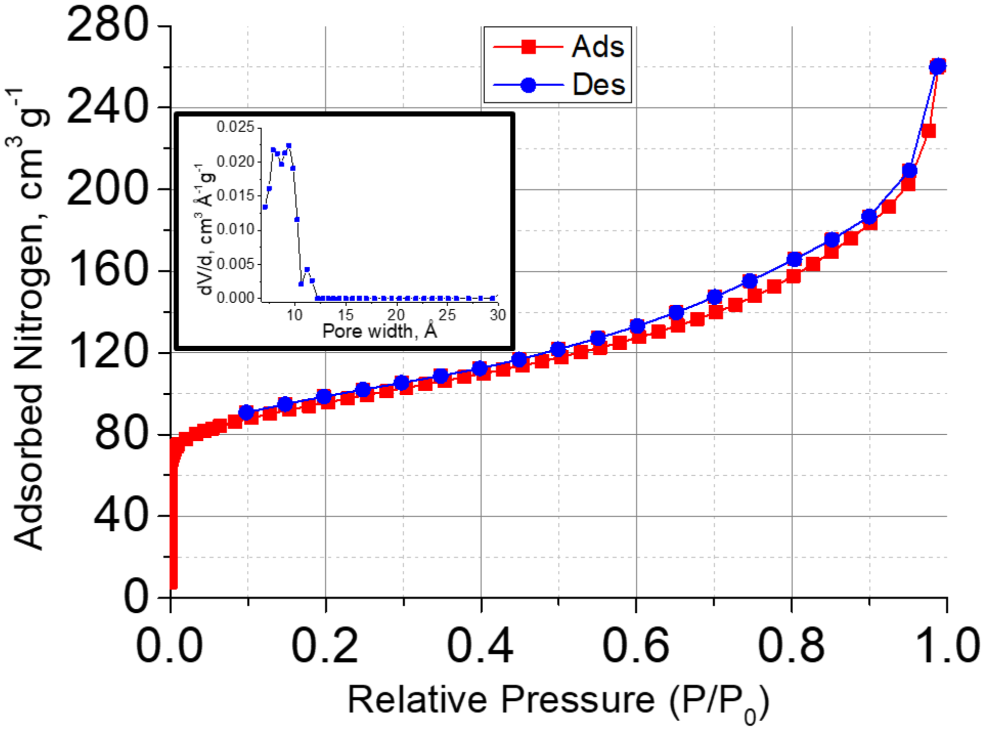

(b)

Figure 3A.1: Nitrogen adsorption-desorption isotherms and for H-MAZ (a) Na-H-MAZ (b).

The inserts show the pore size distributions for these materials.

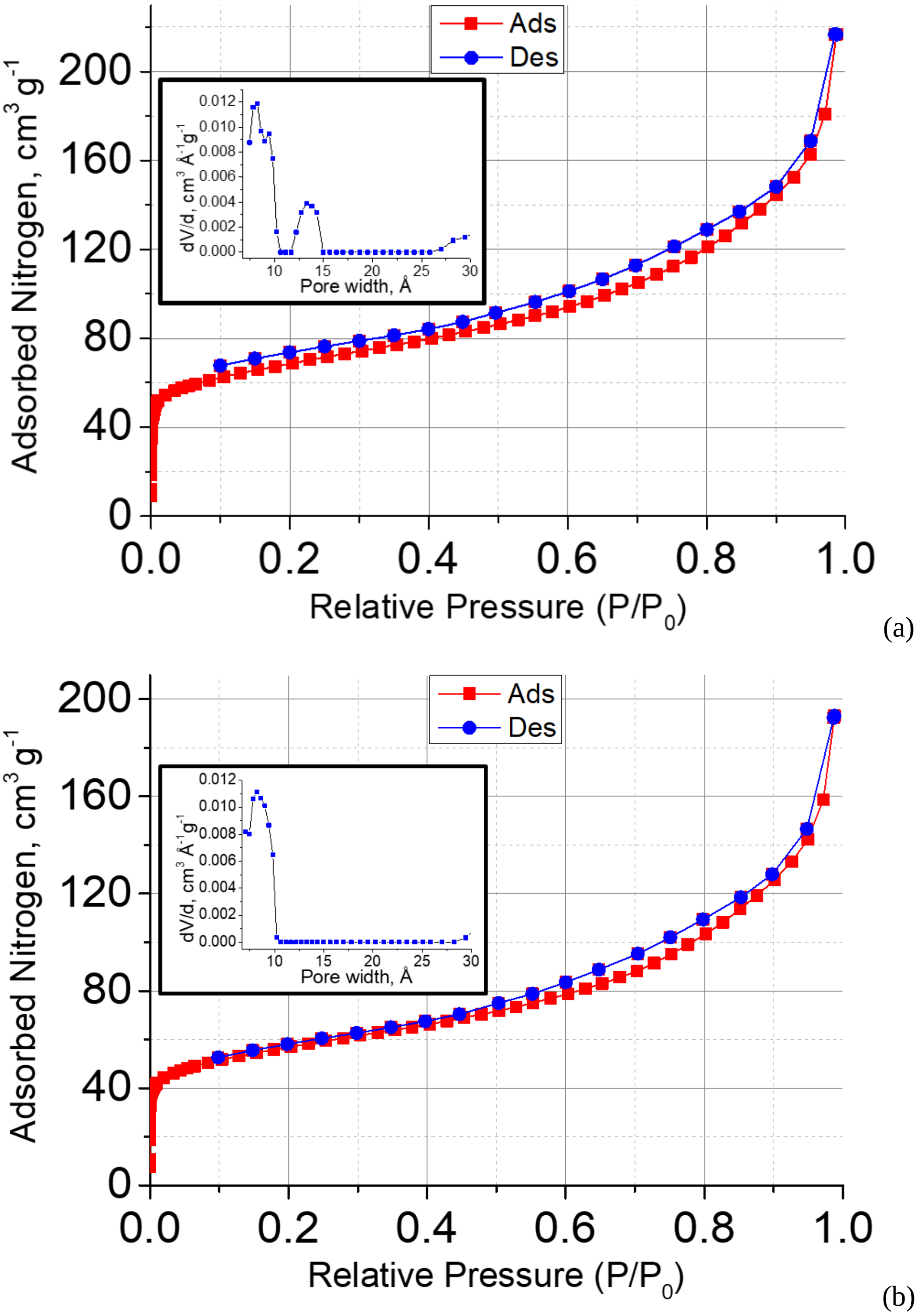

(a)

(b)

Figure 3A.2: Nitrogen adsorption-desorption isotherms for K-H-MAZ (a) and Rb-H-MAZ (b). The inserts show the pore size distributions for these materials.

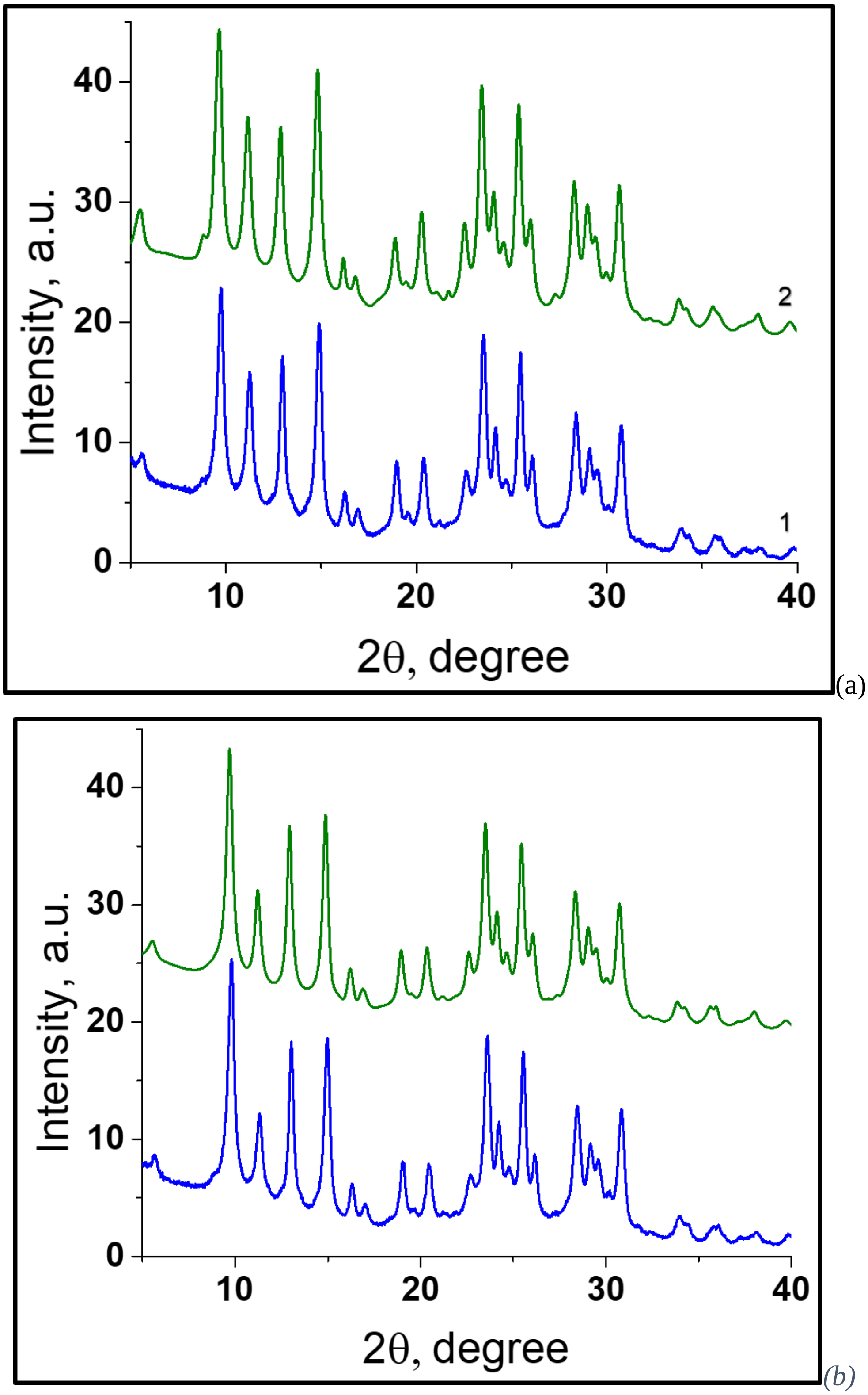

Figure 3A.3: Experimental (1) and simulated (2) XRD patterns of H-MAZ (a) and Na-H-MAZ (b).

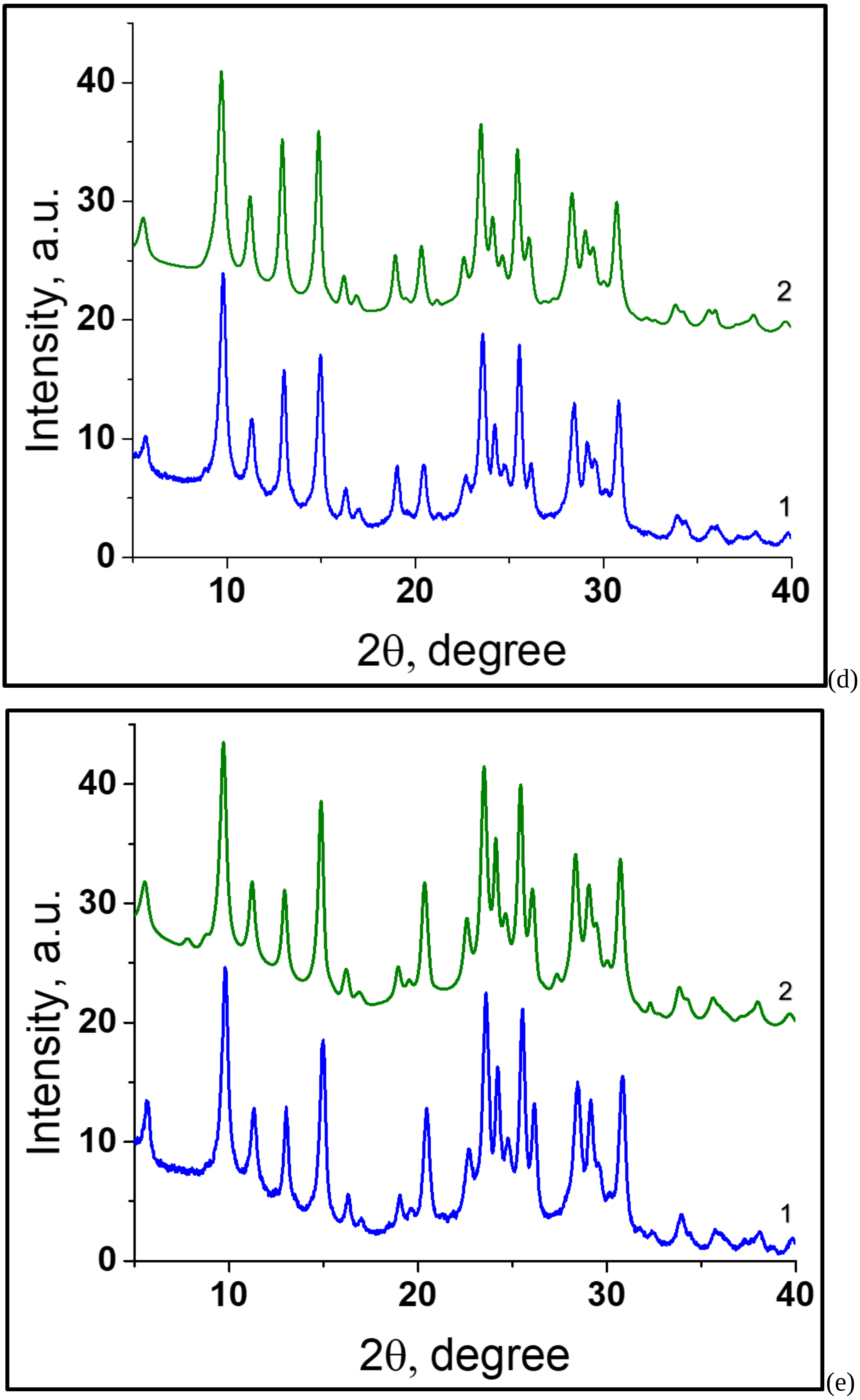

Figure 3A.4: Experimental (1) and simulated (2) XRD patterns of of K-H-MAZ (a) and Rb-H-MAZ (b)

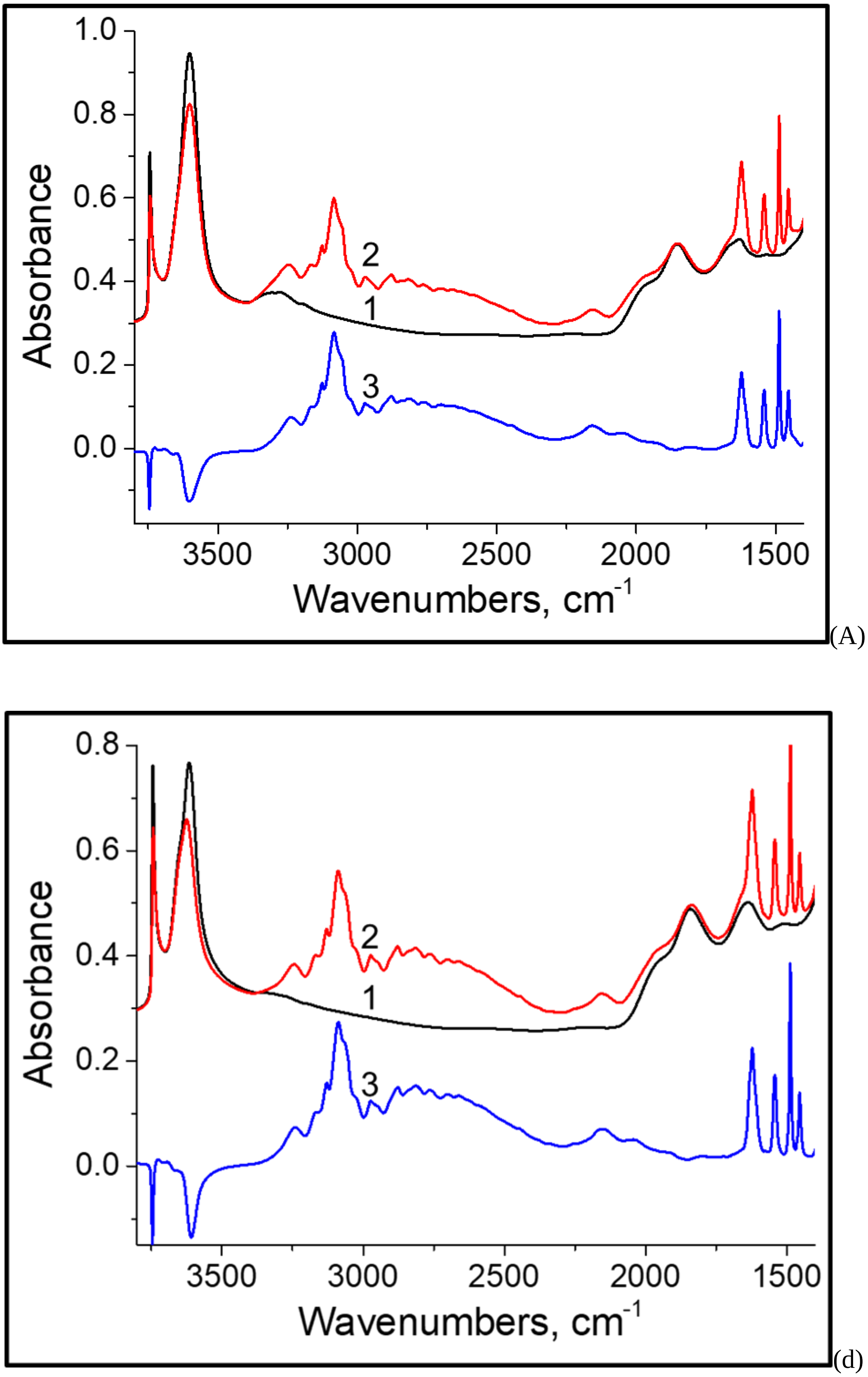

Figure 3A.5: FTIR spectra of (a) Li-H-MAZ and (d) K-H-MAZ: (1) - the material before Py adsorption, (2) - the material after Py adsorption at 200ºC and (3) - the difference spectrum.

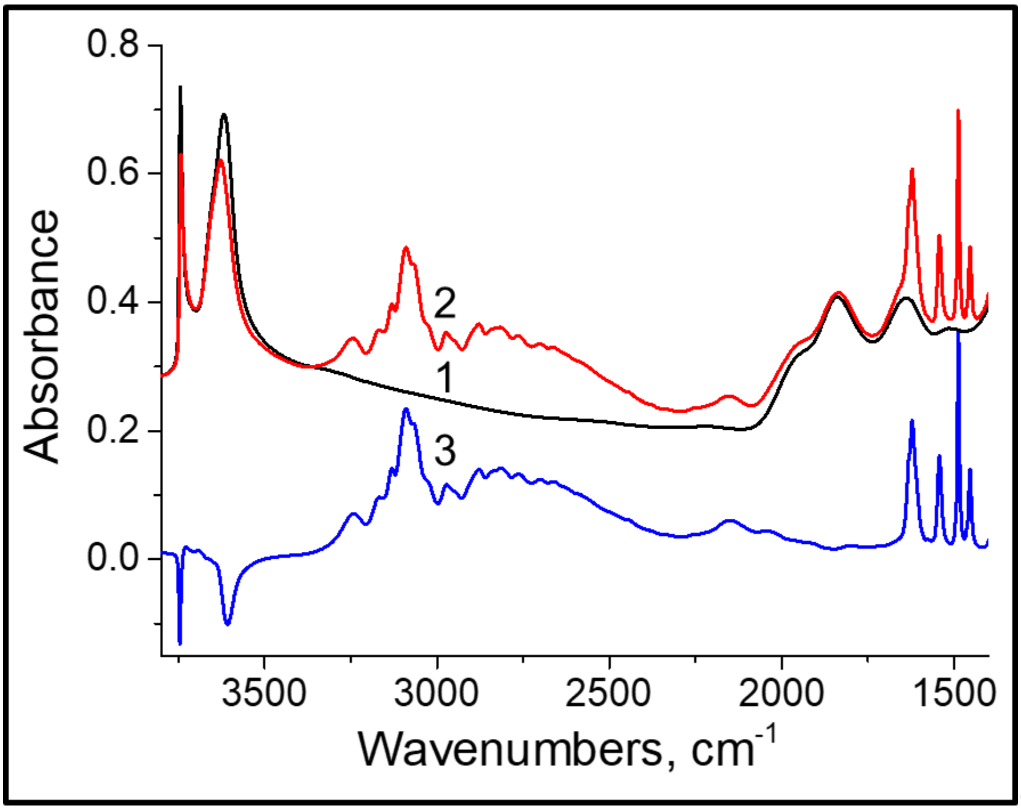

(e)

Figure 3A.6: FTIR spectra of (e) Rb-H-MAZ: (1) - the material before Py adsorption, (2) - the material after Py adsorption at 200°C and (3) - the difference spectrum.

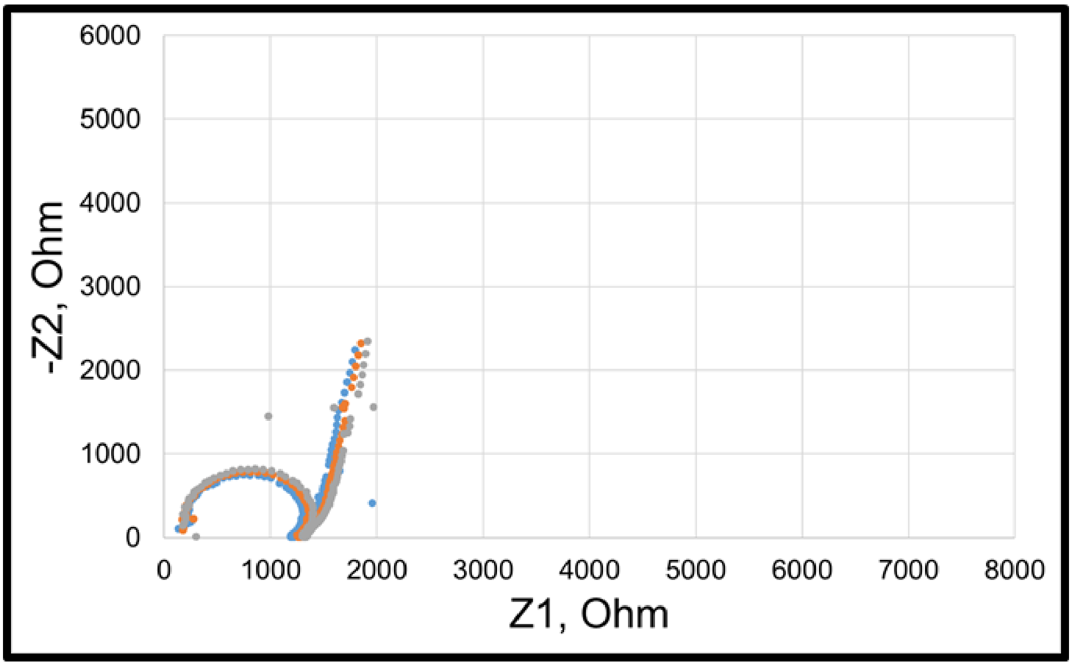

Figure 4A.1: EIS spectrum of K-LTL/graphite electrode In $LiNO_3$ 0.1M.

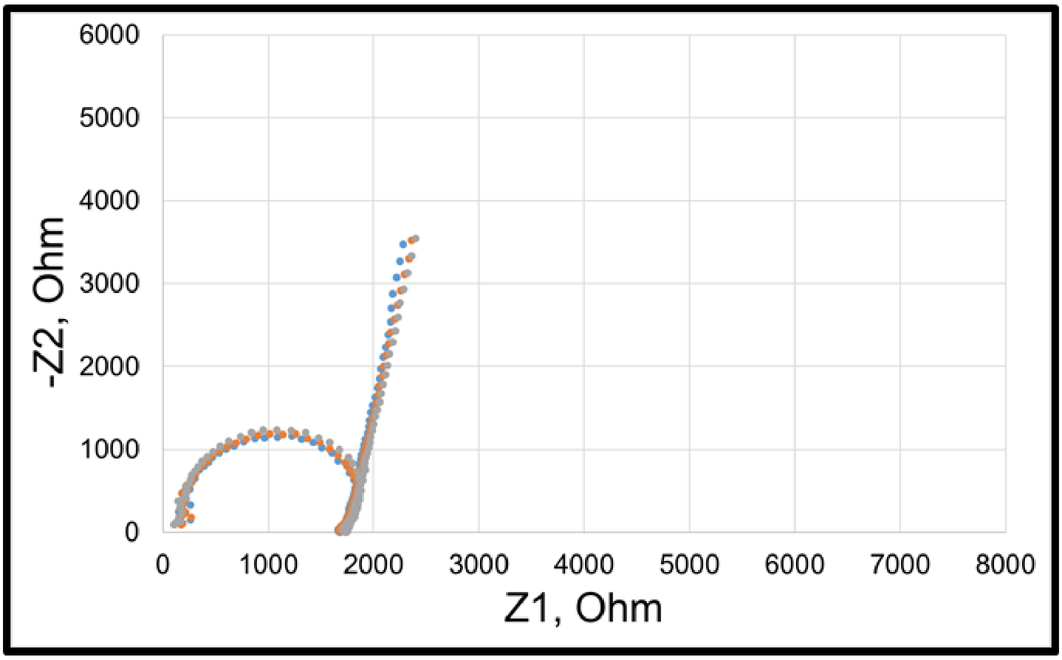

Figure 4A.2: EIS spectrum of K-LTL/graphite electrode In $LiNO_3$ 0.01M.

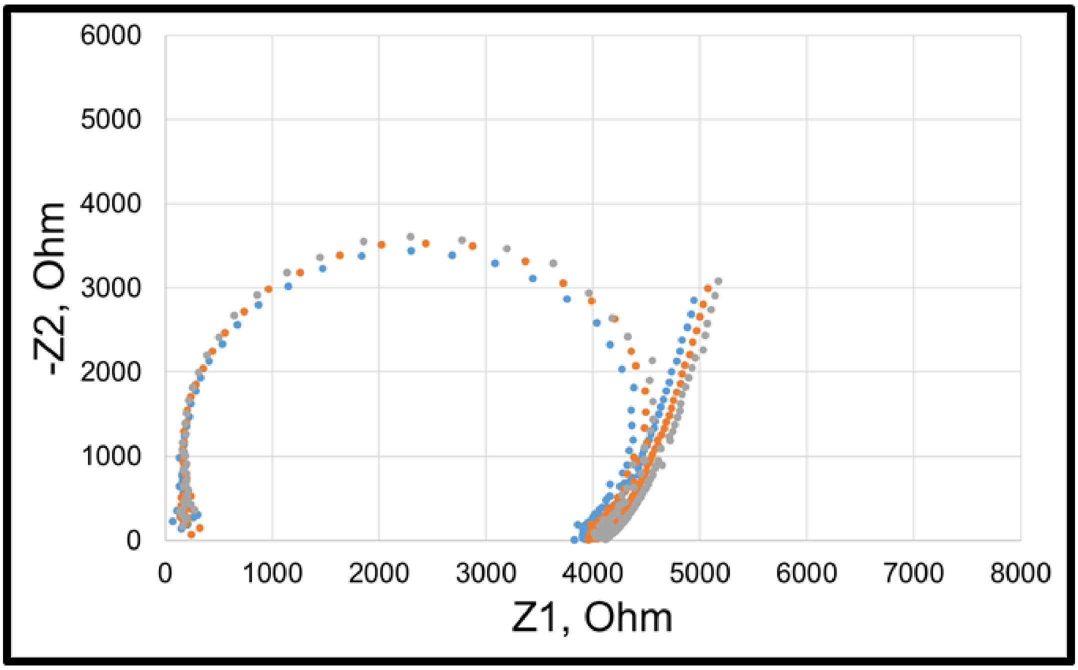

Figure 4A.3: EIS spectrum of K-LTL/graphite electrode In $LiNO_3$ 0.001M.

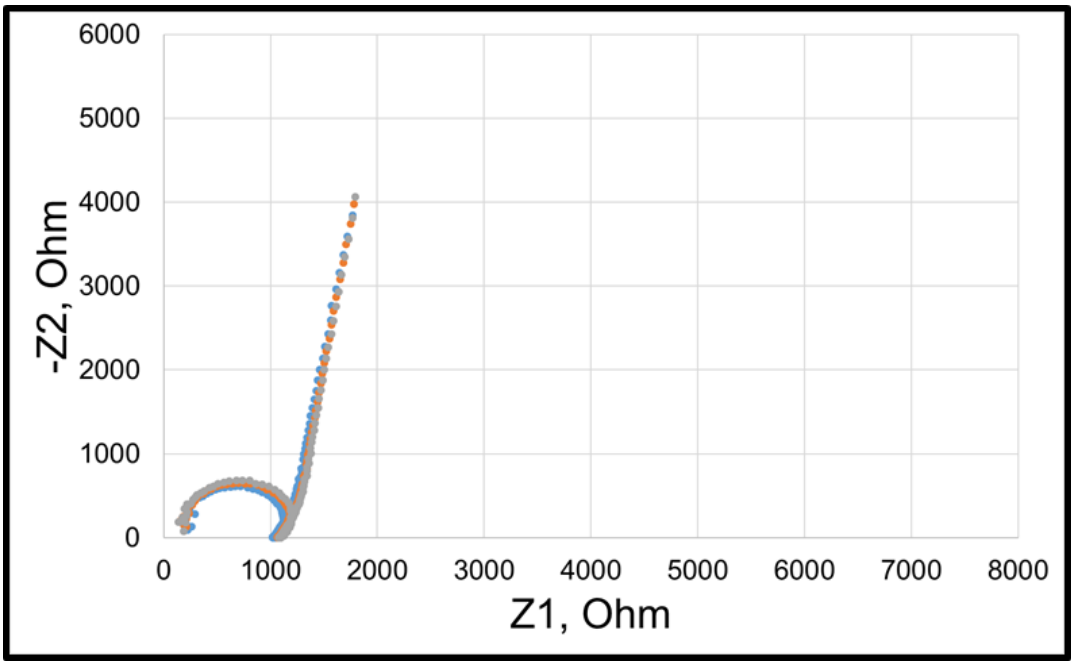

Figure 4A.4: EIS spectrum of K-LTL/graphite electrode In $NaNO_3$ 0.1M.

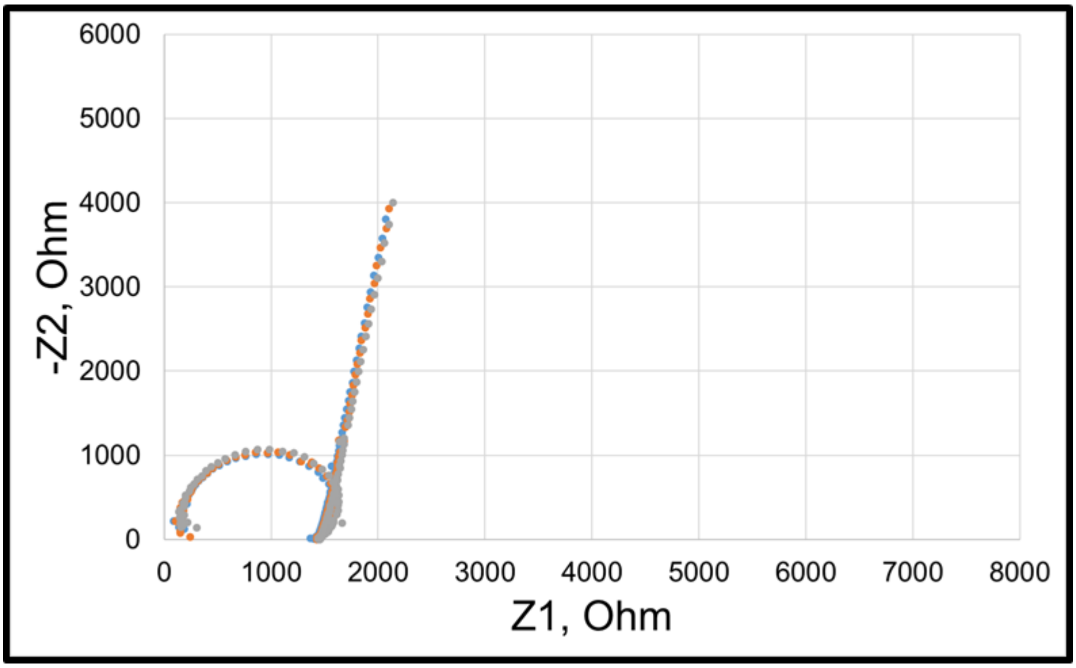

Figure 4A.5: EIS spectrum of K-LTL/graphite electrode In $NaNO_3$ 0.01M.

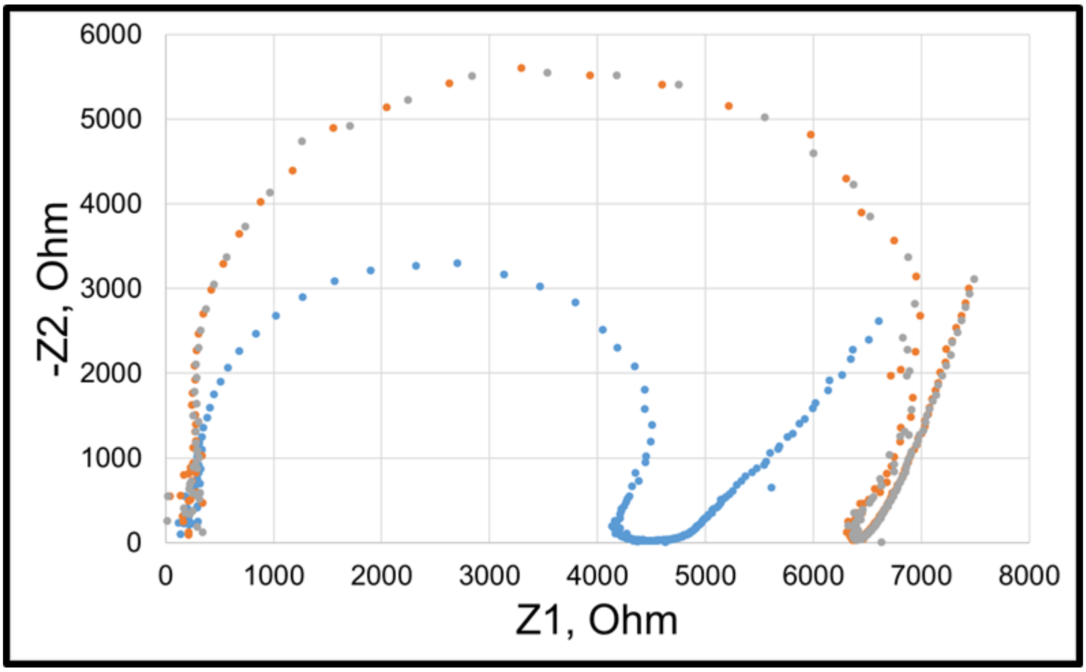

Figure 4A.6: EIS spectrum of K-LTL/graphite electrode In $NaNO_3$ 0.001M.

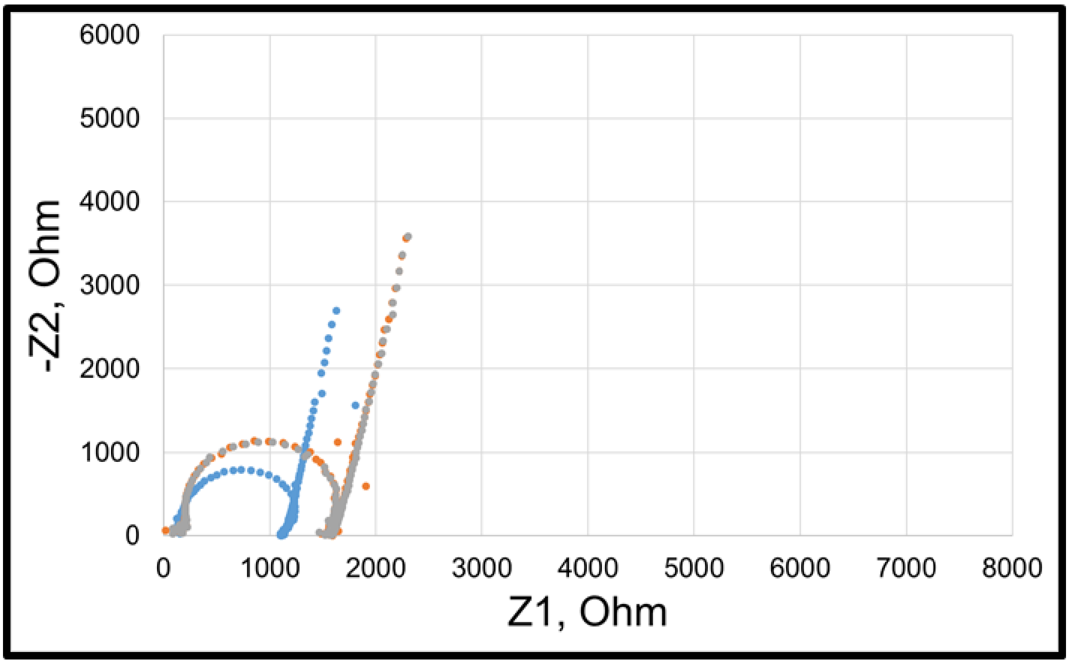

Figure 4A.7: EIS spectrum of K-LTL/graphite electrode In KNO_3 0.1M.

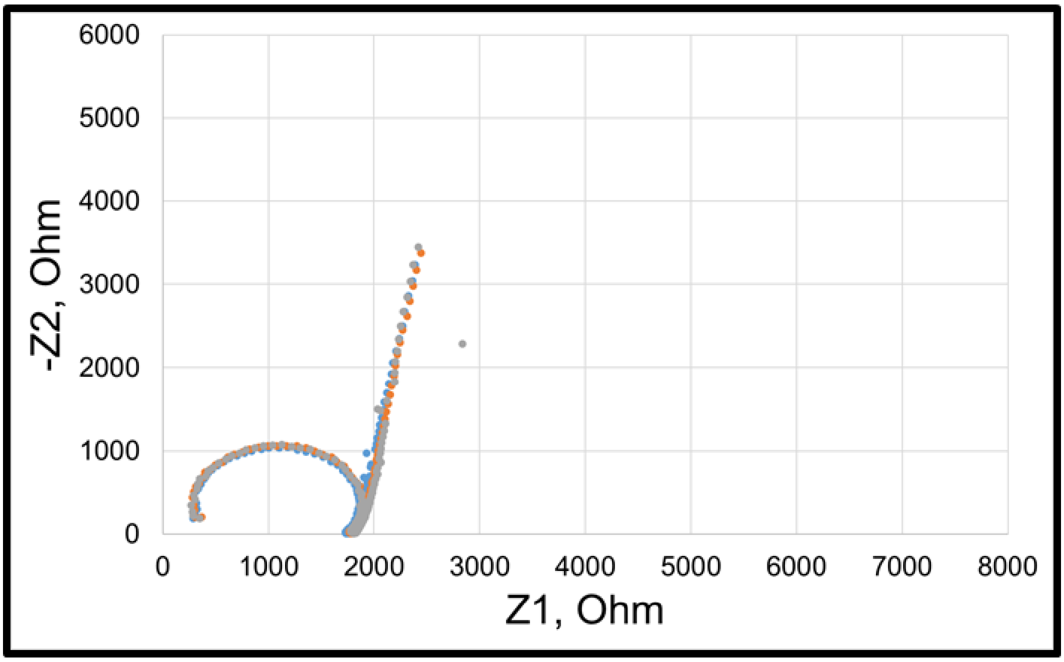

Figure 4A.8: EIS spectrum of K-LTL/graphite electrode In KNO_3 0.01M.

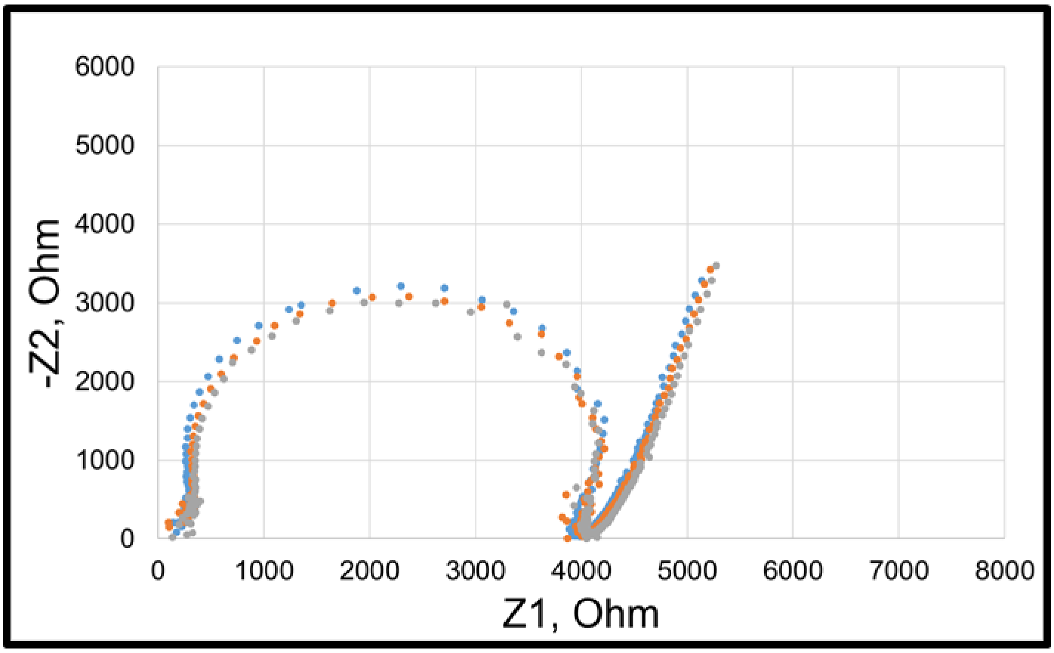

Figure 4A.9: EIS spectrum of K-LTL/graphite electrode In KNO_3 0.001M.

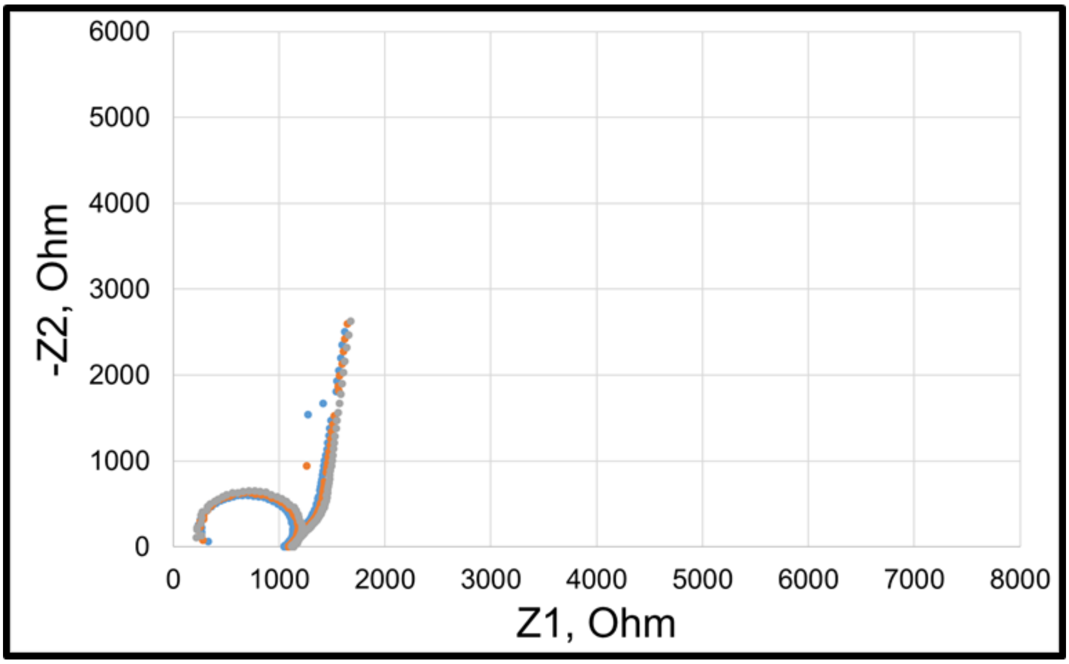

Figure 4A.10: EIS spectrum of K-LTL/graphite electrode In Rb_2CO_3 0.1M.

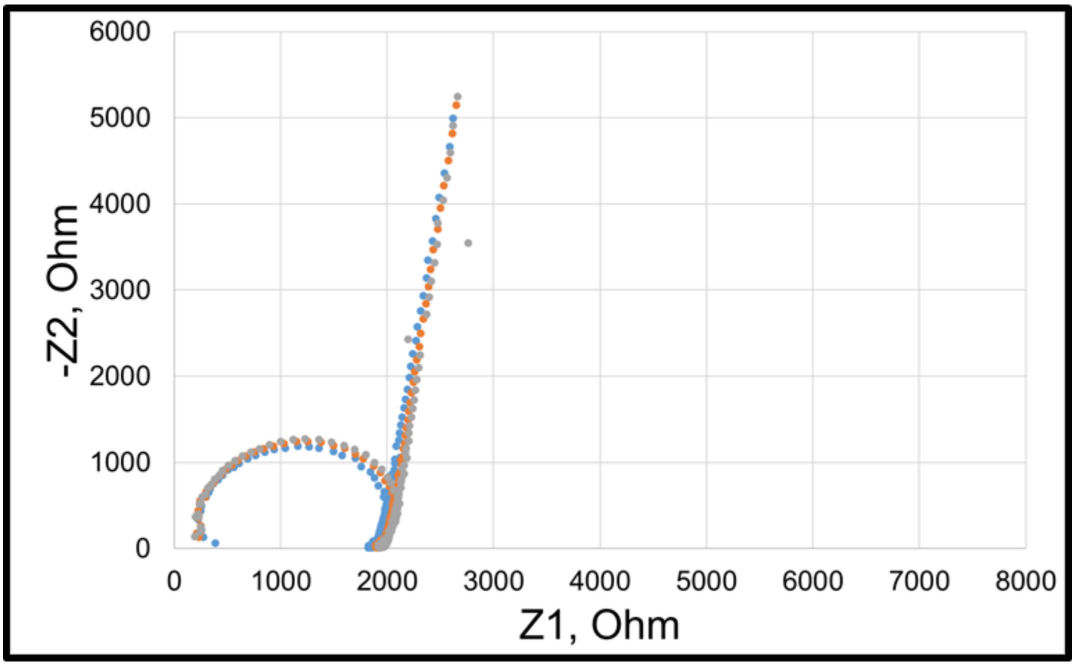

Figure 4A.11: EIS spectrum of K-LTL/graphite electrode In Rb_2CO_3 0.01M.

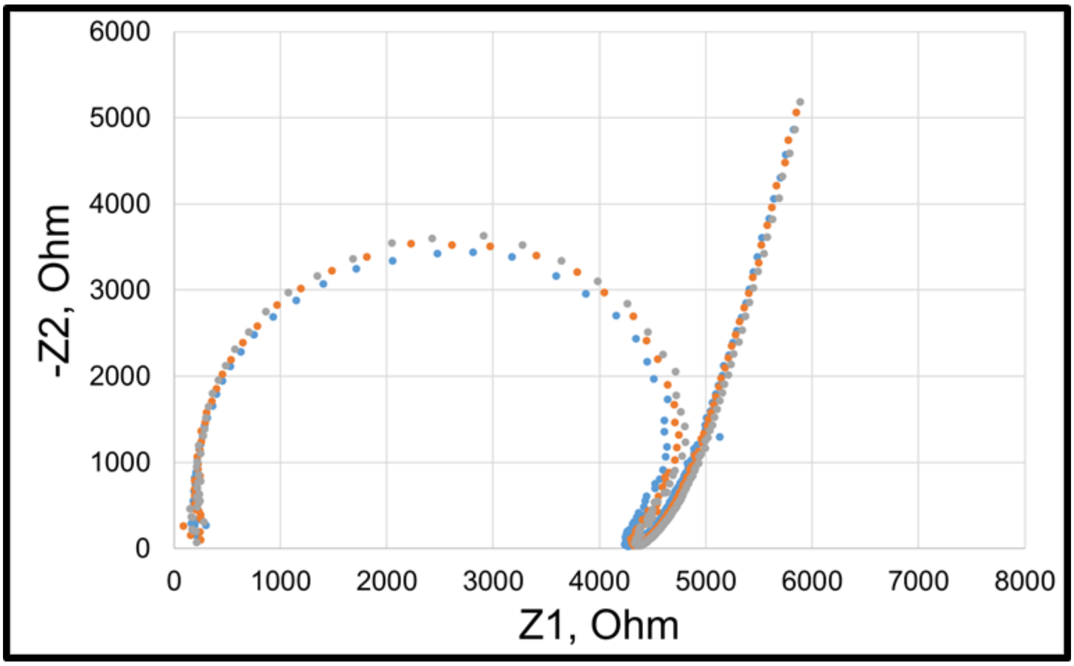

Figure 4A.12: EIS spectrum of K-LTL/graphite electrode In Rb_2CO_3 0.001M.

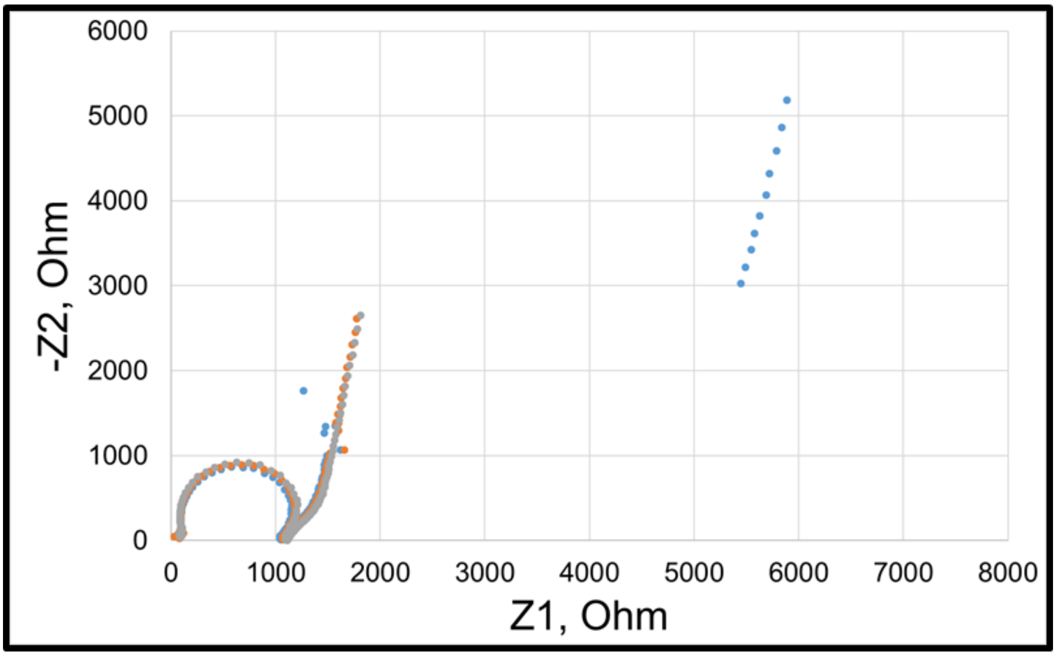

Figure 4A.13: EIS spectrum of K-LTL/graphite electrode In CsCl 0.1M.

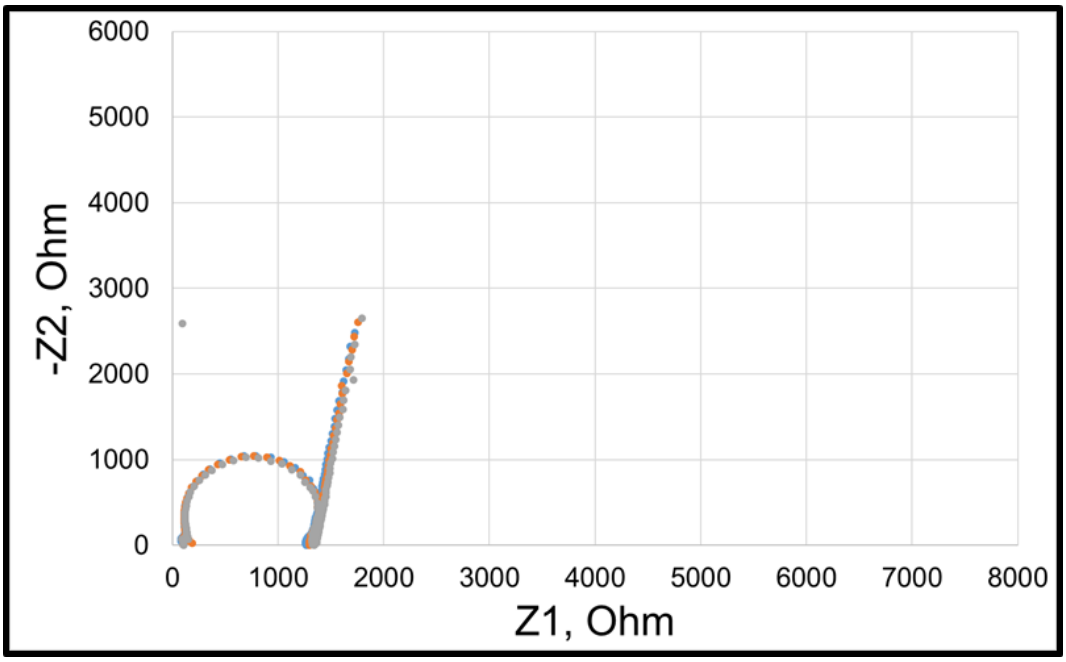

Figure 4A.14: EIS spectrum of K-LTL/graphite electrode In CsCl 0.01M.

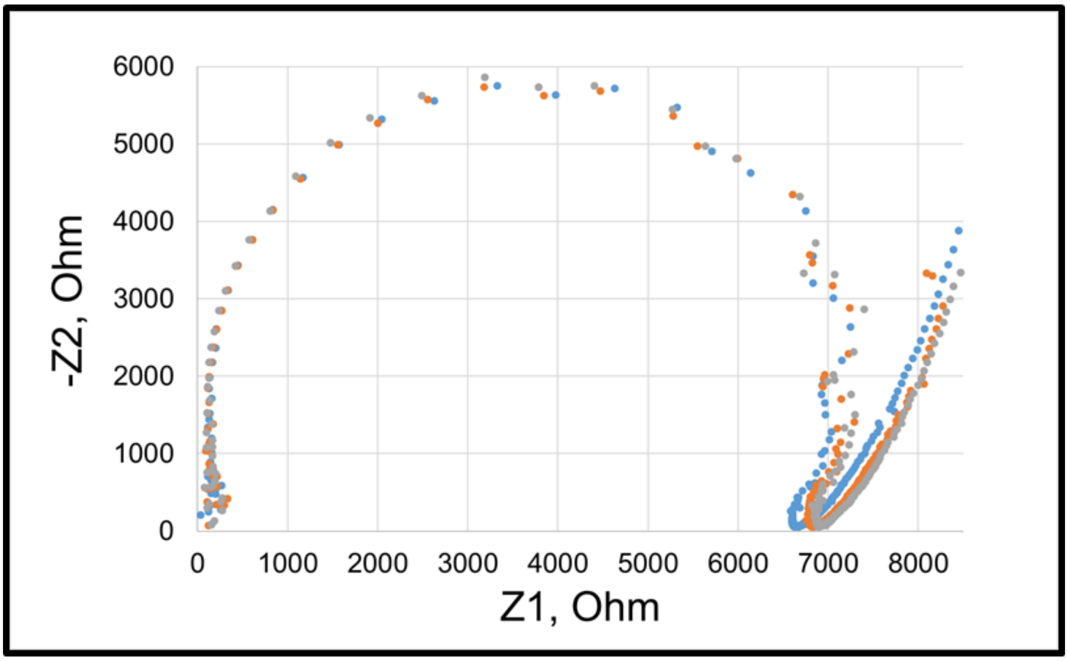

Figure 4A.15: EIS spectrum of K-LTL/graphite electrode In CsCl 0.001M.

LTL Additional figures

XRD

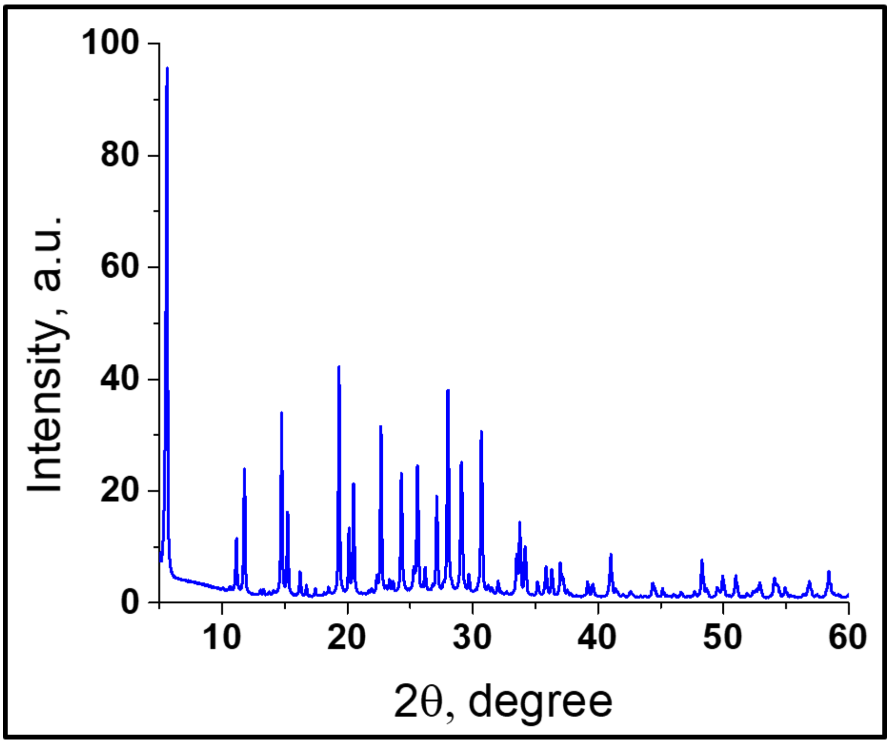

Figure 6.1: Experimental pattern of Li-NH_4-K-LTL-1.

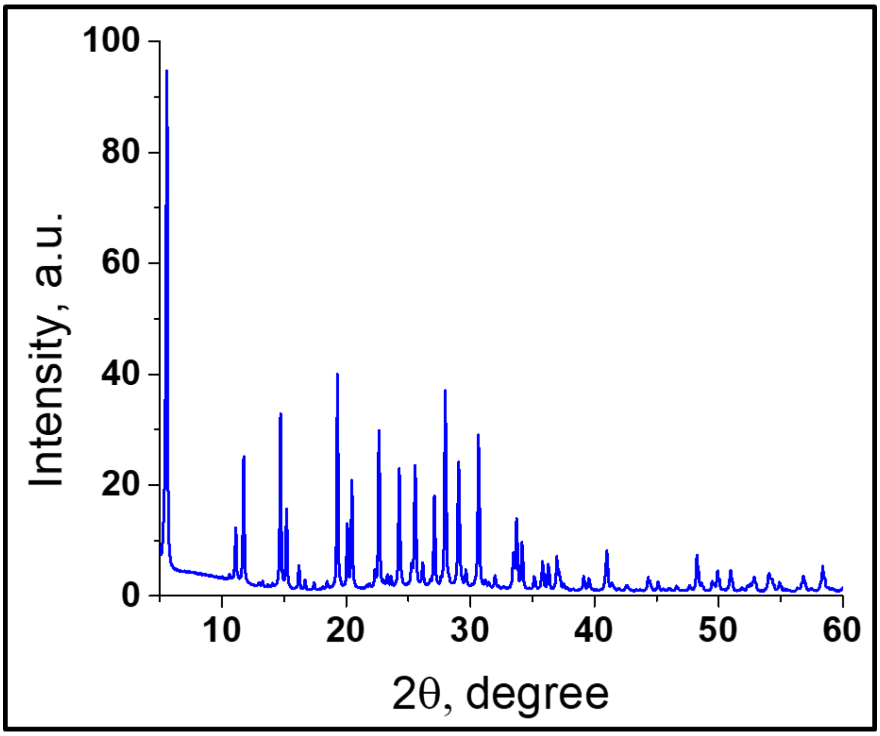

Figure 6.2: Experimental pattern of Li-NH_4-K-LTL-2.

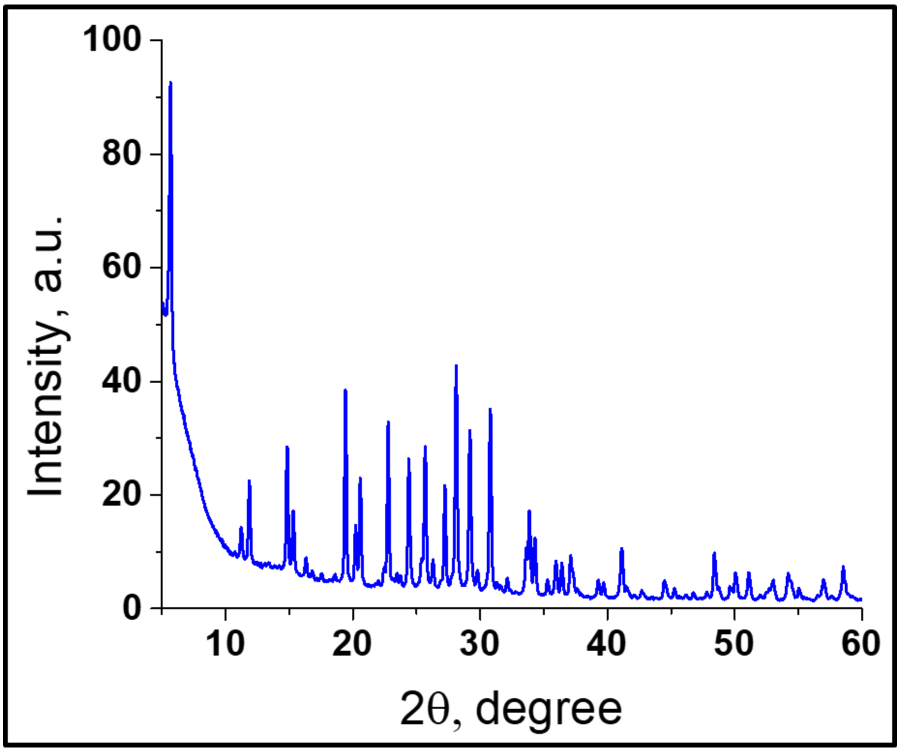

Figure 6.3: Experimental pattern of Li-NH_4-K-LTL-3.

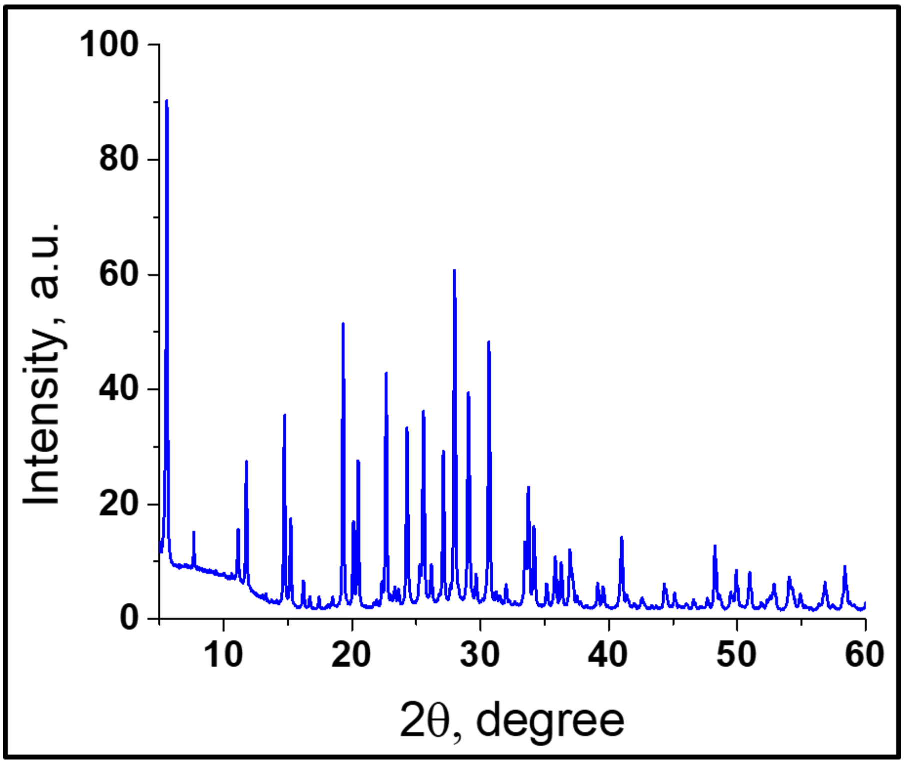

Figure 6.4: Experimental pattern of Na-NH_4-K-LTL-1.

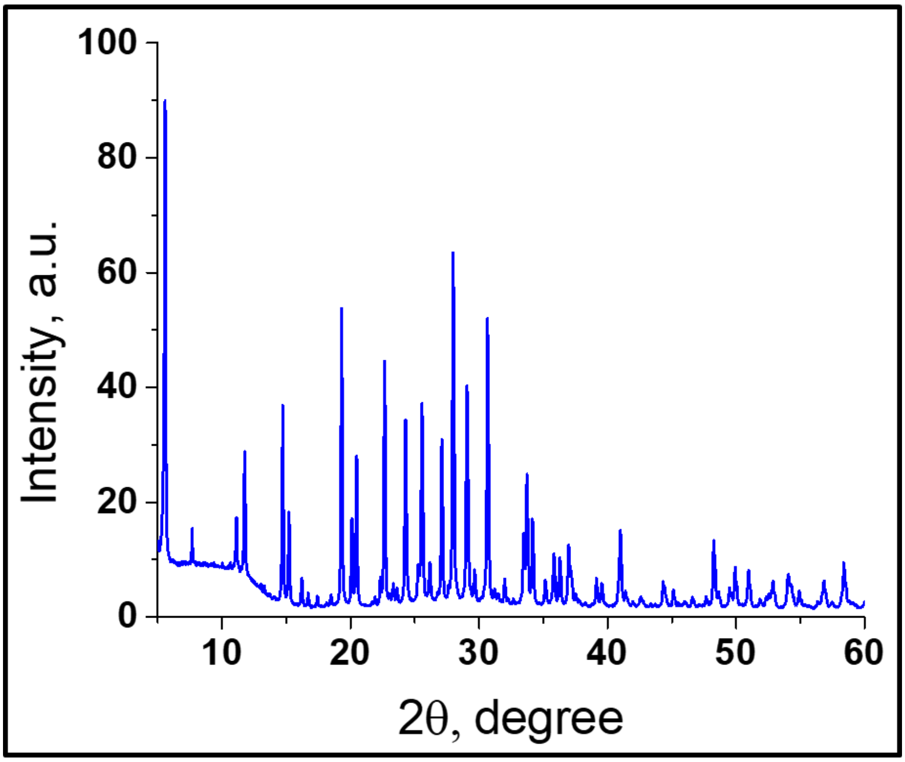

Figure 6.5: Experimental pattern of Na-NH_4-K-LTL-2.

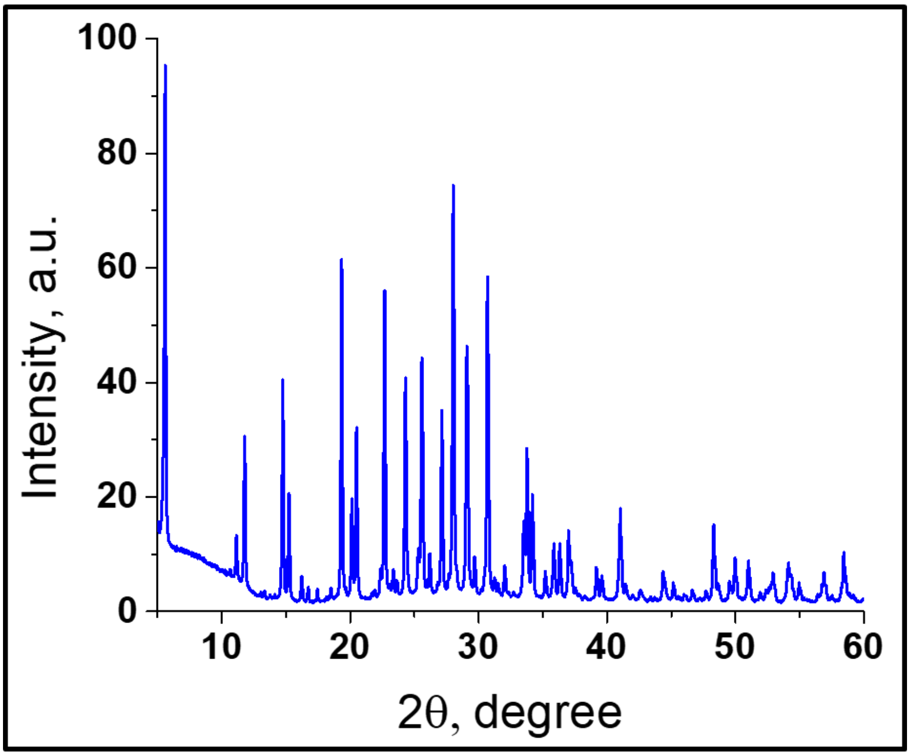

Figure 6.6: Experimental pattern of Na-NH_4-K-LTL-3.

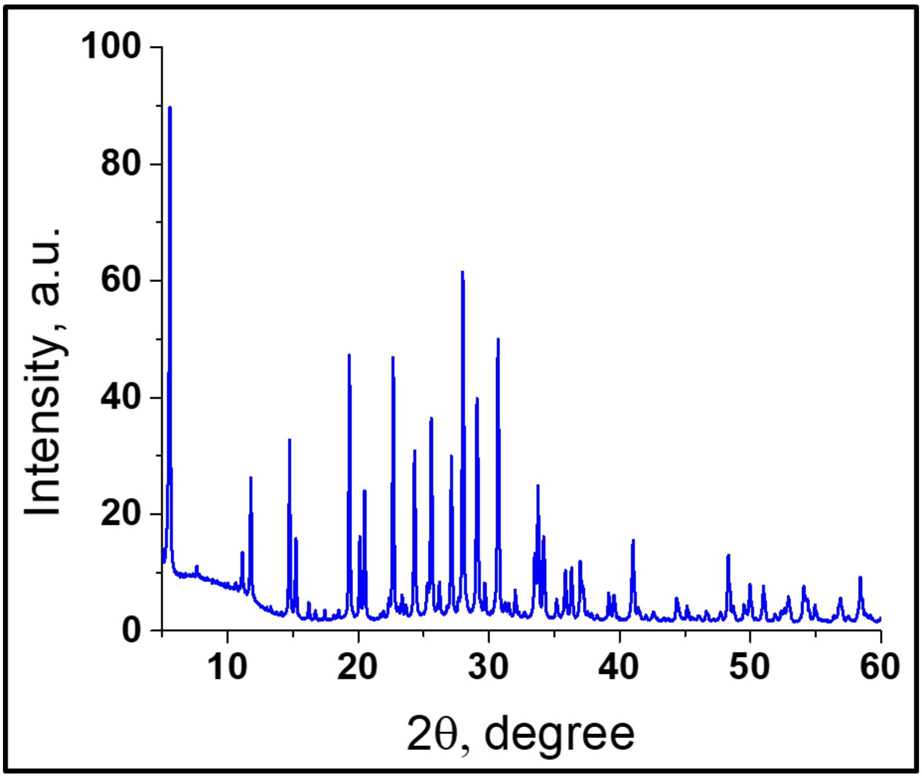

Figure 6.7: Experimental pattern of K-NH$_4$-K-LTL-1.

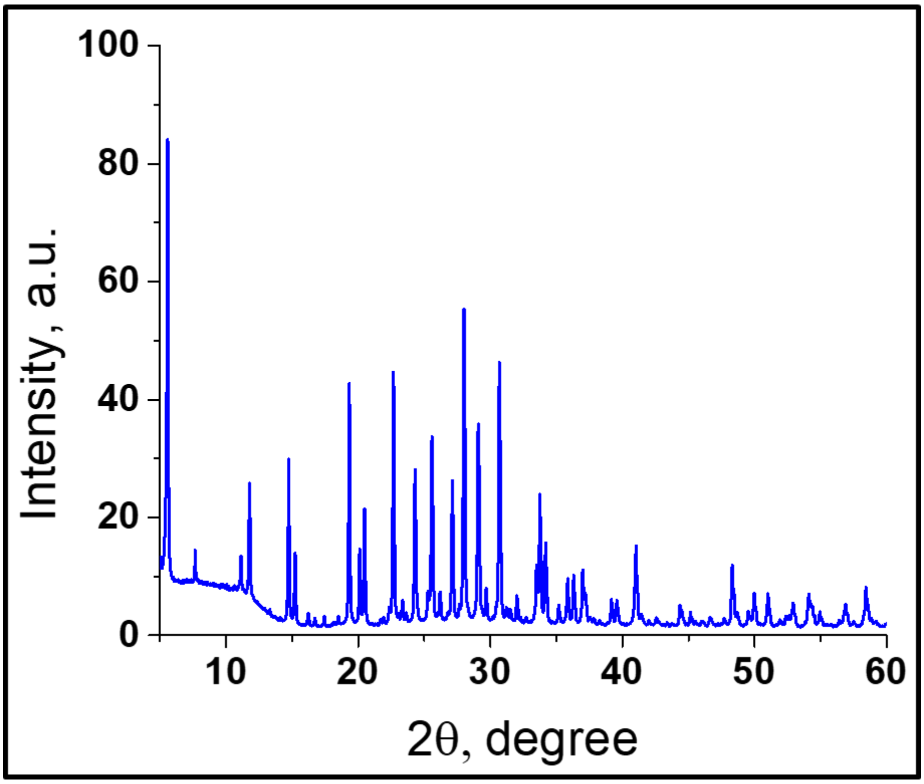

Figure 6.8: Experimental pattern of K-NH$_4$-K-LTL-2.

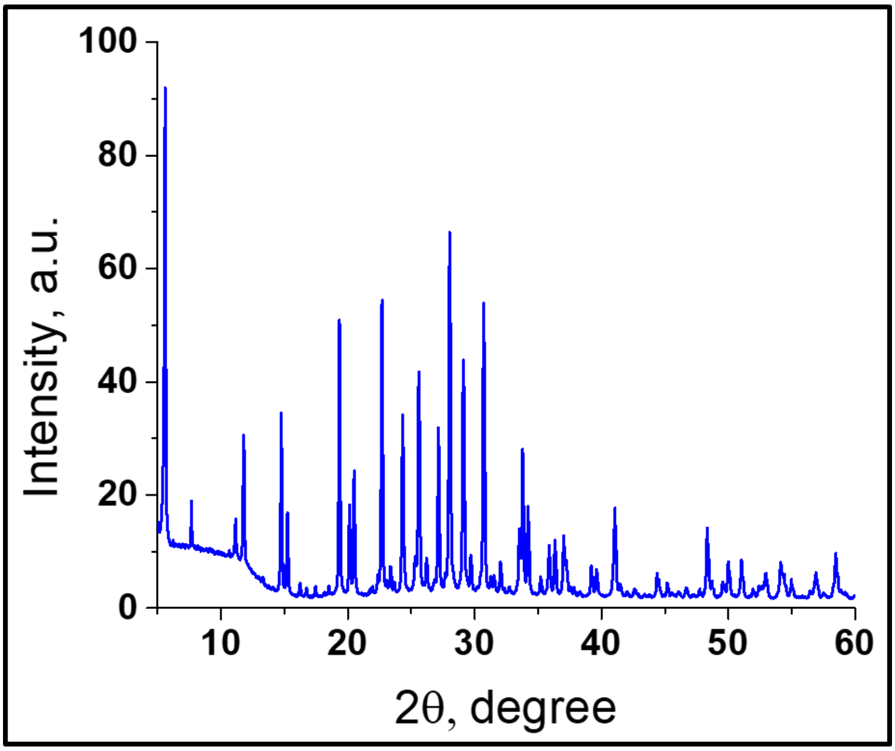

Figure 6.9: Experimental pattern of K-NH_4-K-LTL-3.

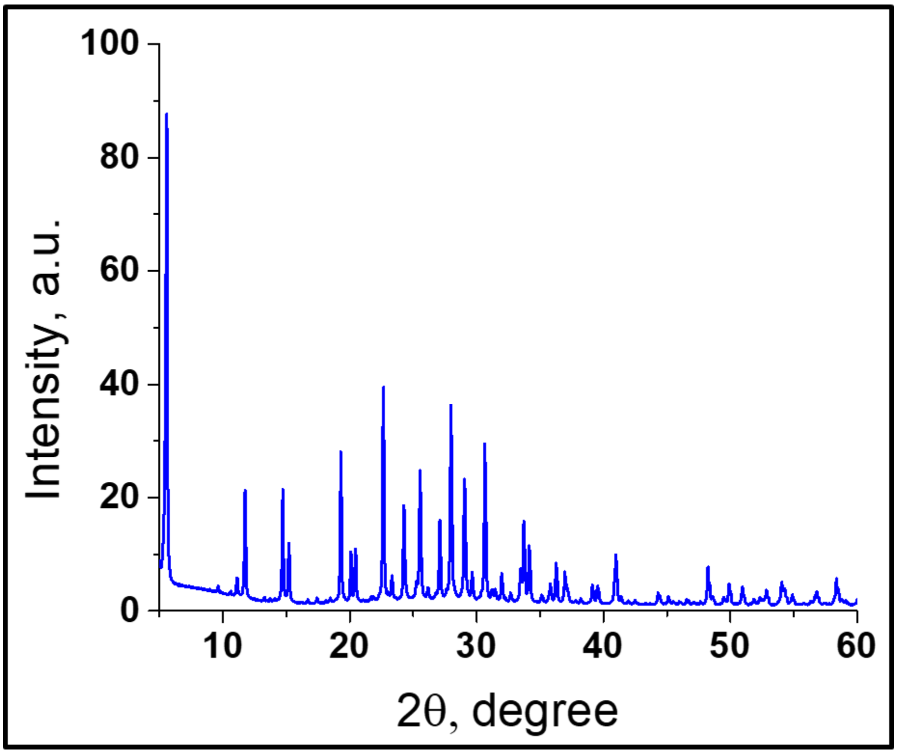

Figure 6.10: Experimental pattern of Rb-NH_4-K-LTL-1.

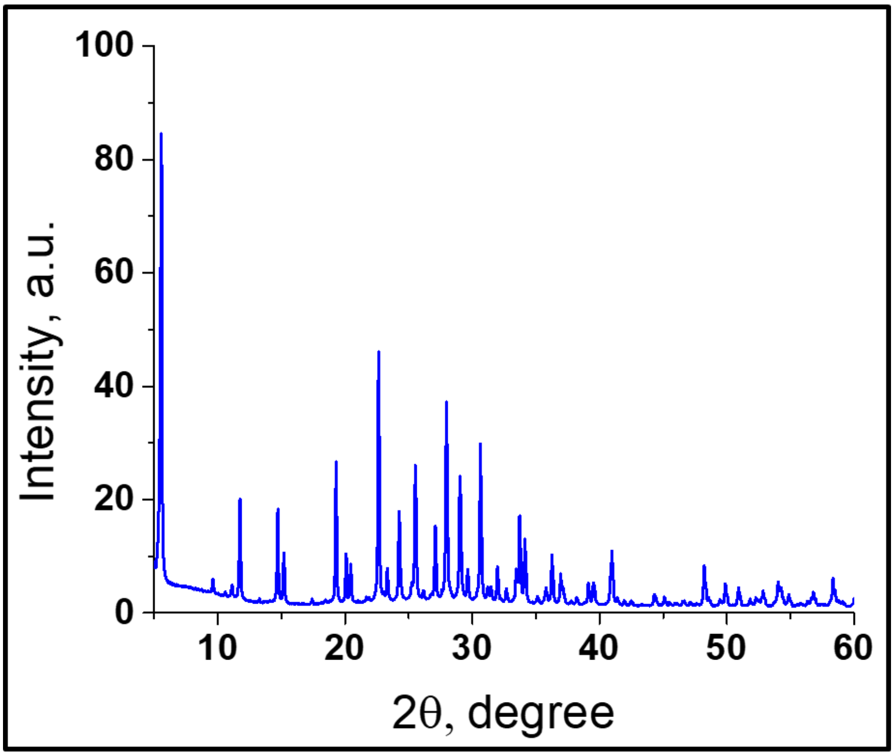

Figure 6.11: Experimental pattern of Rb-NH_4-K-LTL-2.

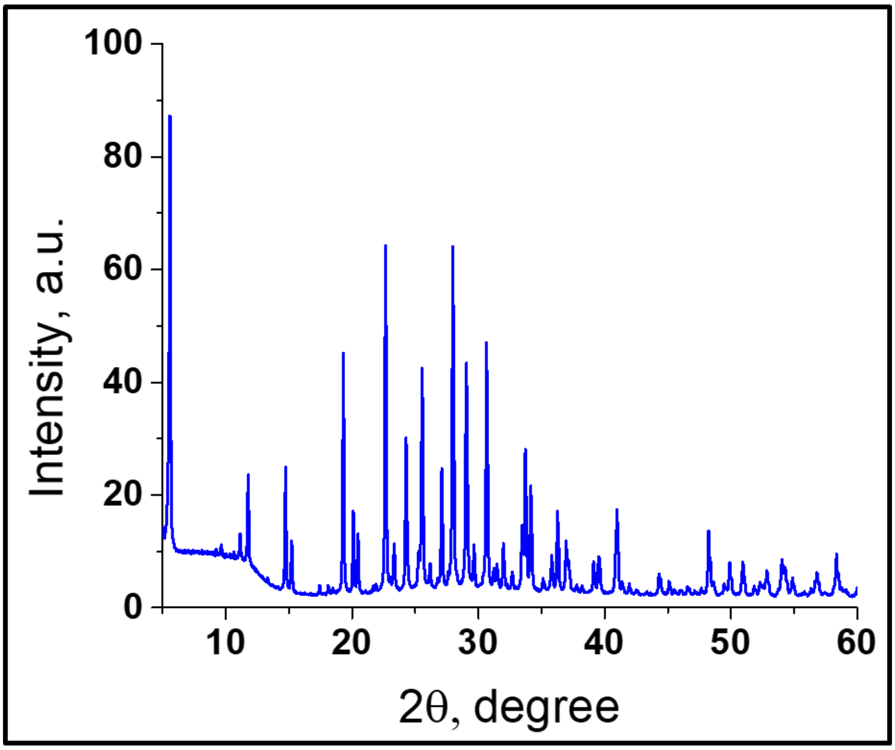

Figure 6.12: Experimental pattern of Rb-NH_4-K-LTL-3.

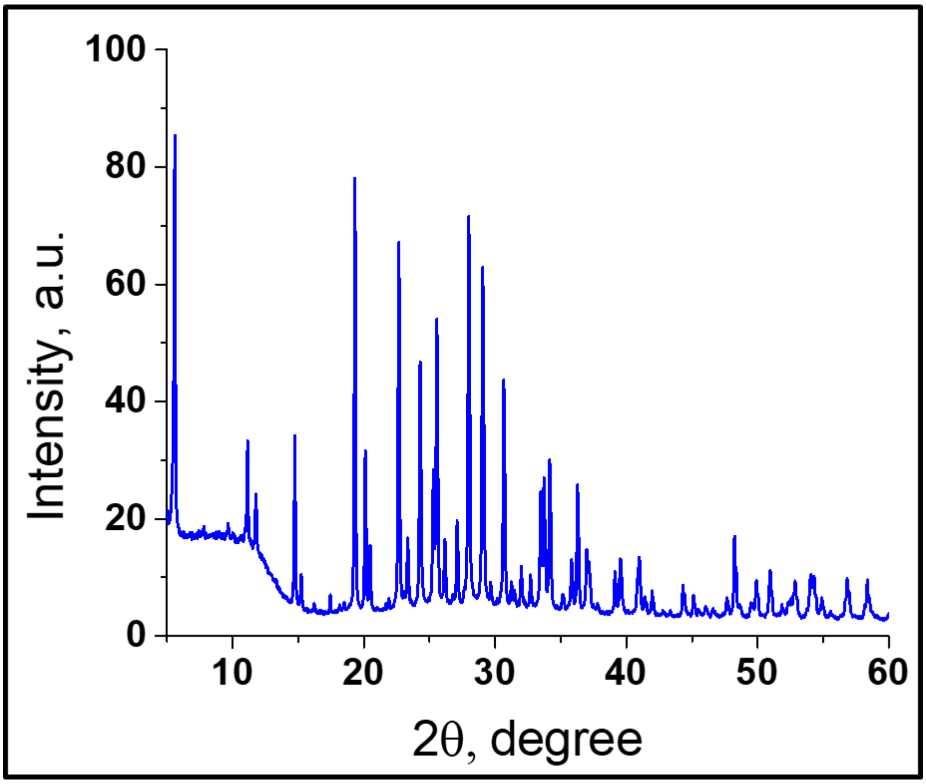

Figure 6.13: Experimental pattern of Cs-NH_4-K-LTL-1.

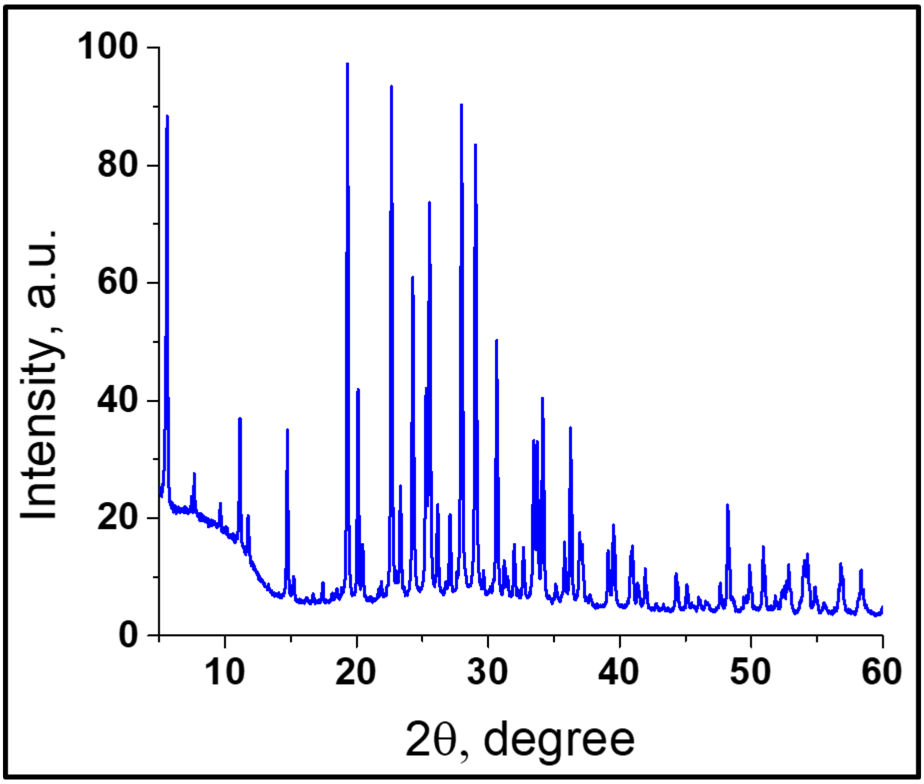

Figure 6.14: Experimental pattern of Cs-NH_4-K-LTL-2.

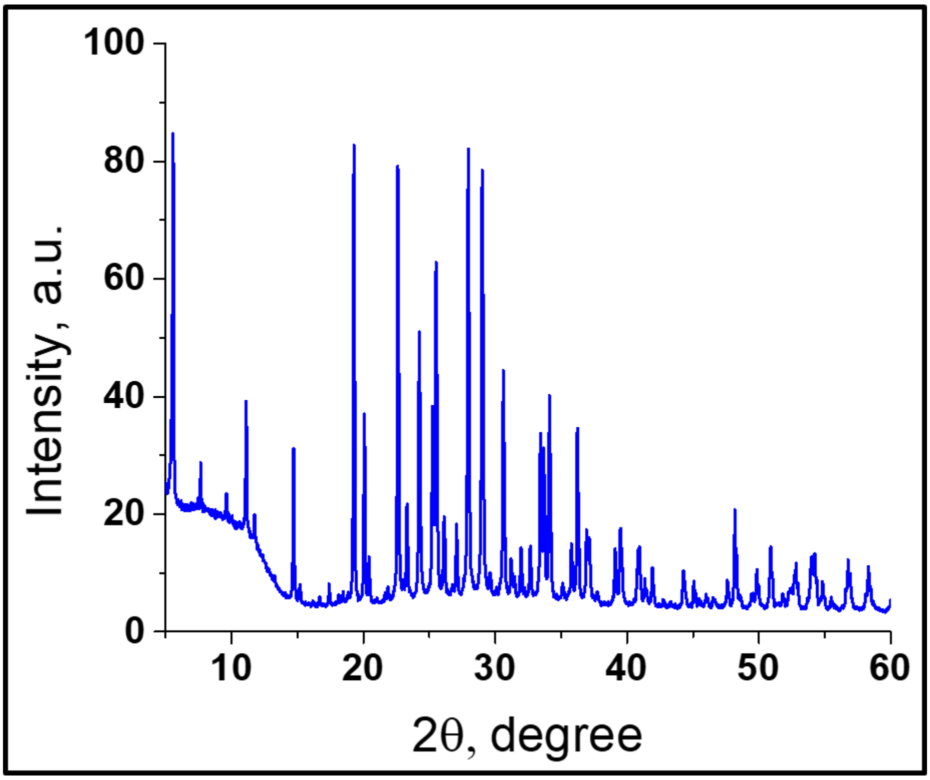

Figure 6.15: Experimental pattern of Cs-NH_4-K-LTL-3.

FTIR

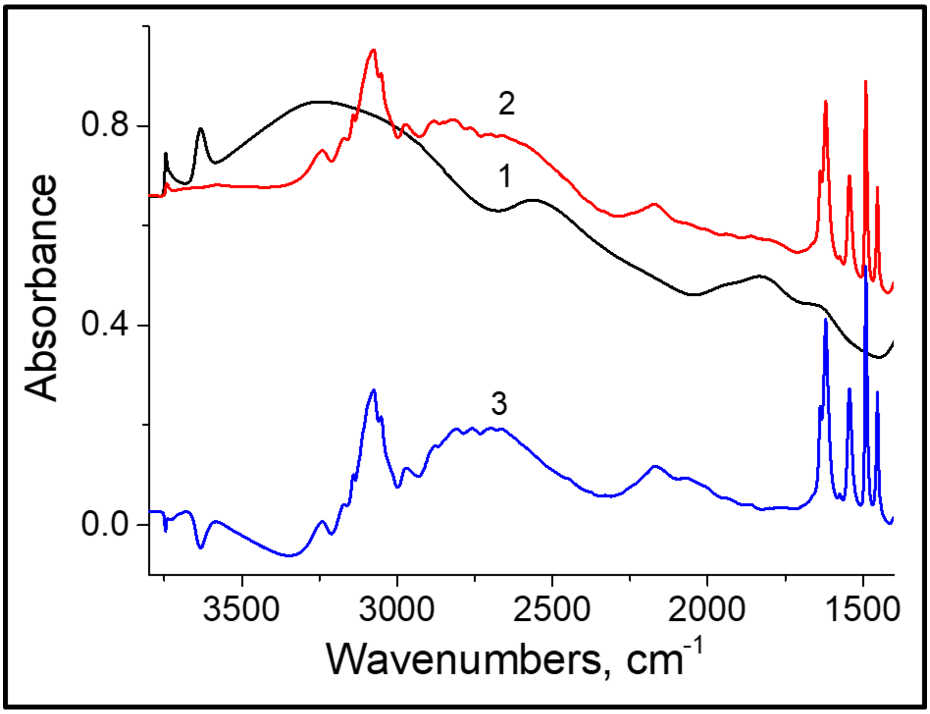

Figure 6.16: FTIR spectra of Li-NH$_4$-K-LTL-1: (1) - the material before Py adsorption, (2) - the material after Py adsorption at 200^{o}C and (3) - the difference spectrum.

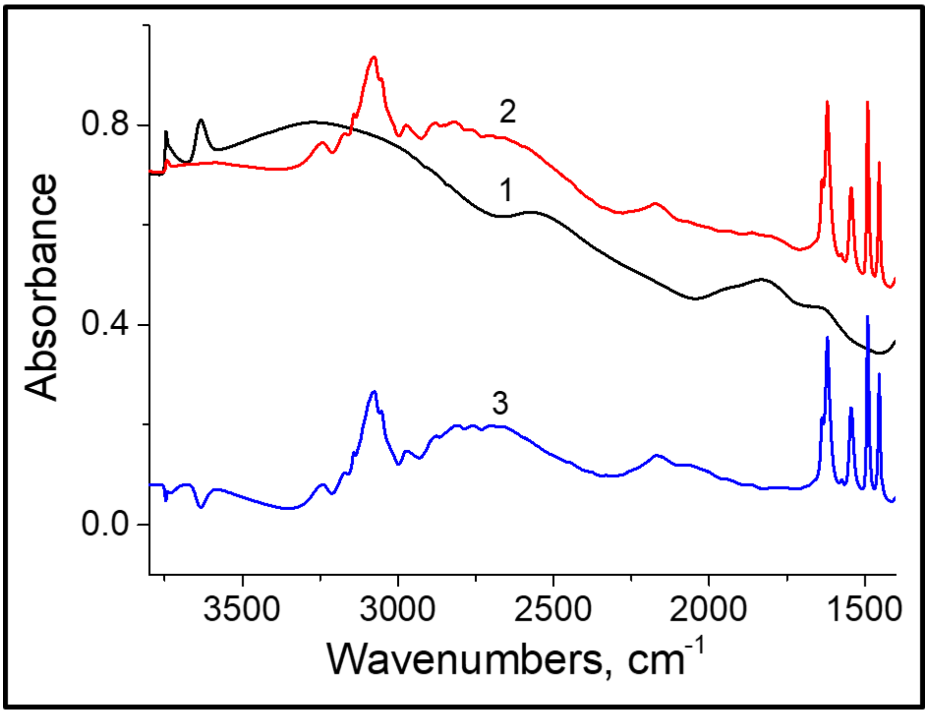

Figure 6.17: FTIR spectra of Li-NH$_4$-K-LTL-2: (1) - the material before Py adsorption, (2) - the material after Py adsorption at 200^{o}C and (3) - the difference spectrum.

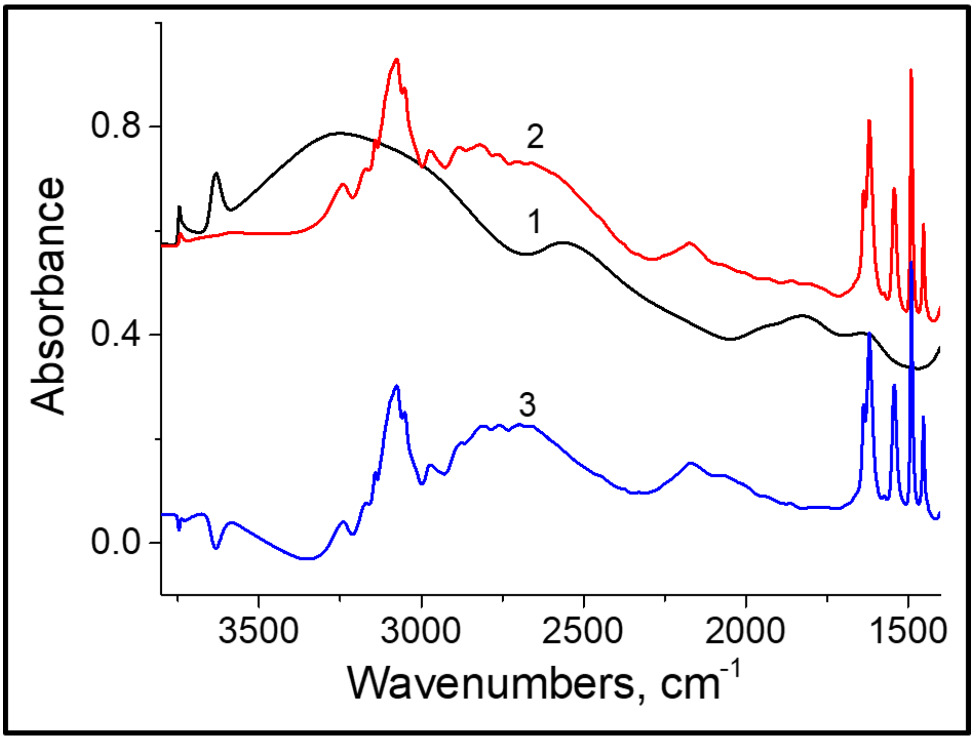

Figure 6.18: FTIR spectra of Li-NH_4-K-LTL-3: (1) - the material before Py adsorption, (2) - the material after Py adsorption at 200°C and (3) - the difference spectrum.

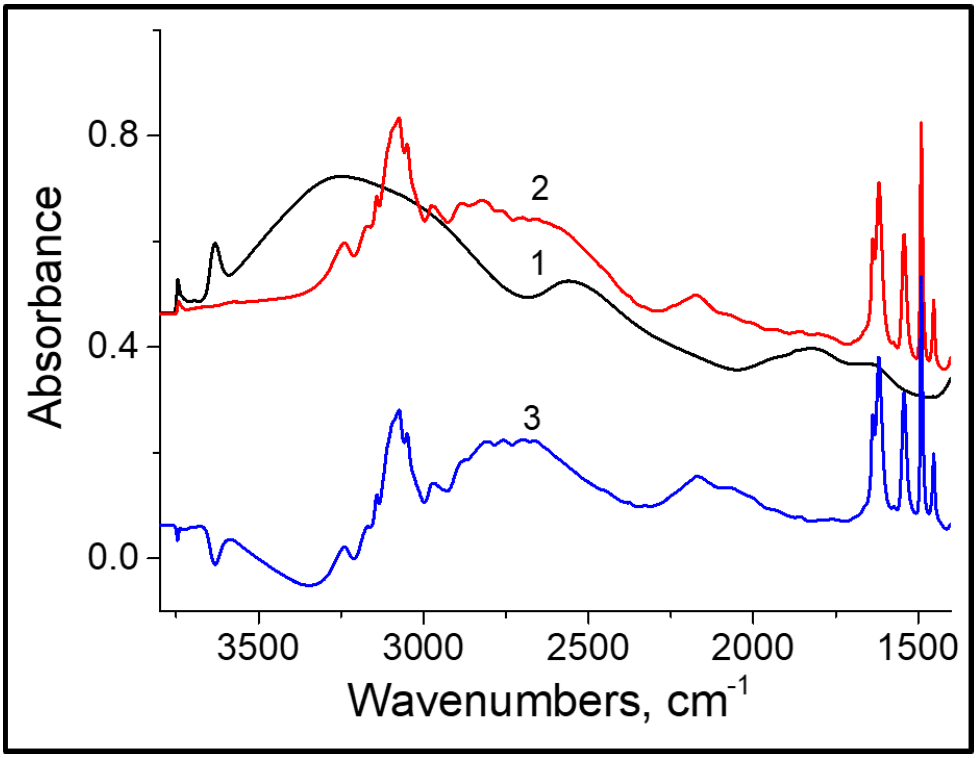

Figure 6.19: FTIR spectra of Na-NH_4-K-LTL-1: (1) - the material before Py adsorption, (2) - the material after Py adsorption at 200°C and (3) - the difference spectrum.

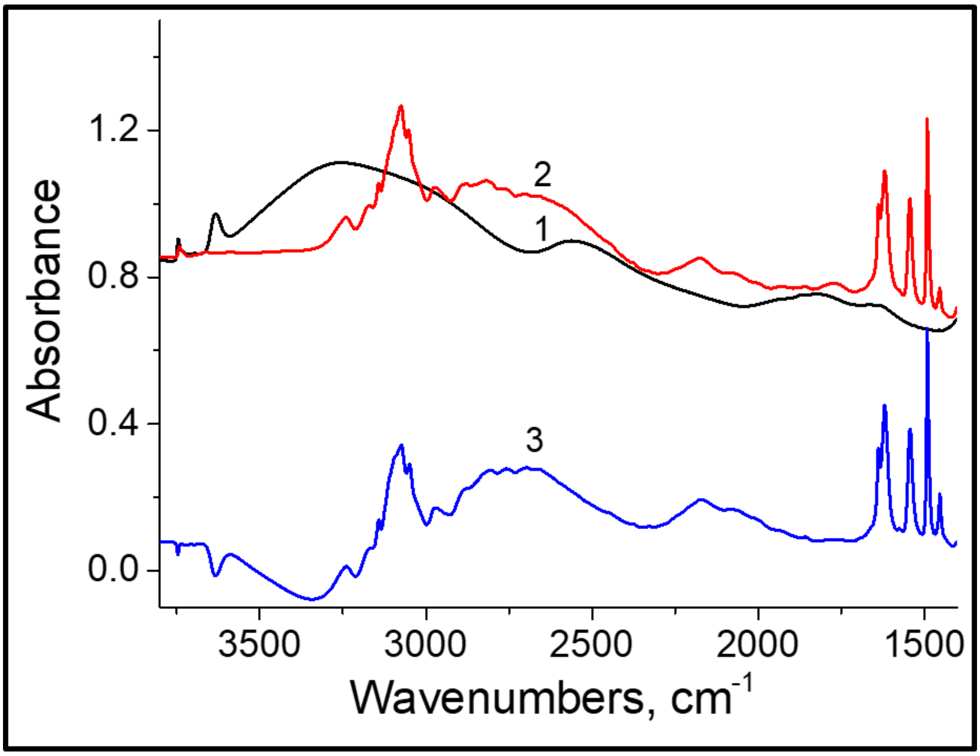

Figure 6.20: FTIR spectra of Na-NH4-K-LTL-2: (1) - the material before Py adsorption, (2) - the material after Py adsorption at 200°C and (3) - the difference spectrum.

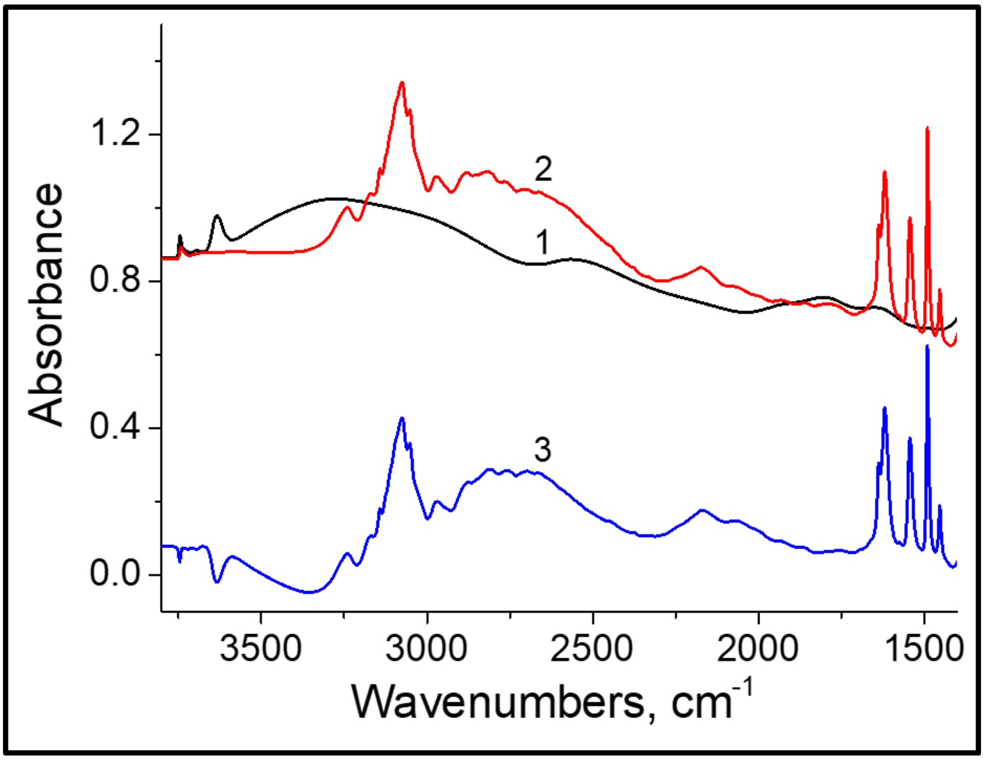

Figure 6.21: FTIR spectra of Na-NH4-K-LTL-3: (1) - the material before Py adsorption, (2) - the material after Py adsorption at 200°C and (3) - the difference spectrum.

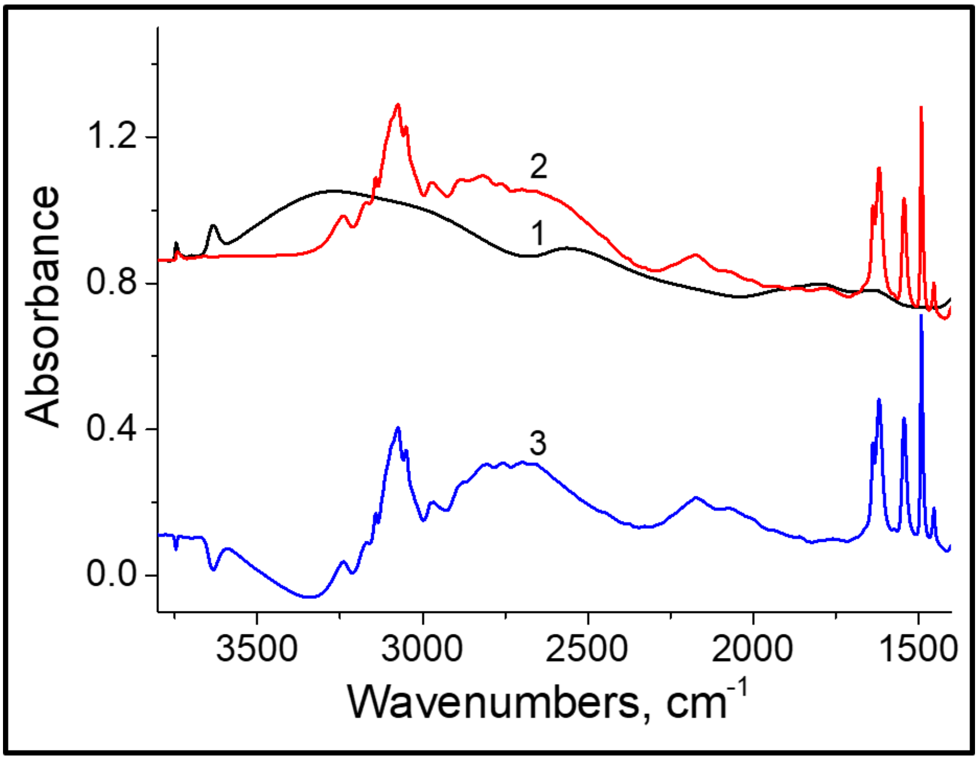

Figure 6.22: FTIR spectra of K-NH4-K-LTL-1: (1) - the material before Py adsorption, (2) - the material after Py adsorption at 200°C and (3) - the difference spectrum.

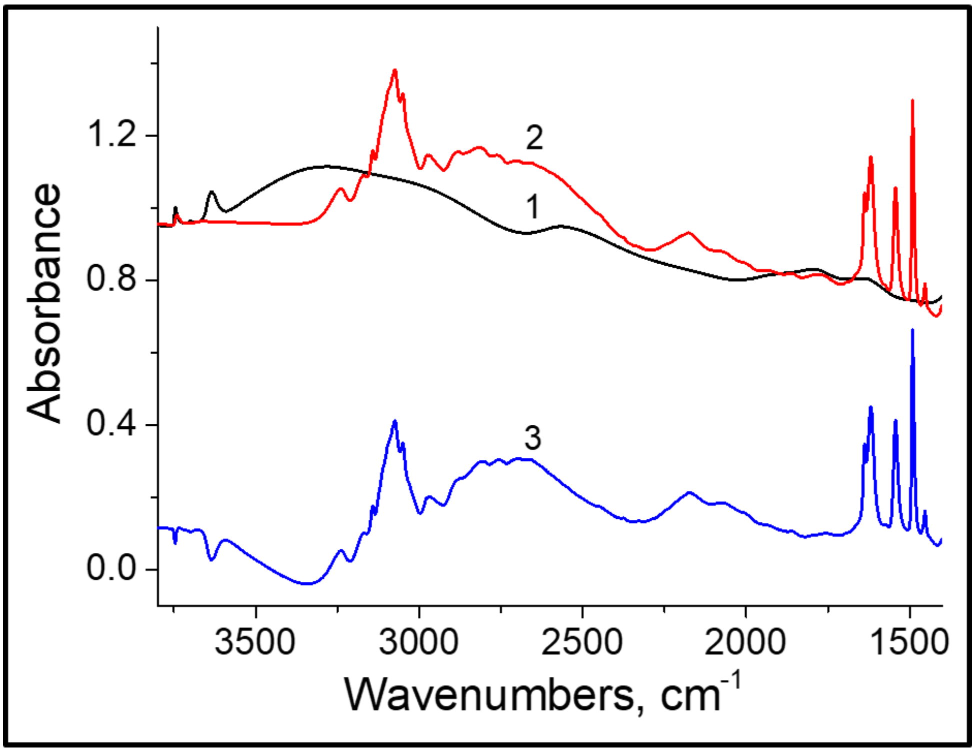

Figure 6.23: FTIR spectra of K-NH4-K-LTL-2: (1) - the material before Py adsorption, (2) - the material after Py adsorption at 200°C and (3) - the difference spectrum.

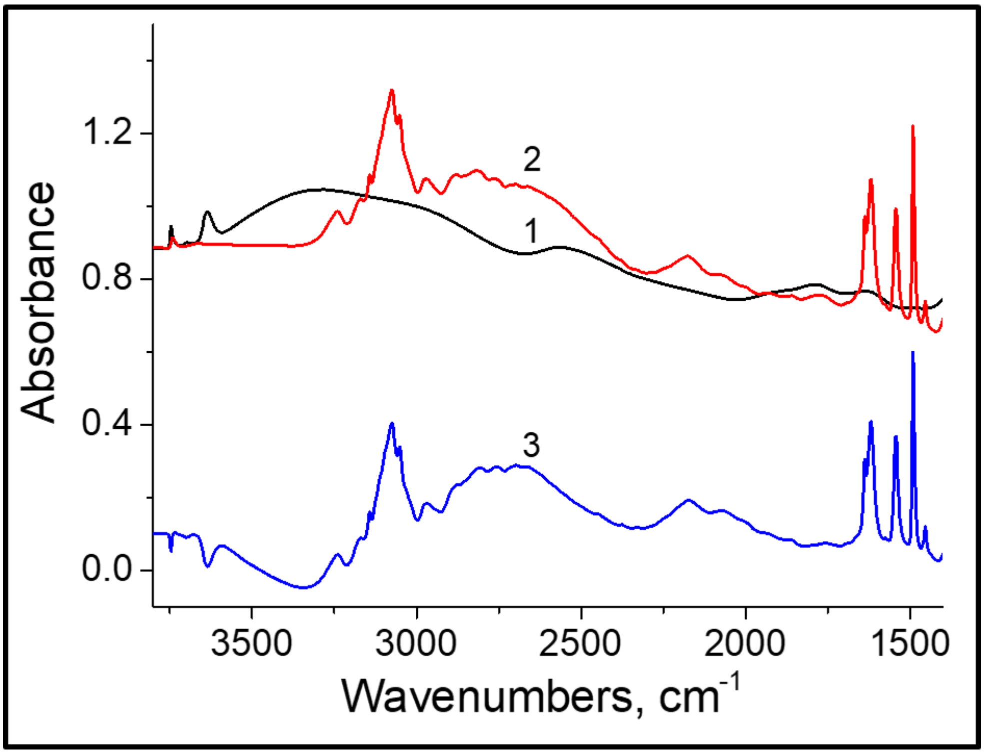

Figure 6.24: FTIR spectra of K-NH$_4$-K-LTL-3: (1) - the material before Py adsorption, (2) - the material after Py adsorption at 200°C and (3) - the difference spectrum.

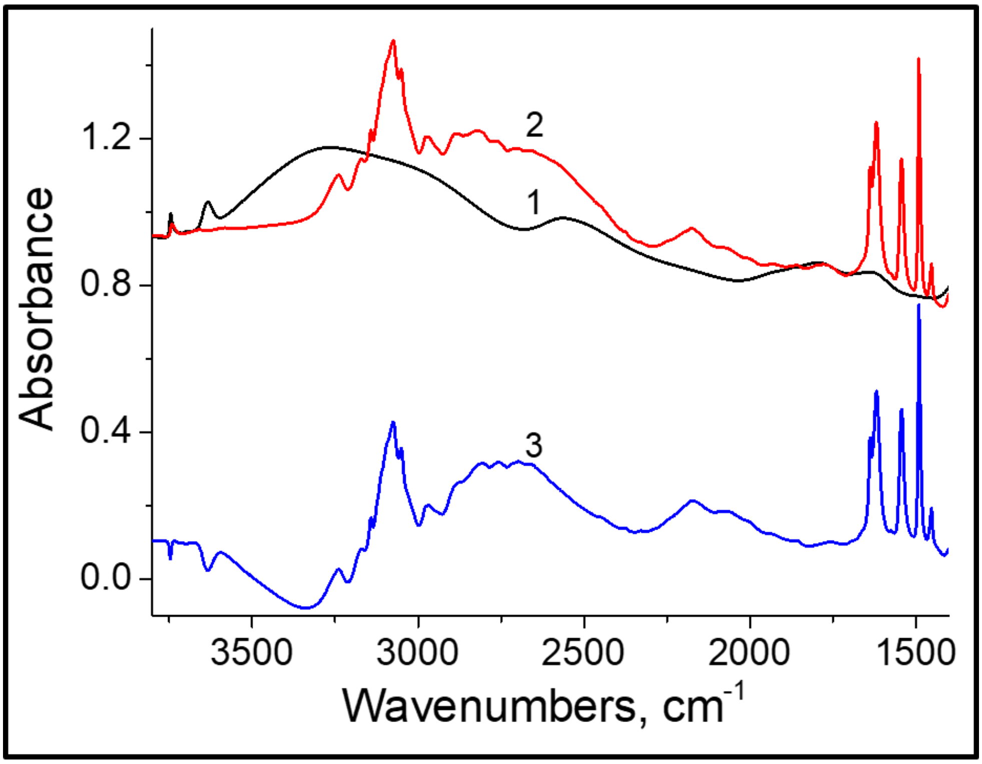

Figure 6.25: FTIR spectra of Rb-NH$_4$-K-LTL-1: (1) - the material before Py adsorption, (2) - the material after Py adsorption at 200°C and (3) - the difference spectrum.

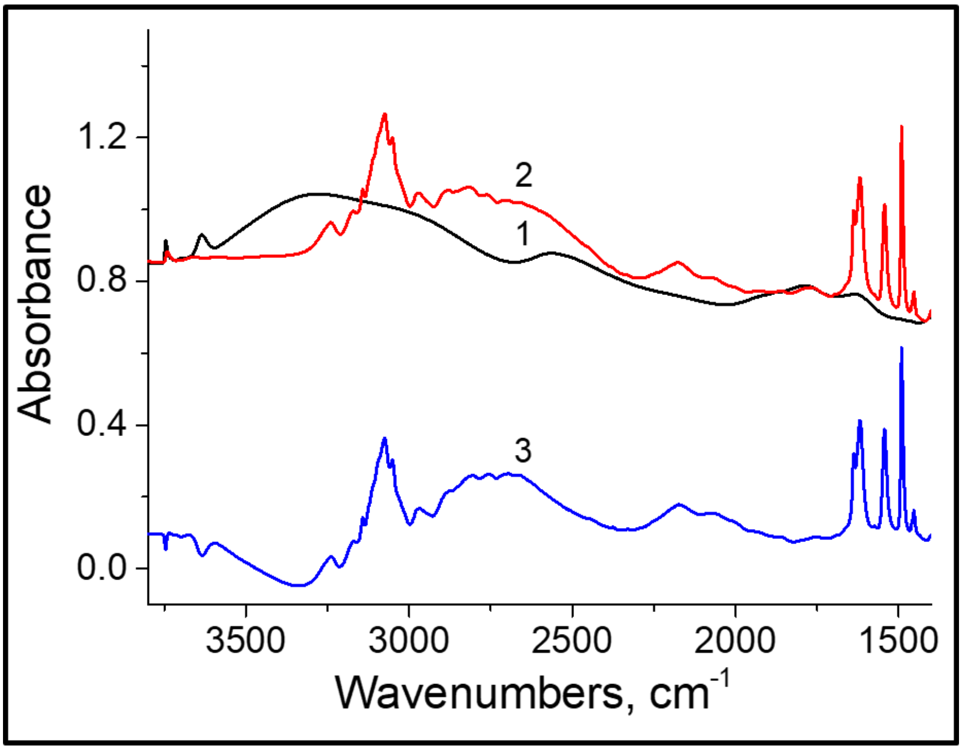

Figure 6.26: FTIR spectra of Rb-NH$_4$-K-LTL-2: (1) - the material before Py adsorption, (2) - the material after Py adsorption at 200°C and (3) - the difference spectrum.

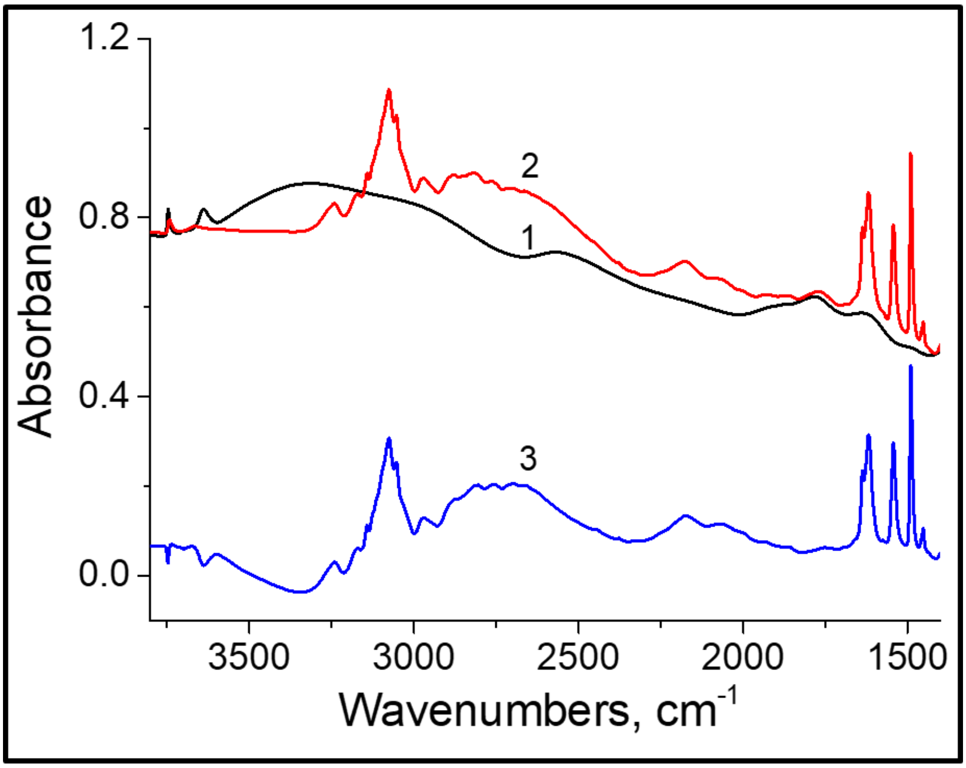

Figure 6.27: FTIR spectra of Rb-NH$_4$-K-LTL-3: (1) - the material before Py adsorption, (2) - the material after Py adsorption at 200°C and (3) - the difference spectrum.

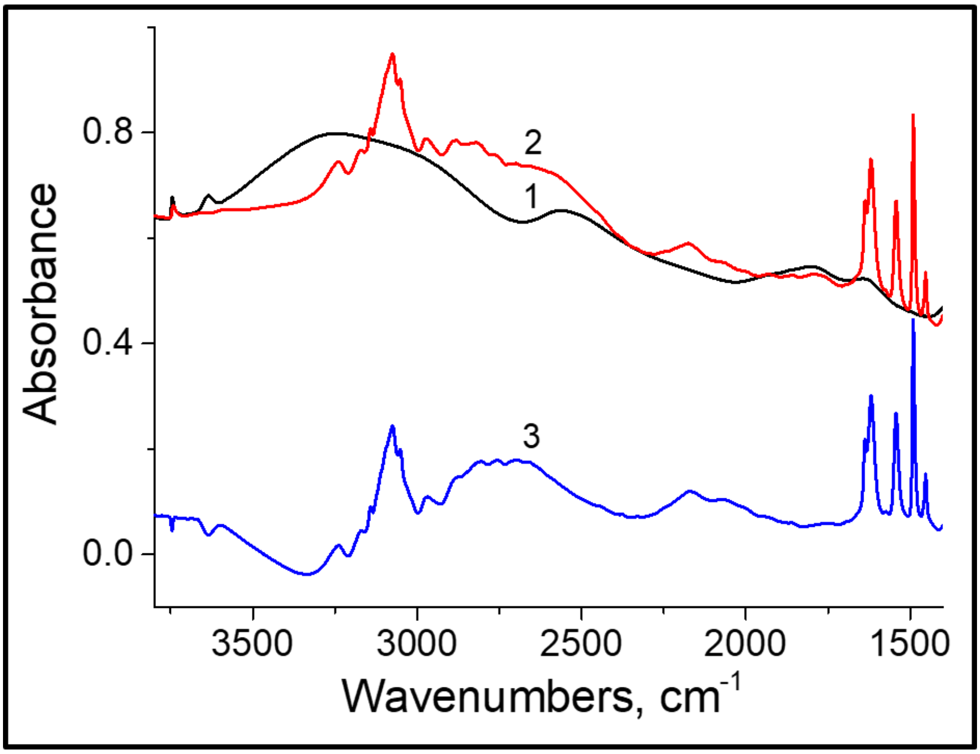

Figure 6.28: FTIR spectra of Cs-NH_4-K-LTL-1: (1) - the material before Py adsorption, (2) - the material after Py adsorption at 200°C and (3) - the difference spectrum.

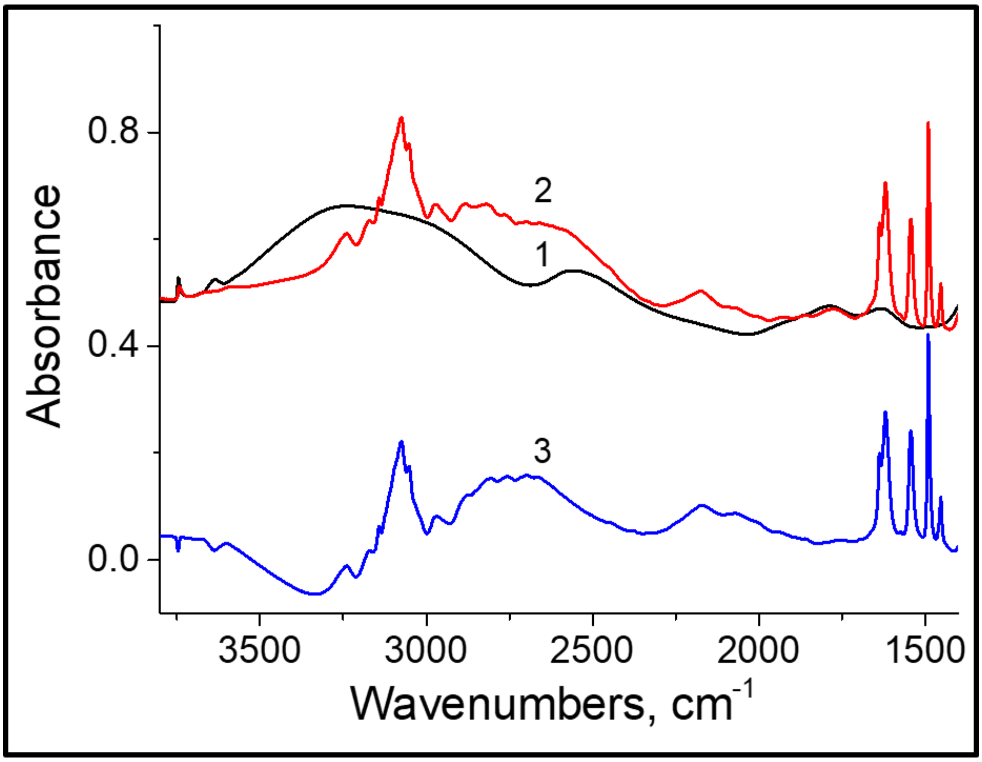

Figure 6.29: FTIR spectra of Cs-NH_4-K-LTL-2: (1) - the material before Py adsorption, (2) - the material after Py adsorption at 200°C and (3) - the difference spectrum.

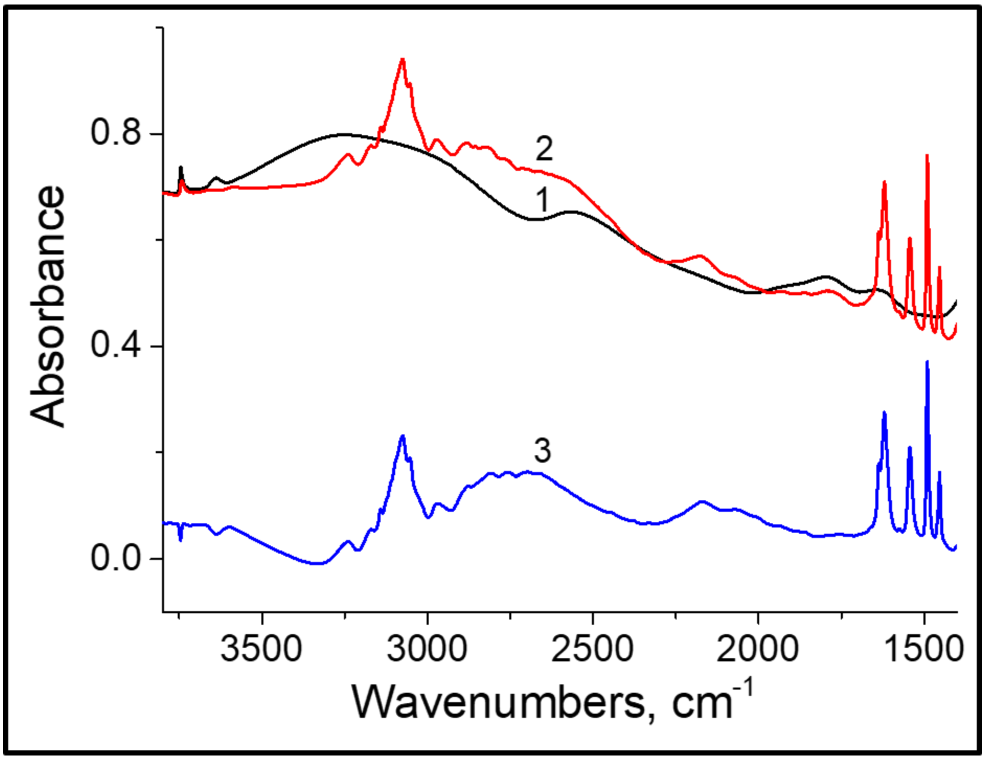

Figure 6.30: FTIR spectra of Cs-NH_4-K-LTL-3: (1) - the material before Py adsorption, (2) - the material after Py adsorption at 200°C and (3) - the difference spectrum.

TGA

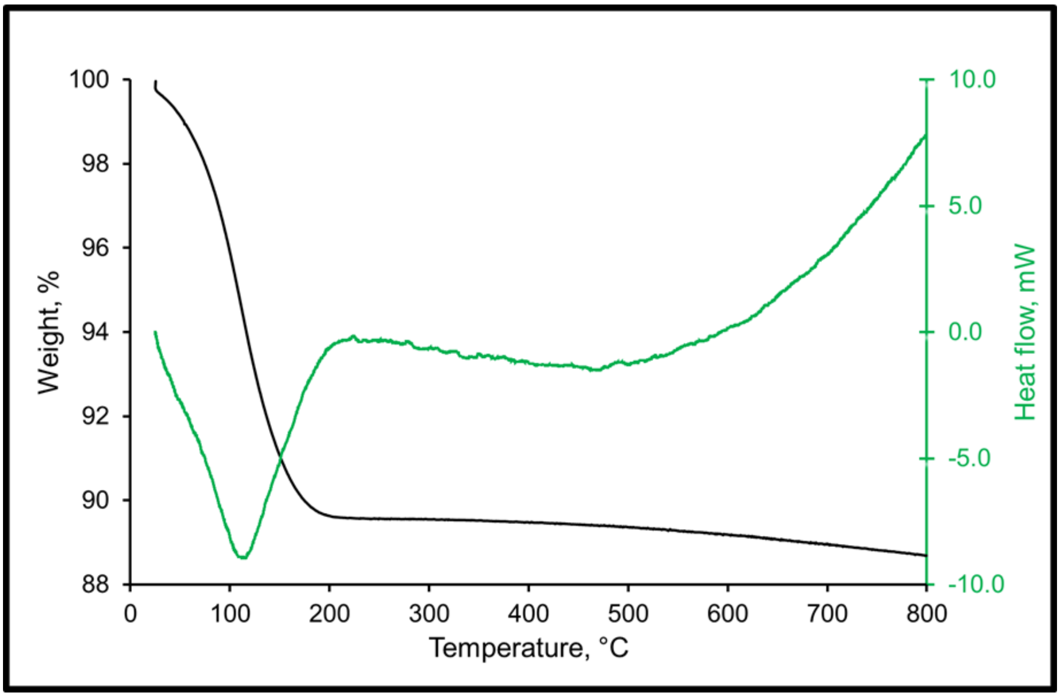

Figure 6.31: TGA curve and Heat flow of K-LTL.

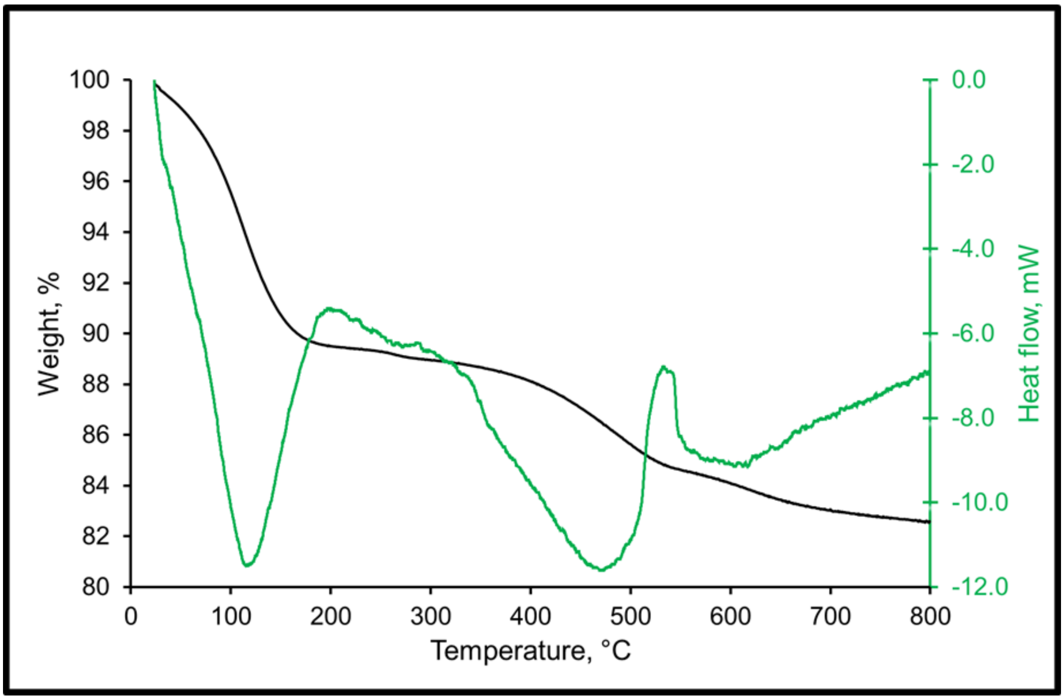

Figure 6.32: TGA curve and Heat flow of NH_4-K-LTL.

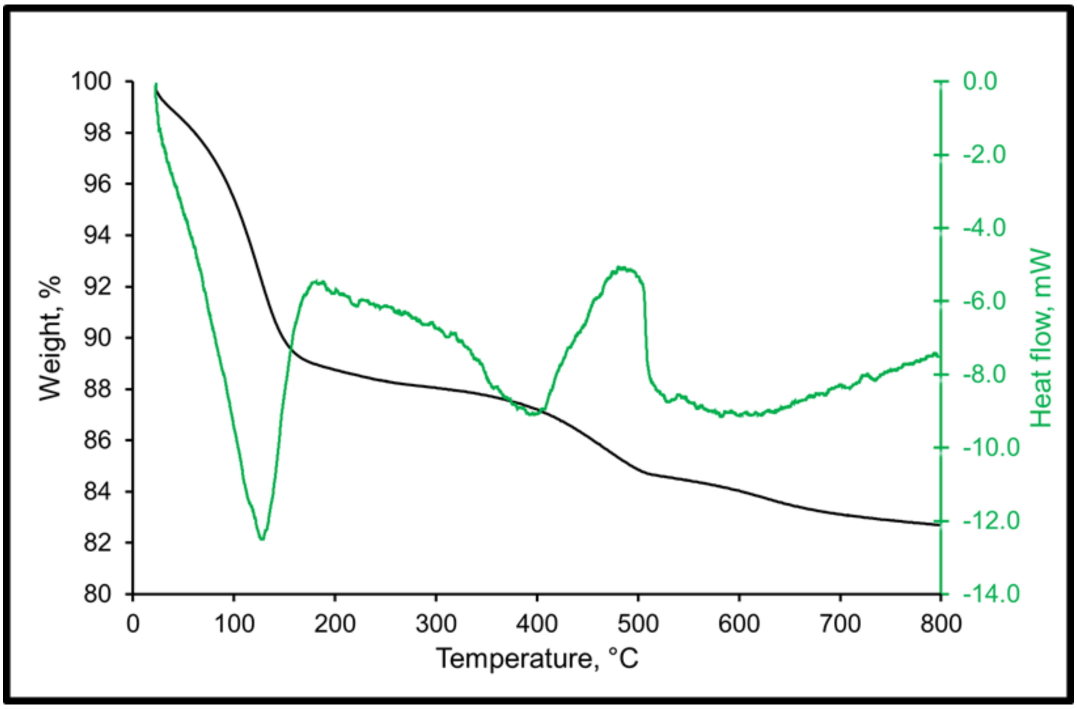

Figure 6.33: TGA curve and Heat flow of Li-NH_4-K-LTL-4.

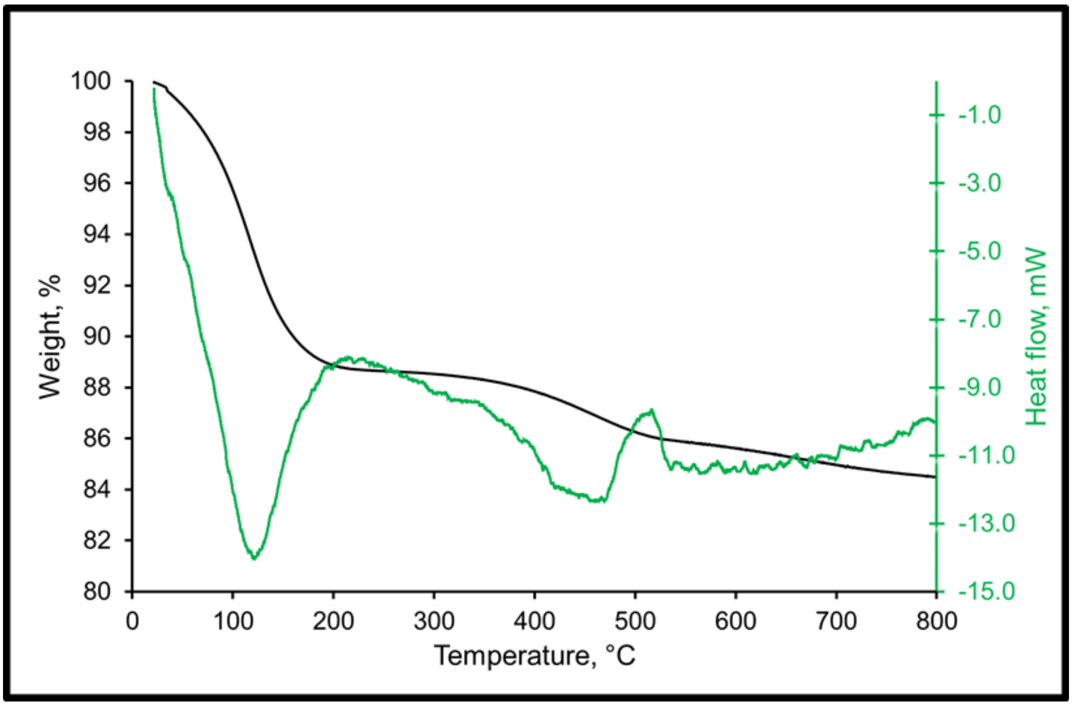

Figure 6.34: TGA curve and Heat flow of Na-NH_4-K-LTL-4.

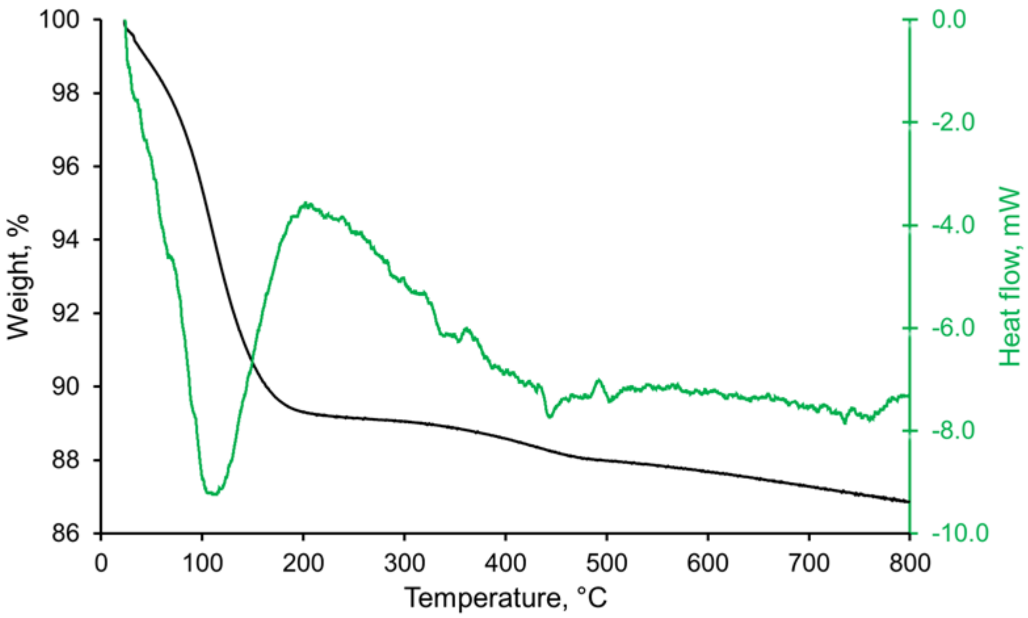

Figure 6.35: TGA curve and Heat flow of K-NH_4-K-LTL-4.

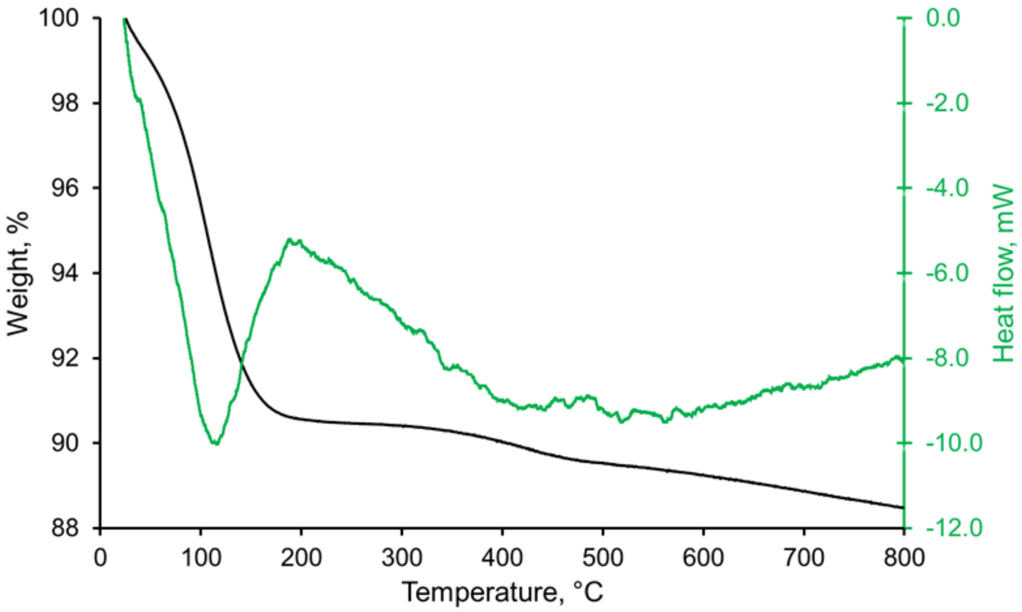

Figure 6.36: TGA curve and Heat flow of Rb-NH_4-K-LTL-4.

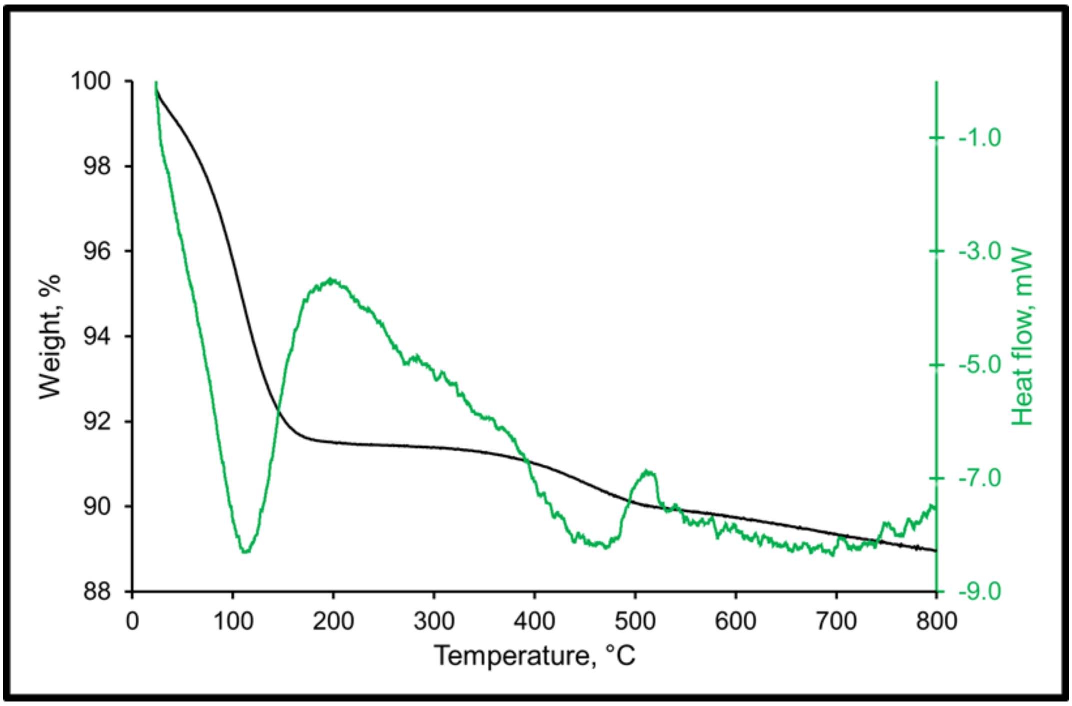

Figure 6.37: TGA curve and Heat flow of Cs-NH_4-K-LTL-4.

MAZ Additional figures

XRD

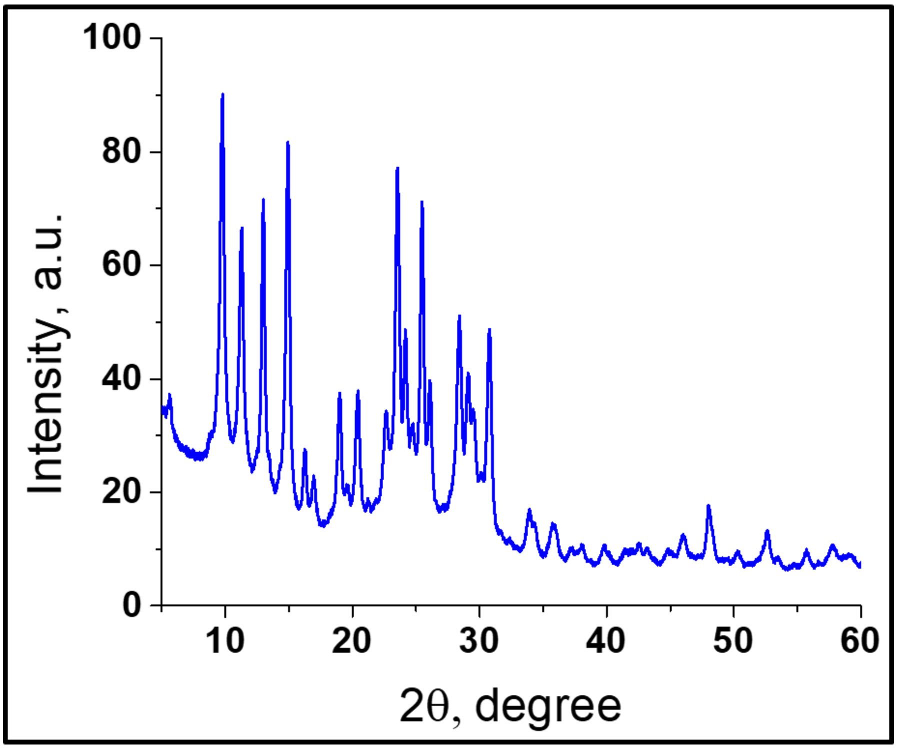

Figure 6.38: Experimental pattern of Li-H-MAZ-1.

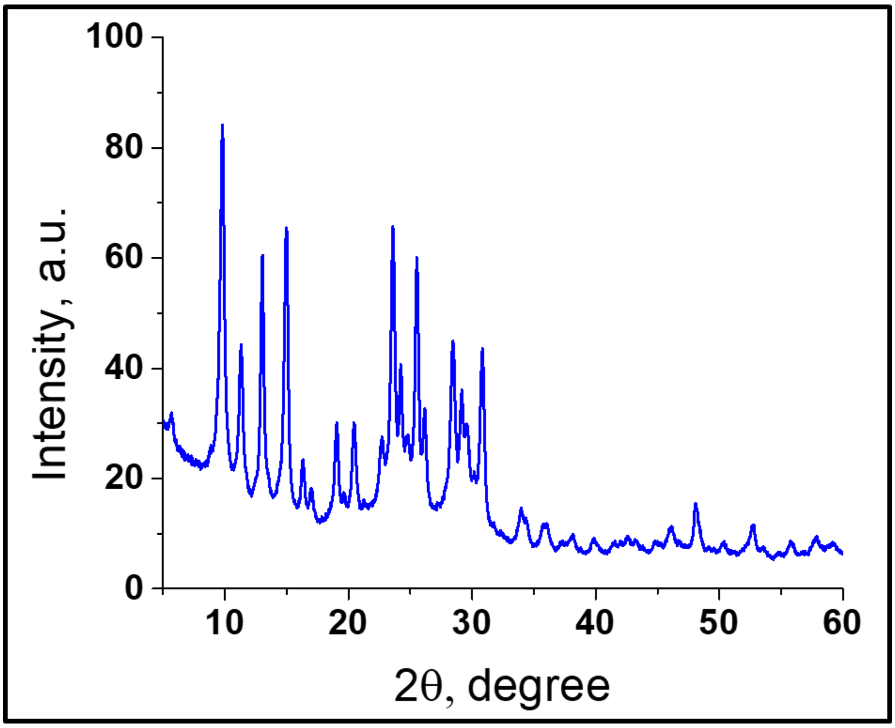

Figure 6.39: Experimental pattern of Na-H-MAZ-1.

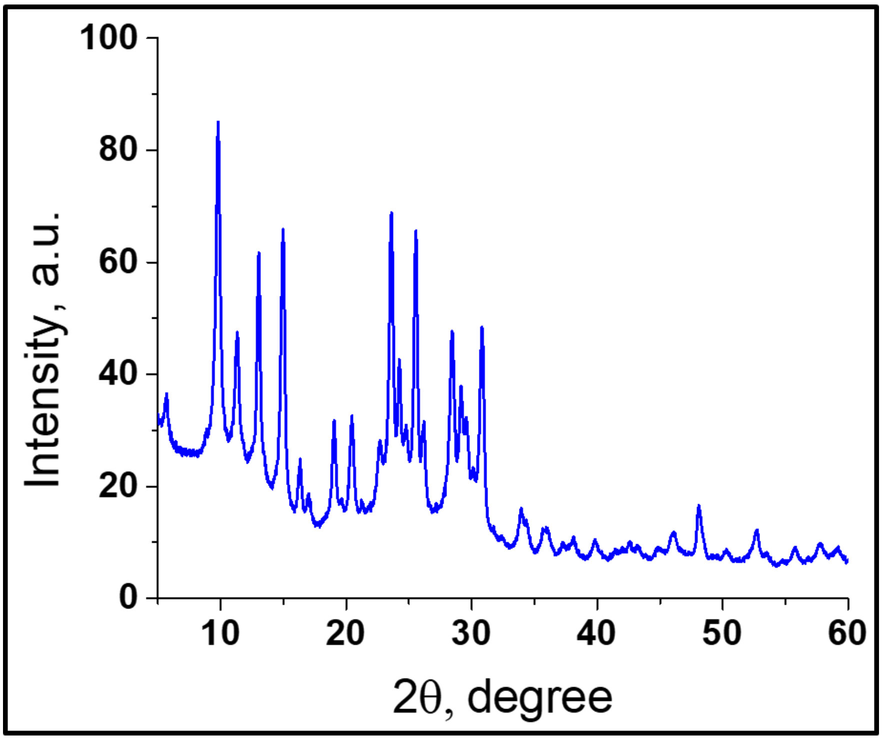

Figure 6.40: Experimental pattern of K-H-MAZ-1.

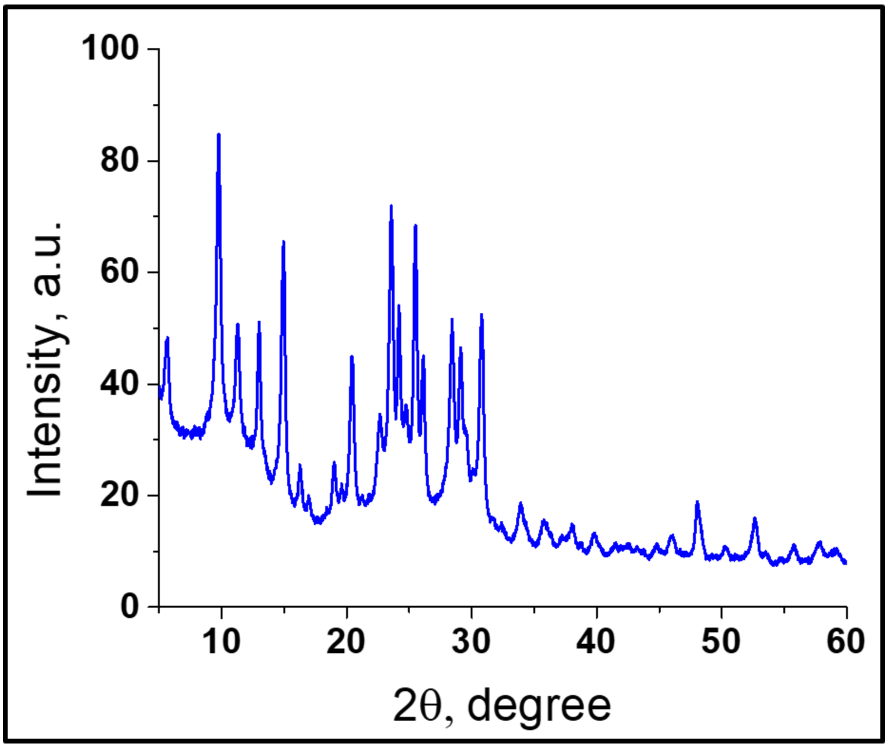

Figure 6.41: Experimental pattern of Rb-H-MAZ-1.

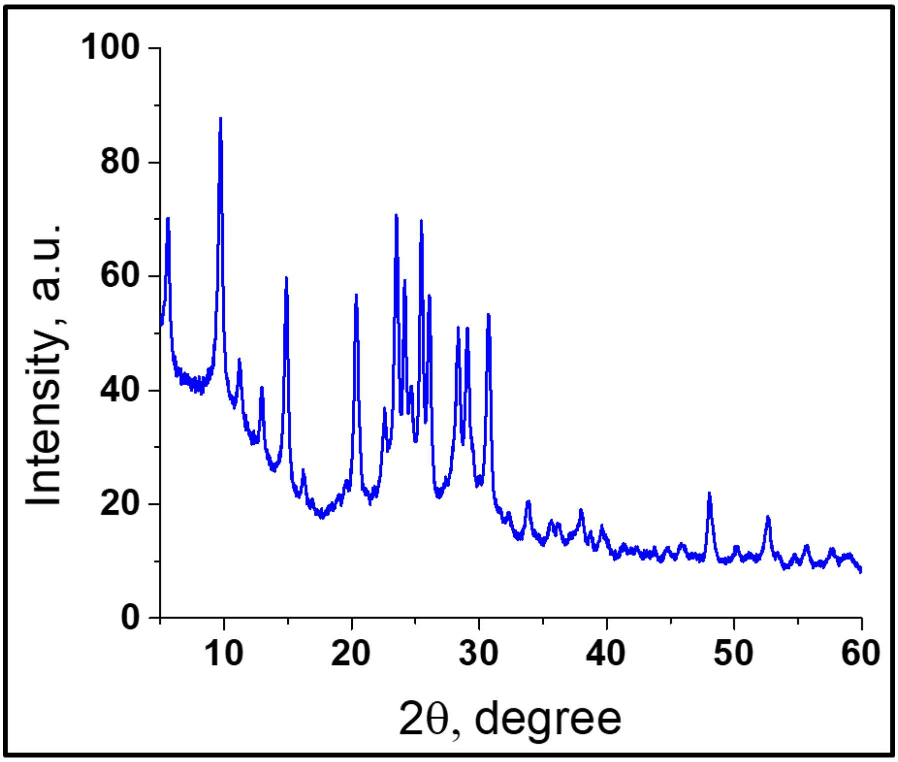

Figure 6.42: Experimental pattern of Cs-H-MAZ-1.

FTIR

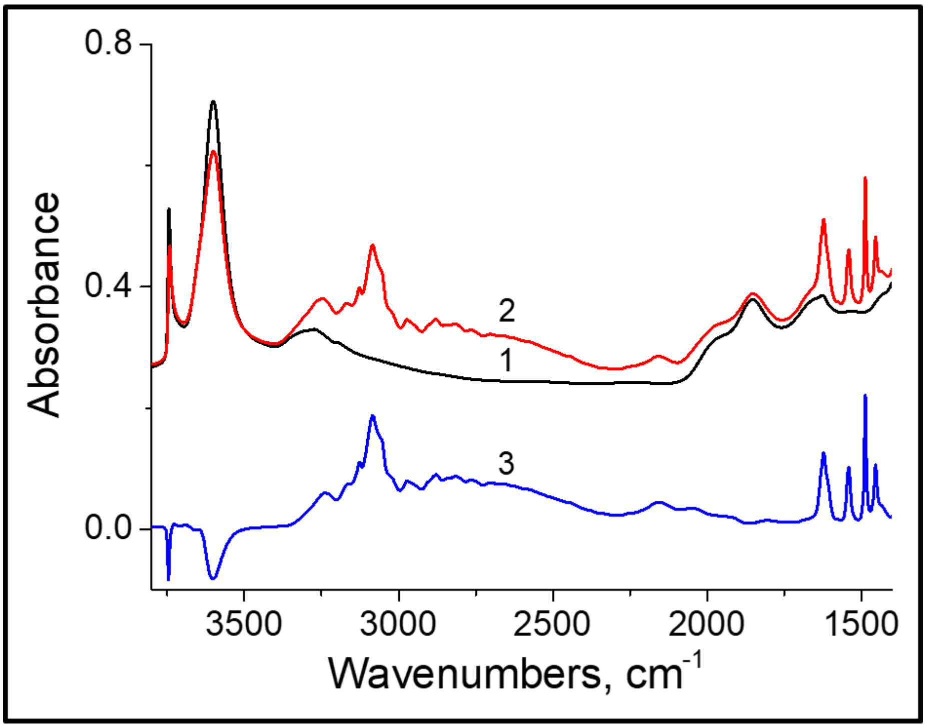

Figure 6.43: FTIR spectra of Li-H-MAZ-1: (1) - the material before Py adsorption, (2) - the material after Py adsorption at 200°C and (3) - the difference spectrum.

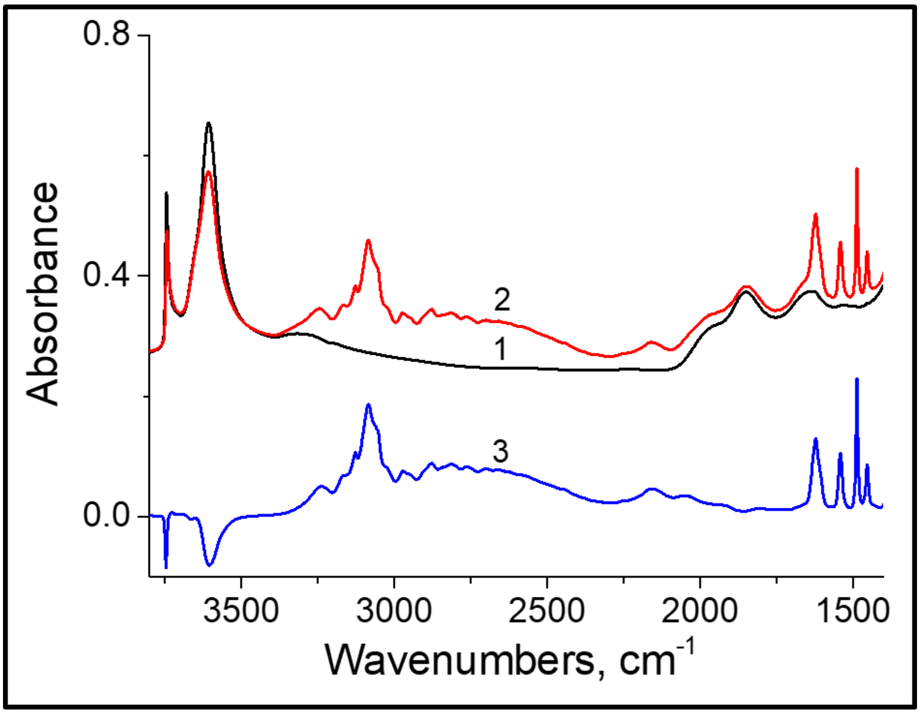

Figure 6.44: FTIR spectra of Na-H-MAZ-1: (1) - the material before Py adsorption, (2) - the material after Py adsorption at 200°C and (3) - the difference spectrum.

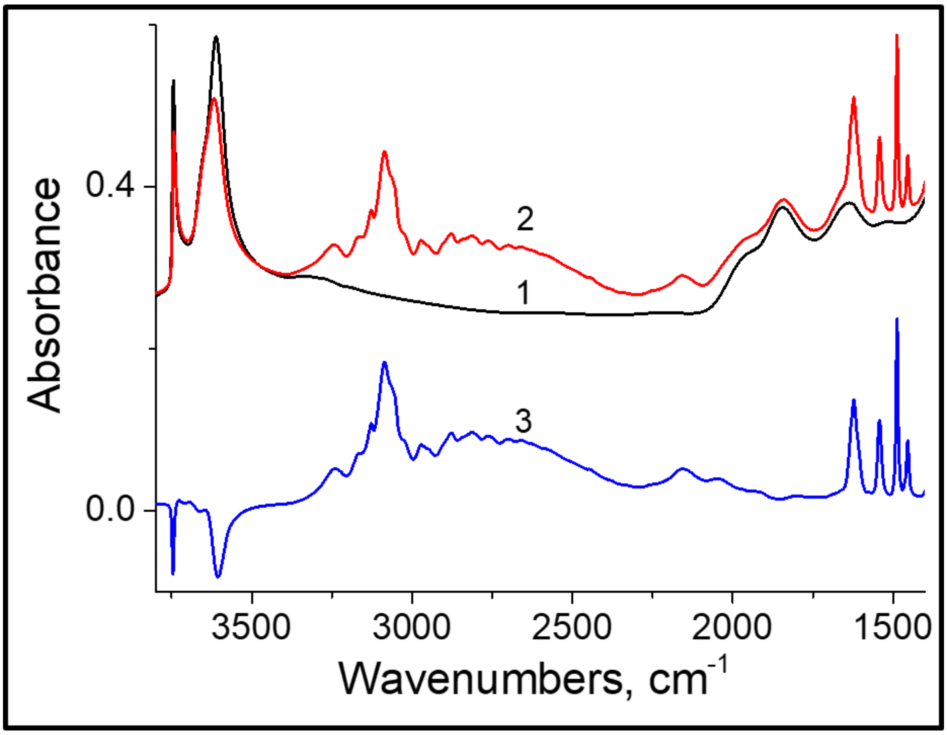

Figure 6.45: FTIR spectra of K-H-MAZ-1: (1) - the material before Py adsorption, (2) - the material after Py adsorption at 200°C and (3) - the difference spectrum.

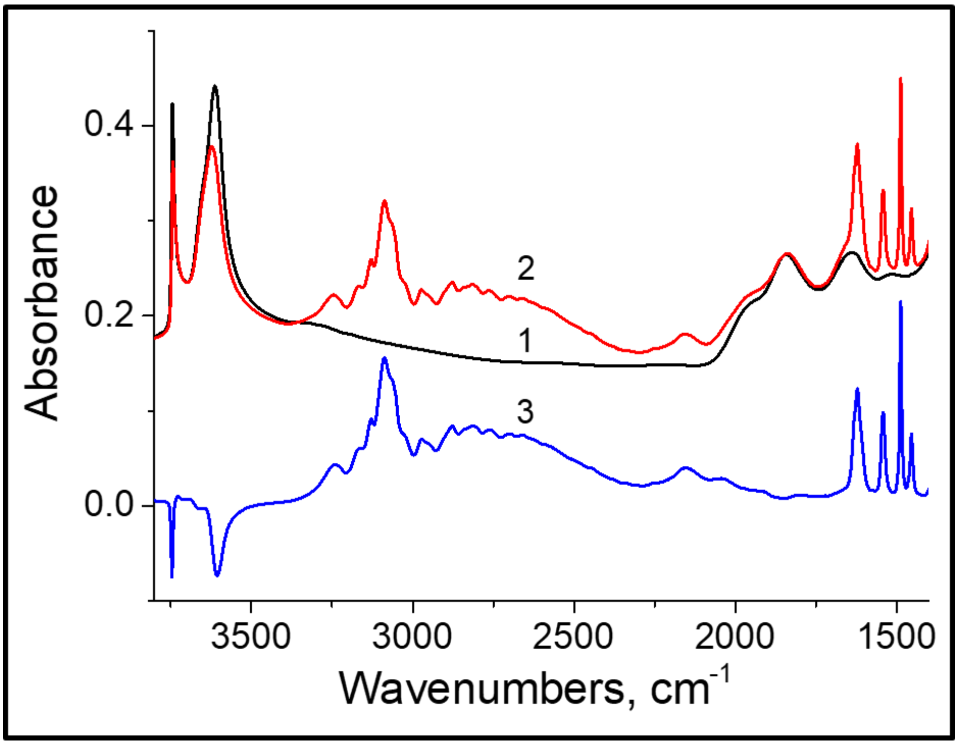

Figure 6.46: FTIR spectra of Rb-H-MAZ-1: (1) - the material before Py adsorption, (2) - the material after Py adsorption at 200°C and (3) - the difference spectrum.

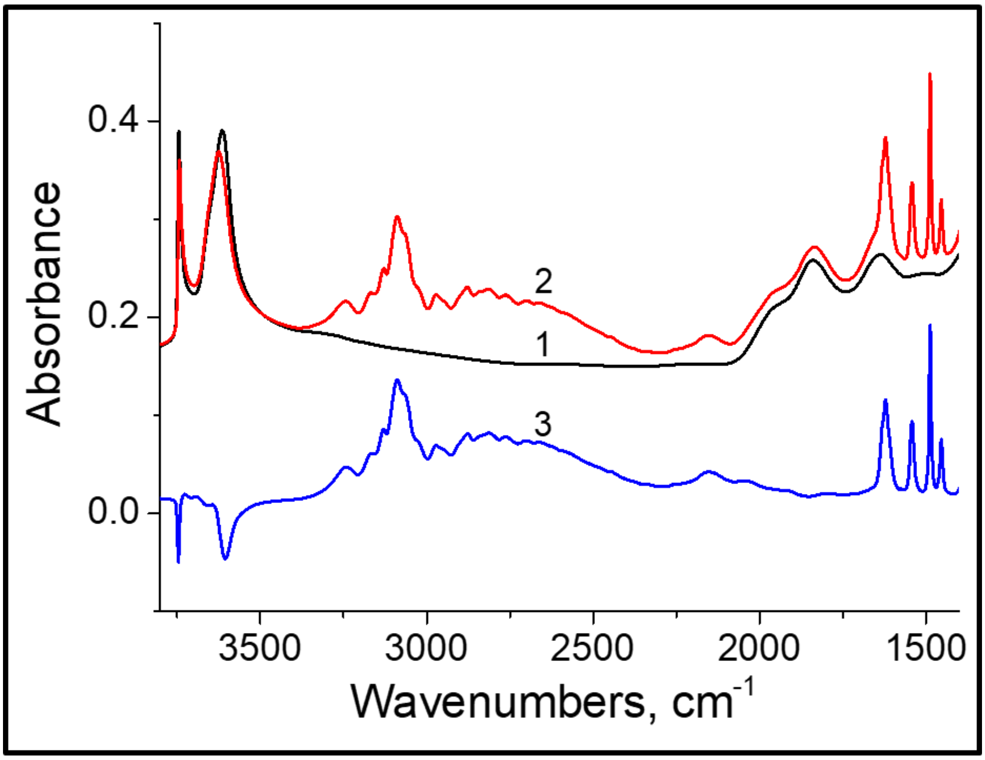

Figure 6.47: FTIR spectra of Cs-H-MAZ-1: (1) - the material before Py adsorption, (2) - the material after Py adsorption at 200ºC and (3) - the difference spectrum.

TGA

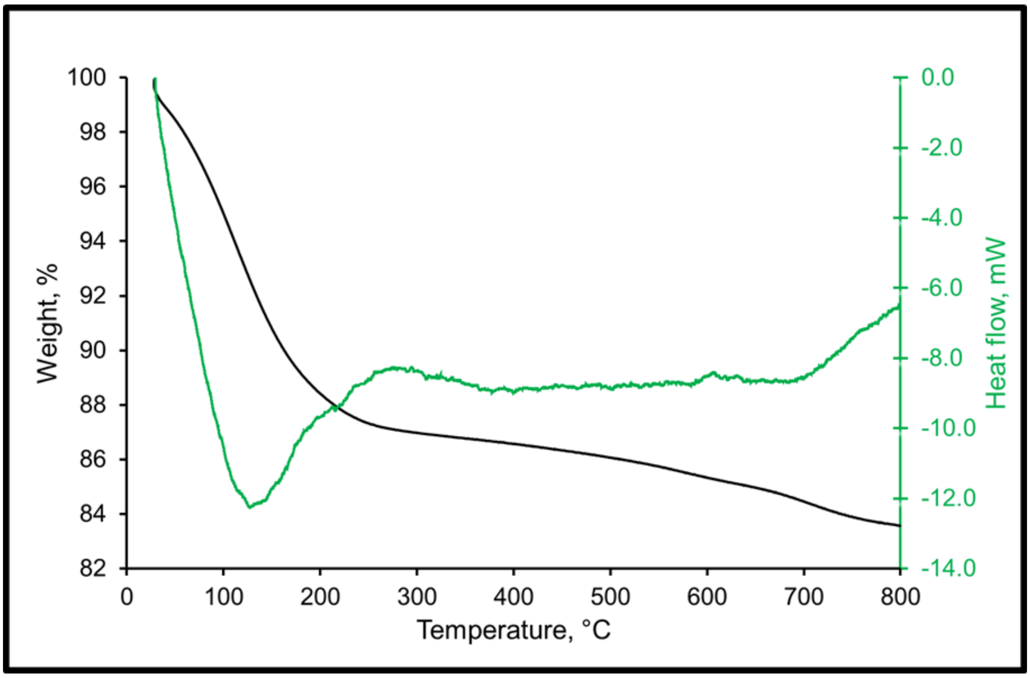

Figure 6.48: TGA curve and Heat flow of H-MAZ.

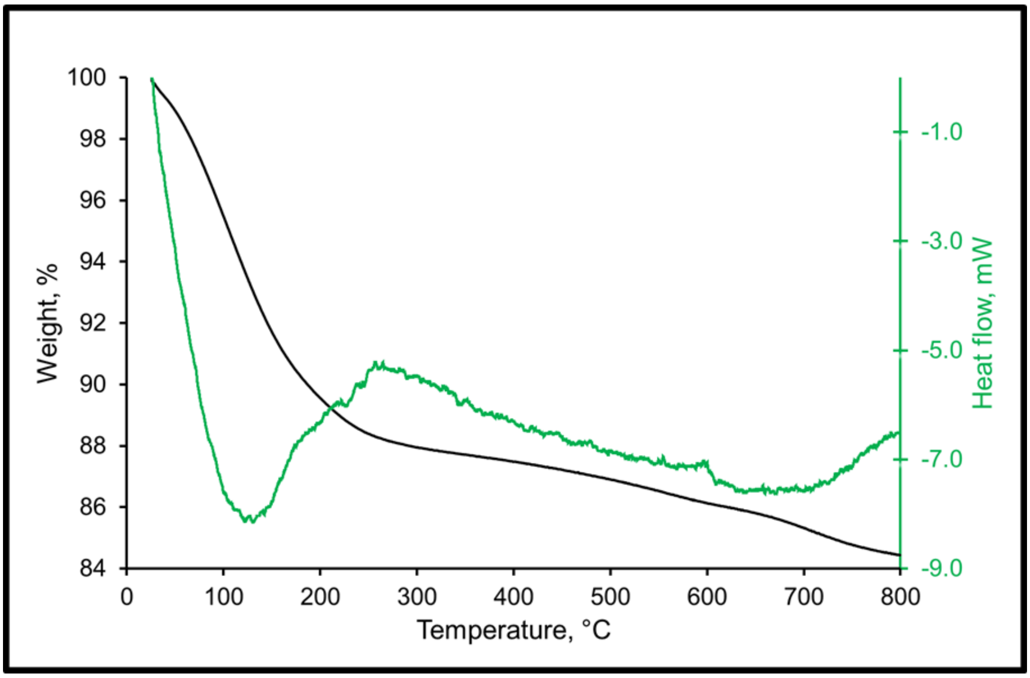

Figure 6.49: TGA curve and Heat flow of Li-H-MAZ-2.

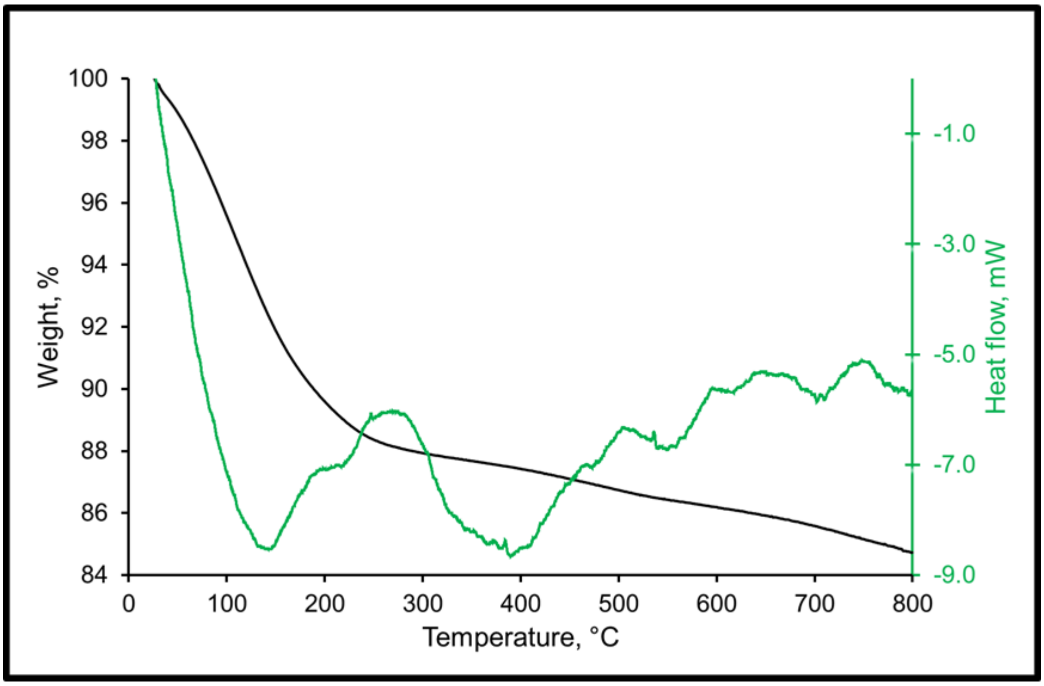

Figure 6.50: TGA curve and Heat flow of Na-H-MAZ-2.

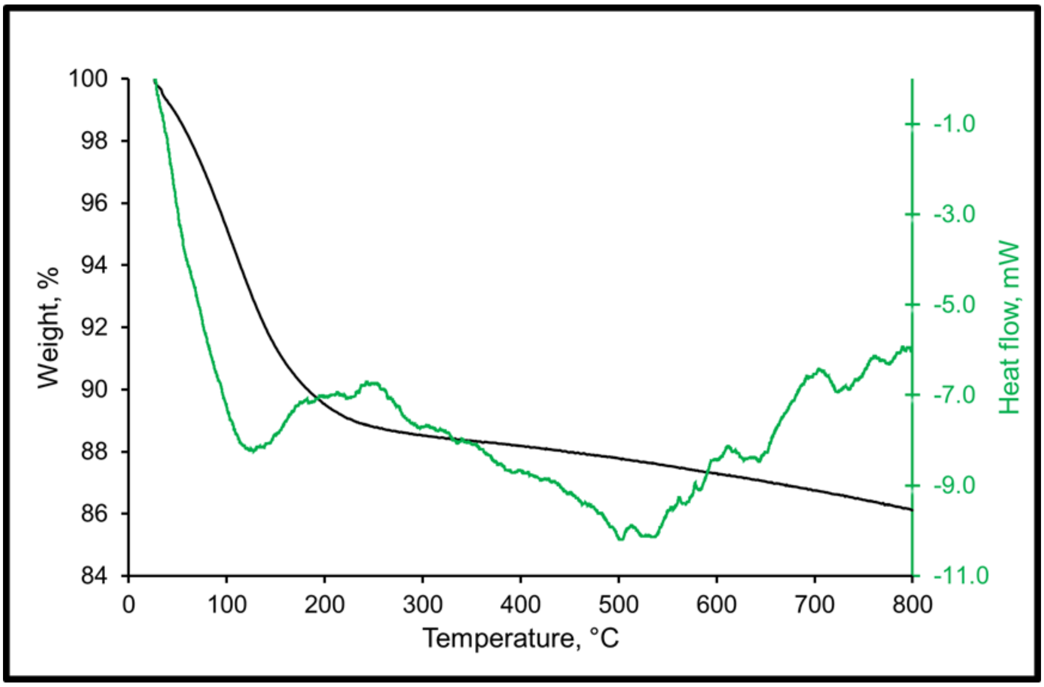

Figure 6.51: TGA curve and Heat flow of K-H-MAZ-2.

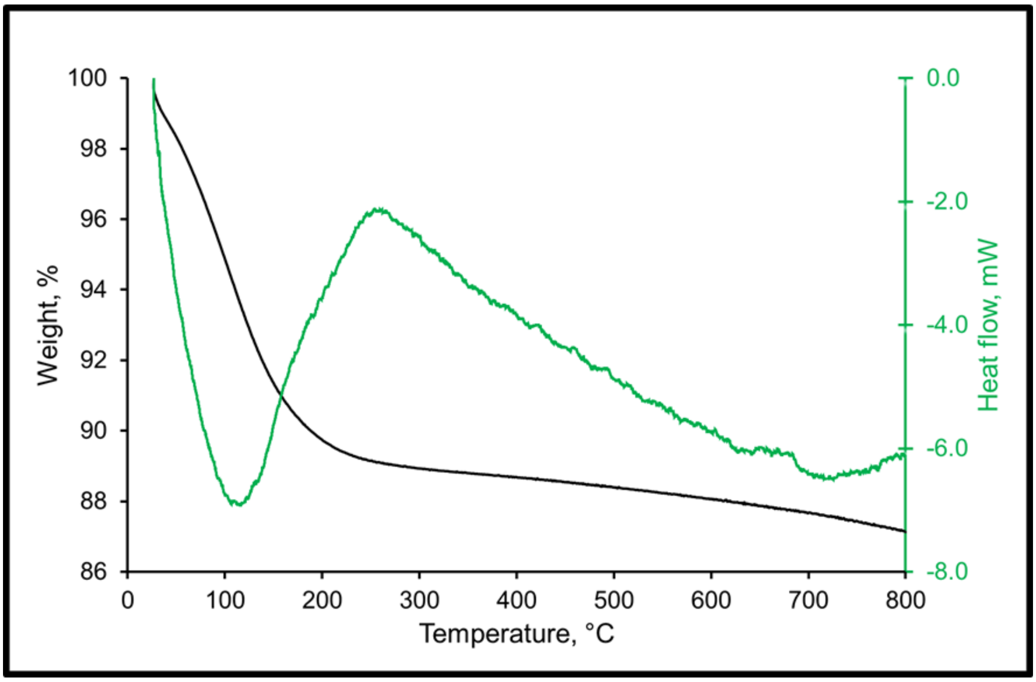

Figure 6.52: TGA curve and Heat flow of Rb-H-MAZ-2.

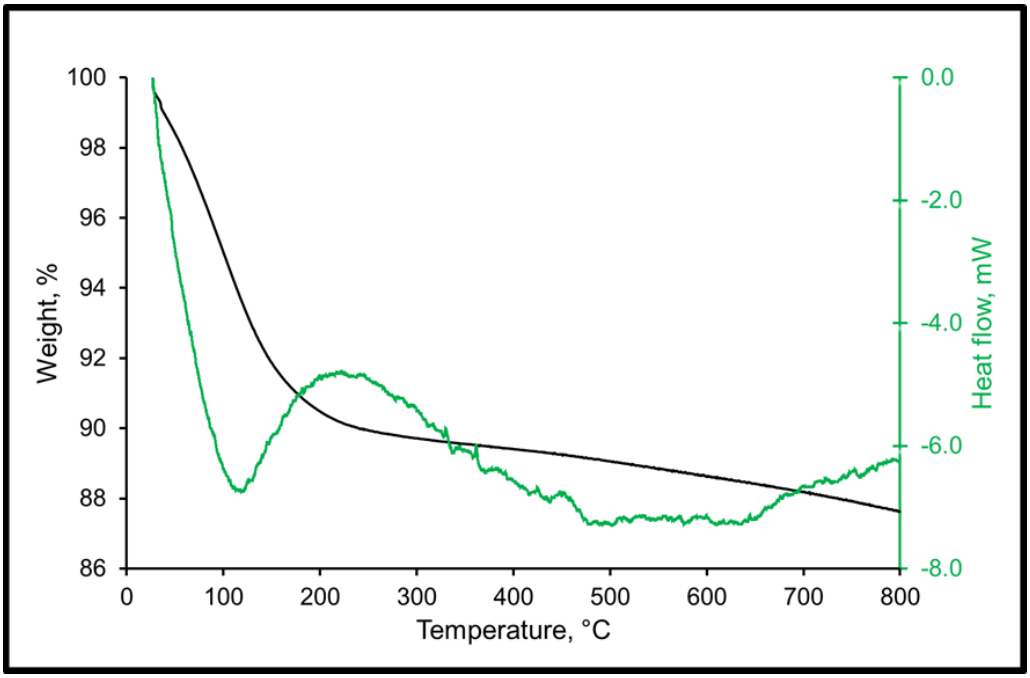

Figure 6.53: TGA curve and Heat flow of Cs-H-MAZ-2.